
Advancing solvent extraction technology for improved management of contaminated liquors

Izaak Fryer-Kanssen

Thesis submitted for the Degree of

Doctor of Philosophy

September 2017

Lancaster University

Department of Chemistry

Supervisor:

Andrew Kerridge

Industrial Supervisor:

Jonathan Austin (NNL)

I, Izaak Fryer-Kanssen, confirm that the work presented in this thesis is my own work, and has not been submitted for the award of a higher degree elsewhere. Where information has been derived from other sources, I confirm that this has been indicated in the thesis. In addition, I confirm that this thesis does not exceed the permitted maximum length.

Abstract

The separation of minor actinides (An) such as americium and curium (Am, Cm) from lanthanides (Ln) in spent nuclear fuel can reduce the radiotoxicity of the eventual waste product as well as the required size and environmental impact of any subsequent geological disposal. In addition, separation of these actinides from the lanthanides is essential for a strategy which aims to put the minor actinides back into the fuel cycle through transmutation by neutron bombardment, which would increase fuel efficiency.

This work uses Density Functional Theory (DFT) and the Quantum Theory of Atoms in Molecules (QTAIM) to investigate the structure, stabilities and covalency of complexes of the lanthanides and minor actinides with several nitrogen donor ligands which have been developed for the difficult task of An^{III}/Ln^{III} separation. A systematic QTAIM study of Ln bond characterisation across the series is reported for one such ligand, bis-triazinyl-pyridine (BTP), confirming the general assumption that bonding in these complexes is ionic in character and largely similar. A small yet significant increase of the charge accumulation in the bonds of the An complexes of BTP was observed, and DFT studies of the An and Ln complexes found a slight energetic preference of the ligand for An complexation, together implying a small electronic contribution to the experimentally observed selectivity of the BTP ligand. A second nitrogen donor ligand, bis-triazinyl-phenanthroline (BTPhen) was studied, finding slightly higher measures of covalency in the metal-ligand bonds and a greatly improved energetic preference for An complexation. The effects of the addition of electron-directing groups to this ligand were investigated, finding little difference in the measures of covalency for these modified ligands. Several other nitrogen donor and mixed nitrogen/oxygen donor ligands were studied, including a novel sandwich complex, ultimately demonstrating a tentative correlation between enhanced covalency and stability.

Acknowledgements

Above all, I would like to thank Andy Kerridge for giving me the opportunity to do this research, and for his invaluable support, guidance and patience throughout the past several years. Although I never thought I would say this, I would also like to thank Andy for the opportunity to move out of London and discover this quiet northern world of low rent in spitting distance of the Lake District.

I would also like to thank Nik Kaltsoyannis and Michael Peach, my secondary supervisors at UCL and Lancaster University, respectively, as well as Jonathan Austin, my industrial supervisor, all of whom have provided advice and assistance throughout my degree. Additionally, I am grateful to the NNL & the NDA for their support and funding, as well as the many conferences, meetings and tours of Sellafield they have organised.

The work presented here would have been significantly more difficult without the computing power of UCL's Legion HPC facility, the NSCCS Slater HPC facility, the High End Computing Cluster (HEC) at Lancaster University and the eternally noisy Roos. I would like to thank all of those who maintain and support these systems, particularly Mike Pacey at Lancaster University.

In a similar vein, I extend my gratitude to Peter Fielden, Lefteris Danos and the rest of the CBC for the purchase and maintenance of the departmental coffee machine.

Last but not at all least, thanks to Liv. I wish her all the best in the completion of her own thesis, and pledge to repay her in kind for her constant love and support.

Contents

Abstract	2
Acknowledgements	3
Table of Figures	8
Table of Tables	12
Chapter 1: Introduction	16
1.1 Spent Nuclear Fuel and the SANEX Process	16
1.2 N-Donor Ligands for Ln ^{III} /An ^{III} Separation	18
1.3 Experimental Studies of An ^{III} /Ln ^{III} complexes	22
1.3.1 Extended X-Ray Absorption Fine Structure Spectroscopy (EXAFS).....	22
1.3.2 Time-Resolved Laser Fluorescence Spectroscopy (TRLFS).....	23
1.3.3 Nano-Electrospray Mass Spectrometry	24
1.3.4 Nuclear Magnetic Resonance (NMR)	25
1.4 Theoretical Studies of An ^{III} /Ln ^{III} complexes.....	26
Chapter 2: Methodology	30
2.1 Basis Sets.....	30
2.2 Bra-Ket Notation	32
2.3 Variational Principle.....	32
2.4 The Schrödinger Equation.....	33
2.5 The Hamiltonian.....	33
2.6 The Born-Oppenheimer Approximation	34
2.7 The Orbital Approximation	35
2.8 Hartree-Fock Theory	35
2.9 Electron Correlation.....	37
2.10 Møller-Plesset Perturbation Theory	38
2.11 Density Functional Theory	39
2.11.1 The Hohenberg-Kohn Theorems.....	40

2.11.2 The Kohn-Sham Equations	40
2.11.3 Exchange-Correlation Functionals	42
2.11.3.1 The Local Density Approximation	43
2.11.3.2 GGA and Meta-GGA xc-Functionals	43
2.11.3.3 Hybrid-GGA and RPA xc-Functionals.....	44
2.12 Relativistic Effects	44
2.13 Effective Core Potentials.....	46
2.14 The Quantum Theory of Atoms in Molecules.....	46
2.14.1 Topological Properties of the Electron Density	49
2.14.2 Integrated Properties of the Electron Density.....	50
2.15 COSMO Solvation.....	51
2.16 Packages.....	52
Chapter 3: Nitrates of Ln and An.....	53
3.1 Introduction	53
3.2 Computational Details	54
3.3 Results.....	56
3.3.1 Trinitrate Binding Energies.....	56
3.3.2 Mononitrate Binding Energies	58
3.3.3 Investigating the xc-Functional Dependency.....	60
3.3.3.1 La ^{III} , Lu ^{III} , Gd ^{III} and Cm ^{III}	60
3.3.3.2 Eu ^{III} and Am ^{III}	63
3.3.4 Solvation of Nitrate Complexes	65
3.3.4.1 Explicit Hydration.....	65
3.3.4.2 Implicit Hydration	71
3.3.4.3 Explicit and Implicit Hydration.....	71
3.4 Conclusion.....	73
Chapter 4: BTP – Does Covalency Imply Stability?	75
4.1 Introduction	75

4.2 Computational Details	77
4.3 Results	78
4.3.1 Geometry	78
4.3.1.1 Aquo Ln Complexes.....	78
4.3.1.2 BTP Ln Complexes	82
4.3.1.3 Aquo & BTP An Complexes	83
4.3.2 QTAIM Analysis	84
4.3.2.1 Topological Analysis of the Electron Density	84
4.3.2.1.1 Aquo Ln Complexes.....	85
4.3.2.1.2 BTP Ln Complexes	87
4.3.2.2 Ln vs. An Bonding in $[M(H_2O)_9]^{3+}$ and $[M(BTP)_3]^{3+}$	89
4.3.3 Energetics.....	92
4.4 Conclusion.....	95
4.5 Publishing Notes	96
Chapter 5: BTPPhen, Modifications of BTPPhen and Other Ligands.....	97
5.1 Part I: BTPPhen vs. BTP	97
5.2 Computational Details	98
5.3 Part I: Results	98
5.3.1 Geometries.....	98
5.3.1.1 Hydrated Nitrate Eu/Am Complexes.....	99
5.3.1.2 BTPPhen Eu/Am Complexes.....	100
5.3.2 QTAIM Analysis	102
5.3.2.1 Eu versus Am Bonding in BTP and BTPPhen Complexes.....	102
5.3.2.2 Eu versus Am Bonding in Aquo and Nitrate Complexes	104
5.3.3 Energetics.....	106
5.3.4 Electron Density vs. Bond Path Length	107
5.4 Part I: Conclusion	108
5.5 Part II: Modifications of the BTPPhen Ligand	109

5.6: Part III: Results	111
5.6.1 Dibromo- & (4-Hydroxyphenyl)-BTPPhen Ligands	111
5.6.2 Dibromo- & (4-Hydroxyphenyl)-BTPPhen Complexes	114
5.6.3 Energetics.....	119
5.7 Part II: Conclusion	120
5.8 Part III: DTPA and Texaphyrin	121
5.8.1 DTPA.....	121
5.8.2 Texaphyrin.....	122
5.9 Part II: Results	123
5.9.1 DTPA Results	123
5.9.2 Texaphyrin Results	126
5.10 Part III: Conclusion	131
5.11 Electron Density vs. Bond Path Length Revisited	132
5.12 General Conclusions.....	133
Chapter 6: Conclusions	134
Appendix A: Data used to Construct Graphs.....	138
Appendix B: Spin Contamination	140
References.....	141

Table of Figures

Figure 1.1: The three stages of the SANEX process, using a separation ligand such as BTP, BTBP or BTPhen. ¹⁰	17
Figure 1.2: N-donor ligands used or proposed for use in the SANEX process for An ^{III} /Ln ^{III} separation: BTP (left), BTBP (middle) and BTPhen (right).	17
Figure 1.3: 2,2':6',2''-terpyridine (Terpy).	19
Figure 1.4: 2,4,6-tri(2-pyridyl)-1,3,5-triazine (TPTZ).	19
Figure 1.5: 2,6-bis(1,2,4-triazin-3-yl)pyridine (BTP), top, CyMe ₄ -BTP, middle, and BzCyMe ₄ -BTP, bottom.	20
Figure 1.6: 6,6'-bis(1,2,4-triazin-3-yl)-2,2'-bipyridine (BTBP).	21
Figure 1.7: 2,9-bis(1,2,4-triazin-3-yl)-1,10-phenanthroline (BTPhen).	21
Figure 1.8: tris((2-pyrazinyl)methyl)amine (TPZA) ligand studied by Denecke et al. ³⁷	23
Figure 2.1: Example of an STO (blue) and a GTO (red).	31
Figure 2.2: Flow diagram for the self-consistent field approach.	37
Figure 2.3: The Jacob's Ladder of xc-functionals, with examples of non-empirical and semi-empirical xc-functionals shown in blue and red, respectively. Reproduced from Perdew, J.P. and Schmidt, K., "Jacob's ladder of density functional approximations for the exchange-correlation energy". ⁷⁸	42
Figure 2.4 Contour plot of the electron density for benzene, showing the nuclear critical points (NCPs, brown circles), bond critical points (BCPs, blue circles), ring critical point (RCP, orange circle) and zero-flux surfaces (blue lines) of the molecule, generated with MultiWFN. ⁹⁷	47
Figure 2.5 Plot of the gradient vector field of the electron density for benzene, showing the nuclear critical points (NCPs, brown circles), bond critical points (BCPs, blue circles), ring critical point (RCP, orange circle) and zero-flux surfaces (blue lines) of the molecule, generated with MultiWFN. ⁹⁷	47
Figure 3.1: Sample optimised Ln/An(NO ₃) ₃ complex.	56
Figure 3.2: Sample optimised [Ln/An(NO ₃) ₃] ²⁺ complex.	58

Figure 3.3: Functional dependence of $[\text{Ln}/\text{An}(\text{NO}_3)]^{2+}$ (Ln = La, Lu, Gd; An = Cm) binding energies, compared to MP2 values (horizontal dashed lines).....	61
Figure 3.4: Functional dependency of $\text{Ln}/\text{An}(\text{NO}_3)_3$ (Ln = La, Lu, Gd; An = Cm) binding energies, compared to MP2 values (horizontal dashed lines).....	63
Figure 3.6: Initial $\text{Ln}/\text{An}(\text{NO}_3)_3(\text{H}_2\text{O})_x$ (Ln = La, Lu, Gd; Cm = Cm, x = 1-5) complex structures, prior to geometry optimisation.	66
Figure 3.7: The optimised 10-coordinate La complex 5a, left, and the 11-coordinate La complex 6a, right.	68
Figure 3.8: The optimised 10-coordinate Lu complex 4a.	68
Figure 3.9: The optimised 8-coordinate Lu complex 5a, left, and the 9-coordinate Lu complex 5a', right, re-optimised from the La 5a complex.	69
Figure 3.11: The optimised 9-coordinate Cm complex 3c, left, and the 10-coordinate Cm complex 4a, right.	70
Figure 3.12: BHLYP/def(2)-SVP-optimised 9-coordinate complexes $\text{Gd}(\text{NO}_3)_3(\text{H}_2\text{O})_3$, left and $\text{Cm}(\text{NO}_3)_3(\text{H}_2\text{O})_3$, right.	73
Figure 3.13: BHLYP/def(2)-SVP-optimised 10-coordinate complexes $\text{Gd}(\text{NO}_3)_3(\text{H}_2\text{O})_4$, left and $\text{Cm}(\text{NO}_3)_3(\text{H}_2\text{O})_4$, right.	73
Figure 4.1: 2,6-bis(1,2,4-triazin-3-yl)pyridine (BTP).....	75
Figure 4.2: Example of the optimised $[\text{Ln}(\text{H}_2\text{O})_9]^{3+}$ complex geometry. Multiple viewing angles shown.....	79
Figure 4.3: Mean Ln—O bond lengths for $[\text{Ln}(\text{H}_2\text{O})_9]^{3+}$ (Ln = Ce – Lu) complexes calculated using the BLYP, B3LYP and BHLYP xc-functionals, obtained in the presence of a continuum solvent, compared to experimental values obtained with EXAFS. ¹⁵⁵	81
Figure 4.4: Example of the optimised $[\text{Ln}(\text{BTP})_3]^{3+}$ complex geometry.	82
Figure 4.5: Mean Ln—N bond lengths for $[\text{Ln}(\text{BTP})_3]^{3+}$ complexes calculated using the BLYP, B3LYP and BHLYP xc-functionals, optimised in the presence of a continuum solvent, compared to experimental values obtained with EXAFS and XRD. ^{37,39,57,121–123}	83
Figure 4.6: Representative molecular graph of $[\text{M}(\text{BTP})_3]^{3+}$. Light blue, red, blue, grey and white spheres represent the metal ion and O, N, C and H atoms respectively while the green	

and red spheres represent bond critical points and ring critical points, respectively. Selected M—N and inter-ligand bonds have been omitted for clarity.	85
Figures 4.7i-4.7vi: Mean values of ρ (i, iv), $\nabla^2\rho$ (ii, v) and H (iii, vi) at the Ln—O BCPs of $[\text{Ln}(\text{H}_2\text{O})_9]^{3+}$ (Ln = Ce – Lu), calculated with BHLYP (i-iii) and B3LYP (iv-vi) and plotted against the f-electron count of the Ln ion. Error bars depict the mean average deviation.....	86
Figures 4.8i-4.8vi: Mean values of ρ (i, iv), $\nabla^2\rho$ (ii, v) and H (iii, vi) at the Ln—N BCPs of $[\text{Ln}(\text{BTP})_3]^{3+}$ (Ln = Ce – Lu), calculated with BHLYP (i-iii) and B3LYP (iv-vi) and plotted against the f-electron count of the Ln ion. Error bars depict the mean average deviation.....	88
Figure 4.9: Energies of Reaction 4a for Ln = Ce – Lu and An = Am, calculated using the BHLYP/def(2)-TZVP//BHLYP/def(2)-SVP and B3LYP/def(2)-TZVP//B3LYP/def(2)-SVP model chemistries. * $[\text{Ln}(\text{BTP})_3]^{3+}$ SPE obtained using the spin-constrained approach of Andrews et al. ¹⁵⁸ $^+[\text{Ln}(\text{BTP})_3]^{3+}$ and $[\text{Ln}(\text{H}_2\text{O})_9]^{3+}$ SPEs both obtained using the spin-constrained approach. Only reaction energies for An = Am are displayed; an identical trend is seen for An = Cm, shifted upward by 0.06 eV with BHLYP and down by 0.05 eV with B3LYP. An anomalous reaction energy for Ln = Pm is omitted for clarity.....	94
Figure 5.1: 2,9-bis(1,2,4-triazin-3-yl)-1,10-phenanthroline (BTPhen).....	97
Figure 5.2: BHLYP/def(2)-SVP-optimised geometries of $[\text{Eu}(\text{NO}_3)_3(\text{H}_2\text{O})_x]$ ($x = 3$, left, and $x = 4$, right), also representative of the Am structures.	100
Figure 5.3: BHLYP/def(2)-SVP-optimised geometry of $[\text{Eu}(\text{BTPhen})_2(\text{NO}_3)]^{2+}$, also representative of the Am complex. Multiple viewing angles shown.	101
Figure 5.4: Plot of ρ_{BCP} against bond path length for $[\text{Eu}/\text{Am}(\text{BTP})_3]^{3+}$ and $[\text{Eu}/\text{Am}(\text{BTPhen})_2(\text{NO}_3)_2]^{2+}$	108
Figure 5.5: 2,9-bis(1,2,4-triazin-3-yl)-1,10-phenanthroline (BTPhen), showing the substitution sites (4-7) investigated in this work.....	109
Figure 5.6: 5,6-dibromo- (left) and 5-(4-hydroxyphenyl)-BTPhen (right).	110
Figure 5.7: 5,6-dibromo-BTPhen (1, left) and 5-(4-hydroxyphenyl)-BTPhen (2, right). Binding nitrogens on the phenanthroline (N_{Ph} , N'_{Ph}) and triazine (N_{Tz} , N'_{Tz}) moieties are labelled. ..	112
Figure 5.8: 4,7-dibromo-BTPhen (3, left) and 4-(4-hydroxyphenyl)-BTPhen (4, right). Binding nitrogens on the phenanthroline (N_{Ph} , N'_{Ph}) and triazine (N_{Tz} , N'_{Tz}) moieties are labelled. ..	113

Figure 5.9: BHLYP/def(2)-SVP-optimised geometries of $[\text{Eu}(1)_2(\text{NO}_3)]^{2+}$, top, and $[\text{Eu}(2)_2(\text{NO}_3)]^{2+}$, bottom. Both examples are also representative of their respective Am complexes.	115
Figure 5.10: BHLYP/def(2)-SVP-optimised geometries of $[\text{Eu}(3)_2(\text{NO}_3)]^{2+}$, top, and $[\text{Eu}(4)_2(\text{NO}_3)]^{2+}$, bottom. Both examples are also representative of their respective Am complexes.	116
Figure 5.11: 2,2',2'',2'''-((((carboxymethyl)azanediyl)bis(ethane-2,1-diyl))bis(azanetriyl))tetraacetic acid Diethylenetriaminepentaacetic acid (DTPA, top) and 2,2'-((((carboxymethyl)azanediyl)bis(ethane-2,1-diyl))bis((2-amino-2-oxoethyl)azanediyl))diacetic acid (NH ₂ -DTPA, bottom)	121
Figure 5.12: Texaphyrin ligand.....	122
Figure 5.13: BHLYP/def(2)-SVP-optimised complexes of $[\text{Eu}(\text{DTPA})(\text{H}_2\text{O})]^{2+}$, left, and $[\text{Eu}(\text{NH}_2\text{-DTPA})(\text{H}_2\text{O})]^{2+}$, right. Structure shown is also representative of the Am complex. Hydrogen atoms are omitted for clarity.....	123
Figure 5.14: Optimised BHLYP/def(2)-SVP $\text{Eu}(\text{Tex})(\text{NO}_3)_2(\text{H}_2\text{O})$ complex. Multiple viewing angles are shown, and the structure is also representative of the Am complex.	126
Figure 5.15: B3LYP/def(2)-SVP-optimised $[\text{Eu}(\text{Tex})_2]^+$ complex. General structure is also representative of the Am complex.	129
Figure 5.16: Plot of ρ_{BCP} against bond path length for $[\text{Eu}/\text{Am}(\text{BTP})_3]^{3+}$, $[\text{Eu}/\text{Am}(\text{BTPhen})_2(\text{NO}_3)_2]^{2+}$, $[\text{Eu}(\text{Tex})_2]^+$ and $\text{Am}(\text{Tex})(\text{NO}_3)_3(\text{H}_2\text{O})$	132

Table of Tables

Table 3.1: SCF binding energies, E_b , calculated with Eq. 3.1, and spin expectation values, $\langle S^2 \rangle$, for $\text{Ln}/\text{An}(\text{NO}_3)_3$ (Ln = La, Lu, Gd; An = Cm), calculated using the sECP, AE and IC methods on PBE/def(2)-TZVP model chemistries.....	57
Table 3.2: SCF binding energies, E_b , calculated with Eq. 3.2, and spin expectation values, $\langle S^2 \rangle$, for $[\text{Ln}/\text{An}(\text{NO}_3)]^{2+}$ (Ln = La, Lu, Gd; An = Cm) using the sECP, AE and IC DFT methods on PBE/def(2)-TZVP and PBE0/def(2)-TZVP model chemistries, compared to MP2-calculated binding energies and spin expectation values.	59
Table 3.3: SCF binding energies, E_b , calculated with Eq. 3.2, and spin expectation values, $\langle S^2 \rangle$, for $[\text{Ln}/\text{An}(\text{NO}_3)]^{2+}$ (Ln = La, Lu, Gd; An = Cm) using the sECP method and a series of xc-functionals on def(2)-TZVP model chemistries, compared to MP2-calculated binding energies and spin expectation values.....	60
Table 3.4: SCF binding energies, E_b , calculated with Eq. 3.1, and spin expectation values, $\langle S^2 \rangle$, for $\text{Ln}/\text{An}(\text{NO}_3)_3$ (Ln = La, Lu, Gd; An = Cm) using the sECP method and a series of xc-functionals, compared to MP2-calculated binding energies and spin expectation values.	62
Table 3.5: SCF binding energies, E_b , calculated with Eq. 3.1, and the difference between the calculated and ideal spin expectation values, $\langle S^2 \rangle_{\text{calc}} - \langle S^2 \rangle_{\text{ideal}}$, for $\text{Ln}/\text{An}(\text{NO}_3)_3$ (Ln = Eu, Gd; An = Am, Cm) using the sECP method and the BLYP, B3LYP and BHLYP xc-functionals. ($\langle S^2 \rangle_{\text{ideal}} = 12$ for Eu and Am, 15.75 for Gd and Cm).....	64
Table 3.6: Binding modes, first-shell hydration numbers, coordination numbers and binding energies, E_b , for $\text{Ln}/\text{An}(\text{NO}_3)_3(\text{H}_2\text{O})_x$ (Ln = La, Lu, Gd; An = Cm). The binding mode is comprised of three letters describing the denticity of the three nitrate ligands, with ‘b’ denoting a bidentate binding mode, and ‘m’ a monodentate binding mode. †Re-optimised using the optimised 5a complex of La as the initial geometry. ††Re-optimised using the optimised 3c complex of Cm as the initial geometry.....	67
Table 3.7: Average M—O bond lengths of BLYP/def(2)-SVP-, B3LYP/def(2)-SVP- and BHLYP/def(2)-SVP-calculated $\text{Ln}/\text{An}(\text{NO}_3)_3$ (Ln = La, Lu, Gd; An = Cm) geometries. All values are in angstroms (Å).....	71
Table 3.8: Average M—O _N and M—O _H bond lengths of BLYP/def(2)-SVP-calculated $\text{Gd}/\text{Cm}(\text{NO}_3)_3(\text{H}_2\text{O})_x$ (x = 3, 4) geometries. All values are in angstroms (Å).	72

Table 4.1: Mean Ln—O bond lengths for $[\text{Ln}(\text{H}_2\text{O})_9]^{3+}$ (Ln = Ce – Lu) complexes calculated using the BLYP, B3LYP and BHLYP <i>xc</i> -functionals, compared to literature theoretical data and experimental values obtained with EXAFS. ¹⁵⁵ All values are in angstroms (Å).....	79
Table 4.2: Mean Ln—O bond lengths for $[\text{Ln}(\text{H}_2\text{O})_9]^{3+}$ (Ln = Ce – Lu) complexes calculated using the BLYP, B3LYP and BHLYP <i>xc</i> -functionals, obtained in the presence of a continuum solvent, compared to experimental values obtained with EXAFS. ¹⁵⁵ All values are in angstroms (Å).....	80
Table 4.3: Mean Ln—N bond lengths for $[\text{Ln}(\text{BTP})_3]^{3+}$ complexes calculated using the BLYP, B3LYP and BHLYP <i>xc</i> -functionals, optimised in the presence of a continuum solvent, compared to literature theoretical data and experimental values obtained with EXAFS and XRD. ^{37,39,57,121–123} All values are in angstroms (Å).	82
Table 4.4: Mean M—O and M—N bond lengths for $[\text{Ln}/\text{An}(\text{H}_2\text{O})_9]^{3+}$ and $[\text{Ln}/\text{An}(\text{BTP})_3]^{3+}$ calculated using the BLYP, B3LYP and BHLYP <i>xc</i> -functionals, optimised in the presence of a continuum solvent and compared to literature experimental values obtained with EXAFS. ^{37,55,155,156} All values are in angstroms (Å).	84
Table 4.5: Topological and integrated properties of BHLYP/def(2)-TZVP//BHLYP/def(2)-SVP- and B3LYP/def(2)-TZVP//B3LYP/def(2)-SVP-calculated ^a electron densities of $[\text{Ln}/\text{An}(\text{BTP})_3]^{3+}$ and $[\text{Ln}/\text{An}(\text{H}_2\text{O})_9]^{3+}$ (Ln = Eu, Gd; An = Cm, Am). ^b	90
Table 4.6: SCF energies of Reaction 4a for Ln = Eu/Gd and An = Am/Cm, calculated using the BHLYP/def(2)-TZVP//BHLYP/def(2)-SVP and BHLYP/def(2)-TZVP//BHLYP/def(2)-SVP model chemistries. Values in parentheses obtained using the BHLYP/def(2)-TZVP model chemistry. * $[\text{Gd}(\text{BTP})_3]^{3+}$ single-point energy obtained using the spin-constrained approach of Andrews et al. ¹⁵⁸	92
Table 5.1: Average M—O _N and M—O _H bond lengths of BHLYP/def(2)-SVP and B3LYP/def(2)-SVP calculated $[\text{Eu}/\text{Am}(\text{NO}_3)_3(\text{H}_2\text{O})_x]$ (<i>x</i> = 3, 4) geometries. B3LYP-derived values are given in parentheses. All values are in angstroms (Å).....	100
Table 5.2: Average M—N and M—O _N bond lengths of BHLYP/def(2)-SVP- and B3LYP/def(2)-SVP-calculated $[\text{Eu}/\text{Am}(\text{BTP})_3]^{3+}$ and $[\text{Eu}/\text{Am}(\text{BTPPhen})_2(\text{NO}_3)]^{2+}$ geometries. B3LYP-derived values are given in parentheses. All values are in angstroms (Å).	102
Table 5.3: Topological and integrated properties of BHLYP/def(2)-TZVP//BHLYP/def(2)-SVP- and B3LYP/def(2)-TZVP//B3LYP/def(2)-SVP-calculated electron densities of $[\text{Eu}/\text{Am}(\text{BTP})_3]^{3+}$ and $[\text{Eu}/\text{Am}(\text{BTPPhen})_2(\text{NO}_3)_2]^{2+}$. ^a	103

Table 5.4: Topological and integrated properties of BHLYP/def(2)-TZVP//BHLYP/def(2)-SVP- and B3LYP/def(2)-TZVP//B3LYP/def(2)-SVP-calculated electron densities of $[\text{Eu}/\text{Am}(\text{H}_2\text{O})_9]^{3+}$ and $[\text{Eu}/\text{Am}(\text{NO}_3)_3(\text{H}_2\text{O})_x]$ ($x = 3, 4$). ^a	105
Table 5.5: SCF energies of reactions 4a and 5a-5f, calculated using the BHLYP/def(2)-TZVP//BHLYP/def(2)-SVP and B3LYP/def(2)-TZVP//BHLYP/def(2)-SVP model chemistries. B3LYP-derived values are given in parentheses.	106
Table 5.6: Integrated properties of BHLYP/def(2)-TZVP//BHLYP/def(2)-SVP-calculated electron densities of ligands BTPPhen, 1, and 2. ^a	112
Table 5.7: Integrated properties of BHLYP/def(2)-TZVP//BHLYP/def(2)-SVP-calculated electron densities of ligands BTPPhen, 3, and 4. ^a	113
Table 5.8: Average M—N and M—O _N bond lengths of BHLYP/def(2)-SVP- and B3LYP/def(2)-SVP-calculated $[\text{Eu}/\text{Am}(\text{L})_2(\text{NO}_3)]^{2+}$ geometries (L = BTPPhen, 1-4). B3LYP-derived values are given in parentheses. All values are in angstroms (Å).	114
Table 5.9: Topological and integrated properties of BHLYP/def(2)-TZVP//BHLYP/def(2)-SVP- and B3LYP/def(2)-TZVP//B3LYP/def(2)-SVP-calculated electron densities of $[\text{Eu}/\text{Am}(\text{L})_2(\text{NO}_3)]^{2+}$ (L = BTPPhen, 1-4). ^a	118
Table 5.10: SCF energies of reactions 5c and 5g-5n, calculated using the BHLYP/def(2)-TZVP//BHLYP/def(2)-SVP and B3LYP/def(2)-TZVP//BHLYP/def(2)-SVP model chemistries. B3LYP-derived values are given in parentheses.	119
Table 5.11: Average M—N, M—O _{DTPA} and M—O _H bond lengths of BHLYP/def(2)-SVP-calculated $[\text{Eu}/\text{Am}(\text{DTPA})(\text{H}_2\text{O})]^{2-}$ and $\text{Eu}/\text{Am}(\text{NH}_2\text{-DTPA})(\text{H}_2\text{O})$ geometries. All values are in angstroms (Å).	124
Table 5.12: Topological and integrated properties of BHLYP/def(2)-TZVP//BHLYP/def(2)-SVP-calculated electron densities of $[\text{Eu}/\text{Am}(\text{DTPA})(\text{H}_2\text{O})]^{2-}$ and $\text{Eu}/\text{Am}(\text{NH}_2\text{-DTPA})(\text{H}_2\text{O})$. ^a	125
Table 5.13: SCF energies of reactions 5p-5t, calculated using a BHLYP/def(2)-TZVP//BHLYP/def(2)-SVP model chemistry.	125
Table 5.14: Average M—N, M—O _N and M—O _H bond lengths of BHLYP/def(2)-SVP- and B3LYP/def(2)-SVP-calculated $\text{Eu}/\text{Am}(\text{Tex})(\text{NO}_3)_2(\text{H}_2\text{O})$ geometries. All values are in angstroms (Å).	127
Table 5.15: Topological and integrated properties of BHLYP/def(2)-TZVP//BHLYP/def(2)-SVP-calculated electron densities of $\text{Eu}/\text{Am}(\text{Tex})(\text{NO}_3)_2(\text{H}_2\text{O})$. ^a	128

Table 5.16: SCF energies of reactions 5u and 5v, calculated using a BHLYP/def(2)-TZVP//BHLYP/def(2)-SVP model chemistry.	128
Table 5.17: Topological and integrated properties of BHLYP/def(2)-TZVP//B3LYP/def(2)-SVP-calculated electron densities of [Eu/Am(Tex) ₂] ⁺ . ^a	130
Table 5.18: SCF energies of reactions 5w-5z, calculated using a BHLYP/def(2)-TZVP//B3LYP/def(2)-SVP model chemistry.....	130
Table A.1: Data used to construct Figures 4.7i-4.7vi; Mean values of ρ_{BCP} , $\nabla^2\rho_{\text{BCP}}$ and H_{BCP} at the Ln—O and Ln—N BCPs of [Ln(H ₂ O) ₉] ³⁺ and [Ln(BTP) ₃] ³⁺ (Ln = Ce – Lu), calculated with BHLYP. All values are given in a.u.	138
Table A.2: Data used to construct Figures 4.8i-4.8vi; Mean values of ρ_{BCP} , $\nabla^2\rho_{\text{BCP}}$ and H_{BCP} at the Ln—O and Ln—N BCPs of [Ln(H ₂ O) ₉] ³⁺ and [Ln(BTP) ₃] ³⁺ (Ln = Ce – Lu), calculated with B3LYP. All values are given in a.u.....	139
Table A.3: Data used to construct Figure 4.9; Energies of Reaction 4a for Ln = Ce – Lu and An = Am, calculated using the BHLYP/def(2)-TZVP//BHLYP/def(2)-SVP and B3LYP/def(2)-TZVP//B3LYP/def(2)-SVP model chemistries. *[Ln(BTP) ₃] ³⁺ SPE obtained using the spin-constrained approach of Andrews et al. ¹⁵⁸ †[Ln(BTP) ₃] ³⁺ and [Ln(H ₂ O) ₉] ³⁺ SPEs both obtained using the spin-constrained approach. Only reaction energies for An = Am are displayed; an identical trend is seen for An = Cm, shifted upward by 0.06 eV with BHLYP and down by 0.05 eV with B3LYP. An anomalous reaction energy for Ln = Pm is omitted for clarity.	140
Table B.1: Comparison between theoretical and calculated expectation values of $\langle S^2 \rangle$ obtained for [Ln(H ₂ O) ₉] ³⁺ and [Ln(BTP) ₃] ³⁺ with the BLYP, B3LYP and BHLYP xc-functionals and the def(2)-SVP basis set.	140

Chapter 1: Introduction

In this thesis, computational methods have been used to investigate the basic underlying processes governing the successful separation of the trivalent actinides and lanthanides in nuclear waste. In this chapter, the context of this research and the relevant literature is discussed, beginning with the broad context of the management and separation of spent nuclear fuel.

1.1 Spent Nuclear Fuel and the SANEX Process

Spent nuclear fuel consists mainly of a mixture of uranium (U) and plutonium (Pu), a small amount of the minor actinides (An), typically considered to comprise neptunium, americium and curium (Np, Am and Cm, respectively) as well as fission products such as the lanthanides (Ln) and transition metals. U and Pu are typically recovered from spent fuel *via* the PUREX (Plutonium and URanium EXtraction) process, producing a raffinate which contains a mixture of the lanthanides and minor actinides, the latter of which are responsible for most of the residual radioactivity.^{1,2} Once U and Pu have been extracted, the challenge is dealing with the long-lived trivalent minor actinides, An^{III}, which account for a mere 0.1 wt% of high level nuclear waste (e.g. spent fuel rods and waste materials from reprocessing) and yet pose a significant danger due to their strong radiotoxicity and lifetimes in the region of 1×10^6 years.¹⁻³ Removal of these minor actinides can reduce the radiotoxicity of the eventual waste product derived from PUREX raffinate, reducing the required size and environmental impact of any subsequent geological disposal. As areas with suitable geology, size and permission to build a waste repository are in short supply, reducing these requirements is a major goal.

The main challenge of actinide extraction is that lanthanides (Ln^{III}, e.g. Eu^{III}) are also present in waste, and in much greater quantity, making selective An^{III} extraction difficult due to the similar chemical properties of the two groups (ionic radii, coordination numbers).^{4,5} Additionally, An^{III}/Ln^{III} separation is essential for the 'Partitioning and Transmutation' concept, which aims to put minor actinides back into the fuel cycle through transmutation by neutron bombardment,⁶ and is impossible in the presence of Ln^{III} ions due to their large neutron cross-section.⁷⁻⁹ Hence, separation of these minor actinides from the lanthanides is essential not only for more cost-effective storage of nuclear waste but also for increased fuel efficiency.

The SANEX (Selective ActiNide EXtraction) process, summarised in **Figure 1.1**, is a ligand-based approach to Ln^{III}/An^{III} separation which utilises the preference of ligands such as bis-triazinyl-pyridines, bis-triazinyl-bipyridines and bis-triazinyl-phenanthrolines (BTPs, BTBPs and

BTPPhens, **Figure 1.2**, also discussed later in this chapter) for complexation with An^{III} over Ln^{III} .^{2,10,11}

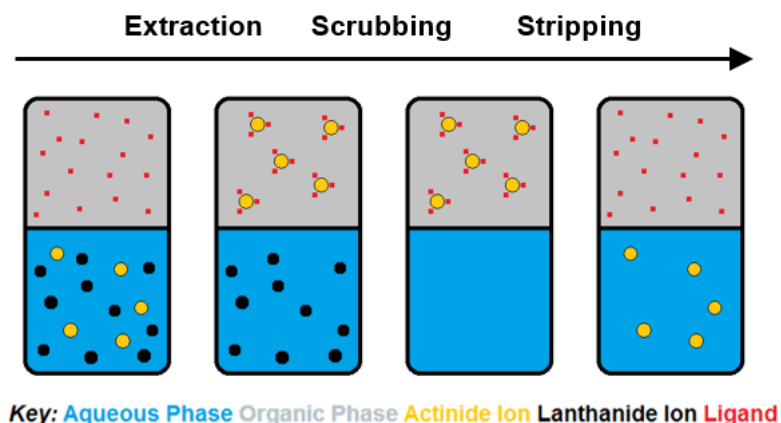


Figure 1.1: The three stages of the SANEX process, using a separation ligand such as BTP, BTBP or BTPPhen.¹⁰

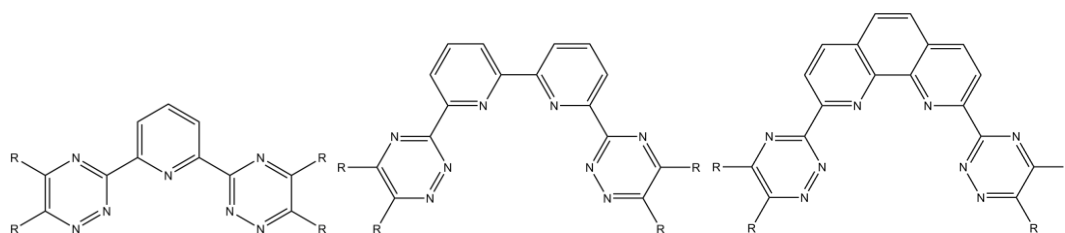


Figure 1.2: N-donor ligands used or proposed for use in the SANEX process for An^{III}/Ln^{III} separation: BTP (left), BTBP (middle) and BTPPhen (right).

The SANEX process has three general stages (**Figure 1.1**).^{2,10,11} First, the waste liquid, containing a mixture of An^{III} and Ln^{III} , is mixed with an organic layer containing the extractant and the An^{III} ions are extracted into the organic phase, forming complexes with the BTP ligands. The aqueous phase can then be scrubbed with nitric acid, and lastly the An^{III} ions can be stripped from the ligands and back-extracted into the aqueous phase. This process is repeated until the An^{III} and Ln^{III} ions are fully separated (~99.9% An^{III} product).^{2,10,11}

The advantages of this solvent extraction process are that it does not require a large energy input, such as other methods like evaporation or distillation, and that the organic phase can usually be recycled, meaning that a smaller amount of chemicals are consumed compared to processes such as precipitation, where the solvent is lost. Furthermore the selectivity exhibited is excellent, leading to high yields of An^{III} and Ln^{III} .¹²⁻¹⁴ However, the design of ligands for use in the SANEX process is challenging due to the harsh, highly acidic conditions and significant radioactivity that the ligand must be capable of withstanding.¹⁵⁻¹⁷ Nevertheless,

significant advances in the design of ligands for Ln^{III}/An^{III} separation have been made as discussed in the following section, although the origin of the selectivity of these ligands is still under investigation, which the work presented in this thesis aims to contribute to.¹⁵⁻¹⁷

1.2 N-Donor Ligands for Ln^{III}/An^{III} Separation

Prior to the 1980s, studies of trivalent lanthanide and actinide complexes were almost exclusively performed with oxygen or mixed oxygen/nitrogen coordinating ligands, due to the affinity of the hard lanthanide and actinide ions for hard oxygen donor atoms.¹⁵ These oxygen-containing ligands proved inappropriate for separation as they were too hydrophilic and hence unsuitable for two-phase solvent extraction processes of the likes of SANEX, where the actinide ions need to be drawn into the organic phase through complexation;¹⁵ it should be noted, however, that mixed O/N-donor ligands are used in the TALSPEAK (Trivalent Actinide-Lanthanide Separation by Phosphorous reagent Extraction from Aqueous Komplexes) process, in which the actinide ions are instead held in the aqueous phase while the lanthanides are removed.¹⁸ Further, some oxygen donor extractants are selective between different lanthanides and different actinides,¹⁵ but only within the same group – unsurprisingly, a selectivity for either Ln or An^{III}, not for one Ln^{III} over another, is required for processes like SANEX. Since the 1980s, studies have instead turned to the ‘softer’, polarisable nitrogen and sulphur donor ligands, which emphasise covalent bonding character. More so the nitrogen ligands, as research is now focused on ligands which satisfy the ‘CHON principle’, which aims to minimize secondary waste by utilising molecules comprised only of carbon, hydrogen, oxygen and nitrogen which can be disposed of through incineration to gaseous products, a major advantage in nuclear reprocessing as any solid residue (such as that left by incinerating phosphorous-containing sulphur donors) is further radioactive waste, whereas the gaseous products can be purified and released.¹⁵ As such, the focus of this section, and indeed this thesis, is on the N-donor separation ligands.

The metal extraction ability of a ligand for a metal, ‘X’, is represented by its distribution ratio, D_X , defined as follows:

$$D_X = \frac{[X]_{\text{org}}}{[X]_{\text{aq}}} \quad (\text{Eq. 1.1})$$

i.e. the equilibrium ratio between the metal concentration in the organic and aqueous phases. The separation ability of a ligand is represented by its separation factor, which is the ratio of the ligand’s distribution ratios for two different metals, e.g. for two metals ‘X’ and ‘Y’:

$$SF_{X/Y} = \frac{D_X}{D_Y} \quad (\text{Eq. 1.2})$$

Early studies of N-donor ligands were based on 2,2':6',2''-terpyridine (Terpy, **Figure 1.3**), for which extraction tests had found a $SF_{Am/Eu}$ of 7.2 in dilute nitric acid solution.^{16,17,19,20}

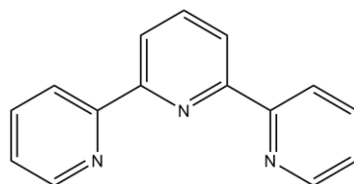


Figure 1.3: 2,2':6',2''-terpyridine (Terpy).

However, this required a synergist and could not be performed in concentrated nitric acid solutions, a significant drawback as the separation ligands need to work at high concentrations of nitric acid, which is the environment in which the ions to be separated are stored.^{15,16,21,22} Modifications of the terpyridine ligand were prone to protonation of the ligands, which competed with metal-ion coordination and lead to lower distribution ratios for Am.^{15,16,21,22}

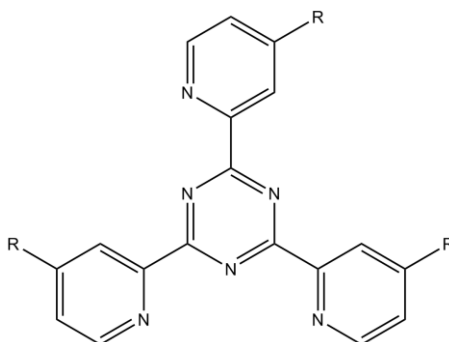


Figure 1.4: 2,4,6-tri(2-pyridyl)-1,3,5-triazine (TPTZ).

2,4,6-tri(2-pyridyl)-1,3,5-triazine (TPTZ, **Figure 1.4**) is another early nitrogen donor ligand which was shown to be able to selectively extract Am^{III} over Eu^{III} , although hydrophilic anion synergists were required to neutralise the positive charge of the complexes.¹⁵ A separation factor greater than 10 was found for TPTZ, and 99.9% of Am^{III} was separated from Eu^{III} and Ce^{III} in 0.125 M HNO_3 in extraction tests, although no significant extraction was observed from more concentrated nitric acid solutions.^{15-17,23}

Many other N-donor ligands were designed and tested for the Ln/An separation process and are well detailed in the literature.¹⁵⁻¹⁷ However, up until the end of the last century they mostly suffered from the same two problems: they could not extract Am^{III} from nitric acid solutions

of greater than 1 M and they required a hydrophilic anion synergist, the latter usually due to the metal not being completely enclosed by the ligand and being able to coordinate water, increasing its hydrophilicity.¹⁶

First studied for use in solvent extraction by Kolarik *et al.* in 1999, 2,6-bis(1,2,4-triazin-3-yl)pyridine (BTP, **Figure 1.5**) immediately presented advantages over previous N-donor extraction ligands: excellent selectivity for Am^{III}, even at low pH levels, without the need for synergist anions.^{12,13}

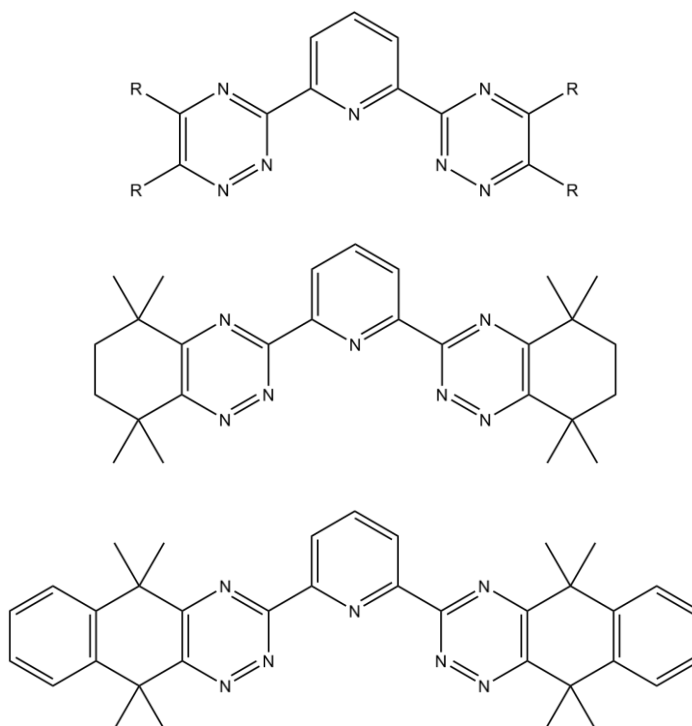


Figure 1.5: 2,6-bis(1,2,4-triazin-3-yl)pyridine (BTP), top, CyMe₄-BTP, middle, and BzCyMe₄-BTP, bottom.

Dipropyl-BTP (R = C₃H₇) was shown to have a $SF_{Am/Eu}$ of ~130 in 0.90 M HNO₃ at room temperature.¹³ The tridentate ligand was found to form 1:3 metal:ligand complexes with Am^{III} via slope analysis of the solvent extraction data, with three nitrate counterions.^{13,17} However, these BTP ligands did have their flaws: indirect radiolysis would break up and destroy the molecule, reducing extraction capabilities, and the ligands were susceptible to acid hydrolysis.^{14,24–28} Modified BTPs CyMe₄- and BzCyMe₄-BTP (**Figure 1.5**) were developed to resist indirect radiolysis and acid hydrolysis.^{29,30} Am/Eu separation factors for these ligands were found to be 5000 and 500 respectively in tests with 0.5 M nitric acid, as well as being resistant towards hydrolysis and showing no signs of degradation.^{17,29} The cost of this

improvement, however, was that stripping of the ligands post-extraction could not be achieved.

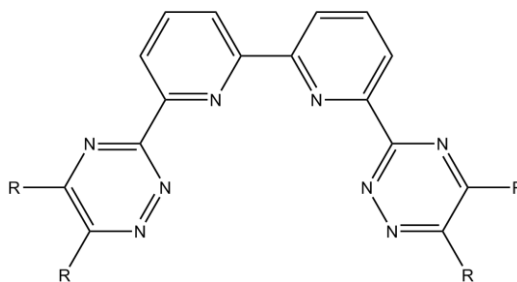


Figure 1.6: 6,6'-bis(1,2,4-triazin-3-yl)-2,2'-bipyridine (BTBP).

The development of 6,6'-bis(1,2,4-triazin-3-yl)-2,2'-bipyridine (BTBP, **Figure 1.5**) was a big breakthrough, as CyMe₄-BTBP was as selective as BTP but stripping of the ligands proved possible.³¹ Like BTPs, synergists were not necessary.¹⁶ In tests, the Am/Eu separation factor for CyMe₄-BTBP was found to be 120-140.³² There were two downsides to the BTBP ligands: slow kinetics and the requirement of a phase transfer agent (e.g. N,N'-dimethyl-N,N' dioctylhexylethoxy-malonamide, DMDOHEMA) unless cyclohexanone was used as the diluent.^{16,31,33-}

35

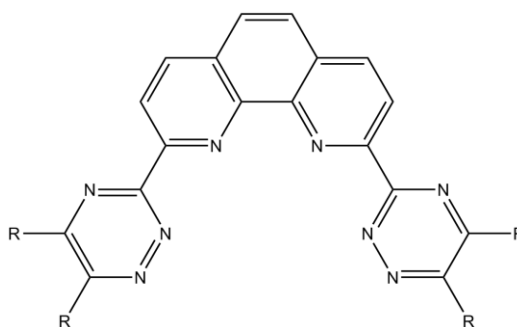


Figure 1.7: 2,9-bis(1,2,4-triazin-3-yl)-1,10-phenanthroline (BTPhen).

A larger breakthrough was the more recent development of 2,9-bis(1,2,4-triazin-3-yl)-1,10-phenanthroline (BTPhen, **Figure 1.6**).^{16,17,30,33,34} BTBP can rotate around the C-C bond between the two pyridine rings, but needs to be in the cis-cis conformation for complexation; BTPhen is essentially a BTBP ligand which has been pre-organised in this conformation by adding a bridge between the pyridine ligands and forcing them to remain planar.^{16,33,36} Despite similar selectivity, the effect of the pre-organisation of the ligand was much faster kinetics, leading to greater extraction ability ($SF_{Am/Eu} = 100-400$ for CyMe₄-BTPhen).^{16,33,36}

Of these N-donor ligands, this work has focused on the BTP (**Chapter 4**) and BTPhen (**Chapter 5, Part I**) ligands. Additionally, recent developments of modified BTPhen ligands have explored

the effect of the addition of electron-directing groups to the phenanthroline moiety, which is discussed in more detail in **Chapter 5, Part II**. Finally, the mixed O/N-donor ligands DTPA and NH₂-DTPA, used in the TALSPEAK process, and N-donor texaphyrin rings, which are known to complex the trivalent lanthanides, are discussed in **Chapter 5, Part III**.

1.3 Experimental Studies of An^{III}/Ln^{III} complexes

The aim of this project is to further understand the reasons behind the separation capabilities of the nitrogen donor ligands used for separating actinides and lanthanides. While these ligands have been improved upon significantly, many developments have been made mostly through trial and error and chemical intuition. Evidence for the origin of the increased stability of the actinide complexes over those of the lanthanides may shed light on ways to improve the separation process. This section and the next discuss the findings of some examples of the experimental and computational methods which have been used to investigate these complexes.

Due to the risks and costs of working with actinides, experimental data is not trivial to obtain. Nevertheless, there is a demand for improving the An^{III}/Ln^{III} separation processes and experimental data is vital for making informed decisions about ligand design. Hence there is a range of experimental literature covering the results of extended x-ray absorption fine structure spectroscopy (EXAFS), time-resolved laser fluorescence spectroscopy (TRLFS), nano-electrospray mass spectrometry and nuclear magnetic resonance (NMR) studies of An^{III}/Ln^{III} complexes.

1.3.1 Extended X-Ray Absorption Fine Structure Spectroscopy (EXAFS)

The x-ray absorption fine structure (XAFS) spectroscopic technique works by shining x-rays of a narrow energy resolution onto a sample using a tuneable x-ray source, such as a synchrotron, and measuring the transmitted x-ray intensity, which decreases as x-rays are absorbed. Extended x-ray absorption fine structure spectroscopy (EXAFS) is a method of using XAFS to probe the structure of a sample by identifying the local structure around specific atoms.

An EXAFS study of An^{III} and Ln^{III} complexes with n-C₃H₇-BTP and another ligand, tris((2-pyrazinyl)methyl)amine (TPZA, **Figure 1.8**) by Denecke *et al.* in 2007 found no obvious structural explanations for the separation abilities of these ligands.³⁷

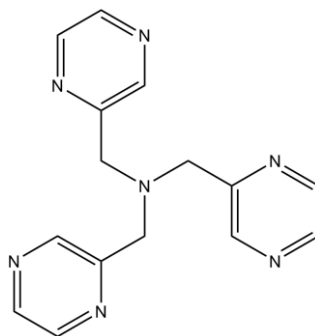


Figure 1.8: tris((2-pyrazinyl)methyl)amine (TPZA) ligand studied by Denecke *et al.*³⁷

U^{III} was found to have signs of increased covalent character of the M-N coordination, in the form of a decreased bond length compared to what would be expected of a pure ionic bond, although no measurable differences were observed for Am, Cm and the mid-series lanthanides.³⁷ Additional data for [Pu(n-C₃H₇-BTP)₃]³⁺ was reported by Banik *et al.* in 2010, who compared the An-N bond distances of isostructural n-C₃H₇BTP complexes of U, Pu, Am and Cm to find that although the An^{III} ionic radius decreases across the actinide series, the An-N bond distances remain almost constant.³⁸ Further n-C₃H₇-BTP complexes with Sm^{III}, Dy^{III}, Ho^{III}, Tm^{III}, Np^{III}, Cf^{III} and Pm^{III} were reported in 2013, again reporting that the An—N bond lengths are essentially independent of the ionic radii of the An^{III} ion but also that the Ln—N bond lengths decrease with the ionic radii of the Ln^{III} ion, which Banik *et al.* speculate indicates a higher ionic bonding character for the lanthanide complexes due to larger differences between their ionic radii and the distance to the first coordination shell.³⁹

1.3.2 Time-Resolved Laser Fluorescence Spectroscopy (TRLFS)

Time-resolved laser fluorescence spectroscopy (TRLFS) is a method which monitors the fluorescence of a sample after excitation with a flash of light, as a function of time. As the fluorescence lifetime of a molecule is sensitive to its environment, the molecular structure of a sample can be probed using TRLFS.

In 2007, Denecke *et al.* used TRLFS to determine any differences in the stoichiometry and stability of the trivalent lanthanide and actinide complexes with BTP.³⁷ By varying the ratio of the ligands and the metal ions ([L]/[M]), they observed that the 1:3 complex of Cm and BTP forms at a much lower [L]/[M] ratio than the 1:3 complex of Eu and BTP, due to the formation of the short lived 1:1 Eu-BTP complex, evidenced by slope analysis and estimations of the lifetime of the 1:1 complex, which match the TRLFS data and eliminate the possibility of it being the 1:2 complex.³⁷ A similar increased ability for the actinides to form 1:3 complexes

with BTP over the lanthanides was also observed with mass spectrometry, discussed in the next section.⁴⁰

The stoichiometry and enthalpy of the complexation of actinides and lanthanides with BTP ligands was further investigated by Trumm *et al.* in 2010, who also investigated similar BTBP ligands.^{41,42} Through TRLFS titrations, Trumm *et al.* determined stability constants for the 1:3 complexation of Cm^{III} and Eu^{III} complexes with n-C₃H₇-BTP which were 320 times larger for the Cm^{III} complex than for the Eu^{III} complex.⁴¹ A Gibbs free energy difference of -13.1 kJ/mol was determined, with the Cm^{III} complex being more stable, in good agreement with a value of -14.0 kJ/mol found *via* titration.⁴¹ This difference was attributed to the difference in enthalpy, as the entropy changes were found to be negligible, suggesting that enthalpy is the driving force of the selectivity exhibited by the BTP ligands.⁴¹ For Cm^{III} and Eu^{III} complexes with t-Bu-C₂-BTBP, a similar change of -10.1 kJ/mol in the Gibbs free energy, was determined, again in good agreement with a value of -11.8 kJ/mol derived from titrations.⁴² For both of the BTP and BTBP studies, the results correspond to separation factors which agree with the results of liquid-liquid extraction tests.^{41,42}

1.3.3 Nano-Electrospray Mass Spectrometry

Mass spectrometry is an analytical technique which can measure the mass-to-charge ratio and abundance of gaseous ions, from which the amount and type of molecules present in a sample can be identified. Electrospray ionisation is a mass-spectrometry technique used to create an aerosol from a liquid sample by applying a high voltage to the liquid, and nano-electrospray ionisation is simply the same technique applied to small samples, which is advantageous when working with f-block elements of which a large amount of sample is not available. A nano-electrospray mass spectrometry investigation of complex formation of BTP with a range of lanthanides was reported by Steppert *et al.* in 2009, showing a correlation between the ability of the lanthanides to form 1:3 complexes with BTP and their distribution ratios for extraction to the organic phase.⁴⁰ Even at a 10:1 ratio of ligand to ion the lanthanides studied were found to form a significant amount of 1:2 and 1:1 complexes.⁴⁰ Due to the lesser ability of the lanthanides to form 1:3 complexes, Steppert *et al.* concluded that the increased hydrophobic shielding of the metal ions by the ligand in the 1:3 complexes, which is also evidenced by there being more water molecules attached to the 1:2 and 1:1 complexes, may be an explanation for the extraction selectivity of the actinides over the lanthanides. However, they do not report any data for the actinides for comparison.⁴⁰

1.3.4 Nuclear Magnetic Resonance (NMR)

Nuclear magnetic resonance (NMR) spectroscopy is a technique which detects the nuclear magnetic resonance response, or free induction decay (FID), following the excitation of a sample with a radio pulse of a specific frequency corresponding to that of an NMR-active isotope present within the sample, such as ^1H or ^{13}C . The spectra produced by NMR spectroscopy displays the signal intensity of this response against chemical shift, a measure of the difference between the signal peak and a reference peak, brought about by the difference in the environment of the emitting atom. From analysing NMR spectra, detailed information about the structure of the sample molecule can be gained, such as the molecular formula and the existence of certain functional groups. Further information can be gained from two-dimensional NMR, which plots two frequency axes rather than a single axis and can show how one environment within a molecule is connected to another, allowing the determination of complicated molecular structures.

A two-dimensional ^1H , ^{15}N -HMQC NMR study of an $[\text{Am}(\text{n-PrBTP})_3](\text{NO}_3)_3$ complex, partially labelled at the vicinal nitrogen positions of the triazine rings to overcome low natural abundance, was reported by Kaden *et al.* in 2013.⁴³ Compared to an isostructural reference Lu^{III} and Sm^{III} complexes, a large upfield shift ($\sim 300\text{ppm}$) of the coordinating nitrogens on the pyridine and triazine moieties were observed. No such shifts of the non-coordinating nitrogen atoms were observed. These upfield shifts place the nitrogen chemical shifts at negative values relative to the $^{15}\text{NH}_4\text{Cl}$ standard, which is usually only observed with amines that are extremely electron-rich. Additionally, the effect of temperature on the chemical shifts of the vicinal triazine nitrogens was reported. Whilst the non-coordinating nitrogen exhibited only slight variation in chemical shift between temperatures of 275 and 335 K (37 Hz), the coordinating nitrogen shifted by 240 Hz. Recent literature considers Am^{III} to be in a diamagnetic ground state, however Kaden *et al.* report that the variation in the shift of the nitrogen attached to the metal centre would suggest that Am^{III} has a weak, temperature-dependant paramagnetism.^{43–46}

Kaden *et al.* give several possible explanations for the large chemical shifts observed for the Am^{III} complex compared to the Lu^{III} complex. Firstly, they suggest that they could arise from electron density transfer from the metal ion to the coordinating nitrogen atoms, and that they would not expect this to propagate far into the aromatic ring system. This is backed by their NMR data, as only the closest nitrogen atoms - those coordinating to the metal ion - display these large differences in chemical shift, compared to the Lu^{III} complex. They note, however, that they would not expect this explanation to account for shifts of such magnitude.⁴³

Secondly, they suggest that a Fermi contact shift (FCS), or unpaired electron spin density delocalised along a covalent bond, combined with the temperature dependent paramagnetism could explain the observed shifts.⁴³ They also suggest that spin-orbit induced spin polarisation could be a third explanation, without reliance on paramagnetic effects.⁴³

These last two explanations are both mediated by a Fermi contact mechanism and arise from a covalent interaction between the metal and the ligand, inferring a larger degree of covalency in the Am—N bonds compared to the lanthanide complexes.⁴³ Additionally, their results agree indirectly with EXAFS data discussed earlier. The EXAFS studies show greater ionic character for the lanthanide complexes than with the actinides due to larger differences between their ionic radii and the distance to the first coordination shell, which is in accordance with the chemical shifts of the non-coordinating and coordinating nitrogen atoms on the triazine moieties.⁴³

1.4 Theoretical Studies of An^{III}/Ln^{III} complexes

As mentioned previously, experimental work involving the actinides is by no means trivial. As such, the use of quantum chemical methods in the field of nuclear waste separation is common, and has become an important ally to the experimental actinide chemist. In this section, some of the theoretical studies reported in the literature for the complexes of An^{III}/Ln^{III} separation ligands will be discussed, in particular those of the N-donor ligands which are the focus of the work presented in this thesis. The computational methods employed in the literature discussed here include Hartree-Fock theory, Density Functional Theory (DFT), second order Møller-Plesset perturbation theory (MP2) and the Quantum Theory of Atoms in Molecules (QTAIM), and are discussed in the following chapter.

In 2004, Guillaumont reported a gas-phase DFT study of M—L bond lengths for a series of An^{III} and Ln^{III} hydrated 1:1 ligand:metal terpyridine and Me-BTP complexes, observing that the studied Ln—L distances decreased as the ionic radius increased, while An—L distances increase from U through to Am.⁴⁷ Additionally, the An—L bond distances were universally shorter than the Ln—L bond distances. Relativistic effects were modelled with both the zeroth-order regular approximation, ZORA, and relativistic effective core potentials, RECPs, for comparison (discussed in **Chapter 2**). Bond lengths calculated using ZORA and RECPs were in good agreement both with each other (a maximum of 0.02 Å difference) and with experimental structural data, including reproducing the U—L/Ce—L bond contraction. Also reported is a greater participation of the An centres in the M—L σ -bond compared to the Ln centres. However, this increase is only by a few percent, with the exception of Uranium, which

donates 5f electrons to the π^* orbital of the ligand, hence shorter U—L bond lengths. The shorter An—L bond distances compared to the Ln—L bond distances and the slight increase of metal centre participation in the M—L bond indicates a slightly stronger covalent effect in the An—L bonds.⁴⁷

The gas-phase geometries of 1:1 metal:ligand complexes of La, Eu and Lu with four ligands were optimised by Gutierrez *et al.* in 2005: terpyridine, TPTZ, ADPTZ (2,6-bis(pyridin-2-yl)-4-amino-1,3,5-triazine) and BTP. Both Hartree-Fock and DFT levels of theory were used for their calculations, with scalar relativistic effects modelled by RECPs, finding a better agreement with experimental X-ray structures for the DFT calculations than the Hartree-Fock calculations.⁴⁸ Observed was a decrease in all Ln—N bond lengths across the lanthanide series.⁴⁸

Further gas-phase quantum chemical calculations of 1:3 complexes of Eu and Cm with BTP were reported by Denecke *et al.* in 2005.⁴⁹ DFT-calculated Cm—N and Eu—N bond lengths were found to be within 0.01 Å of each other for a range of *xc*-functionals (BP, BLYP, B3LYP, BHLYP and TPSS) and in agreement with their EXAFS data.⁴⁹ An MP2 calculation, considered to be a higher level of theory, of the Eu—N bond length was in better agreement with the EXAFS data, from an average of 2.615 Å for TPSS to 2.554 Å for MP2 compared to an experimental value of 2.559 (+/- 0.008) Å.⁴⁹ Although no MP2 data for the Cm^{III} complex was reported, based on their other results they concluded that the Cm—N and Eu—N bond distances were practically identical.⁴⁹

In 2006, Petit *et al.* reported gas-phase and aqueous phase optimisations of 1:3 complexes of La and U, using the scalar relativistic ZORA, the BP *xc*-functional and, for the aqueous optimisations, the COSMO solvation method.⁵⁰ The effects of COSMO solvation on the structure was found to be a slight shortening of the bond lengths, by up to 0.01 Å.⁵⁰ These La and U complexes were used to optimise complexes of Cm and Gd, and the M—N bond lengths of the Gd complexes were found to be up to 0.04 Å shorter than those of the Cm complexes.⁵⁰

In 2010, along with their EXAFS results discussed earlier, Banik *et al.* reported gas-phase 1:3 complexes of Np, Pu, Am and Cm with BTP optimised both with DFT using the BP86 *xc*-functional and with MP2. Both 'standard' small-core RECPs and f-in-core pseudopotentials were employed, however only structures obtained with the small-core RECPs reproduced the constant An—L bond distances observed experimentally.⁵¹

From the computational literature discussed above, the following are apparent: DFT calculations offer an improvement over Hartree-Fock theory, and MP2 over DFT; the bond lengths in the BTP complexes of the mid-series Ln (Gd, Eu) and An (Cm, Am) are similar, with

up to a 0.04 Å Ln/An difference; Ln—N bond lengths decrease across the series, while An—N bond lengths do not; orbital analysis appears to show slightly more covalent character in the An—L complexes than the Ln—L complexes; and RECPs are suitable for use for the modelling of these complexes, while the f-in-core ECPs may not be.

Lan *et al.* have investigated the Eu and Am complexes and reactions of BTBP in great detail.^{52–54} In 2011, they reported DFT-optimised complexes of 1:1 Eu and Am BTBP complexes using RECPs and the B3LYP *xc*-functional, with a series of different R groups on the triazine moieties of the BTBP ligand.⁵² Reported bond lengths between the metal ion and the nitrogen of the triazine moiety were shorter for the Am complexes by ~0.1 Å, and ~0.01 Å for those with the nitrogen of the pyridine moiety.⁵² They reported that electron-donating groups enhance the coordination ability of the BTBP ligand and hence their stability in the gas phase,⁵² and observed Eu BTBP complexes which were more stable than Am, which would not be expected considering that BTBP selectively extracts actinides in separation processes, not lanthanides.⁵² However, after studying changes in Gibbs free energy, they suggest that the weaker complexing ability of Am with nitrate ions and water makes decomposition of the $[\text{Am}(\text{NO}_3)_3(\text{H}_2\text{O})_4]$ complex more favourable in energy and may increase the possibility of forming $[\text{Am}(\text{BTBP})(\text{NO}_3)_3]$.⁵²

In 2012 Lan *et al.* published a second paper, this time also looking at 1:2 ($[\text{ML}_2]^{3+}$ and $[\text{ML}_2(\text{NO}_3)]^{2+}$) BTBP complexes of Eu and Am.⁵³ By taking into account Gibbs free energy changes, they found a preference for the Am complexes over the Eu complexes for the complexing reaction $\text{M}(\text{NO}_3)_3(\text{H}_2\text{O})_4 \rightarrow \text{ML}(\text{NO}_3)_3$ (L = BTBPs).⁵³ Also reported in this paper were calculated changes of electronic energy for a series of other complexing reactions. Not all of these complexing reactions displayed a preference for Am complex formation, for example the reaction $\text{M}(\text{NO}_3)_3(\text{H}_2\text{O})_4 \rightarrow [\text{ML}_2]^{3+}$ was calculated to have a preference for the formation of Eu complexes, although this reaction was endothermic for both.⁵³ Lan *et al.* deduced that the complexation reaction $[\text{M}(\text{NO}_3)(\text{H}_2\text{O})_7]^{2+} \rightarrow [\text{ML}_2(\text{NO}_3)]^{2+}$ is likely to be dominant in the separation process due to it being both exothermic, and hence energetically favourable, as well as selective towards Am.⁵³ Further, they suggested that the most probable complexation reactions with BTBP are those in which the products and reactants contain the same or a similar amount of nitrate ions.⁵³

A recent study by Trumm *et al.* in 2015 presents the complexes of thirteen different ligands with both Cm and Gd using DFT, RECPs and the B3LYP *xc*-functional for geometry optimisations, finding the Gd—L bond lengths to be shorter by 0.02–0.05 Å in all cases.⁵⁵ MP2-

calculated reaction energies on these structures for the exchange reaction $[\text{CmL}_3]^{3+} + \text{Gd}(\text{H}_2\text{O})_9 \rightarrow [\text{GdL}_3]^{3+} + \text{Cm}(\text{H}_2\text{O})_9$ were in favour of the left hand side for all ligands but one, i.e. the ligands favour complexation with the Cm ion over Gd. The addition of solvation effects *via* Hartree-Fock single-point energy calculations using the COSMO solvation model on top of the gas-phase structures shifted the equilibrium of the reaction further to the left.⁵⁵

This overview of some of the computational literature with regards to $\text{An}^{\text{III}}/\text{Ln}^{\text{III}}$ separation is not exhaustive, and additional literature is discussed throughout this thesis. Nevertheless, these studies show that DFT can be applied to investigate the selectivity of the N-donor ligands and calculate energies for reactions which approximate the separation process to provide insight into their separation ability.

Chapter 2: Methodology

In this chapter, an overview of the various computational techniques used in this work is given. For a more in-depth guide to these techniques and the mathematics behind them, the reader is directed to the referenced resources.^{56–59}

2.1 Basis Sets

Basis functions are used to build a description of the molecular orbitals of a system. The basis set is the set of basis functions from which this description is built. For molecular systems, the molecular orbitals are typically built using a linear combination of atomic orbitals described by atom-centred basis functions, although for other applications, such as periodic systems, it is possible to use plane wave functions. In general, the larger the basis set, the better the description of the molecule and hence the quality of the calculation, although this comes at the cost of increased computational expense.

There are two main types of atom-centred basis functions: Slater Type Orbitals (STOs), and Gaussian Type Orbitals (GTOs). STOs take the form:

$$\phi_{\zeta,n,l,m}(r, \theta, \phi) = NY_{l,m}(\theta, \phi)r^{(n-1)}e^{-\zeta r} \quad (\text{Eq. 2.1})$$

Where N is a normalisation constant, $Y_{l,m}$ are spherical harmonic functions, r is the distance from the nucleus, ζ is an exponent that determines the rate of decay, or steepness, of the basis function and n , l and m are quantum numbers. GTOs take a similar form:

$$\phi_{\zeta,n,l,m}(r, \theta, \phi) = NY_{l,m}(\theta, \phi)r^{(2n-2-l)}e^{-\zeta r^2} \quad (\text{Eq. 2.2})$$

An example of the form of STOs and GTOs can be seen in **Figure 2.1**. STOs are dependent only on r in the exponential term, while GTOs have an r^2 dependence. This means that STOs exhibit exponential decay at long values of r and describe the behaviour near the nucleus more accurately with a ‘cusp’ at the atomic nucleus, while the GTOs decay too quickly and have no ‘cusp’ at the nucleus. As a result, GTOs are not as accurate when used for modelling short- and long-ranged electronic behaviour. However, integrating STOs is much more difficult than for GTOs, increasing computational expense. A linear combination of GTOs can be used to build orbitals with sufficient accuracy while still being cheaper than using STOs.

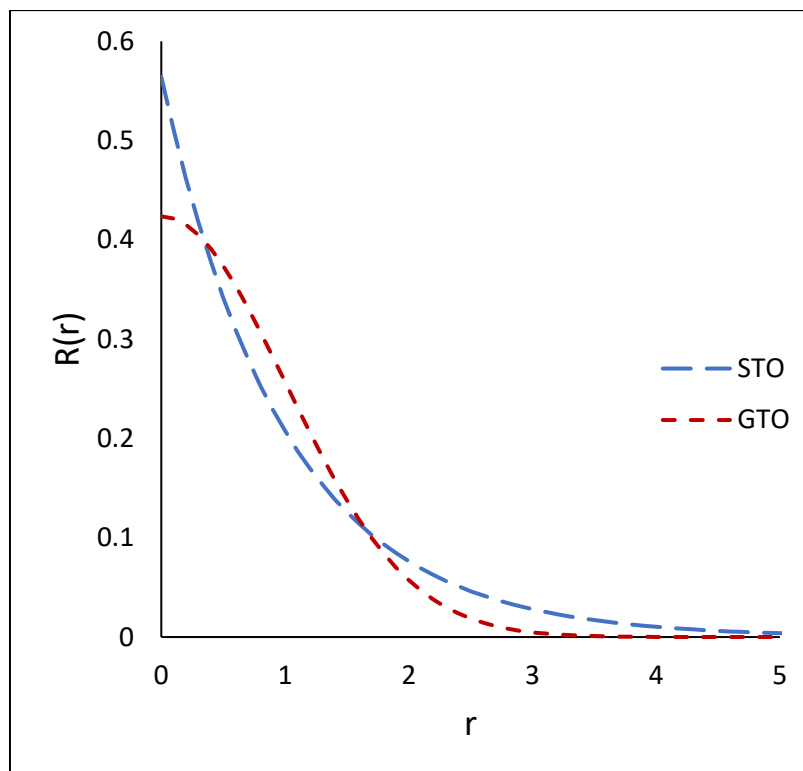


Figure 2.1: Example of an STO (blue) and a GTO (red).

There is a minimum number of basis functions required to describe all of the electrons in an atom. The minimum basis set for a hydrogen or helium atom would contain one s function, while two s functions and one p function would be required for a first row element. Further basis functions can be added to produce better results. Basis sets containing two sets of functions are known as double zeta basis sets (denoted as double- ζ , or 'DZ'), those containing three sets of functions are known as triple zeta (triple- ζ , or 'TZ'), and so on. As the valence electrons are much more likely to be involved in bonding interactions, many basis sets only increase the number of basis functions for the valence electrons, with a minimal basis for the core electrons. This keeps computational cost down while improving accuracy, and is denoted as valence double zeta ('VDZ'), valence triple zeta ('VTZ'), and so on.

Basis set quality can be further improved by adding polarisation and diffuse functions. Polarisation functions are additional basis functions with higher angular momentum, l , than the orbital they supplement; for example, a p function added to the basis set for a hydrogen atom. The addition of polarisation functions provides a more realistic bonding description by accounting for the asymmetric directional polarisation of the electron density caused by the other nuclei. Diffuse functions are, as the name suggests, diffuse, due to their small ζ exponent causing the rate of decay to be low. This is important when modelling anions or other systems with electrons which are loosely bound to the nucleus, as well as for intermolecular bonding.

2.2 Bra-Ket Notation

Dirac notation is used in parts of this chapter, also known as 'bra-ket' notation. Bra-ket notation uses the following abbreviations:

$$\langle f| = f^*(\mathbf{a}) \quad ('bra')$$
 (Eq. 2.3)

$$|f\rangle = f(\mathbf{a}) \quad ('ket')$$
 (Eq. 2.4)

This allows for a compact expression of a quantum state. For every ket there is a bra corresponding to its complex conjugate, and the combination of a bra and a ket describes the overlap of states, i.e:

$$\langle \Psi | \Psi \rangle = \int \Psi^*(\mathbf{a}) \Psi(\mathbf{a}) d\mathbf{a}$$
 (Eq. 2.5)

Additionally, in bra-ket notation, the expectation value of an observable represented by an operator \hat{A} for a system in the state $|\Psi\rangle$ would be:

$$\langle \Psi | \hat{A} | \Psi \rangle$$
 (Eq 2.6)

2.3 Variational Principle

The variational principle is key to much of quantum mechanics. It states that the energy of any trial wavefunction, Ψ' , cannot be lower than the energy of the exact wavefunction, Ψ_0 . The energy of a trial wavefunction can be defined as the expectation value of the wavefunction:

$$E_{\Psi'} = \frac{\langle \Psi' | \hat{H} | \Psi' \rangle}{\langle \Psi' | \Psi' \rangle}$$
 (Eq 2.7)

E_0 , the energy which is the lowest of the infinite solutions to the Schrödinger equation, then must be equal to or less than this trial wavefunction energy, i.e.:

$$E_0 \leq \frac{\langle \Psi' | \hat{H} | \Psi' \rangle}{\langle \Psi' | \Psi' \rangle}$$
 (Eq 2.8)

This provides the basis for convergence in optimisation calculations.

2.4 The Schrödinger Equation

The famous Schrödinger equation is the starting point for most of quantum chemistry. The (time-independent) Schrödinger equation is as follows:

$$\hat{H}\Psi = E\Psi \quad (\text{Eq. 2.9})$$

Where Ψ is the wavefunction, E is the energy of the state represented by the wavefunction, and \hat{H} is the Hamiltonian operator. If Ψ is an eigenfunction of \hat{H} , then it is a solution to the Schrödinger equation. \hat{H} has a set of eigenfunctions, and of these eigenfunctions that which has the lowest energy is the ground state of the system, while all others are excited states.

While the Schrödinger equation can be solved exactly for a one-electron atom,⁶⁰ an exact solution for a many body system, such as a molecule, is generally unobtainable. However, there are many electronic structure calculation methods which approximate a solution. In this chapter, several such methods will be introduced, such as Hartree-Fock theory and Density Functional Theory (DFT).

2.5 The Hamiltonian

The Hamiltonian, \hat{H} , has the general form:

$$\hat{H} = \hat{T} + \hat{V} \quad (\text{Eq. 2.10})$$

Where \hat{T} is the kinetic energy operator and \hat{V} is the potential energy operator. For a molecular system, \hat{T} is:

$$\hat{T} = -\frac{\hbar^2}{2m} \sum_i \frac{1}{2} \nabla_i^2 - \sum_A \frac{1}{2m_A} \nabla_A^2$$

Where i indexes electrons, A indexes nuclei, \hbar is the reduced Planck's constant, m is the mass of an electron and ∇_i^2 is the Laplacian operator, or the sum of the second partial derivatives:

$$\nabla_i^2 = \frac{\partial^2}{\partial^2 x_i} + \frac{\partial^2}{\partial^2 y_i} + \frac{\partial^2}{\partial^2 z_i} \quad (\text{Eq. 2.11})$$

In the absence of external fields, \hat{V} is the sum of the repulsive electron-electron interactions, \hat{V}_{ee} , repulsive nuclear-nuclear interactions, \hat{V}_{nn} , and attractive electron-nuclear interactions, \hat{V}_{ne} . These can be written as follows:

$$\hat{V}_{ee} = \frac{1}{4\pi\epsilon_0} \sum_i \sum_{j>i} \frac{e^2}{\mathbf{r}_{i,j}} \quad (\text{Eq. 2.12})$$

$$\hat{V}_{nn} = \frac{1}{4\pi\epsilon_0} \sum_A \sum_{B>A} \frac{Z_A Z_B e^2}{\mathbf{r}_{A,B}} \quad (\text{Eq. 2.13})$$

$$\hat{V}_{ne} = -\frac{1}{4\pi\epsilon_0} \sum_i \sum_A \frac{Z_A e^2}{\mathbf{r}_{A,i}} \quad (\text{Eq. 2.14})$$

Where ϵ_0 is the permittivity of free space, Z_A is the charge on nucleus A , e is the charge of an electron, and $\mathbf{r}_{A,B}$ and $\mathbf{r}_{A,i}$ are the distances from nucleus A to nucleus B and from nucleus A to the electron i , respectively. The Hamiltonian, \hat{H} , can then be written as follows, in atomic units, (a.u.) for simplicity, where the electron mass, electron charge, \hbar and $4\pi\epsilon_0$ are defined as unity:

$$\hat{H} = -\sum_i \frac{1}{2} \nabla_i^2 - \sum_A \frac{1}{2m_A} \nabla_A^2 - \sum_{A,i} \frac{Z_A}{\mathbf{r}_{A,i}} + \sum_A \sum_{B>A} \frac{Z_A Z_B}{\mathbf{r}_{A,B}} + \sum_i \sum_{j>i} \frac{1}{\mathbf{r}_{i,j}} \quad (\text{Eq. 2.15})$$

2.6 The Born-Oppenheimer Approximation

For multi-particle systems, solving the Schrödinger equation is by no means trivial. To obtain a solution, several simplifications and approximations must be made. The first key approximation is the Born-Oppenheimer approximation,⁶¹ which makes the assumption that the position of the nuclei is fixed on the timescale of electron motion. This assumption is justified due to the large mass and the slow motion of the nuclei in comparison to that of the electron, making any movement by the electron to adapt to a change in the position of the nuclei essentially instantaneous. This assumption allows the molecular wavefunction to be separated into electronic and nuclear components:

$$\Psi_{\text{tot}} = \Psi_{\text{el}} \Psi_{\text{nuc}} \quad (\text{Eq. 2.16})$$

This allows the time-independent Schrödinger equation to be solved for Ψ_{el} , with the nuclear coordinates assumed to be constant, and a simplification of this Hamiltonian by removing the nuclear kinetic energy term, giving the electronic Hamiltonian, \hat{H}_{el} , as follows:

$$\hat{H}_{\text{el}} = -\sum_i \frac{1}{2} \nabla_i^2 - \sum_{A,i} \frac{Z_A}{\mathbf{r}_{A,i}} + \sum_A \sum_{B>A} \frac{Z_A Z_B}{\mathbf{r}_{A,B}} + \sum_i \sum_{j>i} \frac{1}{\mathbf{r}_{i,j}} \quad (\text{Eq. 2.17})$$

2.7 The Orbital Approximation

While the use of the Born-Oppenheimer approximation decouples the electronic and nuclear motions from each other, there remains $4n$ coordinates (three spatial and one spin coordinate, where n is the number of electrons). A further approximation, known as the orbital or Hartree approximation,⁶² can be made, which is that a many-electron wavefunction can be constructed as a product of n one-electron orbitals. This is known as the Hartree product:

$$\Psi(\mathbf{x}_1, \mathbf{x}_2, \dots, \mathbf{x}_n) = \varphi_1(\mathbf{x}_1)\varphi_2(\mathbf{x}_2) \dots \varphi_n(\mathbf{x}_n) \quad (\text{Eq. 2.18})$$

Where \mathbf{x}_n are the spin and spatial coordinates of electrons in spin-orbitals $\varphi_n(\mathbf{x}_n)$, which are the product of a spatial orbital and a spin function, i.e. $\varphi_n(\mathbf{x}_n) = \varphi_i(\mathbf{r}_i)\sigma(i)$, where \mathbf{r}_i is the spatial coordinates of electron i and $\sigma(i)$ is the spin of the electron, which can be considered as either spin “up” (α) or spin “down” (β). However, this is not exact for a many-electron system, as it does not consider electrons to be indistinguishable, nor does it obey the antisymmetry principle, which is that a wavefunction of a system of fermions (e.g. electrons) must be antisymmetric with respect to the exchange of any two fermions.

2.8 Hartree-Fock Theory

Hartree-Fock theory uses the variational method to minimise the electronic energy of a system described by a single Slater determinant⁶³ to give an approximate solution to the Schrödinger equation. The Hartree product (Eq 2.18) is the simplest way to describe a many electron wavefunction, but does not obey the antisymmetry principle. This principle can be satisfied through the use of a single Slater determinant as an approximation for the exact n -body wavefunction:

$$\Psi(\mathbf{x}_1, \mathbf{x}_2 \dots \mathbf{x}_n) = \frac{1}{\sqrt{n!}} \begin{vmatrix} \varphi_1(\mathbf{x}_1) & \varphi_2(\mathbf{x}_1) & \dots & \varphi_n(\mathbf{x}_1) \\ \vdots & \vdots & \ddots & \vdots \\ \varphi_1(\mathbf{x}_n) & \varphi_2(\mathbf{x}_n) & \dots & \varphi_n(\mathbf{x}_n) \end{vmatrix} \quad (\text{Eq. 2.19})$$

By taking the determinant, it is ensured that the sign of the wavefunction changes when any two rows are exchanged, and that the wavefunction is zero if any two rows are identical. The energy of this electronic Hartree-Fock wavefunction, E_{el} , is given by the expectation value of Ψ with respect to the electronic Hamiltonian operator, \hat{H}_{el} , as so:

$$E_{\text{el}} = \langle \Psi | \hat{H}_{\text{el}} | \Psi \rangle \quad (\text{Eq 2.20})$$

However, the next difficulty is finding the wavefunction which minimises the energy of the system. This is achieved with a variational method (see **2.3 The Variational Principle**) to find the molecular orbitals which minimise E_e . These molecular orbitals can be constructed as a linear combination of atomic orbitals (LCAO), written as:

$$\phi_k(\mathbf{r}) = \sum_i c_{ik} \varphi_i(\mathbf{r}) \quad (\text{Eq. 2.21})$$

Where ϕ_k is a molecular orbital, φ_i are the atomic orbitals which constitute the basis set (see **2.1 Basis Sets**), and c_{ik} are the expansion coefficients, which can be varied to minimise the energy of the system and hence define the molecular orbitals which correspond to the minimum electronic energy. The Fock operator, \hat{F} , acts on the molecular spin-orbitals, to produce the energy of each orbital, as shown by the Hartree-Fock equations:

$$\hat{F}_i \phi_i(\mathbf{r}) = E_i \phi_i(\mathbf{r}) \quad (\text{Eq. 2.21})$$

The Fock operator has the form:

$$\hat{F}_i = \hat{h}_i + \sum_j^n [2\hat{J}_j(i) - \hat{K}_j(i)] \quad (\text{Eq. 2.22})$$

Where \hat{h}_i is the one-electron Hamiltonian and \hat{J}_j and \hat{K}_j are the electron-electron Coulomb and exchange operators, respectively. The total Hartree-Fock energy, E_{HF} , is given by the following:

$$E_{\text{HF}} = \sum_i^n \langle \varphi_i | \hat{h}_i | \varphi_i \rangle + \frac{1}{2} \sum_{i,j}^n \langle \varphi_i \varphi_j | \varphi_i \varphi_j \rangle = \sum_i \varepsilon_i - \frac{1}{2} \sum_{i,j}^n \langle \varphi_i \varphi_j | \varphi_i \varphi_j \rangle \quad (\text{Eq. 2.23})$$

An iterative self-consistent field (SCF) method is used to converge the energy of the system, to a specified tolerance. In this approach, a potential is generated from the wavefunction obtained from the initial set of molecular spin-orbitals, which are typically constructed using a simple semi-empirical method such as extended Hückel theory,⁶⁴ then the energy of the wavefunction is minimised with respect to this initial potential. From this minimum energy wavefunction, a new set of improved molecular spin-orbitals can be generated, and with them a new potential. This new potential is fed back in, and the cycle is repeated until the energy obtained from the generated orbitals is the same as that of the orbitals used to generate them,

within a given tolerance – i.e. self-consistency is achieved. This approach is summarised in **Figure 2.2**, below:

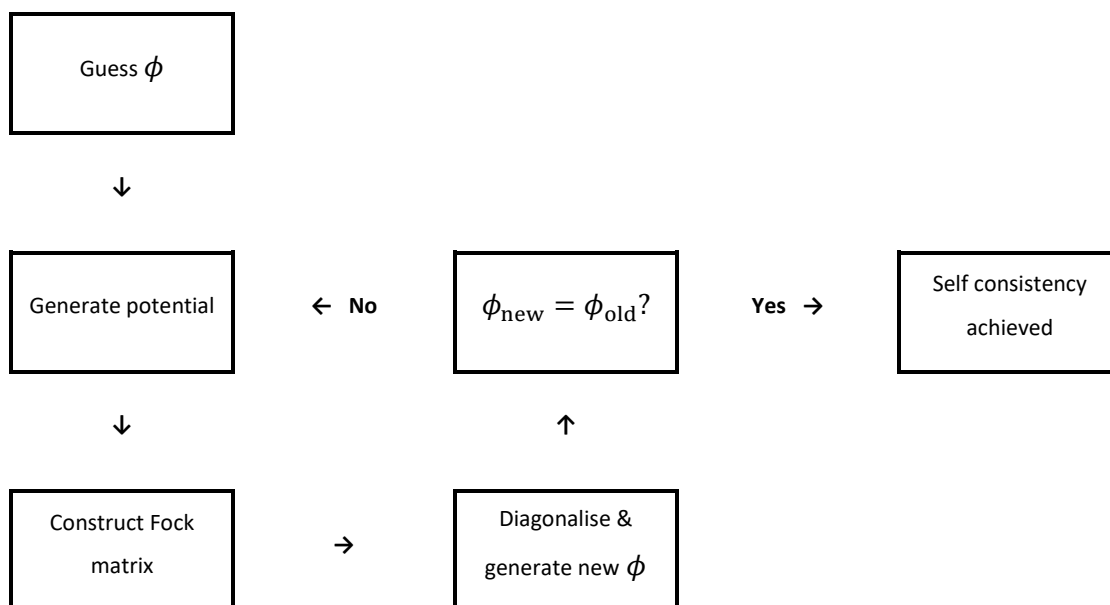


Figure 2.2: Flow diagram for the self-consistent field approach.

2.9 Electron Correlation

Accurate quantum computational methods require a good approximation of electron correlation, which accounts for the instantaneous interactions between electrons in a system. One type of correlation, Fermi correlation, which is that two electrons of like spin cannot occupy the same point in space, is dealt with by the Slater determinant method of Hartree-Fock theory, as it satisfies the antisymmetric principle. However, Coulomb correlation, the correlation in motion due to electrostatic repulsion between electrons, is not fully accounted for by Hartree-Fock theory, which considers each electron to move in a ‘mean field’ of all other electrons instead of considering individual electronic repulsion. This means that for many-electron systems the Hartree-Fock energy, E_{HF} , is always higher than E_0 . The difference between the two is known as the electron correlation energy, and often contributes $\sim 1\%$ of the total energy of a system, which can be problematic when considering relative energies.⁵⁷

2.10 Møller-Plesset Perturbation Theory

Møller-Plesset perturbation theory (MP)⁶⁵ is a post-Hartree-Fock (post-HF) method which improves upon the Hartree-Fock method by including electron correlation effects. Unlike Hartree-Fock, MP is not a variational method. MP takes the output of a Hartree-Fock calculation and adds electron correlation effects on top. Because of this, the calculated MP energy may be lower than E_0 . As a perturbation theory, MP assumes that it is possible to approximate the eigenfunctions of a Hamiltonian by improving a similar Hamiltonian with a perturbed Hamiltonian. This can be expressed as:

$$\hat{H} = \hat{H}_0 + \lambda \hat{H}' \quad (\text{Eq. 2.24})$$

Where \hat{H} is the Hamiltonian, \hat{H}_0 is the unperturbed Hamiltonian, \hat{H}' is a Hamiltonian representing the perturbation and λ is an arbitrary parameter that effects the magnitude of the perturbation. If the eigenfunctions of \hat{H}_0 are known and the perturbation is small, then the eigenfunctions of the improved Hamiltonian can be approximated systematically. The first order MP (MP1) correction to the total energy, E_{c1} , and the first order energy, E_{MP1} , are given by:

$$E_{c1} = \langle \Psi_0 | \hat{H}' | \Psi_0 \rangle = -\frac{1}{2} \sum_{i,j}^n \langle \varphi_i \varphi_j | | \varphi_i \varphi_j \rangle \quad (\text{Eq. 2.25})$$

$$E_{MP1} = E_0 + E_{c1} = \sum_i \varepsilon_i - \frac{1}{2} \sum_{i,j}^n \langle \varphi_i \varphi_j | | \varphi_i \varphi_j \rangle \quad (\text{Eq. 2.26})$$

This is the same as the Hartree-Fock energy, E_{HF} . Correlation is only included at second order (MP2) and higher perturbations. The second order correction to the energy, however, requires the first order correction to the wavefunction to be known. The MP2 energy correction, E_{MP2} , is $E_0 + E_{c1} + E_{c2}$, where E_{c2} is:

$$E_{c2} = \sum_{i < j}^{\text{occ}} \sum_{a < b}^{\text{virt}} \frac{|\langle \varphi_i \varphi_j | | \varphi_a \varphi_b \rangle|^2}{\varepsilon_i + \varepsilon_j - \varepsilon_a - \varepsilon_b} \quad (\text{Eq. 2.27})$$

MP calculations can include increasing orders of correction to the wavefunction, from first-order up to increasingly expensive calculations such as fifth-order (MP5). Due to the costs of higher-order MP calculations (>MP3) being excessively expensive and molecular properties

being described little better with MP3 onwards than at the MP2 level, the second order level of theory is generally the preferred method.

2.11 Density Functional Theory

Post-HF methods offer a way to recover the correlation energy of the system, but scale very poorly with the size of the system. An alternative method of recovering the correlation energy is Density Functional Theory (DFT), a widely used and successful method which has built upon the successes of Hartree-Fock theory while improving on how electron-electron interactions are handled. In DFT, the positions of atomic nuclei and the ground state energy of a system are derived from the electron density, rather than the wavefunction itself. In DFT, the electron density for a many-electron system is:

$$\rho(\mathbf{r}) = n \int \Psi^*(\mathbf{x}_1, \mathbf{x}_2, \dots, \mathbf{x}_n) \Psi(\mathbf{x}_1, \mathbf{x}_2, \dots, \mathbf{x}_n) d\sigma_1 d\mathbf{x}_2 \dots d\mathbf{x}_n \quad (\text{Eq. 2.28})$$

And the total energy of the system in terms of the electron density is:

$$E[\rho(\mathbf{r})] = T[\rho(\mathbf{r})] + V[\rho(\mathbf{r})] \quad (\text{Eq. 2.29})$$

As the energy is a function of the density, and the density is a function of the spatial coordinates of the electrons, the energy is a function of a function. This is known as a *functional*, hence the name of the theory, and is denoted with square brackets, i.e. $E[\rho(r)]$, the energy density functional. Calculations on the density of a system, rather than the wavefunction, are much simpler (and hence faster) as instead of solving for system with $3n$ variables, where n is the number of electrons, the electron density relies on only three variables.

An early DFT model, The Thomas-Fermi-Dirac model, split the energy density functional into three parts, which are a kinetic energy term, T , a nucleus-electron attraction term, V_{ne} , and an electron-electron repulsion term, V_{ee} , as so:

$$E[\rho(\mathbf{r})] = T[\rho(\mathbf{r})] + V_{ne}[\rho(\mathbf{r})] + V_{ee}[\rho(\mathbf{r})] \quad (\text{Eq. 2.30})$$

As with Hartree-Fock theory, the Born-Oppenheimer approximation is made, and hence the nuclear-nuclear repulsion term is said to be constant. Additionally, the electron-electron repulsion is further split into two parts, a Coulomb term, J , and an exchange term, K , as so:

$$E[\rho(\mathbf{r})] = T[\rho(\mathbf{r})] + V_{ne}[\rho(\mathbf{r})] + J[\rho(\mathbf{r})] + K[\rho(\mathbf{r})] \quad (\text{Eq. 2.31})$$

In 1927, Thomas and Fermi used a uniform electron gas (UEG, or ‘Jellium’) model to approximate the exchange and kinetic energy functionals.^{66,67} The UEG model is a system comprised of an infinite number of electrons in an infinite space with uniformly distributed positive charge.^{66,67} The Thomas-Fermi model is the simplest model of interacting electrons and, although useful for calculations of metal clusters, is not a suitable model for molecules of a finite size and with non-uniformly distributed charge, and does not predict bonding.

2.11.1 The Hohenberg-Kohn Theorems

Modern DFT begins with the Hohenberg-Kohn theorems⁶⁸ and Kohn-Sham equations.^{69–71} In 1964, Hohenberg and Kohn developed two theorems, the first being that the energy of a system can be obtained from the electron density:

$$\rho(\mathbf{r}) \rightarrow V_{\text{ext}} \rightarrow H \rightarrow E \quad (\text{Eq. 2.32})$$

I.e., the electron density, $\rho(\mathbf{r})$, determines the external potential, V_{ext} , and hence the Hamiltonian and total energy of the system. The second of the Hohenberg-Kohn theorems is that the variational principle applies to the energy functional, i.e. that the energy given by the electron density of the system is lowest at the true ground state electron density, and the energy obtained from any other electron density is higher.

Hohenberg and Kohn separated the terms in **Eq. 2.31** into two parts, a ‘Hohenberg-Kohn universal functional’, F , and a term representing the interaction of the electron density with an external potential ‘ V_{ext} ’:

$$[\rho(\mathbf{r})] = F[\rho(\mathbf{r})] + \int \rho(\mathbf{r})V_{\text{ext}}(\mathbf{r}) d\mathbf{r} \quad (\text{Eq. 2.33})$$

As the second term can be calculated exactly, knowing the universal functional would allow computation of the exact ground state total energy. Unfortunately, it is not known, and approximations must be made.

2.11.2 The Kohn-Sham Equations

While the Hohenberg-Kohn approach does not require individual electron orbitals to be defined, the problem with ‘orbital-free’ DFT is that, in practice, approximations of the kinetic, exchange and correlation energy functionals must be made as the exact forms are not known. An alternative is the Kohn-Sham approach, which considers a fictitious non-interacting system of electrons with the exact same ground state density as the real, fully interacting, system of

electrons. By considering this fictitious system, the challenge is no longer finding the universal functional, it is instead finding a fictitious system which has the same density as the system with interacting particles. The Kohn-Sham equations introduce orbitals as a way to calculate the kinetic energy.⁶⁹⁻⁷¹ By doing so, only approximations of the exchange and correlation functionals are required.

To map the energy of the non-interacting system onto the interacting system, interactions must be added to the kinetic energy of the non-interacting system, T_{NI} . These include the interactions between the nuclei and the electrons, V_{ne} , Coulombic interactions, J , and an exchange-correlation term, E_{xc} , which includes the small amount of remaining kinetic energy from the interaction of particles and the exchange-correlation interactions between electrons. A general expression for the Kohn-Sham DFT energy, E_{KS} , can be written as:

$$E_{\text{KS}}[\rho(\mathbf{r})] = T_{\text{NI}}[\rho(\mathbf{r})] + V_{\text{ne}}[\rho(\mathbf{r})] + J[\rho(\mathbf{r})] + E_{\text{xc}}[\rho(\mathbf{r})] \quad (\text{Eq. 2.34})$$

The only unknown term in this expression for E_{KS} is the exchange-correlation term. **Eq. 2.34** can be solved using Schrödinger-like equations, known as Kohn-Sham equations:

$$\left(-\frac{1}{2}\nabla^2 + V_{\text{KS}}(\mathbf{r})\right)\varphi_i(\mathbf{r}) = \varepsilon_i\varphi_i(\mathbf{r}) \quad (\text{Eq. 2.35})$$

Where ε_i is the energy corresponding to the orbital φ_i , and V_{KS} is the Kohn-Sham potential, which is the effective potential needed to generate the same electron density as a system with interacting particles. The solutions to these equations are known as Kohn-Sham orbitals, $\varphi_i^{\text{KS}}(\mathbf{r})$, and the total electron density is equal to the sum of the square modulus of the occupied Kohn-Sham orbitals:

$$\rho(\mathbf{r}) = \sum_i |\varphi_i^{\text{KS}}(\mathbf{r})|^2 \quad (\text{Eq. 2.36})$$

These Kohn-Sham equations can be solved using the SCF methodology using an initial set of molecular orbitals, as in Hartree-Fock theory. While there are many similarities between Hartree-Fock theory and Kohn-Sham DFT, the difference is that Hartree-Fock theory is an approximation and Kohn-Sham DFT is an exact method, provided the exact form of E_{xc} is known and that the electron density can be expressed using a single electronic configuration. In practice, however, E_{xc} must be approximated.

2.11.3 Exchange-Correlation Functionals

Many different approximations exist for the exchange-correlation functional (*xc*-functional), allowing for the computational calculation of the ground state energies of molecular systems with various levels of accuracy. John Perdew formulated a ‘Jacob’s Ladder’ of *xc*-functionals, which take a computational chemist from the ‘Hartree World’ to the ‘Heaven of Chemical Accuracy’.

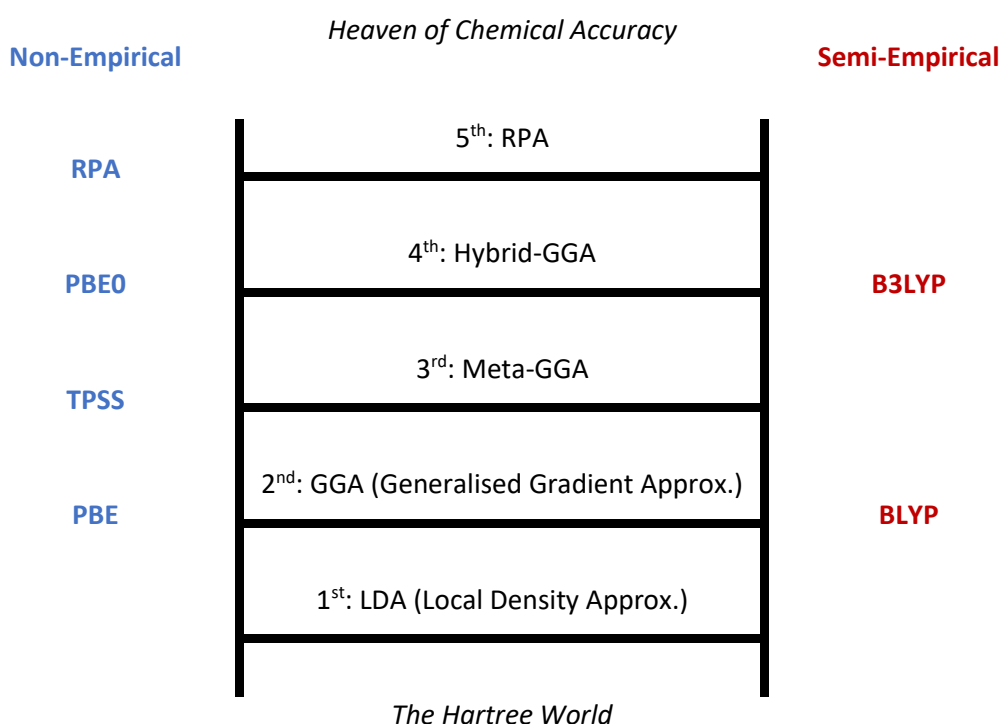


Figure 2.3: The Jacob’s Ladder of *xc*-functionals, with examples of non-empirical and semi-empirical *xc*-functionals shown in blue and red, respectively. Reproduced from Perdew, J.P. and Schmidt, K., “Jacob’s ladder of density functional approximations for the exchange-correlation energy”.⁷²

2.11.3.1 The Local Density Approximation

The simplest form of exchange-correlation functional, and the first rung on the Jacob's Ladder, is the Local Density Approximation (LDA),^{73,74} in which the exchange-correlation energy at a given point is equal to that of a uniform electron gas of the same electron density, for which E_{xc} is known (for all intents and purposes) exactly, as follows:

$$E_{xc}^{LDA}[\rho(\mathbf{r})] = \int \rho(\mathbf{r})\varepsilon_{xc}[\rho(\mathbf{r})] d\mathbf{r} \quad (\text{Eq. 2.37})$$

Where ε_{xc} is the exchange-correlation energy density. The LDA functional has several problems: it favours more homogenous electron densities than the exact density and tends to cause overbinding between atoms in molecules.^{73,74}

2.11.3.2 GGA and Meta-GGA xc-Functionals

The next two rungs on the ladder are the Generalised Gradient Approximation (GGA) and meta-GGA functionals, which improve upon LDA by expressing the exchange-correlation energy not simply as a functional of the density at a given point in space but also in terms of the gradient and higher derivatives of the density. GGA functionals consider the first derivative, $\nabla\rho$, while meta-GGA functionals consider the second, $\nabla^2\rho$, as so:

$$E_{xc}^{GGA}[\rho(\mathbf{r})] = \int \rho(\mathbf{r})\varepsilon_{xc}[\rho(\mathbf{r}), \nabla\rho(\mathbf{r})] d\mathbf{r} \quad (\text{Eq. 2.38})$$

$$E_{xc}^{\text{meta-GGA}}[\rho(\mathbf{r})] = \int \rho(\mathbf{r})\varepsilon_{xc}[\rho(\mathbf{r}), \nabla\rho(\mathbf{r}), \nabla^2\rho(\mathbf{r})] d\mathbf{r} \quad (\text{Eq. 2.39})$$

There are numerous different GGA functionals, which each use different parameters to calculate the exchange-correlation energy, derived either from first principles or semi-empirically using experimental data, such as atomisation energies. Examples of such functionals are the B88P86 (BP) functional, which contains the B88 exchange functional fitted to accurate atomisation energies developed by Becke and the P86 correlation functional developed by Perdew and Wang; the non-empirical Perdew-Burke-Ernzerhof (PBE) functional,^{75,76} which was a refinement upon previous work done by Perdew *et al.*, including the BP functional; and the semi-empirical BLYP functional,⁷⁷ named after Becke for the B88 exchange part and Lee, Yang and Parr for the correlation part, which was parameterised using

the correlation energy of the helium atom. GGA functionals perform well for prediction of structures but not so much for other properties.

On the next rung are the meta-GGA functionals, which are not as numerous, and offer a small improvement over the GGA functionals for little increase in computational cost. An example of a popular meta-GGA functional is the non-empirical functional TPSS,^{75,78} named after Tao, Perdew, Staroverov and Scuseria, were developed as an attempt to increase the accuracy of calculations.

2.11.3.3 Hybrid-GGA and RPA *xc*-Functionals

The exchange contribution to the exchange-correlation energy, which is approximated in the ‘pure’ *xc*-functionals (e.g. PBE, BLYP) is exact in the Hartree-Fock approximation. The fourth rung on the ladder, hybrid-GGA functionals, include a percentage of this Hartree-Fock exact exchange energy. Two examples of popular hybrid functionals are the semi-empirical B3LYP^{77,79–82} functional and the non-empirical PBE0^{75,76,83} functional. The B3LYP functional contains exact exchange, LDA exchange and GGA (B88) exchange and LDA and GGA (LYP) correlation:

$$E_{xc}^{B3LYP} = (1 - a)E_x^{LDA} + aE_x^{HF} + b\Delta E_x^{B88} + (1 + c)E_c^{LDA} + cE_c^{LYP} \quad (\text{Eq. 2.40})$$

The three parameters a , b and c are fit to experimental data, and are ≈ 0.2 , 0.7 and 0.8 respectively. The PBE0 functional instead estimates the exact exchange contribution using perturbation theory, and mixes 25% of Hartree-Fock exact exchange energy with exchange from the PBE functional, as so:

$$E_{xc}^{PBE0} = 0.25E_x^{HF} + 0.75E_x^{PBE} + E_c^{PBE} \quad (\text{Eq. 2.41})$$

The fifth rung and beyond represent the next and future levels of improvement. The Random Phase Approximation (RPA) is one such example, which incorporates virtual orbitals as well as occupied orbitals to better approximate E_{xc} , and improves the treatment of dispersion interactions by DFT.

2.12 Relativistic Effects

While relativistic effects for the lighter atoms are negligible, the relativistic effects on the mass of the electron increase as the speed of the electron approaches c , the speed of light. In heavier atoms, amongst which the lanthanides and actinides studied in this work are most definitely counted, the radial velocity for the innermost electrons becomes a significant proportion of c and these effects become non-negligible. A good demonstration of the effect

that relativity can have on the properties of heavy atoms is the colour of gold. Non-relativistic calculations predict the transition responsible for the distinctive yellow colour to instead be in the ultraviolet region, and only the inclusion of relativistic effects leads to the prediction of transitions in the visible region.^{84,85} However, the Schrödinger equation is non-relativistic, i.e. it does not take into account the effects of special relativity.

One way in which these relativistic effects can be accounted for in calculations is by modifying the Hamiltonian to include terms for scalar relativistic and spin-orbit coupling. The time-independent Dirac equation is:⁸⁶

$$\hat{H}_D \Psi = E \Psi \quad (\text{Eq. 2.42})$$

Where \hat{H}_D is the Dirac Hamiltonian, shown in full here:

$$[c\boldsymbol{\alpha} \cdot \hat{P} + \boldsymbol{\beta}mc^2 + \hat{V}] \Psi = E \Psi \quad (\text{Eq. 2.43})$$

Where c is the speed of light, m is the mass of the electron, \hat{V} is the potential operator, \hat{P} is the momentum operator and $\boldsymbol{\alpha}$ and $\boldsymbol{\beta}$ are two 2 x 2 matrices, as so:

$$\boldsymbol{\alpha} = \begin{pmatrix} 0 & \boldsymbol{\sigma}_{x,y,z} \\ \boldsymbol{\sigma}_{x,y,z} & 0 \end{pmatrix}, \quad \boldsymbol{\beta} = \begin{pmatrix} \mathbf{I} & 0 \\ 0 & -\mathbf{I} \end{pmatrix} \quad (\text{Eqs. 2.44-2.45})$$

$$\boldsymbol{\sigma}_x = \begin{pmatrix} 0 & 1 \\ 1 & 0 \end{pmatrix}, \quad \boldsymbol{\sigma}_y = \begin{pmatrix} 0 & -i \\ i & 0 \end{pmatrix}, \quad \boldsymbol{\sigma}_z = \begin{pmatrix} 1 & 0 \\ 0 & -1 \end{pmatrix} \quad (\text{Eqs. 2.46-2.48})$$

Where $\boldsymbol{\sigma}_{x,y,z}$ are the Pauli spin matrices (shown in Eqs. 2.46-2.48) and \mathbf{I} is a 2 x 2 unit matrix. The wavefunction described by the Dirac equation is a spinor function, rather than a scalar function, and has four components, as it describes an electron-positron pair and the spin pairs of each. This makes the Dirac equation very computationally expensive compared to the non-relativistic Schrödinger equation.

Two of the four components are electron components, known as the large components, and two are the positron components, known as the small components. The small components contribute the least to electron-electron interactions, but the most to computational demand. As such, it is common to use transformations, such as the Foldy-Wouthuysen transformation,⁸⁷ to eliminate or decouple the small components. One popular approximation used is the Douglas-Kroll-Hess (DKH) approximation,^{88,89} which is based on the Foldy-Wouthuysen transformation.⁸⁷ Decoupling the two components leads to an infinite series of operators, the first few orders of which can be used to account for scalar relativistic effects in quantum calculations accurately whilst remaining computationally efficient. The second order expansion, known as DKH2,^{88,89} is sufficient for most calculations and is widely used. Another

popular approximation is the two-component Zeroth-Order Regular Approximation (ZORA),^{90,91} a zeroth-order perturbational expansion of the Dirac equation which is implemented in a way which allows spin-orbit coupling to be included along with the scalar relativistic effects, or neglected, as desired.

2.13 Effective Core Potentials

As mentioned previously, only the valence electrons of an atom are likely to be involved in chemical processes. Effective core potentials (ECPs) replace a number of the core electrons of an atom with a potential field while the valence electrons are treated explicitly. The large number of core electrons in heavy elements such as the lanthanides and actinides means that the use of pseudopotentials can greatly reduce the cost of calculations which include these elements. Pseudopotentials for the f-block elements can treat the f-electrons explicitly or include them in the core, the latter of which, the 'f-in-core' ECPs,^{92,93} decrease computational expense at the cost of accuracy. However, while the 4f orbitals of the lanthanides are generally considered to be 'core-like' and to not directly participate in chemical bonding, care must be taken when using these f-in-core ECPs for the actinides, as the 5f orbitals are more involved in chemical bonding.^{92,93}

Additionally, relativistic effective core potentials (RECPs) provide an alternative method for handling the effects of relativity by including an implicit treatment of relativistic effects in the potential. As direct relativistic effects are most significant for the core electrons, RECPs allow for a non-relativistic Hamiltonian to be used for the valence electrons, and provide indirect relativistic effects for the valence electrons. RECPs have been argued to be more accurate than most common scalar relativistic methods.⁹⁴

2.14 The Quantum Theory of Atoms in Molecules

Bader's Quantum Theory of Atoms in Molecules (QTAIM)⁵⁸ is a quantitative tool which can give an insight into the properties of molecules *via* topological and integrated analysis of the electron density. QTAIM partitions a molecular system into separate mononuclear regions, Ω , which correspond to the atoms of the molecule, bound by a zero-flux surface which satisfies the condition $\nabla\rho(\mathbf{r}) \cdot \vec{n}(\mathbf{r}) = 0$, where $\rho(\mathbf{r})$ is the magnitude of the electron density at a point \mathbf{r} and $\vec{n}(\mathbf{r})$ is a vector normal to the surface at that point.^{58,59,95} In other words, each atom is a basin bounded by a surface which none of the gradient vectors of the density crosses. An example of this can be seen in **Figures 2.4** and **2.5**, which show the electron density and gradient vector field of the electron density for benzene.

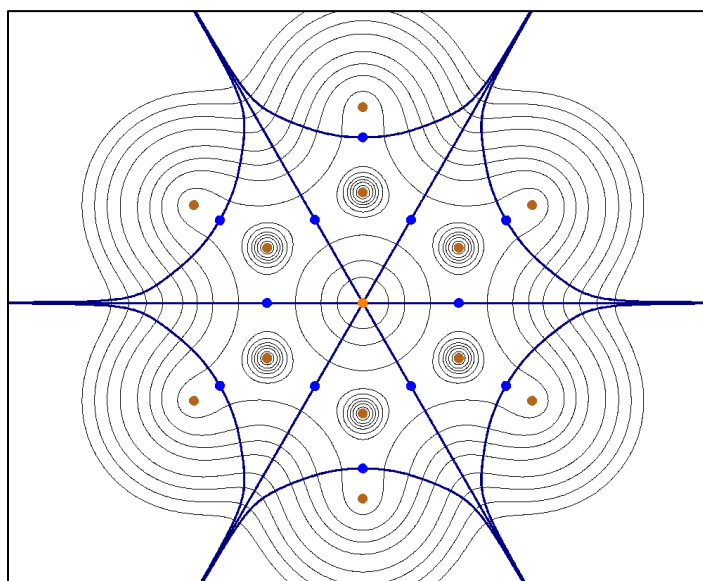


Figure 2.4 Contour plot of the electron density for benzene, showing the nuclear critical points (NCPs, brown circles), bond critical points (BCPs, blue circles), ring critical point (RCP, orange circle) and zero-flux surfaces (blue lines) of the molecule, generated with MultiWFN.⁹⁶

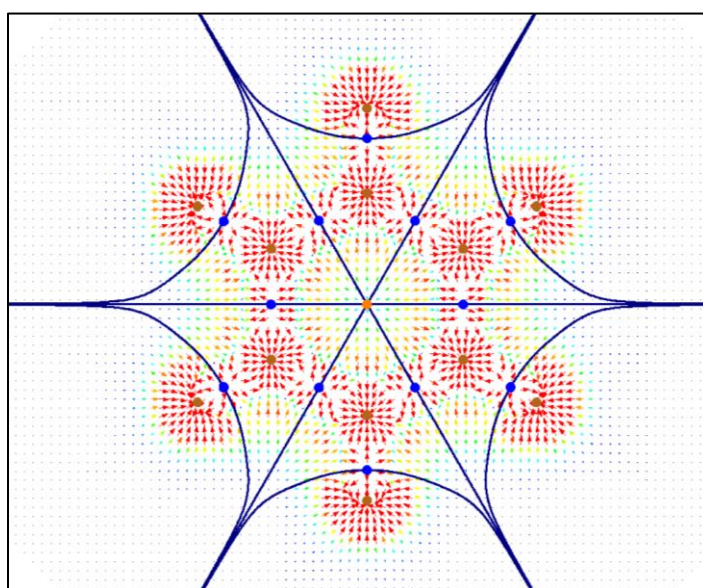


Figure 2.5 Plot of the gradient vector field of the electron density for benzene, showing the nuclear critical points (NCPs, brown circles), bond critical points (BCPs, blue circles), ring critical point (RCP, orange circle) and zero-flux surfaces (blue lines) of the molecule, generated with MultiWFN.⁹⁶

QTAIM can provide insight on the degree of covalency within a molecule, which can be degeneracy-driven, *via* the energetic near-degeneracy of the orbitals involved, or overlap-driven, *via* orbital overlap.⁹⁵ Integration over the atomic basins provides quantitative information about the amount of electrons which are localised within basins or delocalised (shared) between basins, providing insight into both types of covalency, while the magnitude of the electron density at the BCPs indicates the degree of charge accumulation in the bond and hence is a measure of overlap-driven covalency.⁹⁵

In QTAIM, molecular structure is revealed by critical points (CPs) in the electron density, i.e. points in space at which the first derivatives of ρ vanish. Taking the second derivatives of the electron density allows for characterisation of the critical point. In three dimensions, there are nine second derivatives of the electron density, which can be arranged in the Hessian matrix as so, for a critical point at \mathbf{r}_c :^{58,59}

$$A(\mathbf{r}_c) = \begin{pmatrix} \frac{\partial^2 \rho}{\partial x^2} & \frac{\partial^2 \rho}{\partial x \partial y} & \frac{\partial^2 \rho}{\partial x \partial z} \\ \frac{\partial^2 \rho}{\partial y \partial x} & \frac{\partial^2 \rho}{\partial y^2} & \frac{\partial^2 \rho}{\partial y \partial z} \\ \frac{\partial^2 \rho}{\partial z \partial x} & \frac{\partial^2 \rho}{\partial z \partial y} & \frac{\partial^2 \rho}{\partial z^2} \end{pmatrix} \quad (\text{Eq. 2.49})$$

The Hessian matrix, $A(\mathbf{r}_c)$, can be diagonalized by rotating the coordinate system $r(x, y, z)$ to a new system, $r(x', y', z')$, where x' , y' and z' are the principle curvature axes of the CP. The diagonalized Hessian, Λ is:^{58,59}

$$\Lambda = \begin{pmatrix} \frac{\partial^2 \rho}{\partial x'^2} & 0 & 0 \\ 0 & \frac{\partial^2 \rho}{\partial y'^2} & 0 \\ 0 & 0 & \frac{\partial^2 \rho}{\partial z'^2} \end{pmatrix} = \begin{pmatrix} \lambda_1 & 0 & 0 \\ 0 & \lambda_2 & 0 \\ 0 & 0 & \lambda_3 \end{pmatrix} \quad (\text{Eq. 2.50})$$

Where λ_1 , λ_2 and λ_3 are the curvatures of ρ with respect to the principle axes x' , y' and z' and are also used to characterise which type of CP a given CP is. The types of CP are denoted (ω, σ) , where ω is the 'rank', or the number of non-zero curvatures of ρ at the critical point, and σ is the 'signature', or the sum of the signs of the curvatures. CPs with a rank less than 3 are mathematically unstable, and so the rank of a CP is almost always 3. The most common types of CP are the (3, -3) CPs or nuclear critical points (NCPs), where all three curvatures are negative and ρ is a local maximum, and (3, -1) CPs or bond critical points (BCPs), where two

curvatures are negative and ρ is a maximum in the plane of the two negative curvatures and a minimum along the third axis perpendicular to the same plane, i.e. the bond path (which is not the same as a chemical bond)⁹⁷. The two other types of stable CPs are (3, +1) or ring critical points (RCPs), and (3, +3) or cage critical points (CCPs). The number and type of critical points that can coexist in a molecule or crystal should satisfy the Poincaré-Hopf relationship, which is a useful tool for checking whether all of the CPs in a system have been found:^{58,59}

$$n_{\text{NCP}} - n_{\text{BCP}} + n_{\text{RCP}} - n_{\text{CCP}} = \begin{cases} 1 & \text{(Isolated molecules)} \\ 0 & \text{(Infinite crystals)} \end{cases} \quad \text{(Eq. 2.51)}$$

Examples of the NCPs, BCPs and RCP for benzene can be seen in **Figures 2.4** and **2.5**.

2.14.1 Topological Properties of the Electron Density

Analysis of the topology of the electron density can yield information about the properties of a molecule and the bonding within it. Three topological properties at the BCPs are typically used to characterise the bonding in a molecule: the magnitude of the electron density, ρ_{BCP} , the Laplacian of the electron density, $\nabla^2 \rho_{\text{BCP}}$, and the energy density, H_{BCP} .

The magnitude of the electron density at the BCP reflects the strength of the bond. A rule of thumb is that ρ_{BCP} is greater than 0.2 a.u. for covalent interactions and less than 0.1 a.u. for closed-shell interactions, such as ionic, van der Waals or hydrogen bonding.

The Laplacian of the electron density is the sum of the three curvatures of the density. At a BCP, two of these curvatures are negative and the third, which lies along the bond path, is positive. In covalent bonding, the two negative curvatures are generally larger than the positive curvature, meaning that $\nabla^2 \rho_{\text{BCP}}$ for a covalent interaction is generally negative, while the positive curvature is generally larger in an ionic interaction, leading to a positive $\nabla^2 \rho_{\text{BCP}}$. This is not, however, a rule, and situations exist where the Laplacian does not follow this guide, such as in strongly polarised bonds (e.g. C—N, C—O bonds) where the Laplacian can be either negative or positive.

The energy density at the BCP is negative for a covalent interaction, with a larger magnitude of the energy density corresponding to greater covalency, while for ionic interactions the energy density is typically positive.

2.14.2 Integrated Properties of the Electron Density

As stated previously, the electron density of a molecule in QTAIM is partitioned into separate atomic basins. By calculating the integrals of the electron density over these basins, further information about the properties of a molecule can be obtained. Assuming Ψ is real the expectation value of an observable, \hat{O} , is defined in atomic units as:^{58,59}

$$\begin{aligned}\langle \hat{O} \rangle &= \sum_i^{\text{all atoms}} n \int_{\Omega_i} \int \Psi^* \hat{O} \Psi d\tau' d\mathbf{r} \\ &= \sum_i^{\text{all atoms}} \left(\int_{\Omega_i} \rho_0 d\mathbf{r} \right) = \sum_i^{\text{all atoms}} O(\Omega_i)\end{aligned}\tag{Eq. 2.52}$$

Where τ' is all of the spin components and all but one spatial component, and ρ_0 is a 'dressed density'. The molecular expectation value of the operator is obtained from integrating this dressed density over all the atomic volumes in the molecule. The atomic expectation value of the operator, $\langle \hat{O} \rangle_{\Omega}$, or $O(\Omega)$, is obtained by integrating the dressed density over the specific atomic basin Ω .^{58,59} The simplest example of an integrated atomic property is $N(\Omega)$, the atomic electron population, which is obtained by setting \hat{O} to unity.^{58,59}

$$N(\Omega) = \int_{\Omega} \rho d\mathbf{r}\tag{Eq. 2.53}$$

This can be used to obtain the atomic charge, $q(\Omega)$, by simply subtracting $N(\Omega)$ from the nuclear charge, Z_{Ω} .^{58,59}

$$q(\Omega) = Z_{\Omega} - N(\Omega)\tag{Eq. 2.54}$$

The delocalisation index, δ , is obtained by integrating the exchange density over each of two atomic basins, Ω_1 and Ω_2 .^{58,59,95}

$$\delta(A, B) = -2 \sum_{i,j} S_{ij}(A) S_{ij}(B)\tag{Eq. 2.55}$$

Where $S_{ij}(A)$ is the overlap integral between orbitals i and j over the atomic basin, Ω_A . The delocalisation index is a measure of the amount of electron sharing between the two basins.^{58,59,95} The delocalisation index can be calculated for any two basins in a molecule. If the

two basins represent bonded atoms, this can be considered a direct measure of bond order, in the absence of charge transfer.⁵⁹ If this is performed over only one atomic basin, the amount of electrons localised on that atom can be obtained, known as the localisation index, $\lambda(\Omega)$.^{58,59}

$$\lambda(A) = \sum_{i,j} S_{ij}(A)S_{ij}(A) \quad (\text{Eq. 2.56})$$

These two indices and the atomic electron population are related as follows:^{58,59}

$$N(\Omega) = \lambda(\Omega) + \frac{1}{2} \sum_{\Omega_1 \neq \Omega_2} \delta(\Omega_1, \Omega_2) \quad (\text{Eq. 2.57})$$

I.e., the total number of electrons is the sum of the localised electrons and half of all of the delocalised electrons.

2.15 COSMO Solvation

The CONductor-like Screening MOdel (COSMO) is a commonly used method for simulating the effects of solvation in quantum mechanical calculations. COSMO represents the solvent as a dielectric continuum with a permittivity, ϵ , which varies depending on the solvent to be simulated. This continuum surrounds the solute molecules outside of a constructed molecular cavity, built of atom-centred spheres with radii larger than the van der Waals radii of the respective atoms by approximately 20%. The cavity surface is approximated by a grid of polygons, e.g. pentagons and triangles. The use of COSMO allows for the approximation of higher levels of solvation without explicitly modelling the solvent molecules, which would considerably complicate molecular-sized calculations.

2.16 Packages

The work presented in this thesis makes use of several software packages:

TURBOMOLE (<http://www.turbomole.com/>)

TURBOMOLE⁹⁸ is a quantum chemistry software package with a wide range of functionality, developed at the University of Karlsruhe by the research group of Reinhart Ahlrichs. TURBOMOLE employs Gaussian-type basis sets and effective core potentials and is capable of performing Hartree-Fock, DFT and MP2 calculations, as well as other methods not used in this work, such as time-dependent DFT (TD-DFT) and coupled-cluster (CC) calculations. All geometry optimisations and SCF calculations in this work were performed using TURBOMOLE, and exported for QTAIM analysis using the .molden format (and subsequently converted to .wfn and .wfx using the molden2aim program).

Multiwfn (<http://sobereva.com/multiwfn/>)

Multiwfn⁹⁶ is a multifunctional wavefunction analysis program maintained by Tian Lu at Beijing Kein Research Centre for Natural Sciences, used in this work for topological analysis of the electron density.

AIMAll (<http://aim.tkgristmill.com/>)

AIMAll⁹⁹ is a software package for performing QTAIM analysis developed by Todd A Keith, based on the 1994 AIMPAC package developed and maintained by Richard Bader's research group, used in this work for the calculation of topological and integrated properties of the electron density.

GaussView (<http://gaussian.com>)

GaussView¹⁰⁰ is a graphical interface used in this work to build, modify and inspect the structures of the molecules studied, as well as to generate the ball-and-stick molecular representations presented throughout.

Chapter 3: Nitrates of Ln and An

In this chapter, the investigation of the structure, binding energies, coordination numbers and first-shell hydration numbers of nitrate complexes of several trivalent lanthanides and actinides is discussed. As well as being required for work reported in later chapters of this thesis, these small nitrate complexes were used as an opportunity to trial several computational methodologies against high-level benchmarks, to ascertain which approach would be best for the larger and more computationally expensive complexes of ligands such as BTP and BTPhen.

3.1 Introduction

The raffinate from the PUREX process is a mixture of metals, including a large amount of lanthanides and a smaller amount of the minor actinides (Np, Am, Cm), in nitric acid. Therefore, in order to investigate the Ln/An separation process, the environment around the relevant radionuclides in nitric acid must be modelled and understood. This requirement provided a useful benchmarking opportunity, as nitrate ligands are much smaller than large separation ligands such as BTP and BTPhen, hence simulations of the nitrates are comparatively computationally cheap. The speed at which calculations could be performed on the nitrate complexes allowed the use of high-level second-order Møller–Plesset perturbation theory (MP2) calculations against which to benchmark a set of model chemistries.

The nitrate and hydrated nitrate complexes of several of the lanthanides and actinides have previously been studied with quantum-mechanical methods. In 2001, Dobler *et al.* investigated the binding modes of the unsaturated $\text{Ln}(\text{NO}_3)_m^{(3-m)+}$ ($m = 1-3$) and the hydrated $\text{Ln}(\text{NO}_3)_3(\text{H}_2\text{O})_x$ ($x = 4-6$) complexes of Ln = La, Lu and Eu in the gas phase using HF and DFT (B3LYP) methods and the 4f in-core pseudopotentials of Dolg *et al.*,^{101,102} finding that the bidentate binding mode of the nitrate ligands was preferred over the monodentate binding mode for the unsaturated complexes, with the energy difference decreasing as the number of nitrate ligands increased, due to the anion-anion repulsions of the ligands being larger when they are bound to the metal ion through a bidentate binding mode.¹⁰¹ The energy difference between binding modes was found to be lower with DFT than with HF, and small compared to the interaction energy between the Ln^{III} ion and a water molecule, meaning that in the hydrated nitrate complexes the addition of water molecules can lead to stabilisation of the monodentate binding mode.¹⁰¹ For the hydrated nitrate complexes, Dobler *et al.* reported that there was no clear preference for either the bidentate or monodentate binding mode.¹⁰¹

However, a more recent study by Xi *et al.* in 2014 investigated the hydrated nitrate complexes of Eu^{III} and Am^{III} using DFT (B3LYP) and the small-core relativistic effective core potentials (RECPs),^{103–105} finding that the bidentate binding mode for the nitrate ligands was more favourable than the monodentate mode in both the gas phase and in aqueous solution, the latter modelled using COSMO.¹⁰³ Additionally, in 2011, Lan *et al.* reported that at most four water molecules could be coordinated to the metal centre alongside three bidentate nitrate ligands,⁵² and suggested that the $\text{M}(\text{NO}_3)_3(\text{H}_2\text{O})_4$ complex is representative of the environment around the ions prior to complexation with the separation ligand.⁵²

In this chapter, several methodologies are benchmarked against MP2: ‘sECP’, employing the standard Stuttgart-Dresden small core relativistic effective core potentials (RECPs), which replace the core electrons of the Ln/An centre with a spherical pseudopotential; ‘AE’, or all-electron, i.e. calculations without an ECP, modelling all of the electrons in the complex; and ‘IC’, employing 4f/5f in-core pseudopotentials to include the f-electrons in the ECP.

Furthermore, the solvation of the trinitrate complexes of the lanthanides and actinides was investigated, both using explicit solvation methods, where water molecules were added to make $\text{Ln/An}(\text{NO}_3)_3(\text{H}_2\text{O})_x$ complexes, and a continuum solvent model (COSMO), an implicit solvation method. The maximum coordination numbers and first-shell hydration numbers of the trinitrate complexes were calculated with the explicit solvation method, and the effects of the implicit solvation method on the complex geometries of the trinitrates were investigated.

3.2 Computational Details

All calculations were performed using version 6.6 of the TURBOMOLE quantum chemistry code⁹⁸ using scalar-relativistic DFT.

For standard effective core potential calculations (sECP), the ECP-28 (Lu, Gd, Eu), ECP-46 (La) and ECP-60 (Cm, Am) Stuttgart-Dresden small core relativistic ECPs (RECPs) selected by default in TURBOMOLE were used,¹⁰⁶ along with either the def2-SVP (for N, O and C) and def-SVP (for Ln, An) basis sets of polarised double- ζ quality, or the def2-TZVP (for N, O and C) and def-TZVP (for Ln, An) basis sets of polarised triple- ζ quality, referred to from here on as def(2)-SVP and def(2)-TZVP, respectively, as well as their corresponding auxiliary basis sets.^{107,108}

For all-electron (AE) calculations, the SARC-TZVP basis sets and SARC-TZVP-RI auxiliary basis sets of polarised triple- ζ quality were used for the metal ions,^{109,110} along with the def2-TZVP basis set for all other atoms (N, O and C).¹⁰⁸ Additionally, for AE calculations the 2nd order

Douglas-Kroll-Hess (DKH) Hamiltonian was used for consideration of scalar relativistic effects.^{88,89}

For 4f/5f in-core (IC) calculations, the 4f/5f in-core pseudopotentials and basis sets developed by Dolg *et al.* were used for the metal ions,^{92,93,102,104,111,112} as follows: **La** - ECP46MWB core potential with the ECP46MWB basis set, augmented with 2 f and 1 g basis functions from the ECP46MWB-II basis set to make a 5s4p3d2f1g basis; **Lu** - ECP60MWB core potential with the ECP60MWB basis set, augmented with 2 f and 1 g basis functions from the ECP60MWB-II basis set to make a 5s4p3d2f1g basis; **Gd** - ECP53MWB core potential with the ECP53MWB basis set, augmented with 2 f and 1 g basis functions from the ECP53MWB-II basis set to make a 5s4p3d2f1g basis; **Cm** - ECP85MWB core potential with the ECP85MWB-AVTZ basis set, augmented with 2 f and 1 g basis functions from the ECP85MWB-2f and -1g basis sets respectively; the def2-TZVP basis set was used for all other atoms (N, O and C).^{92,93,102,104,108,111,112}

The electronic structure of all systems were set to be in configurations with the highest spin multiplicity, on the assumption that the highest spin state is the ground state. For all calculations, La^{III} and Lu^{III} were modelled as closed shell systems and Gd^{III} and Cm^{III} as open shell systems with 7 unpaired electrons in a high spin $S = 7/2$ state with a single electronic configuration. For calculations with Eu^{III} and Am^{III}, the ions were modelled as open shell systems with 6 unpaired electrons in a high spin $S = 6/2$ state. For the AE calculations, the orbital occupations were manually defined as closed shell for La and Lu and open shell for Gd and Cm. For the IC calculations, the orbital occupations were manually defined as open shell for all Ln/An ions.

For geometry optimisation, a range of DFT functionals were used and are documented in the results section. Geometry optimisations were performed using default convergence criteria in both the presence and absence of a water-like continuum solvent defined using the COSMO model¹¹³ with the default radii $r_O = 1.72 \text{ \AA}$, $r_C = 2.00 \text{ \AA}$, $r_N = 1.83 \text{ \AA}$, $r_H = 1.30 \text{ \AA}$, $r_{Ln} = 2.22 \text{ \AA}$, $r_{An} = 2.22 \text{ \AA}$. All calculations were performed in the gas phase unless otherwise specified. Local energetic minima were identified *via* numerical frequency analysis.

For Møller–Plesset perturbation theory (MP2) calculations, the def(2)-TZVP basis sets and their corresponding auxiliary basis sets were used.^{65,107,108}

3.3 Results

3.3.1 Trinitrate Binding Energies

To find a reliable methodology for use on the larger complexes of separation ligands such as BTP and BTPPhen, several methods were first tested on the smaller nitrate complexes of the lanthanides and actinides. The first three DFT methods tested represented three different ways of modelling the core electrons of the central Ln/An ion, and were as follows:

sECP: 'Standard' effective core potential calculations, utilising the Stuttgart-Dresden small core relativistic ECPs selected by default in TURBOMOLE, which replace 28 (Lu, Gd), 46 (La) and 60 (Cm) core electrons with a pseudopotential.¹⁰⁶

IC: 4f/5f 'in-core' calculations, with the 4f/5f in-core pseudopotentials and accompanying basis sets developed by Dolg *et al*,^{92,93,102,104,111,112} which incorporate the f-electrons into the ECP instead of modelling them explicitly.

AE: All-electron calculations, with no effective core potential, using SARC-TZVP basis sets and SARC-TZVP-RI auxiliary basis sets for the metal ions,^{109,110} and a second order Douglas-Kroll-Hess Hamiltonian for the consideration of scalar relativistic effects.^{88,89}

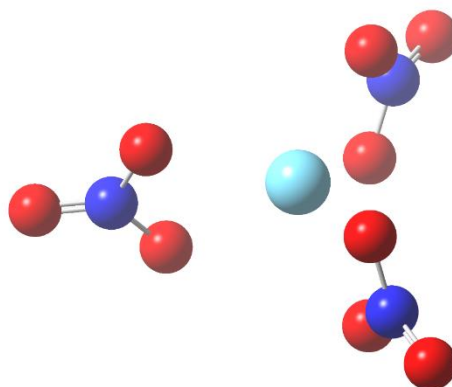


Figure 3.1: Sample optimised Ln/An(NO₃)₃ complex.

The calculations using all three of these methods were initially performed using the Perdew-Burke Ernzerhof GGA xc-functional, PBE.^{114,86,75,76} Three Ln ions (La, Lu, Gd) and one An ion (Cm) were used for these calculations, chosen as La and Lu (f⁰ and f¹⁴, respectively) have a single electronic configuration in the +3 oxidation state, while Gd and Cm can be modelled as high-spin f⁷ open-shell systems, assumed to have a single electronic configuration due to the

weak crystal field energies of the f-block elements being outweighed by the energy cost of pairing up caused by electron repulsion.

To compare the three methods, binding energies for the trinitrate complexes were calculated. Complexes of Ln/An(NO₃)₃ (Ln = La, Lu, Gd; An = Cm) were optimised in the gas-phase using the sECP method and the PBE *xc*-functional. The initial geometries of the complexes prior to optimisation were set with all three nitrate ligands binding to the central ion through a bidentate binding mode, which Dobler *et al.* reported to be the preferred binding mode in the unsaturated nitrate complexes,¹⁰¹ and this binding mode was retained in the optimised structures. Single-point energy (SPE) calculations were then performed using the optimised sECP geometries using the AE and IC methods, to avoid differences due to varying geometries. This same method of sECP geometry optimisations followed by AE and IC SPE calculations was used to calculate SCF energies for a lone nitrate ligand, and further SPE calculations were performed on the free Ln^{III}/An^{III} ions in the gas phase using the sECP, AE and IC methods. Binding energies were then calculated using **Eq. 3.1**:

$$E_b = (E_{\text{TN}} - E_{\text{ion}} - 3E_{\text{nitrate}}) \quad \text{(Eq. 3.1)}$$

Where E_b is the binding energy and E_{TN} , E_{ion} and E_{nitrate} are the self-consistent field (SCF) energies calculated for the Ln/An(NO₃)₃ complex, Ln^{III}/An^{III} ion and lone nitrate molecule, respectively. The calculated PBE gas-phase binding energies and spin expectation values of the Ln/An(NO₃)₃ complexes are displayed in **Table 3.1**.[†]

Table 3.1: SCF binding energies, E_b , calculated with **Eq. 3.1**, and spin expectation values, $\langle S^2 \rangle$, for Ln/An(NO₃)₃ (Ln = La, Lu, Gd; An = Cm), calculated using the sECP, AE and IC methods on PBE/def(2)-TZVP model chemistries.

Method	E_b (eV)				$\langle S^2 \rangle$	
	La	Gd	Lu	Cm	Gd	Cm
sECP	-40.63	-49.01	-46.02	-43.45	16.10	15.76
AE	-55.59	-58.42	-60.30	-57.56	15.76	15.76
IC	-41.00	-43.25	-45.20	-42.29	0.00	0.00

While the trend in Ln binding energies is periodic for those calculated with the AE and IC methods, with La being the highest in energy and Lu the lowest, the same is not true for those calculated with the sECP method, where the Gd complex has a higher binding energy than both La and Lu. Further, while there is a uniform shift of ~14-15 eV downwards for La, Lu and Cm when going from the sECP method to the AE method, and a ~0.4-1.1 eV shift downwards

when going from sECP to IC, the AE binding energy for Gd is 9 eV lower than the sECP binding energy, and the IC binding energy is 6 eV higher. Furthermore, while the spin expectation value, $\langle S^2 \rangle$, for the sECP-calculated $\text{Cm}(\text{NO}_3)_3$ complex was found to be 15.76, in good agreement with the theoretical ideal of 15.75, the value of S^2 for $\text{Gd}(\text{NO}_3)_3$ was found to be 16.10 with the sECP method, suggesting that a significant amount of spin contamination was present in the Gd complex. When the AE method was employed, $\langle S^2 \rangle$ was found to be 15.76 for both Gd and Cm. $\langle S^2 \rangle$ was found to be 0 when the IC method was employed as the f-electrons were not modelled explicitly.

3.3.2 Mononitrate Binding Energies

To investigate whether this binding energy variance was xc-functional-dependent, $[\text{Ln}/\text{An}(\text{NO}_3)]^{2+}$ complexes (Ln = La, Lu, Gd; An = Cm) were optimised using the sECP, AE and IC methods with both PBE and the hybrid functional PBE0, which incorporates a percentage (25%) of Hartree-Fock exact exchange energy.

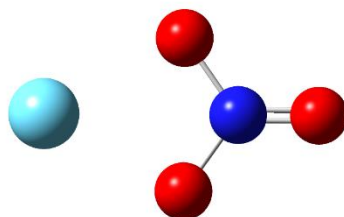


Figure 3.2: Sample optimised $[\text{Ln}/\text{An}(\text{NO}_3)]^{2+}$ complex.

As with the trinitrates above, these SPE calculations were performed on geometries optimised using the sECP method, however PBE-calculated SPEs were performed on PBE-optimised geometries, and PBE0-calculated SPEs were performed on PBE0-optimised geometries. Further geometry optimisations were performed at the MP2 level to obtain binding energies to benchmark against. The binding energies of the mononitrate complexes were calculated using **Eq. 3.2**:

$$E_b = (E_{\text{MN}} - E_{\text{ion}} - 3E_{\text{nitrate}}) \quad \text{(Eq. 3.2)}$$

Where E_b is the binding energy and E_{MN} , E_{ion} and E_{nitrate} are the SCF energies calculated for the $[\text{Ln}/\text{An}(\text{NO}_3)]^{2+}$ complex, $\text{Ln}^{\text{III}}/\text{An}^{\text{III}}$ ion and lone nitrate molecule, respectively. The binding energies and $\langle S^2 \rangle$ values for these mononitrate complexes are displayed in **Table 3.2**.

Table 3.2: SCF binding energies, E_b , calculated with Eq. 3.2, and spin expectation values, $\langle S^2 \rangle$, for $[\text{Ln}/\text{An}(\text{NO}_3)]^{2+}$ (Ln = La, Lu, Gd; An = Cm) using the sECP, AE and IC DFT methods on PBE/def(2)-TZVP and PBE0/def(2)-TZVP model chemistries, compared to MP2-calculated binding energies and spin expectation values.

Method	HF %	E_b (eV)				$\langle S^2 \rangle$	
		La	Gd	Lu	Cm	Gd	Cm
MP2	-	-19.29	-21.99	-23.09	-21.58	15.77	15.77
sECP-PBE0	25	-20.02	-24.12	-23.07	-21.72	16.00	15.76
sECP-PBE	0	-20.46	-28.24	-23.59	-22.41	16.16	15.76
AE-PBE0	25	-20.85	-24.96	-30.91	-20.79	15.76	15.76
AE-PBE	0	-23.55	-25.41	-26.30	-24.95	15.76	15.76
IC-PBE0	25	-20.35	-23.02	-23.89	-22.34	0.00	0.00
IC-PBE	0	-20.73	-21.94	-23.12	-21.38	0.00	0.00

Excluding the Gd complexes, the method which agreed best with the MP2-calculated binding energies was the sECP method, especially when the PBE0 xc-functional was employed, followed closely by those obtained with the IC method. In comparison, the AE method produced poor results, overestimating by up almost 8 eV in one case, and by ~3-4 eV on average. For the Gd ion, however, the sECP method produced binding energies which were greater than the MP2 binding energies by ~2-6 eV, inconsistent with the good agreement with MP2 exhibited by the results obtained for the other three ions. The trend in binding energies observed for the MP2-calculated binding energies for the Ln ions is periodic, further suggesting that the sECP trend in Ln binding energies is erroneous, and that the binding energy for Lu should be lower than that of Gd.

As seen for the trinitrate complexes, only the $\langle S^2 \rangle$ values for the sECP-calculated complexes of Gd showed any appreciable divergence from the theoretical ideal. However, the $\langle S^2 \rangle$ value for the complex optimised with the PBE0 xc-functional diverged from the ideal less than that of the complex optimised with PBE, demonstrating that the use of PBE0 over PBE alleviates the spin contamination in the Gd complex.

3.3.3 Investigating the xc-Functional Dependency

3.3.3.1 La^{III}, Lu^{III}, Gd^{III} and Cm^{III}

To further investigate the poor performance of the sECP method for the complexes of Gd and whether the spin contamination seen in the Gd complexes could be alleviated further, optimisations of the [Ln/An(NO₃)²⁺] complexes were performed with a wider variety of xc-functionals. The functionals employed and the percentage of Hartree-Fock exact exchange energy incorporated into each were as follows: BLYP, 0%;⁷⁷ TPSS, 0%;^{75,78} PBE, 0%;^{75,76} TPSSH, 10%;^{75,78,115} B3LYP, 20%;^{82,77,80,81} PBE0, 25%;^{75,76,83} and BHLYP, 50%.^{77,80,81,79} For each xc-functional and Ln/An ion, a geometry optimisation was performed and the SCF energies were used to calculate binding energies using Eq. 3.2. The binding energies and $\langle S^2 \rangle$ values for these calculations are shown in Table 3.3 and Figure 3.3, compared to the MP2 values calculated previously.

Table 3.3: SCF binding energies, E_b , calculated with Eq. 3.2, and spin expectation values, $\langle S^2 \rangle$, for [Ln/An(NO₃)²⁺] (Ln = La, Lu, Gd; An = Cm) using the sECP method and a series of xc-functionals on def(2)-TZVP model chemistries, compared to MP2-calculated binding energies and spin expectation values.

Method	E_b (eV)					$\langle S^2 \rangle$	
	HF %	La	Gd	Lu	Cm	Gd	Cm
MP2	-	-19.29	-21.99	-23.09	-21.58	15.77	15.77
BHLYP	50	-19.49	-21.67	-22.56	-21.07	15.76	15.76
PBE0	25	-20.02	-24.12	-23.07	-21.72	16.00	15.76
B3LYP	20	-19.87	-24.81	-23.01	-21.59	16.03	15.76
TPSSH	10	-20.11	-26.42	-23.29	-21.96	16.10	15.76
PBE	0	-20.46	-28.24	-23.59	-22.41	16.16	15.76
TPSS	0	-20.28	-28.04	-23.50	-22.24	16.16	15.76
BLYP	0	-20.18	-28.31	-23.39	-22.10	16.19	15.76

The mononitrate binding energies calculated with the three pure xc-functionals, BLYP, TPSS and PBE, were found to be very similar, with no more than a third of an eV difference between functionals at most. Likewise, there was found to be little difference in the binding energies of La, Lu and Cm as the xc-functional was changed for those obtained with the hybrid xc-functionals, although variance in binding energies was slightly higher than with the pure xc-functionals.

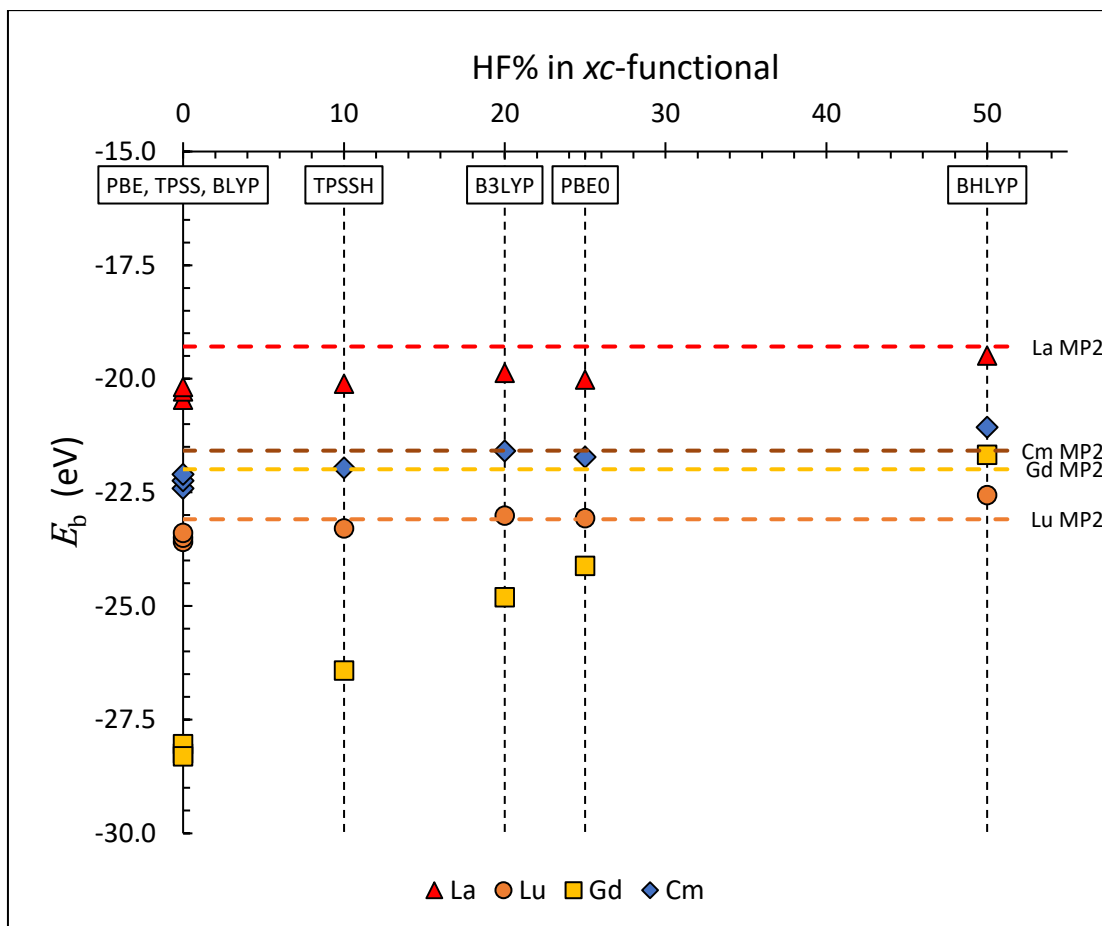


Figure 3.3: Functional dependence of $[\text{Ln}/\text{An}(\text{NO}_3)_2]^{2+}$ ($\text{Ln} = \text{La}, \text{Lu}, \text{Gd}$; $\text{An} = \text{Cm}$) binding energies, compared to MP2 values (horizontal dashed lines).

For Gd, however, the differences in binding energies was large, and the agreement with the MP2 binding energies for the Gd complexes improved rapidly as the percentage of Hartree-Fock exact exchange energy incorporated into the xc -functional increased. The best observed agreement with the MP2-calculated binding energies for the Gd complexes was with the functional with the highest percentage of Hartree-Fock exact exchange energy, BHLYP (50% HF). The $\langle S^2 \rangle$ values of these complexes also followed this trend, becoming closer to the theoretical ideal as the percentage of Hartree-Fock exact exchange increased, until reaching parity with the $\langle S^2 \rangle$ value of Cm (15.76) when the BHLYP functional was employed.

Further DFT and MP2 geometry optimisations were performed with the same range of xc -functionals and methodology employed above for the $\text{Ln}/\text{An}(\text{NO}_3)_3$ ($\text{Ln} = \text{La}, \text{Lu}, \text{Gd}$; $\text{An} = \text{Cm}$) complexes to investigate whether the same behaviour for the Gd complexes observed for the mononitrate complexes also appeared in the trinitrate complexes. Binding energies and $\langle S^2 \rangle$ values for these calculations are shown in **Table 3.4** and **Figure 3.4**.

Table 3.4: SCF binding energies, E_b , calculated with Eq. 3.1, and spin expectation values, $\langle S^2 \rangle$, for Ln/An(NO₃)₃ (Ln = La, Lu, Gd; An = Cm) using the sECP method and a series of xc-functionals, compared to MP2-calculated binding energies and spin expectation values.

Method	E_b (eV)					$\langle S^2 \rangle$	
	HF %	La	Gd	Lu	Cm	Gd	Cm
MP2	-	-39.61	-44.02	-46.18	-43.31	15.76	15.76
BHLYP	50	-39.27	-43.13	-45.11	-42.12	15.76	15.76
PBE0	25	-40.05	-45.17	-45.43	-42.86	15.95	15.76
B3LYP	20	-39.82	-45.57	-45.34	-42.47	15.98	15.76
TPSSH	10	-40.21	-47.20	-45.68	-43.00	16.04	15.76
PBE	0	-40.62	-49.00	-46.01	-43.44	16.10	15.76
TPSS	0	-40.38	-48.73	-45.85	-43.25	16.09	15.76
BLYP	0	-40.01	-48.75	-45.52	-42.79	16.11	15.76

For all four ions, the trinitrate binding energies calculated with the three pure xc-functionals were very similar, as seen for the binding energies of the mononitrate complexes. Similarly, little difference between functionals was observed for the binding energies obtained with the hybrid xc-functionals except for those of the Gd complexes, the binding energies for which again exhibited a large functional dependency. For Gd, the BHLYP xc-functional again showed best agreement with MP2 binding energies, underbinding by 0.89 eV. The $\langle S^2 \rangle$ values for the Gd complex again improved as the percentage of Hartree-Fock exact exchange energy incorporated into the xc-functional employed increased, only reaching parity with that of the Cm complex and those obtained with MP2 when the BHLYP functional was employed. Whilst binding energies for La, Lu and Cm obtained with other xc-functionals may be closer to the MP2-calculated benchmark than those obtained with BHLYP, for these ions all xc-functionals employed produced binding energy values within ~1 eV of the MP2-calculated values at most, whilst BHLYP is the only xc-functional to produce a value within this range for the Gd complex.

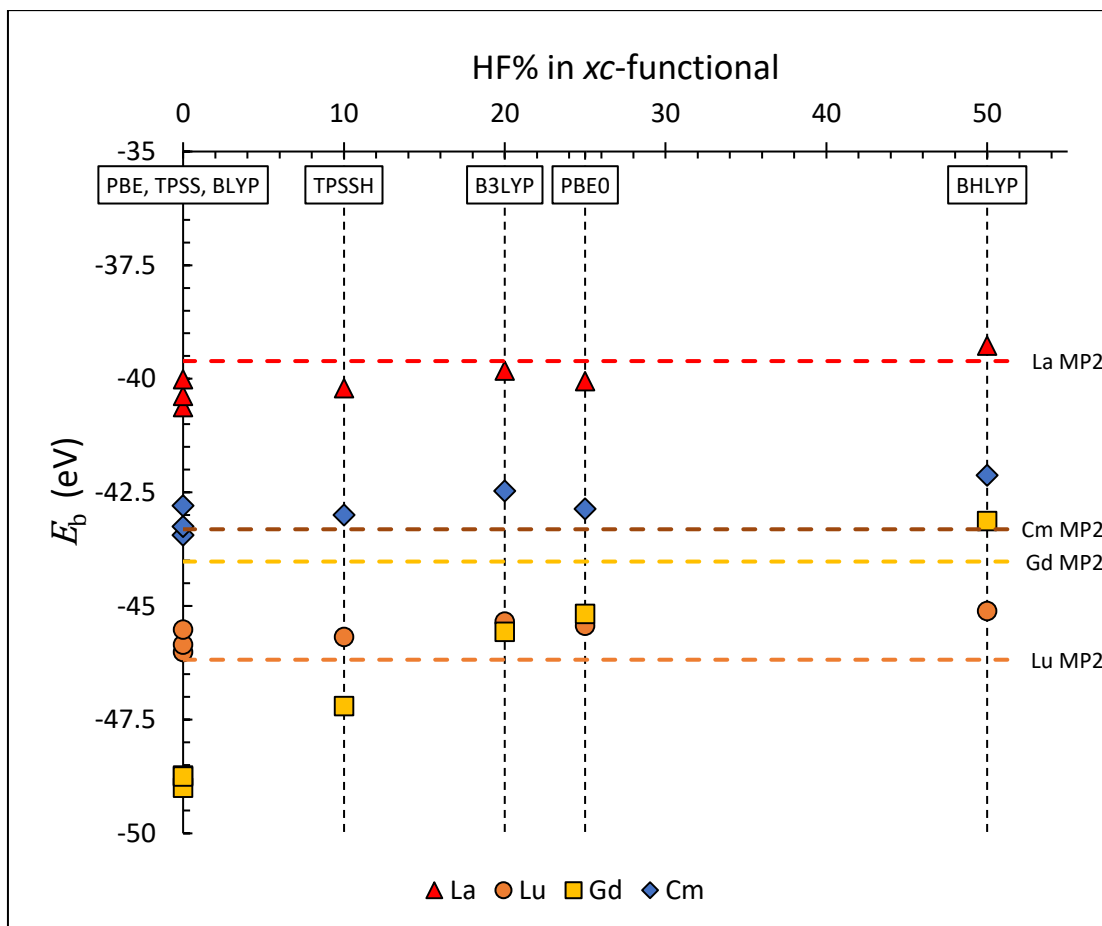


Figure 3.4: Functional dependency of Ln/An(NO₃)₃ (Ln = La, Lu, Gd; An = Cm) binding energies, compared to MP2 values (horizontal dashed lines).

3.3.3.2 Eu^{III} and Am^{III}

Computationally, calculations on complexes of the open shell Eu^{III} and Am^{III} ions are more difficult than those of Gd^{III} and Cm^{III}, as while the f⁷ ions can be modelled in the high spin $S = 7/2$ state with a single electronic configuration, the f⁶ Am and Eu ions have six unpaired electrons in the high spin state, which leaves an empty f-orbital and hence multiple possible electronic configurations. However, Eu and Am are of great interest to the area of Ln/An separation research, and are the two ions most commonly used in tests of new and current separation ligands. As such, most data available for the complexes of separation ligands are for complexes of Eu and Am, and therefore it was necessary to consider these ions for this thesis to investigate the structures and separation ability of these ligands despite the added computational difficulty. Further, it was necessary to ascertain whether the spin contamination seen in the Gd trinitrate complexes, which had such a large effect on energies, was present in the complexes of Am and Eu, as this would result in predicting inaccurate reaction energies for the separation of Am and Eu. Therefore, to investigate whether the

functional dependency on binding energies observed for the Gd complex in the mono- and trinitrate complexes was present in complexes of Eu and Am, geometry optimisations of Eu/Am(NO₃)₃ were performed with the ‘LYP’ family of *xc*-functionals: BLYP, B3LYP and BHLYP. These three *xc*-functionals include a pure functional, BLYP, and two hybrid functionals, B3LYP and BHLYP, incorporating 20% and 50% of Hartree-Fock exact exchange energy respectively. Binding energies and $\langle S^2 \rangle$ values for these calculations are shown in **Table 3.5** and **Figure 3.5**, compared to those calculated for Gd and Cm.

Table 3.5: SCF binding energies, E_b , calculated with **Eq. 3.1**, and the difference between the calculated and ideal spin expectation values, $\langle S^2 \rangle_{calc} - \langle S^2 \rangle_{ideal}$, for Ln/An(NO₃)₃ (Ln = Eu, Gd; An = Am, Cm) using the sECP method and the BLYP, B3LYP and BHLYP *xc*-functionals. ($\langle S^2 \rangle_{ideal} = 12$ for Eu and Am, 15.75 for Gd and Cm)

Method	E_b (eV)					$\langle S^2 \rangle_{calc} - \langle S^2 \rangle_{ideal}$			
	HF %	Gd	Eu	Cm	Am	Gd	Eu	Cm	Am
BHLYP	50	-43.13	-42.91	-42.12	-42.14	0.01	0.01	0.01	0.01
B3LYP	20	-45.57	-43.40	-42.47	-42.63	0.23	0.03	0.01	0.02
BLYP	0	-48.75	-44.16	-42.79	-43.11	0.36	0.22	0.01	0.05

Whilst the calculated $\langle S^2 \rangle$ values for the Eu and Am complexes differ from the theoretical ideal more than those for the Cm complex, and to a similar extent to the Gd complexes for the BLYP-optimised Eu complex, the Eu and Am complexes did not exhibit the same extreme variation in binding energies seen for the Gd complexes, and the difference in binding energies between *xc*-functionals was small in comparison.

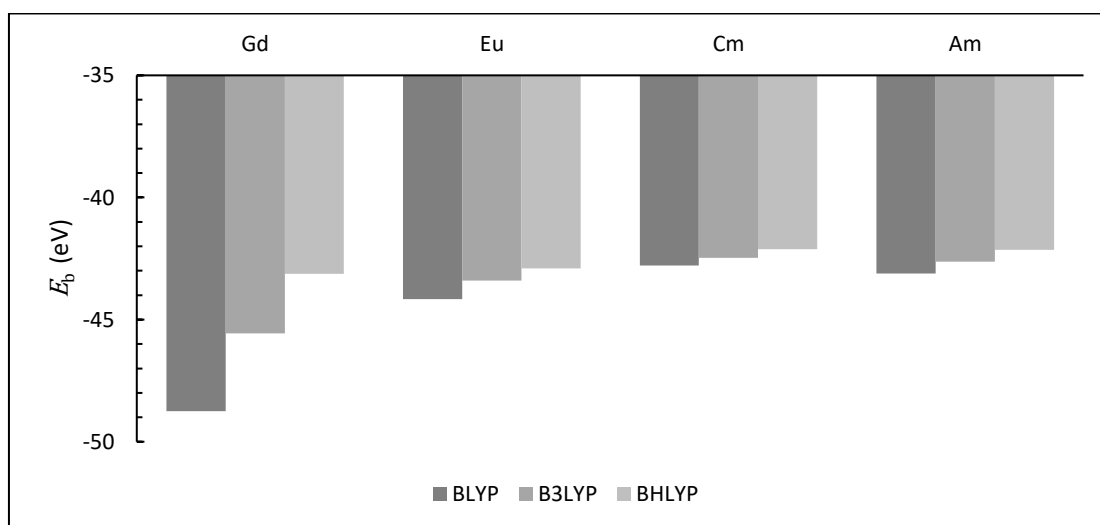


Figure 3.5: Ln/An(NO₃)₃ (Ln = Eu, Gd; An = Am, Cm) binding energies calculated with BLYP, B3LYP and BHLYP.

3.3.4 Solvation of Nitrate Complexes

3.3.4.1 Explicit Hydration

To investigate the maximum coordination numbers and first-shell hydration numbers of the Ln/An trinitrates, an explicit hydration method was employed. Water molecules were systematically added to the trinitrate complex to form six initial Ln/An(NO₃)₃(H₂O)_x complexes with values of *x* ranging from 3 to 5. These initial geometries comprised of three *x* = 3 complexes, two *x* = 4 complexes and one *x* = 5 complex. For the *x* = 3 complexes, three water molecules were placed between the nitrate ligands for the first initial geometry (**3a**, **Figure 3.6**). For the second *x* = 3 complex (**3b**) one of the water molecules was instead placed above/below the plane of the molecule, and for the third (**3b**) two of the water molecules were instead placed above and below the plane of the molecule. The first of the initial *x* = 4 complexes (**4a**) had three water molecules placed between the nitrate ligands, and one placed above/below the plane of the molecule, whilst the second complex (**4b**) had two water molecules placed between the nitrate ligands and two placed above and below the plane of the molecule. Finally, for the initial *x* = 5 complex (**5a**), three water molecules were placed between the nitrate ligands and two water molecules above and below the plane of the molecule. These initial complexes were optimised using the sECP method in the gas phase for the ions La, Lu, Gd and Cm. Binding energies for these complexes were calculated using **Eq. 3.3**:

$$E_b = (E_{\text{tot}} - E_{\text{ion}} - 3E_{\text{nitrate}} - xE_w) \quad (\text{Eq. 3.3})$$

Where E_b is the binding energy, x is the number of water molecules and E_{tot} , E_{ion} , E_{nitrate} and xE_w are the SCF energies calculated for the Ln/An(NO₃)₃(H₂O)_x complex, Ln^{III}/An^{III} ion, lone nitrate molecule and lone water molecule respectively. The binding energies of these complexes as well as their first-shell hydration number, coordination numbers and the binding mode of the nitrates in these complexes are shown in **Table 3.6**. These calculations were performed at the BLYP/def(2)-SVP level. While BLYP had been shown to be unsuitable for Gd, due to the large volume of simulations performed it was only practical to use the pure GGA functional over the hybrid-GGA B3LYP and BHLYP xc-functionals. As such, the Gd data presented here should be treated with caution, although the binding energies between different Gd complexes may be comparable due to error cancellation.

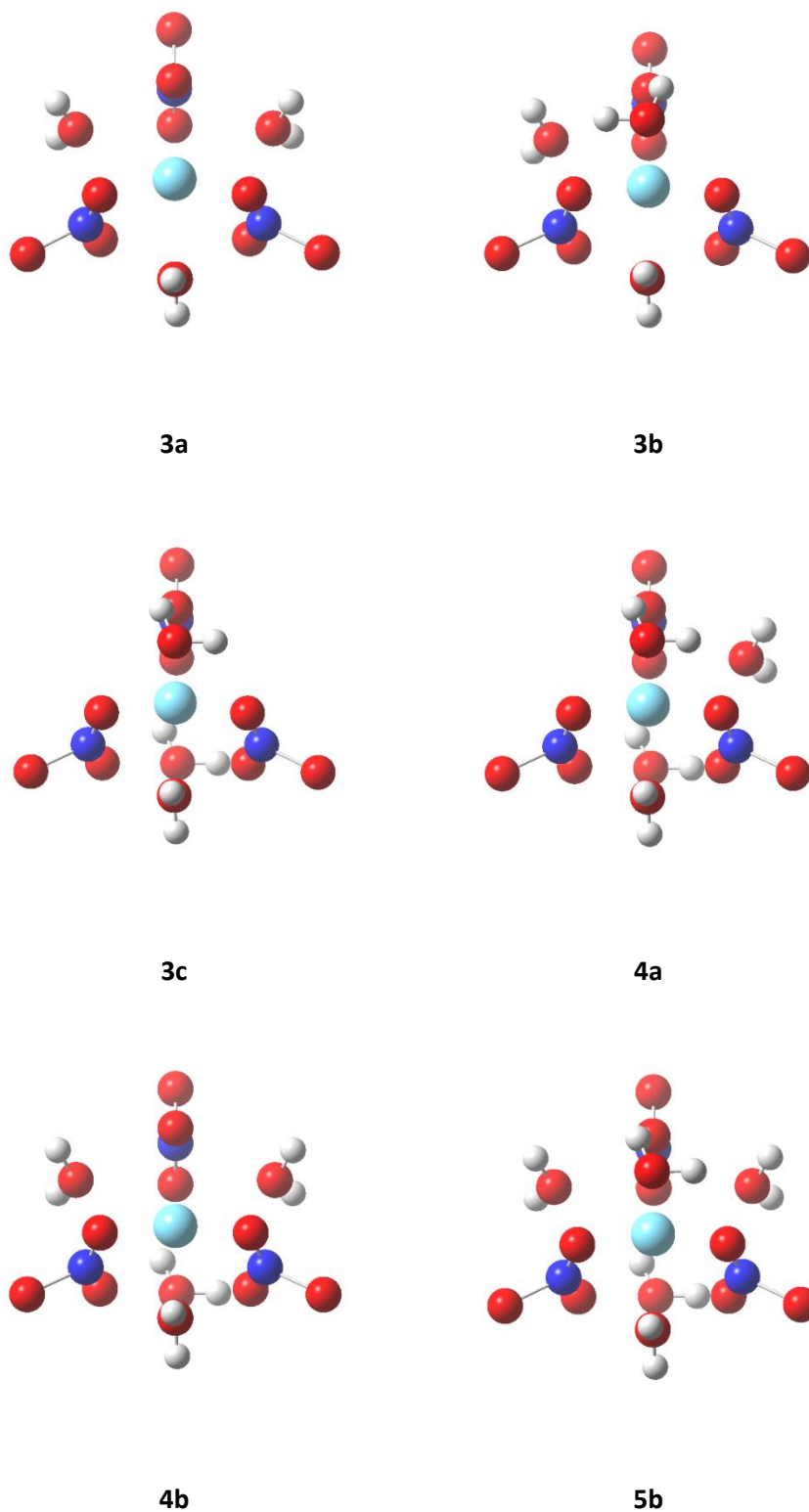


Figure 3.6: Initial Ln/An(NO₃)₃(H₂O)_x (Ln = La, Lu, Gd; Cm = Cm, x = 1-5) complex structures, prior to geometry optimisation.

Table 3.6: Binding modes, first-shell hydration numbers, coordination numbers and binding energies, E_b , for $\text{Ln}/\text{An}(\text{NO}_3)_3(\text{H}_2\text{O})_x$ ($\text{Ln} = \text{La}, \text{Lu}, \text{Gd}$; $\text{An} = \text{Cm}$). The binding mode is comprised of three letters describing the denticity of the three nitrate ligands, with 'b' denoting a bidentate binding mode, and 'm' a monodentate binding mode. [†]Re-optimised using the optimised **5a** complex of La as the initial geometry. ^{††}Re-optimised using the optimised **3c** complex of Cm as the initial geometry.

M	Complex	Nitrate Binding Mode	First-Shell Hydration Number	Coordination Number	E_b (eV)
La	3a	b,b,b	3	9	-16.32
	3b	b,b,b	3	9	-16.33
	3c	b,b,b	3	9	-16.23
	4a	b,b,b	4	10	-17.09
	4b	b,b,b	4	10	-17.15
	5a	b,b,m	5	10	-18.04
	6a	b,b,m	6	11	-18.39
Lu	3a	b,b,b	3	8	-21.60
	3b	b,b,b	3	9	-21.30
	3c	b,b,b	3	9	-21.39
	4a	b,b,b	4	10	-21.87
	4b	b,b,b	4	10	-22.29
	5a	b,b,m	3	8	-22.05
	5a' [†]	b,m,m	5	9	-22.96
Gd	3a	b,b,b	3	9	-22.95
	3b	b,b,m	3	8	-24.32
	3c	b,b,m	3	8	-24.35
	3c' ^{††}	b,b,b	3	9	-24.23
	4a	b,b,m	4	9	-24.81
	4b	b,b,m	4	9	-25.13
	5a	b,b,m	4	9	-25.38
Cm	3a	b,b,b	3	9	-17.35
	3b	b,b,b	3	9	-18.61
	3c	b,b,b	3	9	-18.68
	4a	b,b,b	4	10	-19.36
	4b	b,b,b	4	10	-19.34
	5a	b,b,m	4	9	-20.35
	5a' [†]	b,b,m	5	10	-20.27

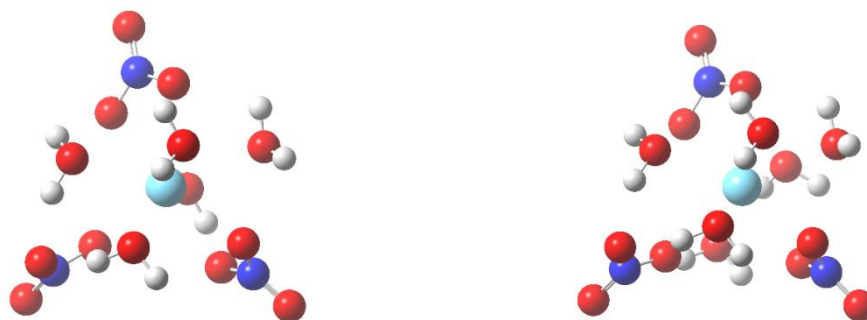


Figure 3.7: The optimised 10-coordinate La complex **5a**, left, and the 11-coordinate La complex **6a**, right.

For the largest ion, La, a maximum coordination number of 10 was found amongst the initial set of geometry optimisations, both for the $x = 4$ complexes, which retained the bidentate binding modes for all three nitrates, and for the $x = 5$ complex, for which one of the nitrates shifted to a monodentate binding mode. To investigate whether the La complex could reach a coordination number of 11, as seen by Dobler *et al.*,¹⁰¹ a sixth water molecule was added to the $x = 5$ complex. This $x = 6$ complex (**6b**) optimised with a coordination number of 11. An $x = 7$ optimisation was attempted, but the maximum first-shell hydration number was found to be 6. The binding energies of the optimised complexes decreased steadily as the first-shell hydration number increased.

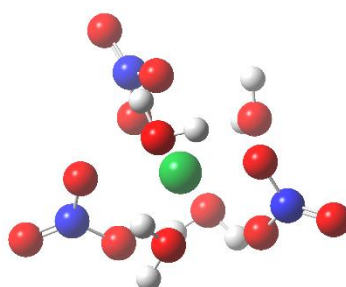


Figure 3.8: The optimised 10-coordinate Lu complex **4a**.

For the smallest ion, Lu, a maximum coordination number of 10 was found. The range in coordination numbers was 8 to 10, as seen by Dobler *et al.*¹⁰¹ This maximum coordination number was found for when $x = 4$.

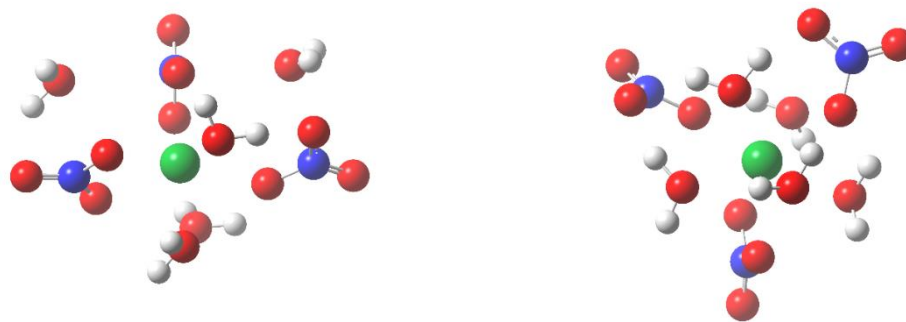


Figure 3.9: The optimised 8-coordinate Lu complex **5a**, left, and the 9-coordinate Lu complex **5a'**, right, re-optimised from the La **5a** complex.

For the $x = 5$ structure, a smaller coordination number of 8 was found, due to two of the waters moving into the second solvation shell and one of the nitrates becoming monodentate. A further optimisation of the $x = 5$ structure, **5a'**, was attempted using the optimised geometry of the La **5a** complex for the initial coordinates, however this also failed to reach a coordination number of 10. In this case, all five waters were coordinated to the Lu centre, but two of the nitrate ligands had moved to a monodentate binding mode. The binding energies of the optimised complexes decreased as waters were added to the complex, however the differences in stability between hydration numbers was smaller than seen for the La complexes.

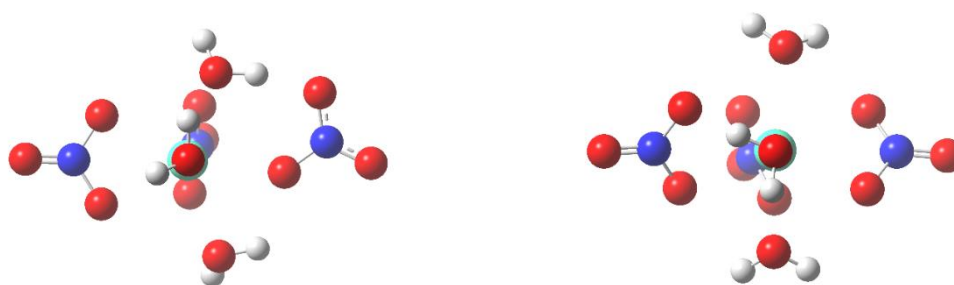


Figure 3.10: The optimised 8-coordinate Gd complex **3c**, left, and the 9-coordinate Gd complex **3c'**, right, re-optimised from the Cm **3c** complex.

For the Gd complexes, the maximum coordination number was found to be 9, and the maximum first-shell hydration number found to be only 4. If the maximum coordination

number follows a periodic trend then Gd would be expected to have a maximum coordination number of either 11 or 10 as the maximum coordination numbers of La and Lu were found to be 11 and 10, respectively; however, the lack of a linear periodic trend might be a consequence of the use of the BLYP *xc*-functional. A further optimisation of the $x = 5$ structure using the optimised geometry of the La **5a** complex for the initial coordinates failed. The binding energies of the structures with a first-shell hydration number of 3 were lower for the two which had a nitrate with a monodentate binding mode than for the b,b,b structure; however, the binding energy of a fourth structure, **3c'**, optimised using the lowest energy $x = 3$ Cm complex, **3c**, as a starting structure optimised with a b,b,b binding mode and a binding energy close to the lower energy b,b,m complexes. As can be seen in **Figure 3.10**, the **3c** complex formed a slightly more stable structure with a water molecule bridging the metal-nitrate bond through a hydrogen bond to one of the oxygen atoms of the monodentate nitrogen ligand, which was not present in the Cm **3c** complex or the re-optimised Gd complex. Overall, the binding energies again decreased as the hydration number increased, reaching a minimum at $x = 5$.

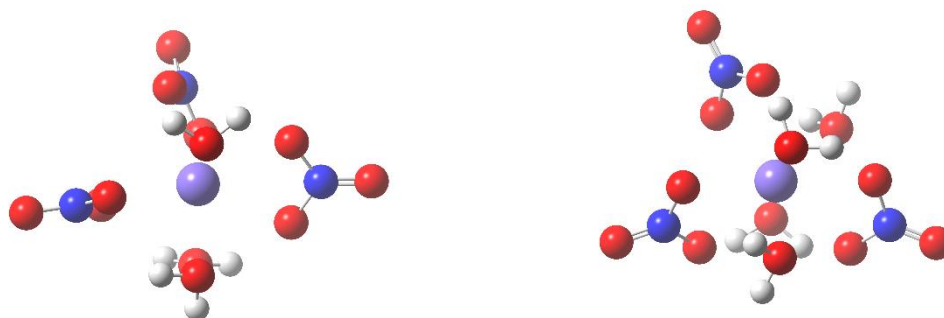


Figure 3.11: The optimised 9-coordinate Cm complex **3c**, left, and the 10-coordinate Cm complex **4a**, right.

The Cm complexes were found to have a maximum coordination number of 10 and a maximum hydration number of 5, although the latter was only found for the **5a'** complex, which was optimised using the **5a** complex of La as a starting point. Unlike Gd, a b,b,b binding mode was found for all complexes up to $x = 5$. Binding energies again decreased as the hydration number increased, reaching a minimum at $x = 5$.

3.3.4.2 Implicit Hydration

To investigate the effects of the COSMO solvation model on the structures of the trinitrates, geometry optimisations of Ln/An(NO₃)₃ (Ln = La, Lu, Gd; An = Cm) were optimised with the BLYP, B3LYP and BHLYP *xc*-functionals. The average metal-nitrate bond lengths of the complexes optimised in the presence of the continuum solvent were compared to those of the complexes optimised in the gas phase, shown in **Table 3.7**.

Table 3.7: Average M—O bond lengths of BLYP/def(2)-SVP-, B3LYP/def(2)-SVP- and BHLYP/def(2)-SVP-calculated Ln/An(NO₃)₃ (Ln = La, Lu, Gd; An = Cm) geometries. All values are in angstroms (Å).

Method	$\bar{R}(\text{M} - \text{O})$											
	BLYP				B3LYP				BHLYP			
	La	Lu	Gd	Cm	La	Lu	Gd	Cm	La	Lu	Gd	Cm
Gas	2.52	2.27	2.41	2.41	2.50	2.26	2.36	2.40	2.49	2.24	2.33	2.39
COSMO	2.55	2.27	2.42	2.42	2.54	2.26	2.37	2.41	2.54	2.25	2.35	2.41

The effect of the COSMO solvation model on the structures of the trinitrates was found to be a slight lengthening of the average M—O bond lengths, by ~0.00-0.02 Å for the complexes of Lu, Gd and Cm and slightly more (~0.03-0.05 Å) for the La complexes.

3.3.4.3 Explicit and Implicit Hydration

The explicit hydration method improves upon the gas-phase trinitrate model of a Ln/An ion in nitric acid as it includes a full first coordination sphere, while the implicit solvation model provides an approximation of higher levels of solvation. These two methods were combined to obtain an accurate model of the ion in a nitric acid environment. Four Gd/Cm(NO₃)₃(H₂O)_{*x*} (*x* = 3, 4) complexes were re-optimised with the BLYP *xc*-functional in the presence of the continuum solvent for comparison with those optimised in the gas phase. The *x* = 3 and *x* = 4 complexes were chosen as these complexes were the first for which Gd and Cm reached maximum coordination numbers. The lowest energy structure for each were chosen for re-optimisation in the presence of a continuum solvent, namely **3c** and **4b** for Gd and **3c** and **4a** for Cm. The average metal-nitrate and metal-water bond lengths for these complexes are shown in **Table 3.8**.

Table 3.8: Average M—O_N and M—O_H bond lengths of BLYP/def(2)-SVP-calculated Gd/Cm(NO₃)₃(H₂O)_x (x = 3, 4) geometries. All values are in angstroms (Å).

Method	Gd, x = 3		Gd, x = 4		Cm, x = 3		Cm, x = 4	
	M—O _N	M—O _H						
Gas	2.66	2.53	2.78	2.51	2.49	2.56	2.52	2.61
Cosmo	2.68	2.46	2.84	2.48	2.52	2.49	2.56	2.55

As in the Ln/An(NO₃)₃ complexes, the effect of the COSMO solvation model on the M—O_N bond lengths was again found to be a lengthening of the bond, by ~0.02-0.03 Å for the x = 3 complexes and ~0.04-0.06 Å for the x = 4 complexes. However, a shortening of the M—O_H bond lengths was observed in the presence of the continuum solvent, by ~0.07 Å for the x = 3 complexes and ~0.03-0.04 Å for the x = 4 complexes.

To investigate whether the BHLYP xc-functional, which was earlier found to be a more suitable functional for use with than BLYP, could improve on the maximum coordination number of 9 found for Gd, the BLYP-optimised complexes of Gd and Cm were re-optimised at the BHLYP/def(2)-SVP level with COSMO solvation.* To try and achieve a coordination number of 10 for Gd, the Cm structures were also used as a starting point for optimisations with Gd, as for the **3c'** complex previously. Using the Cm structures as a starting point lead to the successful optimisation of a 9-coordinate x = 3 and 10-coordinate x = 4 complex for Gd, both with a b,b,b binding mode. The geometry of the final BHLYP/def(2)-SVP complexes of lowest energy for the maximum coordination numbers of both values of x are shown in **Figures 3.12** and **3.13**.

* A secondary intention was to provide structures for later calculations of exchange reaction energies for the complexes of the separation ligands (e.g. BTP, BTPhen), although in **Chapter 4**, nona-aquo complexes were used to calculate exchange reaction energies instead, and in **Chapter 5** only the Am and Eu complexes were investigated, due to the problems encountered for complexes of Gd and the unexpected ease of working with Am and Eu. However, these BHLYP-optimised Gd and Cm complexes were still used as a starting point for the complexes of Am and Eu, presented in **Chapter 5**.



Figure 3.12: BHLYP/def(2)-SVP-optimised 9-coordinate complexes $\text{Gd}(\text{NO}_3)_3(\text{H}_2\text{O})_3$, left and $\text{Cm}(\text{NO}_3)_3(\text{H}_2\text{O})_3$, right.

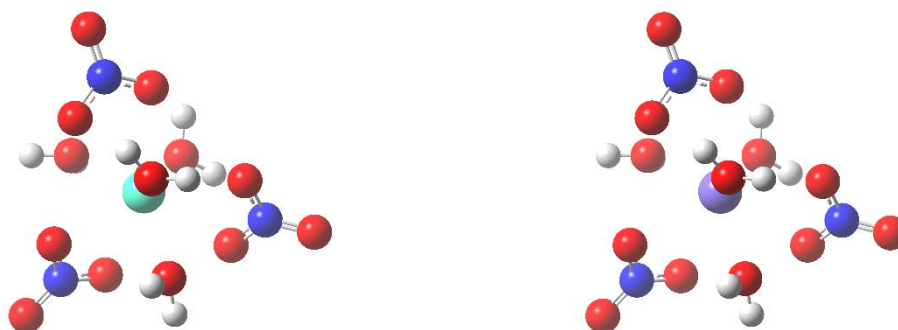


Figure 3.13: BHLYP/def(2)-SVP-optimised 10-coordinate complexes $\text{Gd}(\text{NO}_3)_3(\text{H}_2\text{O})_4$, left and $\text{Cm}(\text{NO}_3)_3(\text{H}_2\text{O})_4$, right.

3.4 Conclusion

In this chapter, three different DFT methods for modelling the core electrons of the Ln/An ion (Ln = La, Lu, Gd; An = Cm) in mono- and trinitrate complexes, the standard small-core relativistic Stuttgart-Dresden ECPs selected by default in TURBOMOLE, an all-electron method, and a 4f/5f in-core ECP method, were compared to high-level MP2 calculations. The standard ECPs were found to give binding energies which were closest to MP2 values, except for when Ln = Gd. Further investigation into this exception revealed that the Gd complexes exhibited a large amount of spin contamination when pure *xc*-functionals were employed. The amount of spin contamination in the Gd complexes decreased when hybrid functionals were used instead, decreasing further as the degree of Hartree-Fock exact exchange energy incorporated into the hybrid *xc*-functionals increased. When the *xc*-functional BHLYP was employed, no

appreciable spin contamination was present in the Gd complexes and the binding energy for this complex was found to be closer to the MP2-calculated binding energy than all other *xc*-functionals employed. For La, Lu and Cm, a good agreement with the MP2-calculated binding energy was observed for all *xc*-functionals employed. Further calculations with the ions Eu and Am revealed that while there was a small amount of spin contamination in the complexes of both ions, this did not appear to have the same effect on their binding energies as seen for the Gd complexes.

Explicit and implicit solvation methods were also employed for the trinitrate complexes. Using explicit solvation methods with the BLYP *xc*-functional, the maximum coordination number for the La, Gd, Lu and Cm trinitrate complexes were found to be 11, 9, 10 and 10 respectively; however, calculations performed with the BHLYP *xc*-functional found a maximum coordination number of 10 for the Gd complexes, fitting the periodic trend set by La and Lu and again highlighting the poor performance of BLYP with complexes of Gd. The COSMO solvation model was found to cause a slight lengthening in the metal-nitrate bond lengths and a slight shortening of the metal-water bond lengths of the Ln/An(NO₃)₃ (Ln = La, Lu, Gd; An = Cm) and Gd/Cm(NO₃)₃(H₂O)_{*x*} (*x* = 3, 4) complexes. Combined, these solvation methods model the first coordination sphere explicitly and implicitly approximate the effects of higher levels of solvation.

Chapter 4: BTP – Does Covalency Imply Stability?

This chapter focuses on the actinide-selective trivalent bis-triazinyl-pyridine (BTP) ligand. The origins of the selectivity of the BTP ligand are investigated using DFT and QTAIM techniques, specifically the relative covalency and stability of BTP complexes of the minor actinides (An = Cm, Am) compared to the lanthanides (Ln = Ce – Lu).

4.1 Introduction

BTP (2,6-bis(1,2,4-triazin-3-yl)pyridine, **Figure 4.1**) is one of several nitrogen donor ligands which have been developed and investigated for Ln^{III}/An^{III} separation, showing strong selectivity for the latter.^{17,116} BTP was the first N-donor extraction ligand to exhibit excellent selectivity ($SF_{Am/Eu}$ up to 150) under highly acidic conditions (1 M HNO₃).^{12,17,116} However, despite almost two decades of research since the solvent extraction ability of BTP was reported by Kolarik *et al.*^{12,13} in 1999, the exact origin of this selectivity is still unclear.

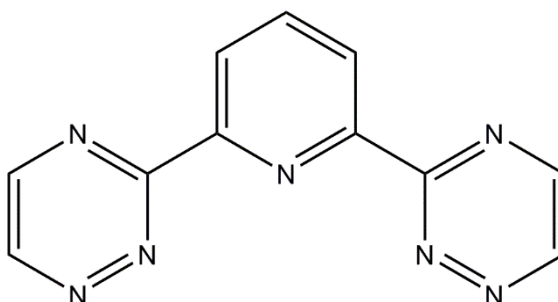


Figure 4.1: 2,6-bis(1,2,4-triazin-3-yl)pyridine (BTP).

The Ln/An separation ability of ligands such as BTP is believed to be due to the greater availability of the An 5f orbitals compared to the more core-like Ln 4f orbitals, which should manifest itself in enhanced covalency in the metal-ligand bonds of the An complexes. This work attempts to determine the magnitude and origin of this selective binding, in particular whether this selectivity is electronically driven and whether metal-ligand interactions in the actinide complexes display an increased covalent character compared to their lanthanide counterparts. The ultimate goal of this ongoing investigation is to be able to aid the design of new separation ligands for more effective Ln/An separation. Computational methods play a vital role in the pursuit of this goal due to the inherent cost and challenge of working with lanthanide and actinide materials, especially the high radiotoxicity of the latter; additionally,

novel ligands and changes to ligands already employed in the separation process can be evaluated without the need to synthesise them.

The tridentate BTP ligand forms 3:1 ligand:metal complexes with the Ln/An centre, forming a symmetrical complex with an overall charge of 3+. In the literature, computational and analytical methods have been used to investigate the differences in structure between selected Ln^{III} and An^{III} complexes. A combined effort of electrospray mass spectroscopy,^{40,117} time-resolved laser-induced fluorescence spectroscopy (TRLFS),^{37,41,42,49,118–120} X-ray photoelectron spectroscopy (XPS) and extended X-ray absorption fine structure spectroscopy (EXAFS)^{37,39,49,51,121–123} with complementary DFT studies^{48–51} have probed the structure of [Ln/An(BTP)_n]³⁺ (*n* = 1 – 3), with a general focus on the complexes of Ln = Eu, Gd and An = U–Cm due to their relevance to the separation process. For the lanthanides, a trend of decreasing metal-ligand bond length with decreasing Ln^{III} ionic radius was observed spectroscopically,^{37,39,49,51,121–123} in contrast to the bond lengths of the actinide complexes, which were observed to be largely independent of An^{III} ionic radius.^{37,51,92,93}

The literature has many examples of computational investigations into the selective binding of these ligands, both for the BTP ligand and other nitrogen donor ligands, such as BTBP (6,6'-bis(1,2,4-triazin-3-yl)-2,2'-bipyridine) and BTPPhen (2,9-bis(1,2,4-triazin-3-yl)-1,10-phenanthroline), two newer developments.^{33,47,50,52–55,124–130} Focal to many of these studies are the differences in energies of the Ln^{III} and An^{III} complexes. Despite the large separation factors exhibited by these ligands, these energetic differences amount to only hundredths to tenths of an electronvolt;^{52,53,55,127} for instance, Lan *et al.* report that for the reaction $M(\text{NO}_3)_3(\text{H}_2\text{O})_4 + \text{L} \rightarrow \text{M}(\text{L})(\text{NO}_3)_3 + 4\text{H}_2\text{O}$, (L = BTBPs) the formation of M(L)(NO₃)₃ is favoured energetically when M = Am compared to M = Eu by 0.13 eV in the DFT-calculated Gibbs free energy for L = BTBP and 0.07 eV for L = CyMe₄-BTBP,⁵² obtained using the B3LYP xc-functional.⁵² For BTP, Trumm *et al.* report the formation of the Cm complex to be 2.3 kcal/mol (~0.1 eV) more favourable than Gd in the gas-phase, calculated at the MP2 level on DFT structures optimised using the BHLYP xc-functional.⁵⁵

Bader's quantum theory of atoms in molecules (QTAIM)⁵⁸, discussed in **Chapter 2**, provides an opportunity to supplement these energetics studies, and further studies presented herein, with a density-based analysis of the covalency of the metal-ligand interactions in the complexes of BTP with lanthanides and actinides. This method of analysis has received attention of late due to the challenges in assessing, and quantifying, the covalent contributions to bonding in f-element compounds as the variations in bonding are small and molecular

orbital theory can be ambiguous when used for analysis. QTAIM has been successfully applied to characterise the bonding of actinides in a variety of coordination environments and oxidation states, and recent studies have presented evidence of correlations between QTAIM measures of covalent bonding character with bond stability.^{131–134} However, QTAIM studies of complexes of the lanthanides are sparse. While there are several QTAIM studies focusing on Ce^{IV} and the trivalent lanthanides,^{126,135–140} there has been no systematic study across the Ln series until the work presented herein. Furthermore, while it may typically be considered a safe assumption that the interactions of the lanthanides would be essentially ionic, recent studies have found unexpected levels of covalency in Ce^{IV} and Ln^{III} compounds,^{137,138,141–143} meaning that verification of this assumption is important to further understanding of the separation process.

This work also uses aquo complexes of the lanthanides and actinides as a ‘baseline’ for comparison purposes and to facilitate the calculation of exchange reaction energies. Ln^{III} hydration has been studied both experimentally and with quantum-chemical methods, finding a 9-coordinate [Ln(H₂O)₉]³⁺ structure with tri-capped trigonal prism geometry for the early and mid-series lanthanides that gradually becomes 8-coordinate, albeit as a dynamic equilibrium.¹⁴⁴ The same trends in coordination were observed for An^{III} hydration.¹⁴⁴

This work presents the first systematic study of aquo and BTP complexes of the lanthanides (Ce – Lu) and two minor actinides relevant to the separation process (Am, Cm) to investigate the relationship between the bond covalency and stability of these complexes.

4.2 Computational Details

All DFT calculations were performed using version 6.6 of the TURBOMOLE quantum chemistry code⁹⁸ using scalar-relativistic DFT. Several *xc*-functionals were considered in order to identify which was most suitable for these simulations: BLYP^{145,146}, a functional based on the generalised gradient approximation (GGA), and two hybrid GGA-functionals, B3LYP^{147,148} and BHLYP⁷⁹, which incorporate 20% and 50% of exact exchange, respectively. All optimisations were performed using def-SVP (Ln, An) and def2-SVP (H, C, N, O) basis sets of polarised double- ζ quality,¹⁰⁸ referred to from here on as def(2)-SVP. Actinide and lanthanide core electrons were replaced with the small-core relativistic ECPs of Dolg and coworkers.^{149–151} Geometry optimisations were performed using default convergence criteria in both the presence and absence of a water-like continuum solvent defined using the COSMO model¹¹³ with the default radii $r_O = 1.72 \text{ \AA}$, $r_C = 2.00 \text{ \AA}$, $r_N = 1.83 \text{ \AA}$, $r_H = 1.30 \text{ \AA}$, $r_{Ln} = 2.22 \text{ \AA}$, $r_{An} = 2.22 \text{ \AA}$. Local energetic

minima were identified *via* numerical frequency analysis. Subsequent single point energy calculations were performed using the def(2)-TZVP basis sets of polarised triple- ζ quality.¹⁰⁸

For a subset of systems, all-electron single-point energy calculations were performed to provide wavefunction files for QTAIM analysis. These calculations used SARC basis sets of polarised triple- ζ quality for the heavy elements.^{109,110} In these all-electron calculations, scalar relativistic effects were incorporated by using the 2nd order Douglas-Kroll-Hess (DKH) Hamiltonian.^{152,153} Topological and integrated properties of the electron density were performed using the AIMAll⁹⁹ (Version 14) and Multiwfn⁹⁶ (Version 3.3) codes. The electronic structure of all systems were set to be in configurations with the highest spin multiplicity, on the assumption that the highest spin state is the ground state as seen for the terpyridine complexes reported by Guillaumont *et al.*⁴⁷

4.3 Results

To investigate the aquo and BTP complexes of the lanthanides and actinides, DFT and the QTAIM were employed. The ‘sECP’ method, which employs the relativistic small-core ECPs, was chosen based on the results of the previous chapter, where the sECP method produced binding energies which were in good agreement with MP2-calculated binding energies. In addition, due the functional dependency exhibited for complexes of Gd, not one *xc*-functional was employed, but three: BLYP, B3LYP and BHLYP, the last of which produced binding energies for the Gd complexes with the closest agreement with those calculated with MP2 and had the least problems with spin contamination.

4.3.1 Geometry

4.3.1.1 Aquo Ln Complexes

Initial optimisations of $[\text{Ln}(\text{H}_2\text{O})_9]^{3+}$ (Ln = Ce – Lu) were performed in the gas phase with the BLYP, B3LYP and BHLYP *xc*-functionals. The initial geometries of the complexes prior to optimisation were set as a tri-capped trigonal prism, based on the work of Ciupka *et al.*¹⁵⁴ Average Ln—O bond lengths for these optimised structures are shown in **Table 4.1**, compared to the MP2, BP86/aug-cc-pVDZ and B3LYP/aug-cc-pVDZ-optimised bond lengths reported by Ciupka *et al.*¹⁵⁴ and the experimental EXAFS data of D’Angelo *et al.*¹⁵⁵

Table 4.1: Mean Ln—O bond lengths for $[\text{Ln}(\text{H}_2\text{O})_9]^{3+}$ (Ln = Ce – Lu) complexes calculated using the BLYP, B3LYP and BHLYP xc-functionals, compared to literature theoretical data and experimental values obtained with EXAFS.¹⁵⁵ All values are in angstroms (Å).

Ln	Ce	Pr	Nd	Pm	Sm	Eu	Gd	Tb	Dy	Ho	Er	Tm	Yb	Lu
BLYP	2.60	2.58	2.56	2.55	2.54	2.53	2.57	-	-	2.47	2.47	2.46	2.46	2.43
B3LYP	2.58	2.56	2.55	2.53	2.52	2.50	2.52	2.50	2.48	2.46	2.45	2.44	2.43	2.42
BHLYP	2.57	2.55	2.54	2.52	2.51	2.49	2.48	-	-	2.44	2.43	2.42	2.41	2.40
BP86 Lit.	2.60	2.58	2.56	2.55	2.54	2.52	2.51	2.50	2.48	2.47	2.46	2.45	2.44	2.44
B3LYP Lit.	2.61	2.59	2.57	2.55	2.54	2.52	2.51	2.50	2.48	2.47	2.46	2.45	2.44	2.43
MP2 Lit.	2.57	2.55	2.54	2.52	2.50	2.49	2.48	2.46	2.45	2.44	2.42	2.41	2.40	2.40
EXAFS Lit.	2.57	2.55	2.53	-	2.49	2.47	2.46	2.44	2.43	2.41	2.39	2.38	2.36	-

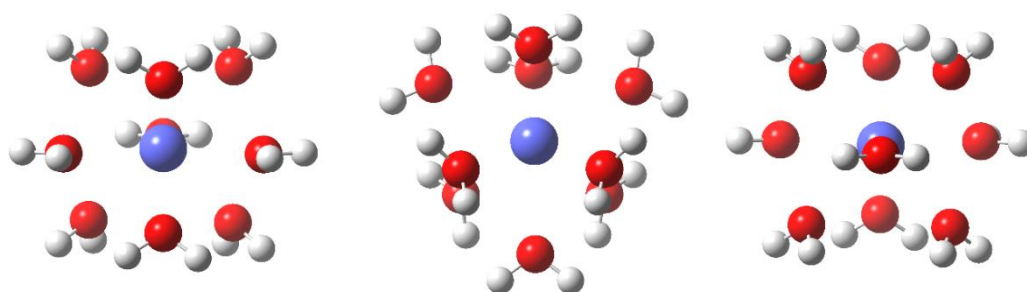


Figure 4.2: Example of the optimised $[\text{Ln}(\text{H}_2\text{O})_9]^{3+}$ complex geometry. Multiple viewing angles shown.

To test the methodology, mean Ln—O bond lengths were compared with literature values obtained using similar methods. The calculated mean BLYP bond lengths were in good agreement with comparable literature BP86 bond lengths, except for some of the mid-series lanthanides (Gd – Dy) where BLYP appeared to severely overestimate for Gd and, in the case of Tb and Dy, failed, despite repeated attempts, to achieve an optimised structure. When the B3LYP functional was employed, mean bond lengths were generally only 0.01 – 0.03 Å longer than the literature B3LYP/aug-cc-pVDZ values. While there were no literature BHLYP values for comparison, the bond lengths obtained with BHLYP were consistent with those obtained with B3LYP and BLYP, shorter than the former by ~0.01 Å. As with the BLYP functional, BHLYP failed to return an optimised structure for Tb and Dy.

Literature bond length values obtained with MP2 are in good agreement with experimental EXAFS data, with little to no difference between them for the early to mid-series lanthanides and a difference of only up to 0.04 Å for the later lanthanides. Compared to the literature

theoretical values, the MP2 values are ~ 0.03 and ~ 0.04 shorter than those reported with the B3LYP/aug-cc-pVDZ and BP86/aug-cc-pVDZ methods, respectively, and closer to the experimental EXAFS values. Similar differences were observed for the DFT-optimised bond lengths in this study, with all three functionals producing structures with mean bond lengths longer than the literature MP2 values. Of the three *xc*-functionals employed, BHLYP was in best agreement with the MP2 values, with mean bond lengths only ~ 0.01 Å longer than those optimised with MP2, while B3LYP and BLYP average bond lengths were ~ 0.02 and ~ 0.04 Å longer, respectively.

While the literature MP2 values are closer to the experimental EXAFS bond lengths, the structures optimised with all three *xc*-functionals are still in good agreement with both, in particular the BHLYP *xc*-functional, the use of which requires less computational expense than MP2 methods. However, the mean Gd—O bond lengths calculated with BLYP and B3LYP were a notable exception, 0.09 and 0.04 Å longer than the MP2-optimised bond lengths, respectively, and larger than the differences seen for any other Ln ion. A likely explanation for this poor performance is spin contamination; as seen for the trinitrate complexes, the spin expectation values for these complexes differed from the theoretical ideal.

These gas-phase $[\text{Ln}(\text{H}_2\text{O})_9]^{3+}$ structures were used as a basis for further geometry optimisations in the presence of a water-like continuum solvent defined using the COSMO solvation model.¹¹³ The average DFT-optimised Ln-O bond lengths of $[\text{Ln}(\text{H}_2\text{O})_9]^{3+}$ (Ln = Ce – Lu) with COSMO solvation obtained with the BLYP, B3LYP and BHLYP *xc*-functionals are shown in **Table 4.2** and **Figure 4.3**, compared to literature experimental EXAFS data.¹⁵⁵

Table 4.2: Mean Ln—O bond lengths for $[\text{Ln}(\text{H}_2\text{O})_9]^{3+}$ (Ln = Ce – Lu) complexes calculated using the BLYP, B3LYP and BHLYP *xc*-functionals, obtained in the presence of a continuum solvent, compared to experimental values obtained with EXAFS.¹⁵⁵ All values are in angstroms (Å).

Ln	Ce	Pr	Nd	Pm	Sm	Eu	Gd	Tb	Dy	Ho	Er	Tm	Yb	Lu
BLYP	2.54	2.52	2.51	2.49	2.48	2.47	2.51	-	-	2.42	2.41	2.41	2.40	2.38
B3LYP	2.53	2.51	2.49	2.48	2.47	2.46	2.47	2.44	2.43	2.41	2.40	2.39	2.38	2.37
BHLYP	2.52	2.50	2.49	2.47	2.46	2.45	2.43	2.43	2.42	2.40	2.38	2.38	2.37	2.36
EXAFS Lit.	2.57	2.55	2.53	-	2.49	2.47	2.46	2.44	2.43	2.41	2.39	2.38	2.36	-

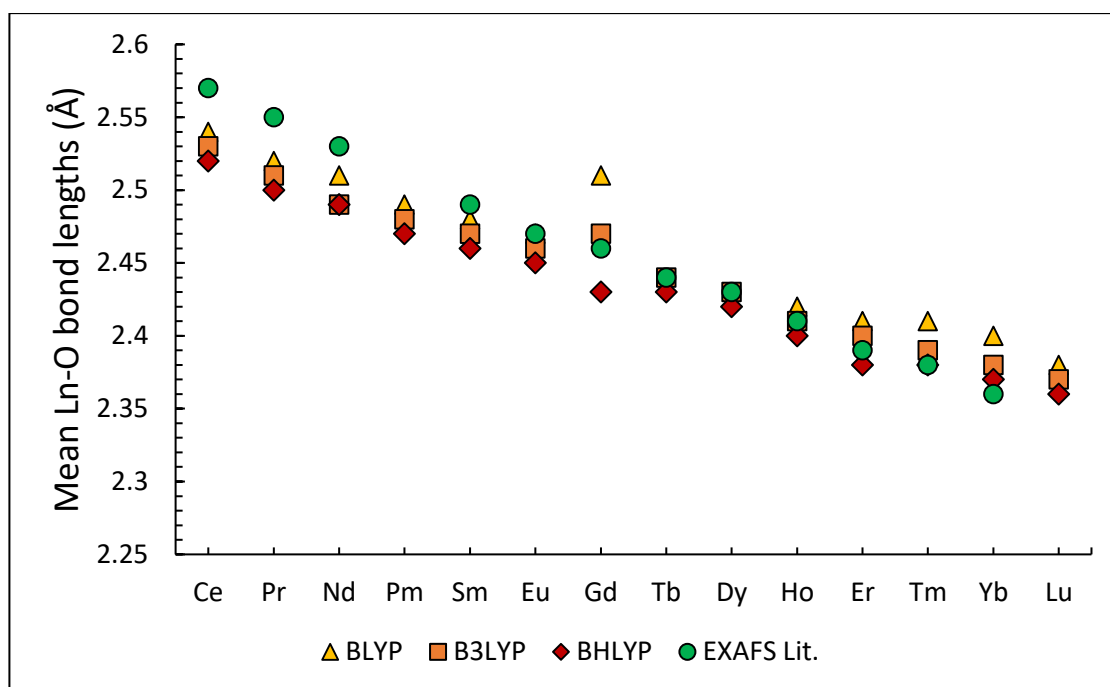


Figure 4.3: Mean Ln—O bond lengths for $[\text{Ln}(\text{H}_2\text{O})_9]^{3+}$ (Ln = Ce – Lu) complexes calculated using the BLYP, B3LYP and BHLYP xc-functionals, obtained in the presence of a continuum solvent, compared to experimental values obtained with EXAFS.¹⁵⁵

The presence of the continuum solvent has a clear effect on the mean bond lengths of the aquo complexes, shortening them by ~ 0.05 Å compared to their gas-phase counterparts regardless of the functional employed. The agreement between the calculated bond lengths and experimental results forms a clear trend; Ln—O bond lengths are underestimated by up to 0.03 Å for the early lanthanides, and this underestimation improves as the Ln series is traversed, becoming a slight overestimation for the later lanthanides. While in most cases all three functionals employed are in close agreement with the experimental data, the hybrid functionals B3LYP and BHLYP give the best agreement, particularly for the mid-series Ln ions (Gd – Dy). Overall, the bond lengths of the BHLYP-optimised structures were $\sim 0.02 - 0.03$ Å shorter than those obtained with BLYP, and ~ 0.01 Å shorter than those obtained with B3LYP, with the exception of Gd.

For the mid-series ions, both B3LYP and BLYP overestimate the Gd—O bond length, quite severely in the case of BLYP. Further, as seen in the gas phase, the structure for Tb and Dy failed to optimise with the BLYP functional, despite repeated attempts; however, unlike in the gas phase, the BHLYP functional returned optimised Tb and Dy structures.

4.3.1.2 BTP Ln Complexes

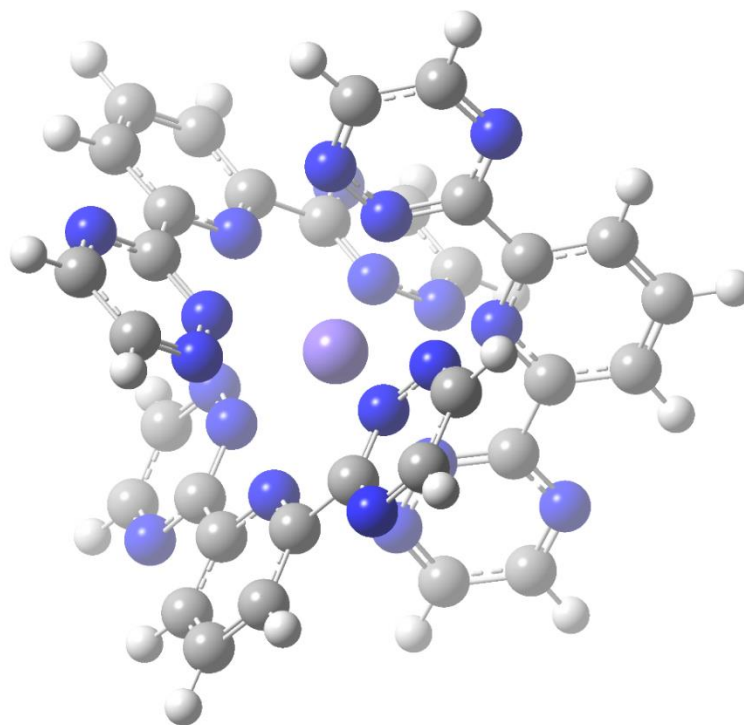


Figure 4.4: Example of the optimised $[\text{Ln}(\text{BTP})_3]^{3+}$ complex geometry.

As for the aquo complexes, initial optimisations of $[\text{Ln}(\text{BTP})_3]^{3+}$ ($\text{Ln} = \text{Ce} - \text{Lu}$) were performed in the gas phase with the BLYP, B3LYP and BHLYP *xc*-functionals, before being re-optimised in the presence of a continuum solvent modelled with COSMO. Average Ln—N bond lengths for the structures optimised in the presence of the continuum solvent are shown in **Table 4.3** and **Figure 4.5**, as well as literature values for comparison, obtained using EXAFS and XRD.^{37,39,51,121–123}

Table 4.3: Mean Ln—N bond lengths for $[\text{Ln}(\text{BTP})_3]^{3+}$ complexes calculated using the BLYP, B3LYP and BHLYP *xc*-functionals, optimised in the presence of a continuum solvent, compared to literature theoretical data and experimental values obtained with EXAFS and XRD.^{37,39,51,121–123} All values are in angstroms (Å).

Ln	Ce	Pr	Nd	Pm	Sm	Eu	Gd	Tb	Dy	Ho	Er	Tm	Yb	Lu
BLYP	2.67	2.66	2.65	2.64	2.64	2.63	2.64	2.59	2.61	2.56	2.55	2.56	2.56	2.52
B3LYP	2.66	2.65	2.63	2.61	2.60	2.59	2.58	2.57	2.56	2.54	2.53	2.52	2.51	2.50
BHLYP	2.65	2.64	2.62	2.60	2.59	2.57	2.56	2.56	2.55	2.53	2.52	2.51	2.51	2.51
EXAFS Lit.	2.62	-	-	-	2.60	2.56	2.55	-	2.56	2.56	-	2.54	-	2.52
XRD Lit.	2.61	-	-	-	2.58	-	-	-	-	-	-	2.50	2.47	-

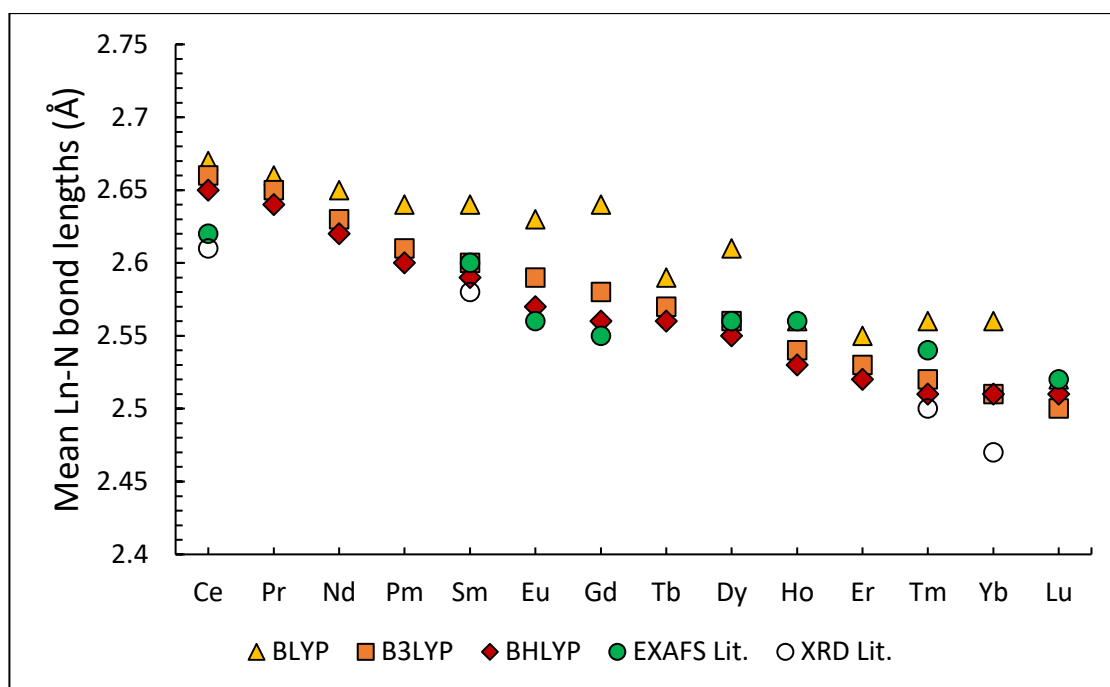


Figure 4.5: Mean Ln—N bond lengths for $[\text{Ln}(\text{BTP})_3]^{3+}$ complexes calculated using the BLYP, B3LYP and BHLYP *xc*-functionals, optimised in the presence of a continuum solvent, compared to experimental values obtained with EXAFS and XRD.^{37,39,51,121–123}

When compared to literature values, the trend of the mean Ln—N bond lengths is less clear than for the aquo complexes; however, all three *xc*-functionals overestimated bond lengths for the lighter lanthanides and, with the exception of BLYP, improved in agreement as the series was traversed. BLYP once again overestimated bond lengths for the mid-series lanthanides, in particular Sm – Gd and Dy, as well as some of the later lanthanides such as Yb. The bond lengths obtained with B3LYP and BHLYP were similar, the latter again longer by ~ 0.01 Å on average. The poor quality of the BLYP-calculated structures is again likely due to the significant spin contamination seen for these complexes, tabulated in **Table B.1** in **Appendix B**. The inclusion of exact exchange significantly reduces this spin contamination, meaning that the bond lengths obtained with B3LYP and BHLYP are not affected to the same extent as BLYP, except for the Tb and Dy complexes, for which the contamination remains pronounced.

4.3.1.3 Aquo & BTP An Complexes

To investigate the differences between the Ln complexes above and analogous An complexes, the structures of $[\text{An}(\text{H}_2\text{O})_9]^{3+}$ and $[\text{An}(\text{BTP})_3]^{3+}$ (An = Cm, Am) were optimised. These two minor actinides were chosen as they have been the focus of much of the existing literature in the field of Ln/An separation. As for the Ln complexes, initial optimisations were performed with the BLYP, B3LYP and BHLYP *xc*-functionals in the gas phase before re-optimising in the

presence of a continuum solvent. Average An—O and An—N bond lengths for these optimised structures are shown in **Table 4.4**, compared to literature EXAFS values.^{37,49,155,156}

Table 4.4: Mean M—O and M—N bond lengths for $[\text{Ln}/\text{An}(\text{H}_2\text{O})_9]^{3+}$ and $[\text{Ln}/\text{An}(\text{BTP})_3]^{3+}$ calculated using the BLYP, B3LYP and BHLYP *xc*-functionals, optimised in the presence of a continuum solvent and compared to literature experimental values obtained with EXAFS.^{37,49,155,156} All values are in angstroms (Å).

Ln/An	$[\text{M}(\text{H}_2\text{O})_9]^{3+}$				$[\text{M}(\text{BTP})_3]^{3+}$			
	$\bar{R}(\text{M} - \text{O}_N)$				$\bar{R}(\text{M} - \text{N})$			
	Eu	Gd	Am	Cm	Eu	Gd	Am	Cm
BLYP	2.47	2.51	2.51	2.51	2.63	2.64	2.62	2.63
B3LYP	2.46	2.47	2.50	2.49	2.59	2.58	2.61	2.61
BHLYP	2.45	2.43	2.49	2.48	2.57	2.56	2.60	2.60
EXAFS Lit	2.47	2.46	2.48	2.45	2.56	2.55	2.56	2.57

In contrast to the Gd—O bond lengths, mean optimised Am—O and Cm—O bond lengths are similar for all three functionals employed, with only a 0.02 Å difference between functionals at most. No significant spin contamination was observed for either actinide ion. Similar bond lengths were found for the Am—N and Cm—N bond lengths also; bond lengths were identical, even, when the B3LYP and BHLYP *xc*-functionals were employed, in agreement with the experimental observation that the metal-ligand bond lengths in the actinide complexes is independent of the ionic radii of the actinide ion.^{37,39,49} M—N bond lengths for Eu and Gd were found to be 0.01 Å longer than Am and Cm with BLYP, and 0.02-0.04 Å shorter with B3LYP and BHLYP. All three functionals employed returned $[\text{An}(\text{H}_2\text{O})_9]^{3+}$ structures with bond lengths comparable to literature EXAFS values, the closest agreement with literature being with the BHLYP functional, followed closely by B3LYP. A similar result was obtained for the structures of the $[\text{An}(\text{BTP})_3]^{3+}$ complexes, although the agreement with EXAFS values for the An complexes was not as close as was seen for the Ln complexes, with the An—N and Ln—N bond lengths of best agreement, i.e. those obtained with BHLYP, being within 0.03-0.04 Å and 0.01 Å of the EXAFS data respectively.

4.3.2 QTAIM Analysis

4.3.2.1 Topological Analysis of the Electron Density

To investigate the bonding character in the $[\text{Ln}/\text{An}(\text{H}_2\text{O})_9]^{3+}$ and $[\text{Ln}/\text{An}(\text{BTP})_3]^{3+}$ (Ln = Ce – Lu) complexes, the Quantum Theory of Atoms in Molecules (QTAIM) was employed. This topological analysis was performed using wavefunction data derived from all-electron single-

point energy (SPE) calculations using SARC basis sets of polarised triple- ζ quality with the B3LYP and BHLYP *xc*-functionals on geometries optimised using COSMO.

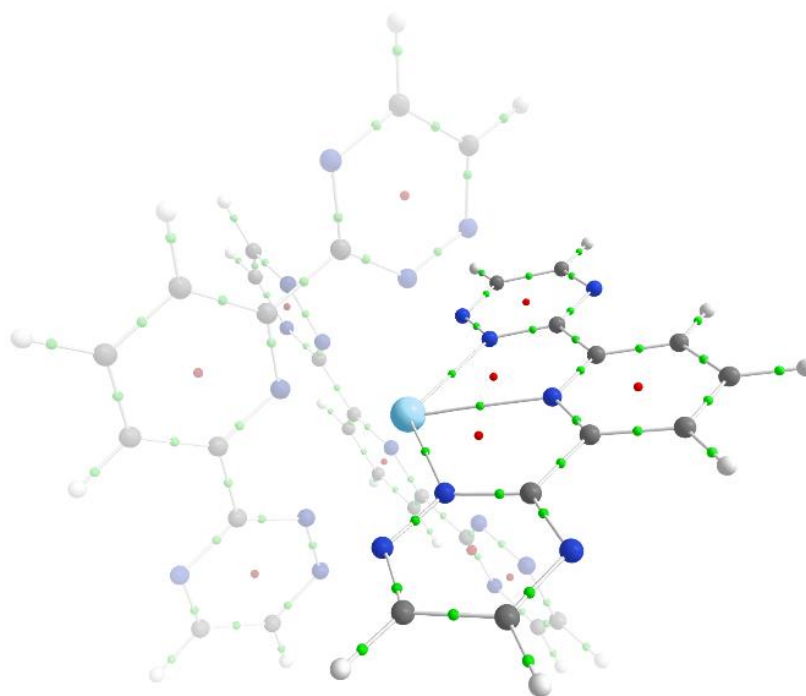
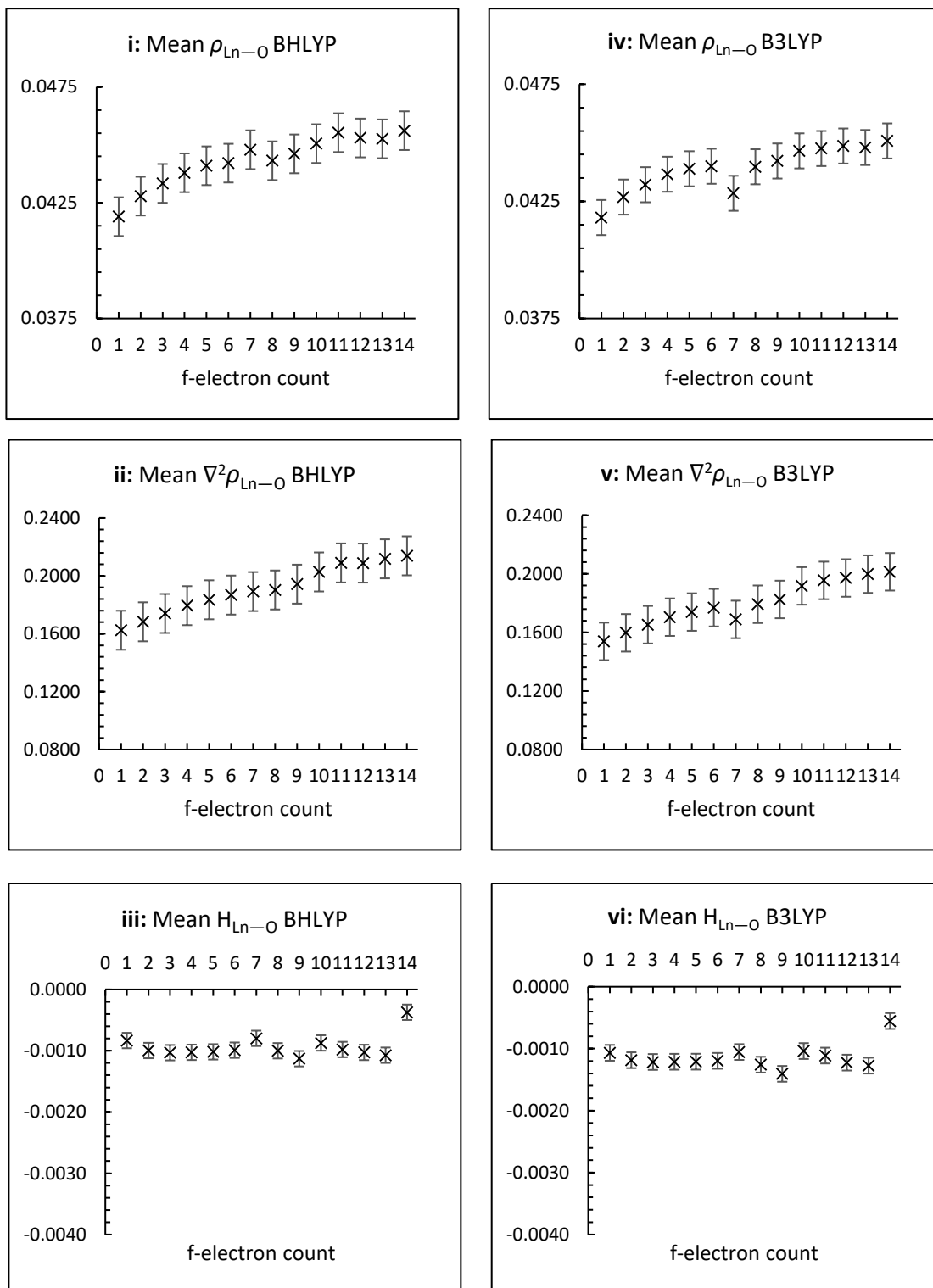


Figure 4.6: Representative molecular graph of $[M(\text{BTP})_3]^{3+}$. Light blue, red, blue, grey and white spheres represent the metal ion and O, N, C and H atoms respectively while the green and red spheres represent bond critical points and ring critical points, respectively. Selected M—N and inter-ligand bonds have been omitted for clarity.

4.3.2.1.1 Aquo Ln Complexes

Three properties of the electron density at the BCP are typically used to characterize the bonding interaction. For a covalent interaction, the energy density at the BCP (H_{BCP}) is negative, the magnitude of the electron density (ρ_{BCP}) is large and positive (typically > 0.2 au by rule of thumb) and its Laplacian ($\nabla^2\rho_{\text{BCP}}$) is negative. These metrics can be used to characterize a bonding interaction, broadly, as covalent or ionic. The electron density at the metal-ligand BCPs of interest to this investigation are an order of magnitude smaller than the typical ‘lower bound’ of 0.2 au for covalency and hence are firmly ionic interactions; however the magnitude of, and variations in, the covalent character of these ionic complexes can be compared nonetheless. These QTAIM metrics for the $[\text{Ln}(\text{H}_2\text{O})_9]^{3+}$ complexes (Ln = Ce – Lu) are displayed in **Figures 4.7i-4.7vi** and **Table A.1** in **Appendix A**.



Figures 4.7i-4.7vi: Mean values of ρ (i, iv), $\nabla^2\rho$ (ii, v) and H (iii, vi) at the Ln—O BCPs of $[\text{Ln}(\text{H}_2\text{O})_9]^{3+}$ (Ln = Ce – Lu), calculated with BHLYP (i-iii) and B3LYP (iv-vi) and plotted against the f-electron count of the Ln ion. Error bars depict the mean average deviation.

As expected, for the Ln series, the small value of $\bar{\rho}_{\text{BCP}}$ and the positive value of its Laplacian are indicative of an ionic interaction. \bar{H}_{BCP} is negative, however its magnitude is so small that it would be more appropriate to consider it as being ≈ 0 . A very weak trend of increasing $\bar{\rho}_{\text{BCP}}$ is seen across the series, with B3LYP derived maximum and minimum values lying 2.9% and 5.4% from the mean, respectively, and a mean absolute deviation (MAD) which is only 1.8% of the mean value. A similarly weak increase is seen for B3LYP, with maximum and minimum values 2.7% and 4.8% from the mean and a MAD of 1.6% across the series.

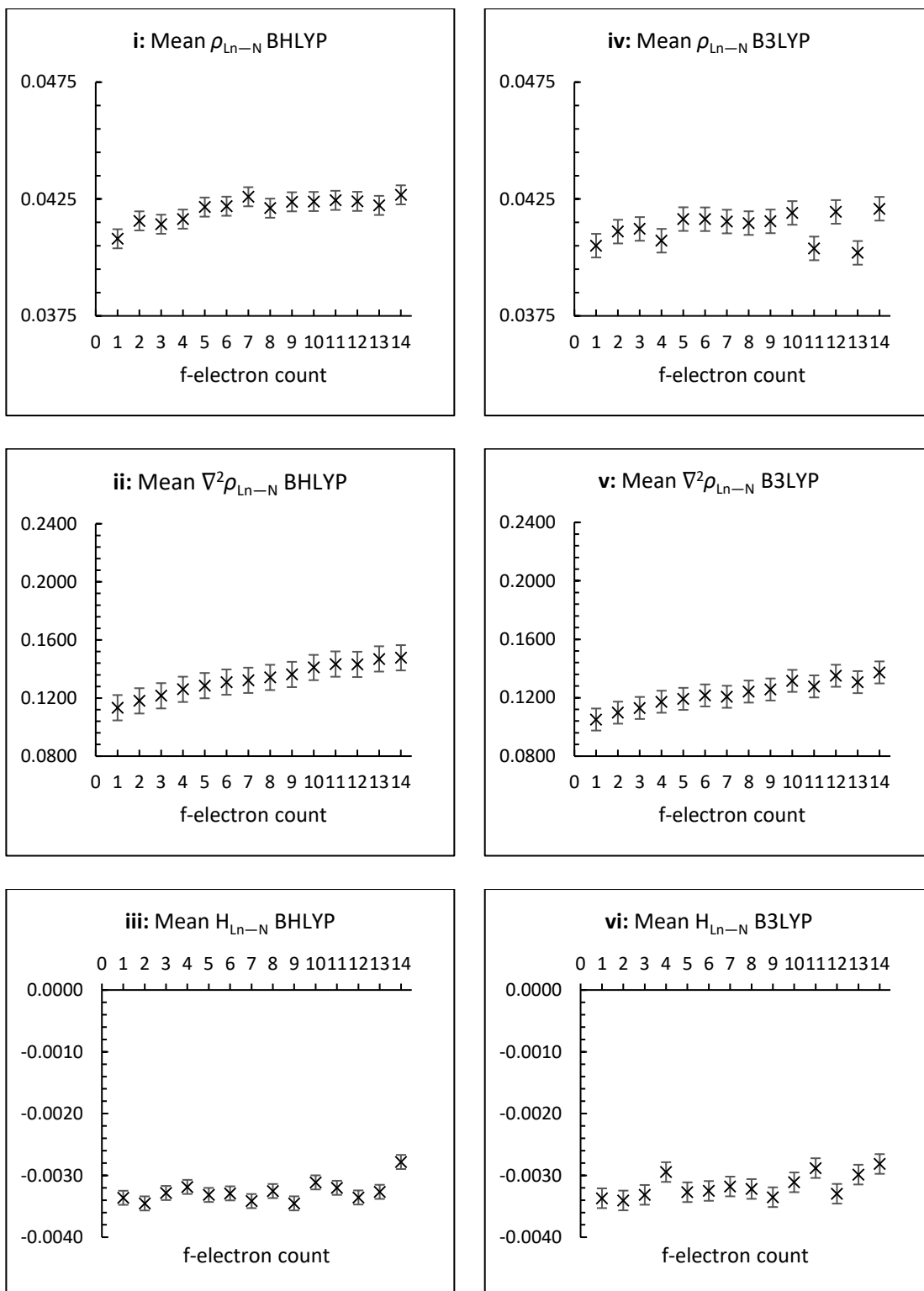
A similar, albeit more pronounced, upwards trend is seen for the Laplacian. With the B3LYP functional, maximum and minimum values of $\overline{\nabla^2\rho}_{\text{BCP}}$ are 13.2% and 13.8% from the mean, respectively, and the MAD is 6.8% from the mean value. With the B3LYP functional, the maximum and minimum values lie 12.1% and 15.7% from the mean and the MAD is 7.1% of the mean. It is unsurprising, however, that this trend is more pronounced than for $\bar{\rho}_{\text{BCP}}$, as $\overline{\nabla^2\rho}_{\text{BCP}}$ is defined as the sum of the principle curvatures of the electron density at the BCP and is therefore more sensitive to small changes in the electronic structure.

For \bar{H}_{BCP} , there is no clear trend, with a B3LYP-derived MAD which is 7.0% of the mean value and 9.1% for the B3LYP-derived data.

4.3.2.1.2 BTP Ln Complexes

As for the aquo complexes, the topological analysis of the $[\text{Ln}(\text{BTP})_3]^{3+}$ (Ln = Ce – Lu) complexes was performed using wavefunction data derived from all-electron single-point energy (SPE) calculations using SARC basis sets of polarised triple- ζ quality with the B3LYP and B3LYP xc-functionals on geometries optimised using COSMO. The QTAIM metrics for the $[\text{Ln}(\text{BTP})_3]^{3+}$ complexes and B3LYP- and B3LYP-derived mean average deviations (MADs) are shown in **Figures 4.8i-4.8vi** and **Table A.2** in **Appendix A**.

The same trends in QTAIM metrics exhibited by the aquo complexes of the Ln series can be seen for the BTP complexes. The small value of $\bar{\rho}_{\text{BCP}}$ and the positive value of its Laplacian, $\overline{\nabla^2\rho}_{\text{BCP}}$, indicates that the metal-ligand interaction is ionic in nature, as expected. There is a slight increase as the series is traversed for $\bar{\rho}_{\text{BCP}}$ and $\overline{\nabla^2\rho}_{\text{BCP}}$, while \bar{H}_{BCP} shows little to no variation across the series and can be effectively considered to be zero.



Figures 4.8i-4.8vi: Mean values of ρ (i, iv), $\nabla^2\rho$ (ii, v) and H (iii, vi) at the Ln—N BCPs of $[\text{Ln}(\text{BTP})_3]^{3+}$ (Ln = Ce – Lu), calculated with BHLYP (i-iii) and B3LYP (iv-vi) and plotted against the f-electron count of the Ln ion. Error bars depict the mean average deviation.

4.3.2.2 Ln vs. An Bonding in $[M(H_2O)_9]^{3+}$ and $[M(BTP)_3]^{3+}$

As stated previously, much of the existing literature in the field of Ln/An separation is focused on the separation of the minor actinides Am and Cm from the lanthanides. As such, these actinides have been the focus of this investigation. In terms of the lanthanides to be separated from, the lanthanide Eu is the most commonly used in literature due to its prevalence in waste and its chemical similarity to Am, and most separation factors given for separation ligands are in terms of the ability of the ligand to separate Am from Eu. However, despite issues discussed earlier for the nitrate complexes, from a computational perspective it might be expected that the formally $4f^7$ Gd^{III} would be more accurately simulated with the employed methodology than Eu due to the half-filled 4f shell of the former. Additionally, the simulation of open-shell complexes is a challenge for DFT and more reliable data might be expected from comparisons of complexes with related electronic structures. The formally $4f^7$ Gd^{III} might provide a more reliable comparison for the $5f^7$ Cm^{III} to complement the $4f^6$ Eu^{III} and $5f^6$ Am^{III} pairing. As such, this investigation focuses on the characterisation of bonding of the complexes of Am, Cm, Eu and Gd.

To compare the bonding character in the Ln/An complexes, several integrated properties of the electron density were also considered: the atomic charge ($q(M)$), the localisation ($\lambda(M)$) and delocalisation ($\delta(M, N)$) indices, discussed in **Chapter 2**, and the difference between the total electron density in the atomic basin and the localisation index ($N(M) - \lambda(M)$). Furthermore, if the stabilisation of the An complexes is covalency driven, then the difference in covalent character between the An—N and Ln—N bonds would be expected to be more pronounced than the difference of the An—O and Ln—O bonds in the aquo complexes. Due to the computational expense of obtaining these integrated properties, these were not evaluated for all Ln complexes. Reported in **Table 4.5** are the topological and integrated properties of $[Ln/An(BTP)_3]^{3+}$ and $[Ln/An(H_2O)_9]^{3+}$ for Ln = Gd, Eu and An = Cm, Am.

While values obtained with both the BHLYP and B3LYP xc-functionals are displayed in **Table 4.5**, due to the similarity between the two only the BHLYP results are discussed here, unless specified. Looking first at the data for the BTP complexes, there is little difference in the atomic charges between metal centres, with only 0.02 a.u. more charge on the Ln centres over the An centres. However, it has previously been argued that the localisation indices are more informative in relation to bonding.^{133,137,157}

Table 4.5: Topological and integrated properties of BHLYP/def(2)-TZVP//BHLYP/def(2)-SVP- and B3LYP/def(2)-TZVP//B3LYP/def(2)-SVP-calculated^a electron densities of $[\text{Ln}/\text{An}(\text{BTP})_3]^{3+}$ and $[\text{Ln}/\text{An}(\text{H}_2\text{O})_9]^{3+}$ (Ln = Eu, Gd; An = Cm, Am).^b

Complex	$q(\text{M})$	$\bar{q}(\text{N})$	$N(\text{M}) - \lambda(\text{M})$	$\bar{\delta}(\text{M}, \text{N})$	$\bar{\rho}_{\text{BCP}}(\text{M}-\text{N})$	$\bar{\nabla}^2 \rho_{\text{BCP}}(\text{M}-\text{N})$
$[\text{Eu}(\text{BTP})_3]^{3+}$	2.29 (2.18)	-0.99 (-0.84)	1.04 (1.14)	0.202 (0.224)	0.0418 (0.0417)	0.135 (0.126)
$[\text{Am}(\text{BTP})_3]^{3+}$	2.27 (2.17)	-0.99 (-0.84)	1.23 (1.34)	0.245 (0.263)	0.0436 (0.0443)	0.150 (0.139)
$\Delta_{\text{Am}/\text{Eu}}$	-	-	18% (19%)	21% (17%)	4% (6%)	-
$[\text{Gd}(\text{BTP})_3]^{3+}$	2.29 (2.19)	-0.99 (-0.84)	1.02 (1.11)	0.203 (0.222)	0.0422 (0.0419)	0.136 (0.126)
$[\text{Cm}(\text{BTP})_3]^{3+}$	2.27 (2.17)	-0.98 (-0.84)	1.16 (1.27)	0.230 (0.249)	0.0438 (0.0437)	0.146 (0.136)
$\Delta_{\text{Cm}/\text{Gd}}$	-	-	14% (15%)	13% (12%)	4% (4%)	-
Complex	$q(\text{M})$	$\bar{q}(\text{O})$	$N(\text{M}) - \lambda(\text{M})$	$\bar{\delta}(\text{M}, \text{O})$	$\bar{\rho}_{\text{BCP}}(\text{M}-\text{O})$	$\bar{\nabla}^2 \rho_{\text{BCP}}(\text{M}-\text{O})$
$[\text{Eu}(\text{H}_2\text{O})_9]^{3+}$	2.44 (2.38)	-1.23 (-1.20)	0.94 (1.00)	0.200 (0.214)	0.0443 (0.0440)	0.192 (0.182)
$[\text{Am}(\text{H}_2\text{O})_9]^{3+}$	2.46 (2.38)	-1.27 (-1.20)	1.04 (1.13)	0.223 (0.242)	0.0455 (0.0454)	0.202 (0.191)
$\Delta_{\text{Am}/\text{Eu}}$	-	-	10% (13%)	11% (13%)	3% (3%)	-
$[\text{Gd}(\text{H}_2\text{O})_9]^{3+}$	2.41 (2.37)	-1.19 (-1.20)	0.96 (0.98)	0.203 (0.209)	0.0451 (0.0425)	0.191 (0.170)
$[\text{Cm}(\text{H}_2\text{O})_9]^{3+}$	2.46 (2.37)	-1.27 (-1.20)	1.02 (1.11)	0.218 (0.236)	0.0449 (0.0448)	0.201 (0.190)
$\Delta_{\text{Cm}/\text{Gd}}$	-	-	6% (13%)	8% (13%)	0% (5%)	-

^a SARC basis sets of TZVP quality were used for An and Ln. ^b $N(\Omega)$ = integrated electron density in atomic basin Ω , $q(\Omega)$ = total charge of basin Ω , $\lambda(\Omega)$ = localisation index of basin Ω , $\bar{\rho}_{\text{BCP}}$ = mean magnitude of the electron density at the BCPs, $\bar{\delta}(\Omega_1, \Omega_2)$ = mean delocalisation index between atomic basins Ω_1 and Ω_2 , $\bar{\nabla}^2 \rho_{\text{BCP}}$ = mean Laplacian of ρ at the BCPs and $\Delta_{\text{An}/\text{Ln}}$ = percentage by which a given metric is greater for An over Ln. B3LYP-derived values are given in parentheses. All values are in atomic units.

The electron density in an atomic basin can be separated into two contributions: that which is localised in the atomic basin, and that which is delocalised between pairs of basins. The number of electrons in the atomic basin that are delocalised, or shared, with other basins can be obtained by the difference between the total electron density in the atomic basin, $N(\text{M})$, and the localisation index, $\lambda(\text{M})$. The calculated values for $N(\text{M}) - \lambda(\text{M})$ reveal a significant

increase of 18% for Am over Eu and 14% for Cm over Gd, indicating an increased covalent interaction in the An systems as measured by electron sharing, which can be thought of as degeneracy-driven covalency.⁹⁵

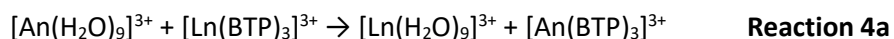
For the topological data, a larger value for both $\bar{\delta}(M, N)$ and $\bar{\rho}_{BCP}$ is observed for the An complexes. Averaged delocalisation indices are 21% greater for Am than for Eu, and 13% greater for Cm in comparison to Gd, while $\bar{\rho}_{BCP}$ values are 4% greater for Am than for Eu and 3% greater for Cm than for Gd. Further, comparing the $\bar{\rho}_{BCP}$ value for An complexes (0.0437 au) with the mean Ln values presented previously reveals that the An $\bar{\rho}_{BCP}$ value is 4% larger than the mean Ln value of 0.0421 au. Whilst this percentage is small, the An $\bar{\rho}_{BCP}$ value is 3 standard deviations larger than the mean Ln value. For the B3LYP-derived data, this increase is 6% and the An $\bar{\rho}_{BCP}$ value is 4 standard deviations larger than the mean Ln value. This data demonstrates that An—N $\bar{\rho}_{BCP}$ values are markedly larger than the corresponding Ln—N values. Together with the integrated data, this topological data indicates enhanced covalency in the Am and Cm complexes over that in their direct Ln analogues and the rest of the Ln series.

Turning attention to the aquo complexes, for the number of nonlocalized electrons in the metal basin, $N(M) - \lambda(M)$, there is an increase of 10% for Am over Eu and 6% for Cm over Gd, significantly less than the 18% and 14% increases found for the BTP complexes. $\bar{\delta}(M, O)$ values are 11% and 8% for Am over Eu and Cm over Gd respectively, and $\bar{\rho}_{BCP}$ values are 3% greater for Am over Eu and slightly smaller for Cm than for Gd. Together, this topological and integrated data shows that the enhanced covalency seen for the An complexes of BTP over their Ln analogues is more pronounced than in the aquo complexes. Furthermore, the An—O $\bar{\rho}_{BCP}$ value is only 2% larger than the Ln—O value, and within 1 standard deviation, while the An—N $\bar{\rho}_{BCP}$ value is 4% larger and 3 standard deviations away from the Ln—N value. Similar differences and standard deviations are found the B3LYP-derived values, with the mean An—O value being 3% larger and 1 standard deviation from the mean Ln—O value and the mean An—N value being 6% larger and 4 standard deviations from the mean Ln—N value.

Note: BLYP-derived densities were also considered, however, unlike the similarities between the B3LYP- and BLYP-derived densities, the An/Ln QTAIM ratios were significantly different when the BLYP functional was employed. As such, caution should be used when employing pure GGA functionals in the study of bonding in these systems.

4.3.3 Energetics

While the QTAIM analysis of the BTP complexes reveals an increased level of covalency in the ligand-actinide bonds compared to that of the lanthanides, the question of whether this translates to increased stability of the actinide complexes, and hence selectivity, remains. To investigate the relative stability of Ln/An BTP complexes the following exchange reaction was considered:



Self-consistent-field (SCF) energies for **Reaction 4a** were first evaluated for Ln = Eu, Gd and An = Am, Cm using B3LYP/ and BHLYP/def(2)-TZVP-calculated energies on B3LYP/ and BHLYP/def(2)-SVP-optimised geometries. As vibrational frequency analysis was only performed on the def(2)-SVP-optimised geometries, SCF energies were chosen for analysis over free energies, however zero-point and thermal corrections have also previously been found to make only a minor contribution to Am/Eu selectivities.^{128,130} As previously stated, these four Ln/An ions were chosen due to their relevance to the separation process and the availability of data for comparison in the literature. The reaction energies, E_r , for these ions are tabulated in **Table 4.6**.

Table 4.6: SCF energies of **Reaction 4a** for Ln = Eu/Gd and An = Am/Cm, calculated using the BHLYP/def(2)-TZVP//BHLYP/def(2)-SVP and BHLYP/def(2)-TZVP//BHLYP/def(2)-SVP model chemistries. Values in parentheses obtained using the BHLYP/def(2)-TZVP model chemistry. *[Gd(BTP)₃]³⁺ single-point energy obtained using the spin-constrained approach of Andrews *et al.*¹⁵⁸

Ln	An	E_r			
		eV		kJ/mol	
		B3LYP	BHLYP	B3LYP	BHLYP
Eu	Am	-0.05	-0.01 (-0.02)	-4.82	-0.96 (-1.93)
Gd	Cm	-0.12*	-0.02 (-0.02)	-11.58*	-1.93 (-1.93)
Eu	Cm	-0.10	+0.05 (+0.04)	-9.65	+4.82 (+3.86)
Gd	Am	-0.07*	-0.08 (-0.09)	-6.75*	-7.72 (-8.68)

The BHLYP/def(2)-TZVP//BHLYP/def(2)-SVP reaction energies for **Reaction 4a** reveal that the $\text{Eu} \leftrightarrow \text{Am}$ and $\text{Gd} \leftrightarrow \text{Cm}$ exchange reactions are weakly favourable for the actinide species. Additionally, the $\text{Gd} \leftrightarrow \text{Am}$ reaction was found to be favourable, while the $\text{Eu} \leftrightarrow \text{Cm}$ reaction was not; however, as discussed previously, it might be expected that the $4f^6 \leftrightarrow 5f^6$ and $4f^7 \leftrightarrow 5f^7$ reactions would be modelled more reliably than the mixed f^6/f^7 exchange reactions, and the very similar reaction energies give weight to that assumption. While all of the B3LYP/def(2)-TZVP//B3LYP/def(2)-SVP reaction energies were calculated to be favourable for Am and Cm, it should be noted that a spin-constrained simulation with a spin constraint parameter of $\tau = 0.75$ was required to obtain SCF energies for $[\text{Gd}(\text{BTP})_3]^{3+}$ else significant spin contamination occurred.¹⁵⁸ To investigate basis set dependence on these reaction energies, a set of aquo and BTP complexes were reoptimized using BHLYP/def(2)-TZVP model chemistry (although without vibrational frequency analysis due to the computational expense), revealing only slight variations in the reaction energy (≤ 0.01 eV in favour of the An complex), justifying the use of the def(2)-TZVP//def(2)-SVP model chemistries.

Large differences in reaction energies are not required to give significant Ln/An separation factors. An energy difference of 0.12 eV corresponds to a separation factor of 100,¹⁵⁹ which represents a 99% separation of species. Combined with the QTAIM bonding analysis, these reaction energies support the existence of a weak covalency-induced stabilisation of the An BTP complexes and hence a selectivity of the BTP ligand for complexation with An over Ln.

Finally, while more reliable data might be expected from comparisons of complexes with related electronic structures, SPE calculations were performed on optimised geometries for complexes of the rest of the Ln series to investigate reaction energy trends across the series. These reaction energies are shown in **Figure 4.9**, and tabulated in **Table A.3** in **Appendix A**.

Perhaps surprisingly, a strong trend across the series was found, with a broad increase of the relative stability of $[\text{Ln}(\text{BTP})_3]^{3+}$ as the series is traversed, with BTP complexation with the An complexes being strongly favoured over early Ln analogues, deteriorating to a marginal difference for the mid-series lanthanides (e.g. Eu, Gd) before becoming stable relative to the An analogues for the later lanthanides.

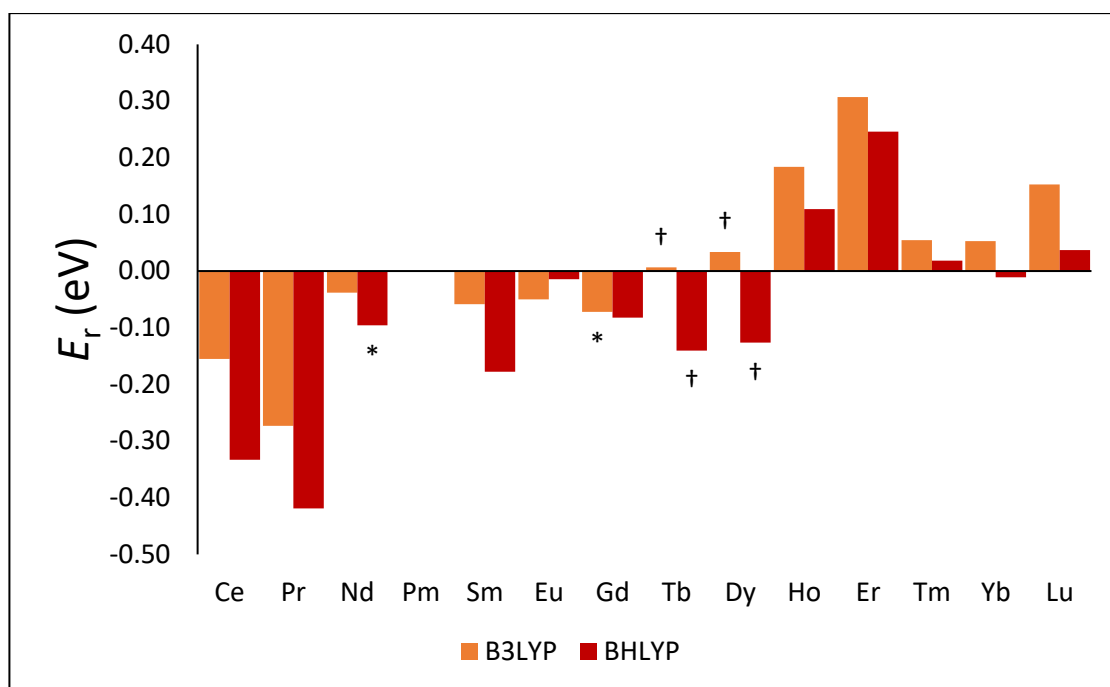


Figure 4.9: Energies of **Reaction 4a** for Ln = Ce – Lu and An = Am, calculated using the BHLYP/def(2)-TZVP//BHLYP/def(2)-SVP and B3LYP/def(2)-TZVP//B3LYP/def(2)-SVP model chemistries. * $[\text{Ln}(\text{BTP})_3]^{3+}$ SPE obtained using the spin-constrained approach of Andrews *et al.*¹⁵⁸ † $[\text{Ln}(\text{BTP})_3]^{3+}$ and $[\text{Ln}(\text{H}_2\text{O})_9]^{3+}$ SPEs both obtained using the spin-constrained approach. Only reaction energies for An = Am are displayed; an identical trend is seen for An = Cm, shifted upward by 0.06 eV with BHLYP and down by 0.05 eV with B3LYP. An anomalous reaction energy for Ln = Pm is omitted for clarity.

The use of a nona-aquo complex for all Ln ions in this study may be the cause of this apparent stability of the later lanthanides, as this model is only accurate up to Ln = Gd as there is debate as to whether the coordination number of the aquo complexes drops to 8 for the lanthanides beyond Gd; for Ln > Gd, EXAFS data shows a coordination number below 9,¹⁴⁴ and a recent *ab initio* molecular dynamics study of the hydration of Dy^{III} and Ho^{III} reports energetically stable complexes with a coordination number of 8.¹⁶⁰ However, the methodology employed in this investigation does not allow for an unbiased comparison between the eight- and nine-coordinated aquo complexes, and an ‘8 + 1’ model with one water in the second solvation shell would be incompatible with the COSMO solvation model. It should also be noted that several single-point energies had to be obtained using a spin-constrained approach and that the Pm ↔ Am reaction energy was omitted from **Figure 4.9**, for which reaction energies were ~6 eV too large and considered anomalous, which spin-constrained calculations failed to alleviate.¹⁵⁸

4.4 Conclusion

This chapter focuses on the metal-ligand bonding character and relative energetic stabilities of aquo and BTP complexes of the lanthanides (Ce – Lu) and two minor actinides (Am, Cm) to investigate the relationship between the bond covalency and stability of these complexes. The geometries of the $[\text{Ln}/\text{An}(\text{H}_2\text{O})_9]^{3+}$ and $[\text{Ln}/\text{An}(\text{BTP})_3]^{3+}$ complexes were optimised with three different *xc*-functionals: BLYP, B3LYP and BHLYP. While the BLYP functional performed poorly, with large amounts of spin contamination in the structures of many of the lanthanide complexes, both the B3LYP- and BHLYP-optimised complexes were in good agreement with literature structures obtained *via* EXAFs, especially when optimised in the presence of a continuum solvent. In particular, BHLYP returned structures free of spin-contamination and in excellent agreement with literature values.

The metal-ligand bonding in these complexes were investigated with Bader's QTAIM. While the metal-ligand interactions in f-element complexes are typically considered to be predominantly ionic in nature (with some exceptions), one of the predominant theories for the selective binding of the minor actinides by ligands such as BTP is that the greater availability of the 5f orbitals of the actinides compared to their 4f analogues results in enhanced covalency in An—ligand bonding. Characterisation of the covalent contributions to the bonding in the complex electronic structure of f-element compounds poses a significant challenge for orbital-based analysis methods, however, and recently the QTAIM approach has become an increasingly popular method for characterizing and quantifying the metal-ligand bonding character in complexes of the actinide species. Despite this, the QTAIM approach had not been applied systematically to the lanthanide series until the work presented in this chapter.

The QTAIM analysis presented here demonstrates that there is little variation in the covalent contribution to bonding in the Ln complexes, in keeping with the general understanding of Ln bonding, as well as evidence of an increased covalent bonding character for both An BTP complexes over their Ln analogues, an increase which is greater than that found in the aquo complexes of the same. Additionally, reaction energies for an exchange reaction between the aquo and BTP complexes Eu, Gd, Cm and Am were calculated with DFT, revealing a weak selectivity of BTP for Am over Eu and Cm over Gd. Together, the results of this combined QTAIM and DFT approach implies a small electronic contribution to the selectivity found experimentally.

In the following chapter, this approach is applied to complexes of the newer BTPPhen ligand (2,9-bis(1,2,4-triazin-3-yl)-1,10-phenanthroline), a current front-runner in the field of f-element separation ligands, and the bonding character and reaction energies of the BTPPhen ligand are compared with BTP.

4.5 Publishing Notes

The work discussed in this chapter was published in: Izaak Fryer-Kanssen, Jonathan Austin and Andrew Kerridge: Topological Study of Bonding in Aquo and Bis(triazinyl)pyridine Complexes of Trivalent Lanthanides and Actinides: Does Covalency Imply Stability? *Inorganic Chemistry*, 55, 10034-10042, 2016, DOI: 10.1021/acs.inorgchem.6b00968

Chapter 5: BTPPhen, Modifications of BTPPhen and Other Ligands

This chapter is separated into three parts. In **Part I**, the actinide selectivity of the bis-triazinylphenanthroline ligand (BTPPhen) is compared to that of the BTP ligand discussed in the previous chapter, through the use of DFT and QTAIM techniques. In addition, the effect of using nitrate complexes of the lanthanide and actinide species when calculating exchange reaction energies, in place of the aquo complexes used in the previous chapter, is investigated, as is the bonding nature in these complexes. In **Part II**, the same techniques are used to investigate what effect, if any, modifying the BTPPhen ligand has on the selectivity of the ligand. Finally, in **Part III**, two other non-SANEX ligands are investigated: DTPA, currently employed in the TALSPEAK process, and texaphyrins, which are not currently used for An^{III}/Ln^{III} separation but are known to complex the trivalent lanthanides, presenting a novel opportunity for the application of the analysis method employed in the previous chapters of this work.

5.1 Part I: BTPPhen vs. BTP

BTPPhen (2,9-bis(1,2,4-triazin-3-yl)-1,10-phenanthroline, **Figure 5.1**) is the current favoured SANEX separation ligand, an improvement over the (1,2,4-triazin-3-yl)-2,2'-bipyridine (BTBP) ligands with much faster reaction kinetics, owing to the *cis*-locked nature of the 1,10-phenanthroline moiety which replaces the 2,2'-bipyridine of the BTBPs.^{17,33,34}

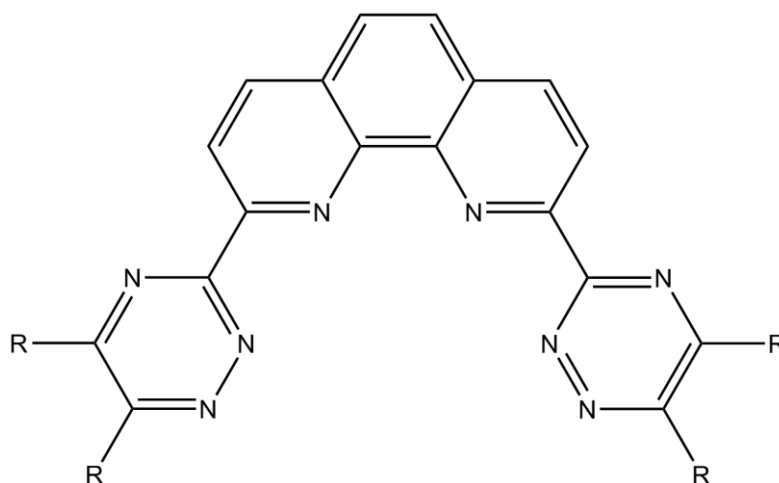


Figure 5.1: 2,9-bis(1,2,4-triazin-3-yl)-1,10-phenanthroline (BTPPhen)

As previously discussed, the high Am^{III}/Eu^{III} separation factors exhibited by ligands such as BTP and BTPPhen is thought to be due to an enhanced covalent interaction in the actinides due to

the increased radial extent, and hence chemical availability, of the 5f orbitals, compared to the more core-like 4f orbitals of the lanthanides. In support of this, recent studies have provided growing evidence of correlations between covalent bond character and bond stability.^{131,132,134,161,162} In the previous chapter, Bader's QTAIM⁵⁸ and DFT methods were used to investigate the selectivity of the BTP ligand. QTAIM analysis revealed an increase in the covalent character of the metal-ligand bonds of $[\text{An}(\text{H}_2\text{O})_9]^{3+}$ and $[\text{An}(\text{BTP})_3]^{3+}$ complexes (An = Am, Cm) compared to their Ln analogues (Ln = Eu, Gd), which was more pronounced than in Ln/An aquo complexes.¹⁶² $[\text{An}(\text{H}_2\text{O})_9]^{3+} + [\text{Ln}(\text{BTP})_3]^{3+} \rightarrow [\text{Ln}(\text{H}_2\text{O})_9]^{3+} + [\text{An}(\text{BTP})_3]^{3+}$ exchange reaction energies calculated with DFT were shown to favour An complexation by BTP for the $\text{Eu} \leftrightarrow \text{Am}$ and $\text{Gd} \leftrightarrow \text{Cm}$ reactions. Together, this selectivity of the BTP ligand and increase in covalent bonding character for Am over Eu and Cm over Gd implies a small but significant electronic contribution to An-BTP bond stability and the selectivity found experimentally.

In **Part I** of this chapter, the results of similar DFT-based quantum chemical simulations and subsequent QTAIM analysis of $[\text{Eu}/\text{Am}(\text{BTPPhen})_2(\text{NO}_3)]^{2+}$ are presented, in order to provide insight into the origin of the experimentally observed selectivity of the BTPPhen ligand for the actinide, and to compare the DFT and QTAIM results of the two ligands. Exchange reaction energies for the BTPPhen ligand are evaluated with DFT and the covalent character in the metal-BTPPhen bonds is quantified with QTAIM. Additionally, the results of the same simulation and analysis applied to the $[\text{Eu}/\text{Am}(\text{NO}_3)_3(\text{H}_2\text{O})_x]$ ($x = 3, 4$) complexes is presented in an effort to better replicate the conditions of the separation process.

5.2 Computational Details

All DFT calculations in this chapter were performed using version 6.6 of the *TURBOMOLE* quantum chemistry code. Three *xc*-functionals were employed: BLYP,^{145,146} B3LYP^{147,148} and BHLYP.⁷⁹ Topological and integrated properties of the electron density were investigated with the AIMAll code (Version 14).⁹⁹ The same model chemistries as in **Chapter 4** were used, except all-electron calculations were not required, and QTAIM analysis was instead performed on wavefunction files obtained from def(2)-TZVP SPE calculations.

5.3 Part I: Results

5.3.1 Geometries

In the previous chapter, the structures of $[\text{Ln}(\text{H}_2\text{O})_9]^{3+}$ and $[\text{Ln}(\text{BTP})_3]^{3+}$ for Ln = Ce – Lu obtained using the BLYP, B3LYP and BHLYP *xc*-functionals were reported. For $[\text{Ln}(\text{H}_2\text{O})_9]^{3+}$, the hybrid B3LYP and BHLYP *xc*-functionals gave Ln—O bond lengths typically ~0.01-0.03 Å shorter than

those obtained with BLYP, with a more pronounced difference in the middle of the series (Gd-Dy). Similar functional differences were observed for Ln—N bond lengths in $[\text{Ln}(\text{BTP})_3]^{3+}$, with BLYP significantly overestimating bond lengths for the middle of the series. High expectation values of \hat{S}^2 (in comparison to formal values) for these poor-quality BLYP structures was indicative of significant spin contamination, which the inclusion of exact exchange was found to significantly reduce. These overestimated expectation values, along with the poor performance of the BLYP xc-functional when compared to experimentally determined structural data, indicated that the origin of this poor performance lay in the description of the electronic structure of the Ln ion. As such, throughout this chapter, only results obtained with the B3LYP and BHLYP xc-functionals are reported. Of these two xc-functionals, BHLYP produced BTP and aquo complex structures with bond lengths which were closest to EXAFS literature data, and $\langle \hat{S}^2 \rangle$ values which were closest to the theoretical ideal, as also seen for the nitrates in **Chapter 3**. Gd and Cm were chosen for study in the previous chapters as they are similar to the more relevant Eu and Am yet can be easier to work with as they can be modelled as spin 7/2 complexes with a single electronic configuration. However, due to the problems encountered for the complexes of Gd, and the unexpected ease of working with the Eu and Am complexes, only complexes of Eu and Am were investigated.

Additionally, bond lengths were found to be typically ~ 0.05 Å shorter in the presence of a continuum aqueous solvent than in the gas phase, and in better agreement with experimental values. For this reason, the COSMO solvent model was also employed for the complexes presented here.

5.3.1.1 Hydrated Nitrate Eu/Am Complexes

In the previous chapter, the BTP complexes of Ln and An were compared with their aqueous complex analogues. However, in the SANEX process, the ions must be extracted from the nitric acid environment of the PUREX raffinate. As such, in this chapter the structures of $[\text{Eu}/\text{Am}(\text{NO}_3)_3(\text{H}_2\text{O})_x]$ ($x = 3, 4$) complexes have been optimised and analysed, to investigate whether the separation ligands exhibit greater Am affinity when the ions are initially bound by nitrate ligands. These values of x were chosen based on the results in **Chapter 3**, in which the maximum coordination number for the Gd and Cm hydrated nitrates were first achieved with 3 and 4 waters, respectively. The optimised Gd and Cm structures were used as starting points for the Eu and Am optimisations with $x = 3$ and 4. Average optimised M—O_N and M—O_H bond lengths for the $[\text{Eu}/\text{Am}(\text{NO}_3)_3(\text{H}_2\text{O})_x]$ ($x = 3, 4$) complexes are reported in **Table 5.1**.

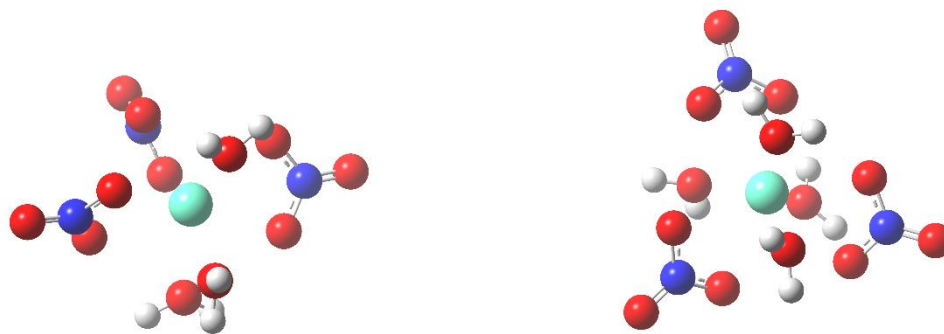


Figure 5.2: B3LYP/def(2)-SVP-optimised geometries of $[\text{Eu}(\text{NO}_3)_3(\text{H}_2\text{O})_x]$ ($x = 3$, left, and $x = 4$, right), also representative of the Am structures.

Table 5.1: Average $\text{M}-\text{O}_\text{N}$ and $\text{M}-\text{O}_\text{H}$ bond lengths of B3LYP/def(2)-SVP and B3LYP/def(2)-SVP calculated $[\text{Eu}/\text{Am}(\text{NO}_3)_3(\text{H}_2\text{O})_x]$ ($x = 3, 4$) geometries. B3LYP-derived values are given in parentheses. All values are in angstroms (\AA).

Complex	$\bar{R}(\text{M}-\text{O}_\text{N})$	$\bar{R}(\text{M}-\text{O}_\text{H})$
$[\text{Eu}(\text{NO}_3)_3(\text{H}_2\text{O})_3]$	2.47 (2.48)	2.41 (2.43)
$[\text{Am}(\text{NO}_3)_3(\text{H}_2\text{O})_3]$	2.51 (2.51)	2.46 (2.48)
$[\text{Eu}(\text{NO}_3)_3(\text{H}_2\text{O})_4]$	2.51 (2.51)	2.47 (2.50)
$[\text{Am}(\text{NO}_3)_3(\text{H}_2\text{O})_4]$	2.54 (2.54)	2.52 (2.54)

As in the BTP complexes, B3LYP-calculated bond lengths are similar to those obtained with B3LYP, with at most 0.03 \AA difference. In both the $x = 3$ and $x = 4$ complexes, the average $\text{M}-\text{O}_\text{H}$ bond lengths are shorter than the $\text{M}-\text{O}_\text{N}$ bond lengths, by $\sim 0.03\text{-}0.05 \text{ \AA}$ when $x = 3$ and up to 0.04 \AA when $x = 4$. Bond lengths are consistently longer by $\sim 0.03 - 0.07 \text{ \AA}$ when $x = 4$ than when $x = 3$, likely due to the additional steric crowding caused by the additional bound water. The bond lengths in the Eu complexes are $\sim 0.03\text{-}0.05 \text{ \AA}$ shorter than their Am counterparts.

5.3.1.2 BTPPhen Eu/Am Complexes

Unlike the tridentate BTP ligands, which form 3:1 complexes with a metal centre, the larger tetradentate BTPPhen ligand forms 2:1 complexes with Ln and An ions.³⁴ The $[\text{Ln}/\text{An}(\text{BTPPhen})_2]^{3+}$ complex has a coordination number of only 8 and can accommodate solvent molecules to achieve a coordination number of 9 or 10.³⁴ As the ions to be separated by the SANEX process are maintained in a nitric acid solution, the solvent molecule chosen to accommodate this site in this study was a nitrate ion. The $[\text{Eu}/\text{Am}(\text{BTPPhen})_2(\text{NO}_3)]^{2+}$ complex

incorporates a bidentate nitrate ligand, as reported for the $[\text{Ln}(\text{CyMe}_4\text{-BTPPhen})_2(\text{NO}_3)]^{2+}$ complexes isolated and characterised by Lewis *et al* (Ln = Eu) and Whittaker *et al* (Ln = Pr, Eu, Tb, Yb).^{34,163} Average optimised M—N and M—O_N bond lengths for $[\text{Eu}/\text{Am}(\text{BTPPhen})_2(\text{NO}_3)]^{2+}$ are reported in **Table 5.2**.

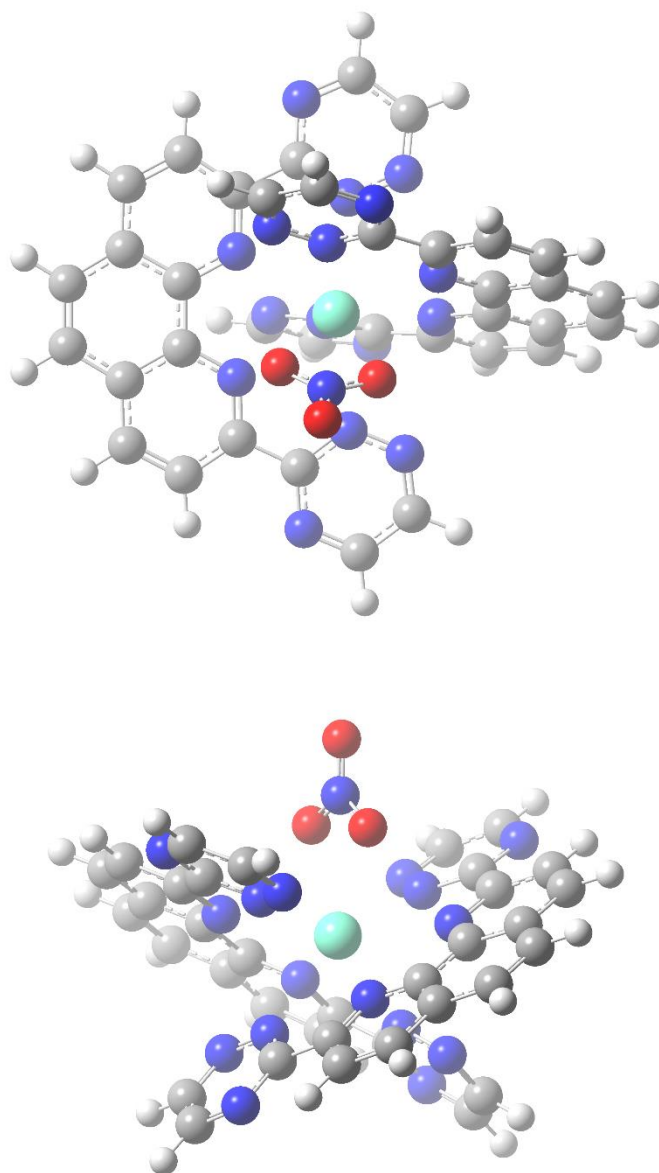


Figure 5.3: BHLYP/def(2)-SVP-optimised geometry of $[\text{Eu}(\text{BTPPhen})_2(\text{NO}_3)]^{2+}$, also representative of the Am complex. Multiple viewing angles shown.

Table 5.2: Average M—N and M—O_N bond lengths of B3LYP/def(2)-SVP- and B3LYP/def(2)-SVP-calculated [Eu/Am(BTP₃)³⁺] and [Eu/Am(BTPhen)₂(NO₃)²⁺] geometries. B3LYP-derived values are given in parentheses. All values are in angstroms (Å).

Complex	$\bar{R}(\text{M} - \text{N})$	$\bar{R}(\text{M} - \text{O}_\text{N})$
[Eu(BTP ₃) ³⁺]	2.57 (2.59)	-
[Am(BTP ₃) ³⁺]	2.60 (2.61)	-
[Eu(BTPhen) ₂ NO ₃] ²⁺	2.61 (2.63)	2.55 (2.55)
[Am(BTPhen) ₂ NO ₃] ²⁺	2.63 (2.65)	2.60 (2.58)

Compared to the the M—N bond lengths in the BTP complexes, the BTPhen M—N bond lengths are ~0.03-0.04 Å longer. As in the BTP complexes, the B3LYP- and B3LYP-calculated bond lengths for the BTPhen complexes are similar, with at most a 0.02 Å difference, an increase in the case of the B3LYP-calculated M—N bonds and shorter for the M—O_N bonds, compared to B3LYP. However, the B3LYP-calculated bond lengths are more accurate when compared to experimental values: B3LYP- and B3LYP-calculated Eu—N bond lengths in BTPhen are ~0.05 and ~0.03 Å longer, respectively, than the mean [Eu(CyMe₄-BTPhen)₂(NO₃)²⁺] Eu—N bond lengths (2.587, 2.582 Å) reported by Lewis *et al.*³⁴

The Am—N bond lengths are ~0.02 Å longer than the Eu—N bond lengths in the BTPhen complexes, consistent with the ~0.03 Å Eu/Am-N bond length difference in the BTP complexes and Ln/An—N bond length differences seen in other theoretical studies, for example that of Trumm *et al* in 2015 in which the bond lengths for thirteen Gd complexes were all 0.02-0.05 Å shorter than their Cm analogues.⁵⁵ This ~0.03 Å difference also corresponds to the difference in ionic radii of Am and Eu (0.98 and 0.95 Å, respectively).¹⁶⁴

5.3.2 QTAIM Analysis

5.3.2.1 Eu versus Am Bonding in BTP and BTPhen Complexes

To investigate the bonding character in the [Eu/Am(BTPhen)₂(NO₃)²⁺] and [Eu/Am(NO₃)₃(H₂O)_x] (x = 3, 4) complexes, the QTAIM was again employed. In the previous chapter, these calculations were based on single-point-energy calculations using SARC all-electron basis sets^{109,110} of polarised triple-zeta quality along with the second-order Douglas-Kroll-Hess Hamiltonian^{152,153} in order to account for scalar relativistic effects; however, recently added functionality in the employed analysis software allowed densities generated using the def(2)-TZVP basis sets and ECPs to be used. This allowed for better consistency throughout the analysis, as the geometry optimisations, SCF calculations and QTAIM analysis

could all be performed with the use of ECPs. As such, the QTAIM results presented here are based on densities generated from SCF calculations which employ an ECP. For comparison, the QTAIM analysis of the $[\text{Eu}/\text{Am}(\text{H}_2\text{O})_9]^{3+}$ and $[\text{Eu}/\text{Am}(\text{BTP})_3]^{3+}$ complexes was repeated using ECPs, and is also presented here. Reported in **Table 5.3** are the topological and integrated properties of $[\text{Eu}/\text{Am}(\text{BTPPhen})_2(\text{NO}_3)]^{2+}$ as well as those derived from the repeated analysis of $[\text{Eu}/\text{Am}(\text{BTP})_3]^{3+}$ discussed above. As previously argued, H_{BCP} can be considered effectively equal to 0 in these complexes, and as such has been discounted here.

Table 5.3: Topological and integrated properties of BHLYP/def(2)-TZVP//BHLYP/def(2)-SVP- and B3LYP/def(2)-TZVP//B3LYP/def(2)-SVP-calculated electron densities of $[\text{Eu}/\text{Am}(\text{BTP})_3]^{3+}$ and $[\text{Eu}/\text{Am}(\text{BTPPhen})_2(\text{NO}_3)_2]^{2+}$.^a

Complex	$q(\text{M})$	$\bar{q}(\text{N})$	$N(\text{M}) - \lambda(\text{M})$	$\bar{\delta}(\text{M}, \text{N})$	$\bar{\rho}_{\text{BCP}}(\text{M}-\text{N})$	$\bar{\nabla}^2 \rho_{\text{BCP}}(\text{M}-\text{N})$
$[\text{Eu}(\text{BTP})_3]^{3+}$	2.29 (2.18)	-0.99 (-0.84)	1.02 (1.12)	0.204 (0.221)	0.0422 (0.0416)	0.131 (0.122)
$[\text{Am}(\text{BTP})_3]^{3+}$	2.25 (2.13)	-0.98 (-0.84)	1.21 (1.36)	0.240 (0.264)	0.0451 (0.0453)	0.137 (0.128)
$\Delta_{\text{Am}/\text{Eu}}$	-	-	18% (21%)	17% (19%)	7% (9%)	-
$[\text{Eu}(\text{BTPPhen})_2(\text{NO}_3)_2]^{2+}$	2.31 (2.19)	-1.07 (-0.91)	1.00 (1.12)	0.187 (0.201)	0.0386 (0.0377)	0.121 (0.112)
$[\text{Am}(\text{BTPPhen})_2(\text{NO}_3)_2]^{2+}$	2.27 (2.15)	-1.06 (-0.91)	1.18 (1.33)	0.222 (0.240)	0.0417 (0.0414)	0.128 (0.120)
$\Delta_{\text{Am}/\text{Eu}}$	-	-	18% (19%)	19% (20%)	8% (10%)	-

^a $N(\Omega)$ = integrated electron density in atomic basin Ω , $q(\Omega)$ = total charge of basin Ω , $\lambda(\Omega)$ = localisation index of basin Ω , $\bar{\rho}_{\text{BCP}}$ = mean magnitude of the electron density at the BCPs, $\bar{\delta}(\Omega_1, \Omega_2)$ = mean delocalisation index between atomic basins Ω_1 and Ω_2 , $\bar{\nabla}^2 \rho_{\text{BCP}}$ = mean Laplacian of ρ at the BCPs and $\Delta_{\text{An}/\text{Ln}}$ = percentage by which a given metric is greater for An over Ln. B3LYP-derived values are given in parentheses. All values are in atomic units.

There is a slight excess of 0.04 (0.05)[†] a.u. in the atomic charge on the metal centres of the Eu complexes compared to the Am complexes with both B3LYP and BHLYP; however, as previously argued, the localisation indices are more informative than $q(\text{M})$ with regard to bonding.^{133,137,157} The difference between the total electron density in the atomic basin and the localisation index, $N(\text{M}) - \lambda(\text{M})$, provides the number of shared electrons in the atomic basin. $\Delta(N(\text{M}) - \lambda(\text{M}))_{\text{Am}/\text{Eu}}$, the percentage by which $N(\text{M}) - \lambda(\text{M})$ is greater for the Am

[†] B3LYP-derived values shown in parentheses.

complexes over that of the Eu complexes, is significant in both the BTP and BTPhen complexes – 18% (21%) and 18% (19%), respectively.

For both the BTP and BTPhen complexes, the small values of $\bar{\rho}_{\text{BCP}}$ and the positive values of their Laplacian indicate that the metal-ligand interaction is predominantly ionic, as would be expected. The magnitudes of the M—N $\bar{\rho}_{\text{BCP}}$ values of the BTPhen complexes are lower than those of the BTP complexes, however this might be expected as the lengths of the M—N bonds are longer in the BTPhen complexes. Instead, $\Delta\bar{\rho}_{\text{Am/Eu}}$, the percentage by which the Am $\bar{\rho}_{\text{BCP}}$ values are larger than their Eu counterparts, can be considered. Despite the Eu—N bond lengths being shorter than the Am—N bond lengths, $\Delta\bar{\rho}_{\text{Am/Eu}}$ is 7% (9%) for the BTP complexes, while $\Delta\bar{\rho}_{\text{Am/Eu}}$ for the BTPhen complexes is slightly larger at 8% (10%). In the same way, while the absolute values for $\bar{\delta}$ are lower in the BTPhen complexes than the BTP complexes, $\Delta\bar{\delta}_{\text{Am/Eu}}$, the percentage by which $\bar{\delta}(\text{Am}, \text{N})$ is greater than $\bar{\delta}(\text{Eu}, \text{N})$, can be considered instead. This relative metric is 17% (19%) for the BTP complexes and 19% (20%) for the BTPhen complexes.

Altogether, the QTAIM analysis of the BTP and BTPhen complexes show a greater difference in covalency for the BTPhen complexes than seen in the BTP complexes. While these percentages are small, reported in the previous chapter was an all-electron calculated 4% increase in the BHLYP-derived value of $\bar{\rho}_{\text{BCP}}$ for An which is ~3 standard deviations larger than the mean Ln (Ln = Ce - Lu) value (corresponding B3LYP-derived $\bar{\rho}_{\text{BCP}}$ values are 6% larger and 4 standard deviations from the mean Ln value).¹⁶²

For the remainder of this chapter, due to the similarity between the BHLYP- and B3LYP-derived results, only the BHLYP-derived results will be discussed, unless specified otherwise.

5.3.2.2 Eu versus Am Bonding in Aquo and Nitrate Complexes

It has previously been argued that if covalent stabilisation of the An-N bond plays a role in the actinide selectivity of BTP, and hence BTPhen, complexes, then the difference in covalent character between the An—N and Ln—N bonds should be expected to be more pronounced than in the M—O bonds of the aquo complexes.¹⁶² QTAIM analysis of the nona-aquo complexes of Eu and Am confirmed that this was the case, with $\Delta(N(\text{M}) - \lambda(\text{M}))_{\text{Am/Eu}}$, $\Delta\bar{\rho}_{\text{Am/Eu}}$ and $\Delta\bar{\delta}_{\text{Am/Eu}}$ values which were all lower than their equivalents in the BTP complexes.¹⁶² Here, this argument is extended to the $[\text{Eu}/\text{Am}(\text{NO}_3)_3(\text{H}_2\text{O})_x]$ ($x = 3, 4$) complexes of Eu and Am, the topological and integrated properties for which are tabulated in **Table 5.4**, as well as the repeated analysis of $[\text{Eu}/\text{Am}(\text{H}_2\text{O})_9]^{3+}$.

Table 5.4: Topological and integrated properties of BHLYP/def(2)-TZVP//BHLYP/def(2)-SVP- and B3LYP/def(2)-TZVP//B3LYP/def(2)-SVP-calculated electron densities of $[\text{Eu}/\text{Am}(\text{H}_2\text{O})_9]^{3+}$ and $[\text{Eu}/\text{Am}(\text{NO}_3)_3(\text{H}_2\text{O})_x]$ ($x = 3, 4$).^a

Complex	$q(\text{M})$	$\bar{q}(\text{O}_\text{N})$	$\bar{q}(\text{O}_\text{H})$	$N(\text{M}) - \lambda(\text{M})$	$\bar{\delta}(\text{M}, \text{O})$	$\bar{\rho}_{\text{BCP}}(\text{M} - \text{O})$	$\overline{\nabla^2 \rho}_{\text{BCP}}$
$[\text{Eu}(\text{H}_2\text{O})_9]^{3+}$	2.46 (2.37)	-	-1.27 (-1.20)	0.91 (1.00)	0.196 (0.213)	0.0442 (0.0440)	0.187 (0.177)
$[\text{Am}(\text{H}_2\text{O})_9]^{3+}$	2.45 (2.36)	-	-1.27 (-1.20)	1.05 (1.14)	0.225 (0.244)	0.0455 (0.0455)	0.188 (0.178)
$\Delta_{\text{Am}/\text{Eu}}$	-	-	-	15% (15%)	15% (14%)	3% (4%)	-
$[\text{Eu}(\text{H}_2\text{O})_3(\text{NO}_3)_3]$	2.40 (2.27)	-0.67 (-0.62)	-1.27 (-1.20)	0.98 (1.09)	0.205 (0.227)	0.0470 (0.0465)	0.185 (0.172)
$[\text{Am}(\text{H}_2\text{O})_3(\text{NO}_3)_3]$	2.38 (2.25)	-0.67 (-0.62)	-1.27 (-1.20)	1.12 (1.25)	0.234 (0.259)	0.0484 (0.0485)	0.185 (0.173)
$\Delta_{\text{Am}/\text{Eu}}$	-	-	-	14% (14%)	14% (14%)	3% (4%)	-
$[\text{Eu}(\text{H}_2\text{O})_3(\text{NO}_3)_4]$	2.41 (2.28)	-0.67 (-0.62)	-1.26 (-1.20)	0.96 (1.08)	0.182 (0.213)	0.0421 (0.0440)	0.167 (0.177)
$[\text{Am}(\text{H}_2\text{O})_3(\text{NO}_3)_4]$	2.38 (2.26)	-0.67 (-0.62)	-1.26 (-1.19)	1.11 (1.24)	0.210 (0.244)	0.0438 (0.0455)	0.170 (0.178)
$\Delta_{\text{Am}/\text{Eu}}$	-	-	-	16% (15%)	15% (15%)	4% (6%)	-

^a $N(\Omega)$ = integrated electron density in atomic basin Ω , $q(\Omega)$ = total charge of basin Ω , $\lambda(\Omega)$ = localisation index of basin Ω , $\bar{\rho}_{\text{BCP}}$ = mean magnitude of the electron density at the BCPs, $\bar{\delta}(\Omega_1, \Omega_2)$ = mean delocalisation index between atomic basins Ω_1 and Ω_2 , $\overline{\nabla^2 \rho}_{\text{BCP}}$ = mean Laplacian of ρ at the BCPs and $\Delta_{\text{An}/\text{Ln}}$ = percentage by which a given metric is greater for An over Ln. B3LYP-derived values are given in parentheses. All values are in atomic units.

While the $N(\text{M}) - \lambda(\text{M})$, $\bar{\rho}_{\text{BCP}}$, $\bar{\delta}(\text{M}, \text{O})$ and $\overline{\nabla^2 \rho}_{\text{BCP}}$ values vary in magnitude slightly between complexes, they are broadly similar, and the small values of $\bar{\rho}_{\text{BCP}}$ and positive $\overline{\nabla^2 \rho}_{\text{BCP}}$ again indicate an ionic metal-ligand interaction. Looking once more at the percentage differences, $\Delta(N(\text{M}) - \lambda(\text{M}))_{\text{Am}/\text{Eu}}$ values are 14-16% (14-15%) for the nona-aquo and hydrated nitrate complexes, compared to the 18% increase (19-21%) in the BTP and BTPPhen complexes; $\Delta\bar{\rho}_{\text{Am}/\text{Eu}}$ values are 3-4% (4-6%) compared to 7-8% (9-10%) and $\Delta\bar{\delta}_{\text{Am}/\text{Eu}}$ values are 14-15% (14-15%) compared to 17-19% (19-20%). The differences in these values between the nona-aquo and the hydrated nitrate complexes is even more slight than the differences between the BTP and BTPPhen complexes. Nevertheless, a weaker increase in covalent bonding character is observed in the nona-aquo complexes and both hydrated nitrate complexes than in the BTP and BTPPhen complexes.

5.3.3 Energetics

BHLYP/def(2)-TZVP single-point energy calculations were performed at BHLYP/def(2)-SVP-optimised geometries. Results from these calculations were used to calculate self-consistent-field (SCF) energies of the exchange reactions **5a** – **5f**, tabulated in **Table 5.5**, compared with exchange reaction **4a** from **Chapter 4**. To more accurately reflect the conditions of the separation process, the exchange reactions **5a** and **5b** are considered here, which replace the nona-aquo complexes in reaction **4a** with the Ln/An[(H₂O)₃(NO₃)_x] (x = 3, 4) complexes. To investigate the stability of the BTPPhen complexes of Am over Eu, the exchange reactions **5c** – **5e** are considered, as well as an exchange reaction between the BTP and BTPPhen complexes, reaction **5f**.

Table 5.5: SCF energies of reactions **4a** and **5a-5f**, calculated using the BHLYP/def(2)-TZVP//BHLYP/def(2)-SVP and B3LYP/def(2)-TZVP//BHLYP/def(2)-SVP model chemistries. B3LYP-derived values are given in parentheses.

Reaction		<i>E_r</i> (eV)
4a	$[\text{Eu}(\text{BTP})_3]^{3+} + [\text{Am}(\text{H}_2\text{O})_9]^{3+} \rightarrow [\text{Eu}(\text{H}_2\text{O})_9]^{3+} + [\text{Am}(\text{BTP})_3]^{3+}$	-0.01 (-0.05)
5a	$[\text{Eu}(\text{BTP})_3]^{3+} + [\text{Am}(\text{NO}_3)_3(\text{H}_2\text{O})_3] \rightarrow [\text{Eu}(\text{NO}_3)_3(\text{H}_2\text{O})_3] + [\text{Am}(\text{BTP})_3]^{3+}$	-0.09 (-0.04)
5b	$[\text{Eu}(\text{BTP})_3]^{3+} + [\text{Am}(\text{NO}_3)_3(\text{H}_2\text{O})_4] \rightarrow [\text{Eu}(\text{NO}_3)_3(\text{H}_2\text{O})_4] + [\text{Am}(\text{BTP})_3]^{3+}$	-0.03 (0.02)
5c	$[\text{Eu}(\text{BTPPhen})_2\text{NO}_3]^{2+} + [\text{Am}(\text{H}_2\text{O})_9]^{3+} \rightarrow [\text{Eu}(\text{H}_2\text{O})_9]^{3+} + [\text{Am}(\text{BTPPhen})_2\text{NO}_3]^{2+}$	-0.19 (-0.22)
5d	$[\text{Eu}(\text{BTPPhen})_2\text{NO}_3]^{2+} + [\text{Am}(\text{NO}_3)_3(\text{H}_2\text{O})_3] \rightarrow [\text{Eu}(\text{NO}_3)_3(\text{H}_2\text{O})_3] + [\text{Am}(\text{BTPPhen})_2\text{NO}_3]^{2+}$	-0.26 (-0.21)
5e	$[\text{Eu}(\text{BTPPhen})_2\text{NO}_3]^{2+} + [\text{Am}(\text{NO}_3)_3(\text{H}_2\text{O})_4] \rightarrow [\text{Eu}(\text{NO}_3)_3(\text{H}_2\text{O})_4] + [\text{Am}(\text{BTPPhen})_2\text{NO}_3]^{2+}$	-0.21 (-0.14)
5f	$[\text{Eu}(\text{BTP})_3]^{3+} + [\text{Am}(\text{BTPPhen})_2\text{NO}_3]^{2+} \rightarrow [\text{Eu}(\text{BTPPhen})_2\text{NO}_3]^{2+} + [\text{Am}(\text{BTP})_3]^{3+}$	-0.17 (-0.17)

As stated previously, the reaction energies required to give significant separation factors are not large; an energy difference of 0.12eV corresponds to a separation factor of 100, or a 99% separation of species.¹⁵⁹ *E_r* values of -0.01 eV (-0.05 eV) were reported for reaction **4a**. When [Ln/An(NO₃)₃(H₂O)_x] replaces the aqueous complexes in reaction **4a** (i.e., reactions **5a** and **5b**), the reaction energy is shifted in favour of the formation of the actinide BTP complex, to -0.09 eV when x = 3 and -0.03 eV when x = 4. This shift is likely due to a weaker complexation ability of Am with the nitrate anions and water molecules, as noted by Lan *et al.* in their studies of

BTBP selectivity.^{52,54} It is worth noting that this may mean that the E_r values presented here underestimate the An selectivity of the BTPPhen ligand as the bis-BTPPhen complexes contain a nitrate in the inner sphere. Additionally, the B3LYP-derived reaction energies shift in the opposite direction, by 0.01 when $x = 3$ and by 0.07 when $x = 4$, leading to a positive reaction energy for the latter (0.02 eV). However, the BHLYP-derived structures were in better agreement with literature values, and the energy difference introduced by small changes in structure may be significant.

Most notably, when the separation ligand is BTPPhen instead of BTP, the reaction energy is shifted in favour of the actinide by 0.17 eV (with both B3LYP and BHLYP), as seen in reaction **5f**. While the reaction energy for the BTP ligand is evident of weak selectivity, those of the BTPPhen ligand are much higher. This correlates with the results of the QTAIM analysis, which shows a slightly greater difference in covalency for the BTPPhen complexes than seen in the BTP complexes. The same shifts in reaction energy are observed for when $[\text{Ln}/\text{An}(\text{NO}_3)_3(\text{H}_2\text{O})_x]$ replaces the aqueous complexes in reaction **5c**, although unlike for the BTP ligand all B3LYP derived reaction energies are in favour of the actinide as the shift in favour of the lanthanide is outweighed by the greater selectivity of the BTPPhen ligand.

5.3.4 Electron Density vs. Bond Path Length

The average M—N bond length in the BTPPhen complexes is longer than in the BTP complexes, and the average magnitude of the electron density is lower. To investigate the relationship between the electron density and the distance between the ligand and the ion, ρ_{BCP} was plotted against bond path length, shown in **Figure 5.4**. As can be seen, the correlation between the bond path length and ρ_{BCP} is largely independent of the ligand.

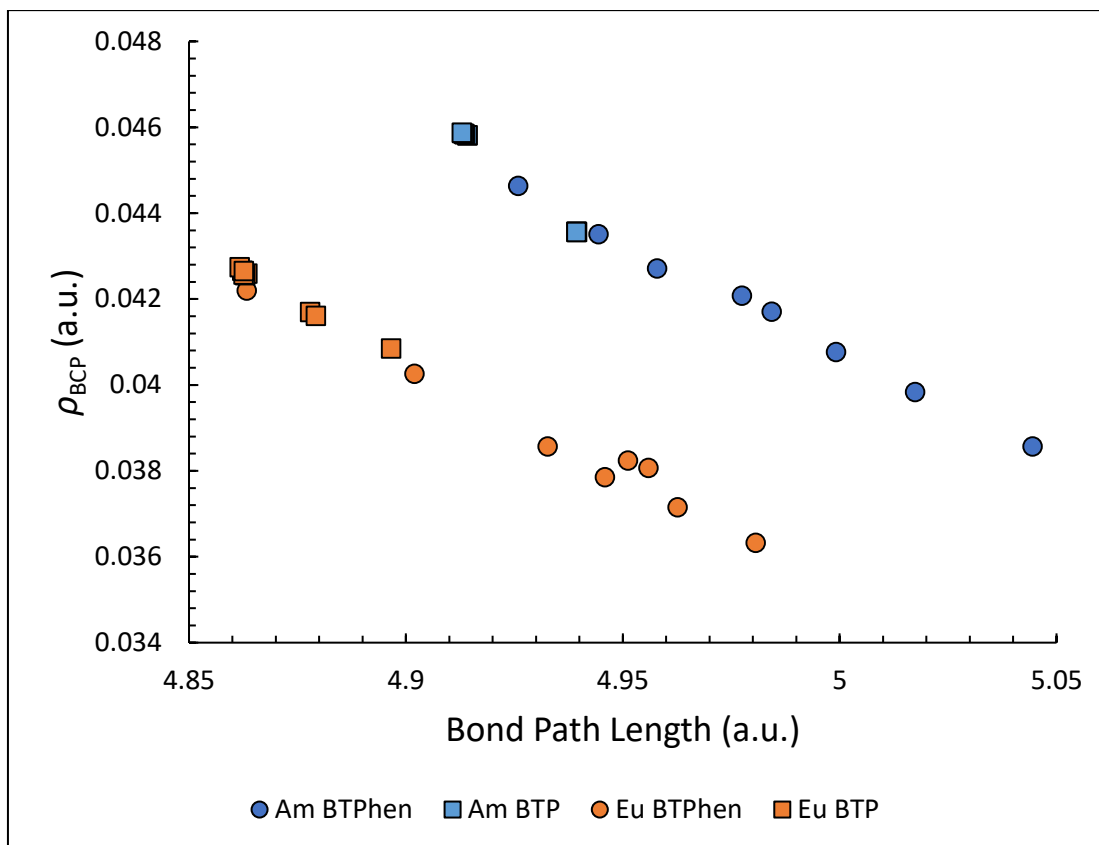


Figure 5.4: Plot of ρ_{BCP} against bond path length for $[\text{Eu}/\text{Am}(\text{BTP})_3]^{3+}$ and $[\text{Eu}/\text{Am}(\text{BTPhen})_2(\text{NO}_3)_2]^{2+}$.

5.4 Part I: Conclusion

In **Part I** of this chapter, the bonding nature of the separation ligands BTP and BTPhen with Eu^{III} and Am^{III} has been investigated through QTAIM analysis on DFT-optimised electron densities of $[\text{Eu}/\text{Am}(\text{BTPhen})_2(\text{NO}_3)_2]^{2+}$ with BHLYP/def(2)-TZVP//BHLYP/def(2)-SVP and B3LYP/def(2)-TZVP//B3LYP/def(2)-SVP model chemistries. This analysis has revealed an increased relative covalent bonding character for the Am complexes of BTPhen over Eu which was slightly more than the increase seen for the BTP complexes, despite smaller absolute values. Additionally, exchange reaction energies for the BTPhen ligand with nona-aquo complexes as a reference show evidence of stronger selectivity of the BTPhen ligand for Am over Eu than the BTP ligand by $\sim 0.17\text{eV}$ at the SCF level.

As these ligands were designed to operate in $\geq 1\text{ M}$ nitric acid solutions, this same analysis was also performed on $[\text{Eu}/\text{Am}(\text{NO}_3)_3(\text{H}_2\text{O})_x]$ ($x = 3, 4$) complexes as a better reference than the nona-aquo complexes used for comparison in the previous chapter. QTAIM analysis revealed only slight differences in any increased covalent bonding character for Am over Eu between these hydrated nitrate complexes (for both $x = 3$ and 4) and the aquo complexes. However,

BHLYP-derived exchange reaction energies using the hydrated nitrates as a reference shift in favour of the actinide for both BTP and BTPhen.

Recent work in the field of Ln/An separation *via* solvent extraction has investigated how functionalisation effects the selectivity of the BTPhen ligand.^{21,165,166} **Part II** of this chapter investigates how modification of the BTPhen ligand affects the exchange reaction energies and QTAIM metrics presented here.

5.5 Part II: Modifications of the BTPhen Ligand

Recent work has investigated the effects of electronic modulation of the BTPhen ligand on its selectivity for actinides over lanthanides.^{21,165,166} In 2013, Afsar *et al.* reported that bromine substitution at the 5- and 5,6-positions (shown in **Figures 5.5** and **5.6**) of the 1,10-phenanthroline moiety of the C5-BTPhen ligand significantly enhances the Am^{III}/Eu^{III} selectivity of the ligand.¹⁶⁷ A significantly lower distribution factor for Eu (D_{Eu}) was observed, which in the case of the substitution at the 5,6-positions was an order of magnitude lower than in the unsubstituted C5-BTPhen ligand, while the distribution factor for Am (D_{Am}) remained the same.²¹ Later, in 2015, Afsar *et al.* replaced the bromine in a mono-substituted CyMe₄-BTPhen ligand with a 4-hydroxyphenyl group to create a 5-(4-hydroxyphenyl)-BTPhen ligand which was more selective for Am over Ln than the base CyMe₄-BTPhen ligand, and exhibited very high D_{Am} values, with D_{Eu} values inbetween that of the base CyMe₄-BTPhen ligand and the brominated 5-Br-CyMe₄-BTPhen.¹⁶⁵

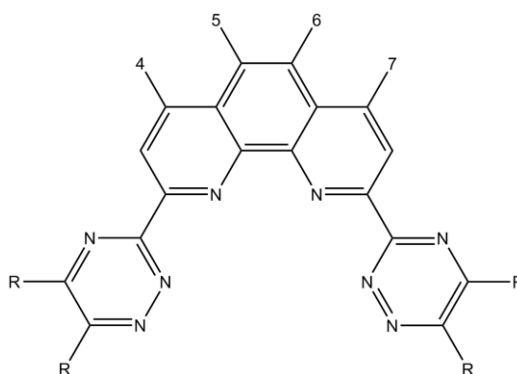


Figure 5.5: 2,9-bis(1,2,4-triazin-3-yl)-1,10-phenanthroline (BTPhen), showing the substitution sites (4-7) investigated in this work.

Additionally, in 2016, Edwards *et al.* presented the first examples of 4,7-disubstituted CyMe₄-BTPhen ligands and their complexes.¹⁶⁶ In these ligands, *ortho/para*-directing methoxy, chloro and phenyl functional groups were added at the 4- and 7-positions of the BTPhen ligand, which are *para* to the two binding nitrogens of the phenanthroline moiety.¹⁶⁶ These ligands were

found to be of comparable selectivity for Am over Eu, despite also having large differences in D values (D_{Am} for the chloro- and methoxy-substituted ligands being ~ 1.9 and ~ 1800 , respectively).¹⁶⁶

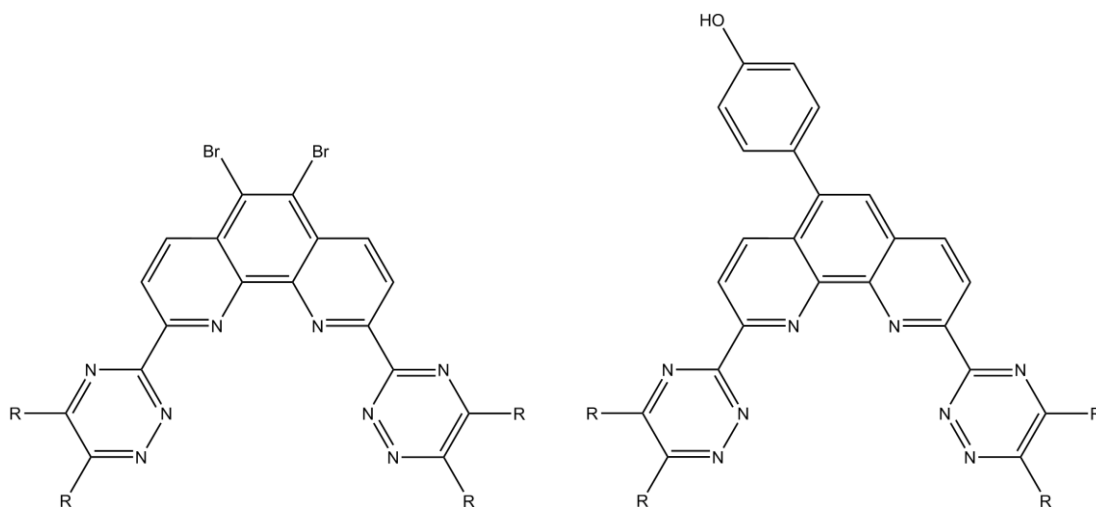


Figure 5.6: 5,6-dibromo- (left) and 5-(4-hydroxyphenyl)-BTPhen (right).

Electron-directing effects may be the cause of the enhanced selectivity seen for these functionalised BTPhen ligands. For example, as suggested by Afsar *et al.*, the inductively electron-withdrawing effect of added bromo groups may reduce the electron donating capacity of the binding nitrogens and hence the ligand's ability to complex with the heavy metal ions, leading to lower D values, while the mesomeric electron donating effect of the phenol group may increase their electron donating capacity, leading to higher D values.^{165,167}

However, whether the increase or decrease in the complexation ability of the ligands as a result of electron-directing effects leads to enhanced selectivity is unclear. For the 5- and 5,6-dibromo-BTPhen ligands reported by Afsar *et al.*, the effect on the D_{Eu} values appears to be far greater than on the D_{Am} values, however for the 5-(4-hydroxyphenyl)-BTPhen ligands both D_{Eu} and D_{Am} are affected to different degrees, and no appreciable difference in separation factor is seen for the three different 4,7-disubstituted ligands reported by Edwards *et al.*¹⁶⁵⁻¹⁶⁷

Also reported by Edwards *et al.* were computational studies of the parent and modified free ligands with DFT and the B3LYP xc-functional.¹⁶⁶ Proton affinities were used to quantify ligand basicity, and the ligands substituted with the chloro groups were found to be least basic, followed by the parent ligand, in agreement with their experimental results.¹⁶⁶ Frontier orbital analysis of the parent and modified ligands found 4,7-functionalisation to have only a subtle effect on the occupation of the HOMO and LUMO orbitals, although the HOMO-LUMO energy gaps were found to correlate with $\ln(D)$ values for the ligand.¹⁶⁶ Natural bond orbital (NBO)

analysis of the functionalised ligands revealed small changes in the natural atomic charges of the binding nitrogen atoms due to the presence of the directing groups.¹⁶⁶ Additionally, Edwards *et al.* highlight the effect of the adjacent N atom to the binding nitrogen of the triazine (known as the α -effect), which is a significant reduction of the charge on the binding nitrogen compared to the nitrogen of the phenanthroline, increasing the softness, and hence An-selectivity, of the ligand.¹⁶⁶ Investigations of the BQPhen ligand by Yang *et al.* in 2015 and Wu *et al.* in 2016 confirm this effect, as the BQPhen ligand contains no neighbouring nitrogens to the nitrogen in the same position and no reduction in charge is seen.^{127,168}

In **Part I** of this chapter, DFT calculations on the parent BTPPhen ligand found exchange reaction energies up to 0.26 eV in favour of Am over Eu, and QTAIM metrics showed an increased covalent bonding character for the Am complexes over those of Eu. To investigate the effects, if any, that functionalisation of the parent BTPPhen ligand with electron-directing groups has on its actinide selectivity, these same techniques are here applied to several modified BTPPhen ligands.

5.6: Part III: Results

5.6.1 Dibromo- & (4-Hydroxyphenyl)-BTPPhen Ligands

To investigate whether the electron-directing effects of the bromo and phenol functionalisation have any impact on the measures of selectivity reported earlier in this chapter for the parent BTPPhen ligand, the 5,6-dibromo (**1**, **Figure 5.7**) and 5-(4-hydroxyphenyl) (**2**, **Figure 5.7**) substituted BTPPhen ligands were first studied on their own. The lone ligands were optimised at the BHLYP/def(2)-SVP level and SPE calculations at the BHLYP/def(2)-TZVP level were used to generate wavefunction files for QTAIM analysis. The values of q , λ and N for the binding nitrogens of these lone ligands are shown in **Table 5.6**.

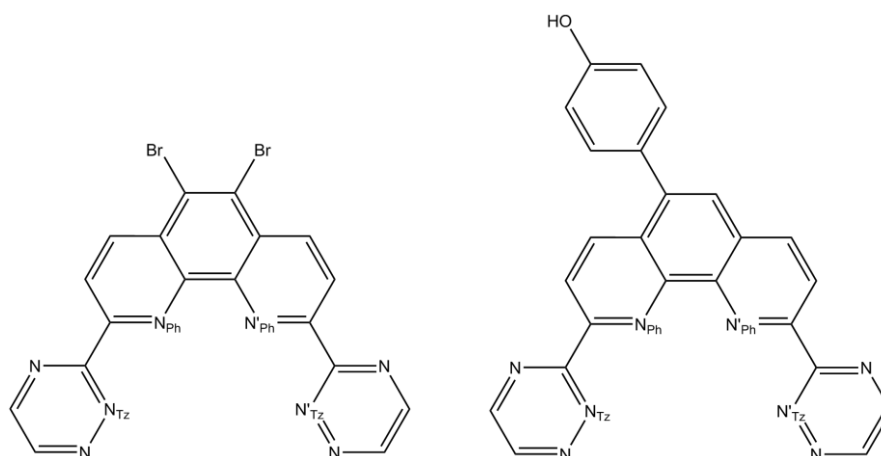


Figure 5.7: 5,6-dibromo-BTPhen (**1**, left) and 5-(4-hydroxyphenyl)-BTPhen (**2**, right). Binding nitrogens on the phenanthroline (N_{Ph} , N'_{Ph}) and triazine (N_{Tz} , N'_{Tz}) moieties are labelled.

Table 5.6: Integrated properties of B3LYP/def(2)-TZVP//B3LYP/def(2)-SVP-calculated electron densities of ligands BTPhen, **1**, and **2**.^a

Ligand	$q(\Omega)$				$\lambda(\Omega)$				$N(\Omega)$			
	N_{Ph}	N'_{Ph}	N_{Tz}	N'_{Tz}	N_{Ph}	N'_{Ph}	N_{Tz}	N'_{Tz}	N_{Ph}	N'_{Ph}	N_{Tz}	N'_{Tz}
BTPhen	-1.295	-1.295	-0.684	-0.684	6.686	6.686	6.032	6.032	8.295	8.295	7.684	7.684
1	-1.288	-1.288	-0.682	-0.682	6.677	6.677	6.030	6.030	8.288	8.288	7.682	7.682
2	-1.297	-1.292	-0.685	-0.684	6.688	6.684	6.033	6.032	8.297	8.292	7.685	7.684

^a $N(\Omega)$ = integrated electron density in atomic basin Ω , $q(\Omega)$ = total charge of basin Ω , $\lambda(\Omega)$ = localisation index of basin Ω . All values are in atomic units.

Both N_{Tz} and N'_{Tz} have significantly smaller values of q , λ and N than N_{Ph} and N'_{Ph} (~50% for q), which is due to the α -effect caused by the adjacent N atom, as discussed previously. Compared to the parent BTPhen ligand, there is a decrease in q , λ and N for all of the binding nitrogens in **1**, an observation similar to that of the natural atomic charge analysis of the 4,7-dichloro-BTPhen complex reported by Edwards *et al.*¹⁶⁶ This is most pronounced on N_{Ph} and N'_{Ph} , which are closest to the electron-withdrawing Br groups. For **2**, there is a slight increase in all three metrics for N_{Ph} and N_{Tz} , a slight decrease for N'_{Ph} and no difference for N'_{Tz} , altogether amounting to no difference in the total q , λ and N values for the binding nitrogens compared to the parent BTPhen ligand. The asymmetry seen in the values for **2** reflects the asymmetry of the ligand, with the greatest effect on q , λ and N being for N_{Ph} , which is closest to the substitution site.

As the total charge of the ligand is neutral, $-\sum q(\Omega)$ for the atomic basins of the substituted groups can be considered as a measure of the charge donated (more negative) or withdrawn (more positive) by said groups. This measure is 0.08 a.u. for **1** and -0.05 a.u. for **2**. The net

effect on the charge of the rest of the ligand from replacing two hydrogens with the two electron-withdrawing Br groups of **1** is a decrease of 0.22 a.u., while replacing one hydrogen with the electron-donating phenol group of **2** leads to a decrease of 0.02 a.u., as the value of q for the hydrogen atom is more positive than the total value of the phenol group.

While this QTAIM data shows that there is an effect on the integrated properties of the electron density of the binding nitrogens upon the addition of electron-directing groups to the phenanthroline moiety, the effect is small – half a percentage difference at most. However, the binding nitrogens in these 5,6- and 5-substituted ligands are far from the directing substituents. To investigate whether substitution instead at the closer 4- and 7-positions of the BTPhen ligand, which are also *para* to the binding nitrogens of the phenanthroline moiety, and hence should have more of an effect on their electron density, QTAIM analysis was performed on lone 4,7-dibromo-BTPhen (**3**, **Figure 5.8**) and 4-(4-hydroxyphenyl)-BTPhen (**4**, **Figure 5.8**) ligands, the results of which are displayed in **Table 5.7**.

Table 5.7: Integrated properties of B3LYP/def(2)-TZVP//B3LYP/def(2)-SVP-calculated electron densities of ligands BTPhen, **3**, and **4**.^a

Ligand	$q(\Omega)$				$\lambda(\Omega)$				$N(\Omega)$			
	N_{Ph}	N'_{Ph}	N_{Tz}	N'_{Tz}	N_{Ph}	N'_{Ph}	N_{Tz}	N'_{Tz}	N_{Ph}	N'_{Ph}	N_{Tz}	N'_{Tz}
BTPhen	-1.295	-1.295	-0.684	-0.684	6.686	6.686	6.032	6.032	8.295	8.295	7.684	7.684
3	-1.288	-1.288	-0.681	-0.681	6.677	6.677	6.029	6.029	8.288	8.288	7.681	7.681
4	-1.297	-1.294	-0.684	-0.684	6.686	6.684	6.031	6.032	8.297	8.294	7.684	7.684

^a $N(\Omega)$ = integrated electron density in atomic basin Ω , $q(\Omega)$ = total charge of basin Ω , $\lambda(\Omega)$ = localisation index of basin Ω . All values are in atomic units.

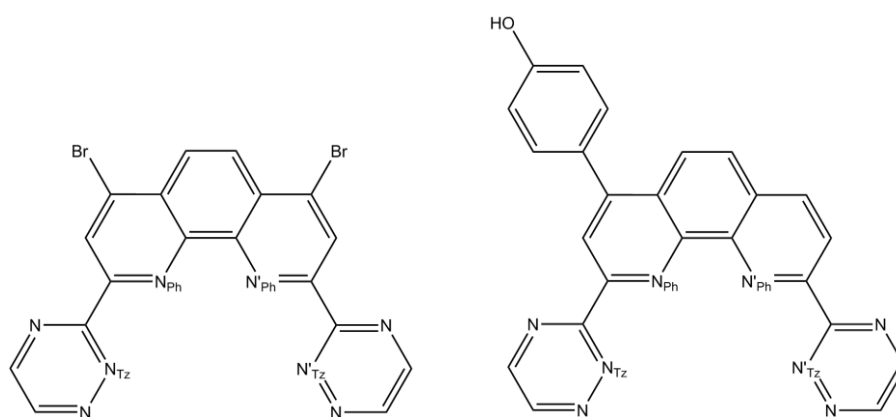


Figure 5.8: 4,7-dibromo-BTPhen (**3**, left) and 4-(4-hydroxyphenyl)-BTPhen (**4**, right). Binding nitrogens on the phenanthroline (N_{Ph} , N'_{Ph}) and triazine (N_{Tz} , N'_{Tz}) moieties are labelled.

As can be seen from the QTAIM data in **Table 5.7**, there is little difference between the integrated properties of the electron density for the binding nitrogens for the 4- and 4,7-

substituted ligands and those for the 5- and 5,6-substituted ligands. However, the values for q , λ and N for N'_{ph} in ligand **2** are closer to those of the parent ligand than in ligand **4**.

5.6.2 Dibromo- & (4-Hydroxyphenyl)-BTPPhen Complexes

To investigate the effects of the bromo and phenol functionalisation on selectivity of the ligand further, complexes of Eu^{III} and Am^{III} with the 5,6- and 4,7-dibromo (ligands **1** and **3**, respectively) and 5- and 4-(4-hydroxyphenyl) (ligands **2** and **4**) BTPPhen ligands were optimised, using the B3LYP- and B3LYP-optimised geometries of the $[\text{Eu}/\text{Am}(\text{BTPPhen})_2(\text{NO}_3)]^{2+}$ complexes as a starting point and performed in the presence of a continuum solvent modelled with COSMO. B3LYP-level optimisations were performed for ligands **1** and **2** only. Average optimised M—N and M—O_N bond lengths for these complexes are reported in **Table 5.8**.

Table 5.8: Average M—N and M—O_N bond lengths of B3LYP/def(2)-SVP- and B3LYP/def(2)-SVP-calculated $[\text{Eu}/\text{Am}(\text{L})_2(\text{NO}_3)]^{2+}$ geometries (L = BTPPhen, **1-4**). B3LYP-derived values are given in parentheses. All values are in angstroms (Å).

Complex	$\bar{R}(\text{Eu} - \text{N})$	$\bar{R}(\text{Am} - \text{N})$	$\bar{R}(\text{Eu} - \text{O}_N)$	$\bar{R}(\text{Am} - \text{O}_N)$
$[\text{M}(\text{BTPPhen})_2\text{NO}_3]^{2+}$	2.61 (2.63)	2.63 (2.65)	2.55 (2.55)	2.60 (2.58)
$[\text{M}(\mathbf{1})_2\text{NO}_3]^{2+}$	2.61 (2.62)	2.63 (2.64)	2.54 (2.55)	2.58 (2.58)
$[\text{M}(\mathbf{2})_2\text{NO}_3]^{2+}$	2.61 (2.63)	2.63 (2.64)	2.55 (2.55)	2.59 (2.58)
$[\text{M}(\mathbf{3})_2\text{NO}_3]^{2+}$	2.61	2.63	2.54	2.58
$[\text{M}(\mathbf{4})_2\text{NO}_3]^{2+}$	2.61	2.63	2.55	2.60

As might be expected for such small differences in the ligand, functionalisation of the BTPPhen ligand makes next to no difference on the metal-ligand bond lengths. The average M—O_N bond lengths for complexes of ligands **1-4** are within 0.02 Å of those for the parent BTPPhen ligand and the average M—N bond lengths are in almost all cases identical to the parent ligand.

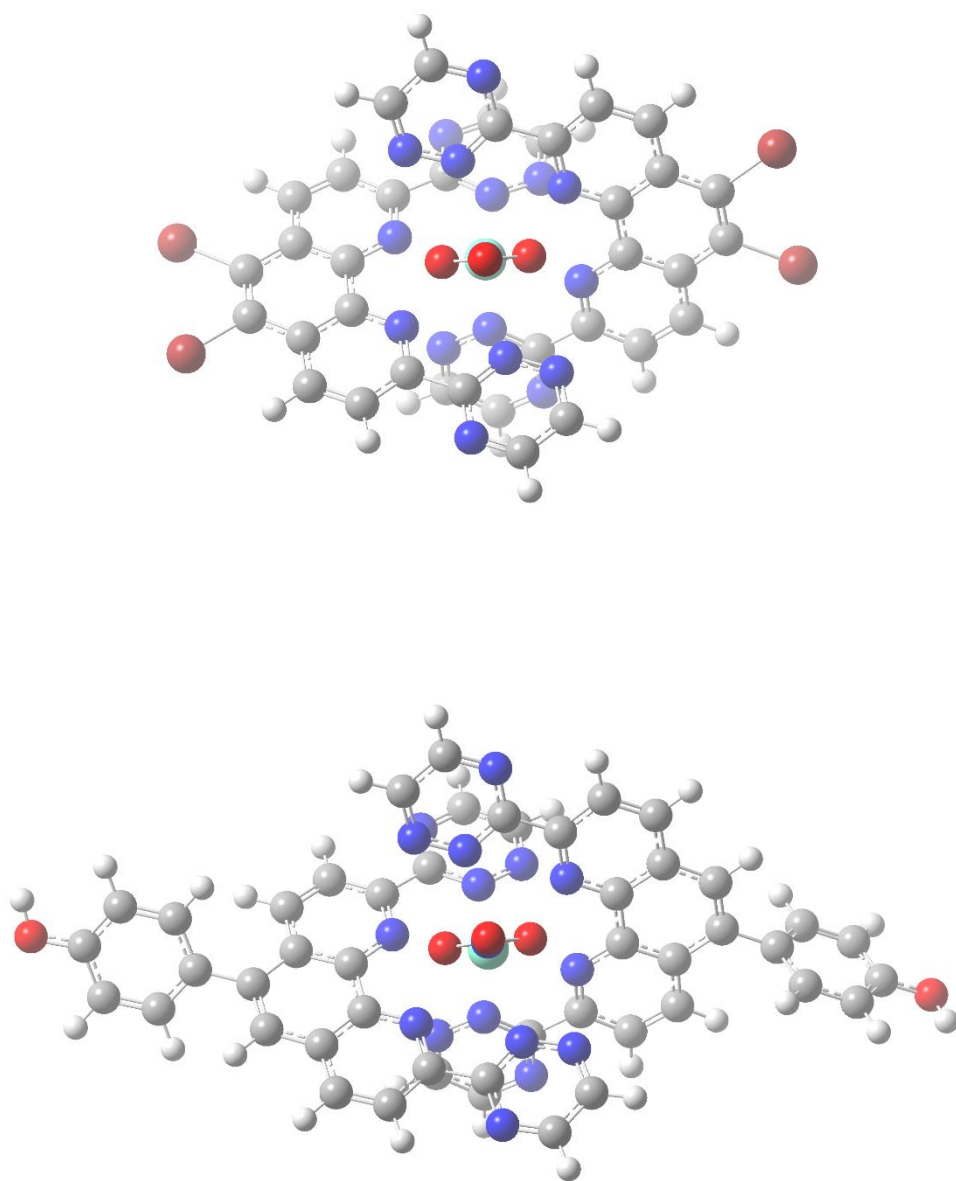


Figure 5.9: BHLYP/def(2)-SVP-optimised geometries of [Eu(**1**)₂(NO₃)₂]²⁺, top, and [Eu(**2**)₂(NO₃)₂]²⁺, bottom. Both examples are also representative of their respective Am complexes.

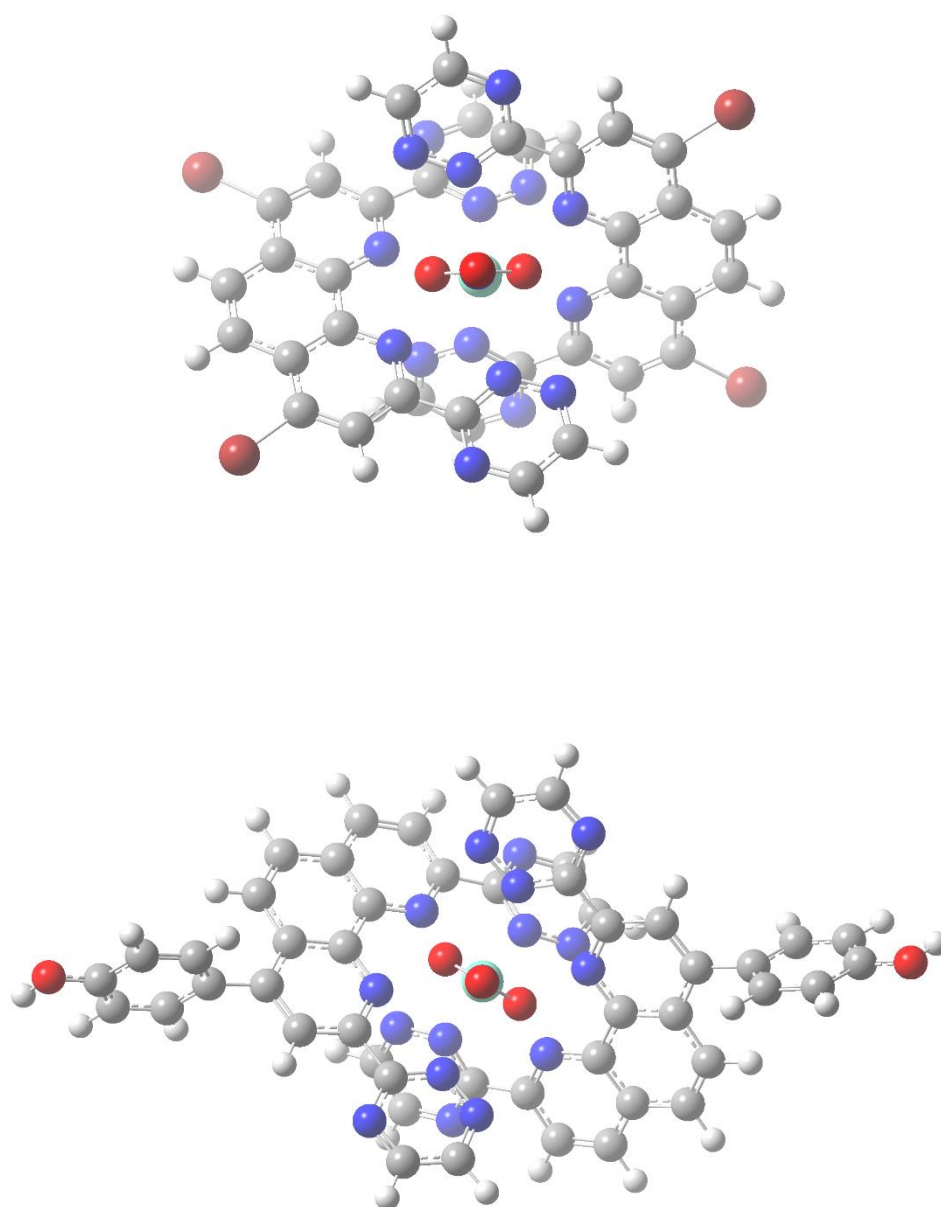


Figure 5.10: BHLYP/def(2)-SVP-optimised geometries of $[\text{Eu}(\mathbf{3})_2(\text{NO}_3)]^{2+}$, top, and $[\text{Eu}(\mathbf{4})_2(\text{NO}_3)]^{2+}$, bottom. Both examples are also representative of their respective Am complexes.

To investigate the bonding character in the complexes of **1-4** compared to the parent BTPhen ligand, the QTAIM was employed, using densities taken from def(2)-TZVP B3LYP (**1** and **2** only) and BHLYP (**1-4**) single-point-energy calculations on the def(2)-SVP optimised structures reported above.

If the enhanced separation ability of the modified BTPhen ligands is due to the electron directing effects of the added functional groups, then this might be expected to be reflected in the QTAIM data. For example, bromo groups inductively withdraw electron density from the rings, reducing the ability of the ligand to donate electrons to the metal centre. This could be reflected in the charge (q) on the coordinating nitrogen atoms, or in the electron density at, and the delocalisation index of, the metal-ligand BCPs. In addition, if this effect is more pronounced for either Eu or Am over the other, then an increase or decrease in $\Delta(N(M) - \lambda(M))_{Am/Eu}$, $\Delta\bar{\rho}_{Am/Eu}$ and $\Delta\bar{\delta}_{Am/Eu}$ would be expected. The topological and integrated properties of $[Eu/Am(L)_2(NO_3)]^{2+}$ (L = BTPhen, **1-4**) are reported in **Table 5.9**. From this data, it can be seen that 5,6-bromo- and 5-(4-hydroxyphenyl)-substitution functionalisation of the BTPhen ligand has next to no effect on the relative $\Delta(N(M) - \lambda(M))_{Am/Eu}$, $\Delta\bar{\rho}_{Am/Eu}$ and $\Delta\bar{\delta}_{Am/Eu}$ values, nor does it have any appreciable effect on the magnitudes of $q(M)$, $\bar{q}(N)$, $N(M) - \lambda(M)$, $\bar{\delta}(M, N)$, $\bar{\rho}_{BCP}$ or $\bar{\nabla}^2\rho_{BCP}$.

Table 5.9: Topological and integrated properties of BHLYP/def(2)-TZVP//BHLYP/def(2)-SVP- and B3LYP/def(2)-TZVP//B3LYP/def(2)-SVP-calculated electron densities of $[\text{Eu}/\text{Am}(\text{L})_2(\text{NO}_3)]^{2+}$ (L = BTPPhen, **1-4**).^a

Complex	$q(\text{M})$	$\bar{q}(\text{N}_{\text{coord}})$	$N(\text{M}) - \lambda(\text{M})$	$\bar{\delta}(\text{M}, \text{N})$	$\bar{\rho}_{\text{BCP}}(\text{M}-\text{N})$	$\overline{\nabla^2 \rho}_{\text{BCP}}(\text{M}-\text{N})$
$[\text{Eu}(\text{BTPPhen})_2(\text{NO}_3)]^{2+}$	2.31 (2.19)	-1.07 (-0.91)	1.00 (1.12)	0.187 (0.201)	0.0386 (0.0377)	0.121 (0.112)
$[\text{Am}(\text{BTPPhen})_2(\text{NO}_3)]^{2+}$	2.27 (2.15)	-1.06 (-0.91)	1.18 (1.33)	0.222 (0.240)	0.0417 (0.0414)	0.128 (0.120)
$\Delta_{\text{Am}/\text{Eu}}$	-	-	18% (19%)	19% (20%)	8% (10%)	-
$[\text{Eu}(\mathbf{1})_2(\text{NO}_3)]^{2+}$	2.31 (2.18)	-1.07 (-0.91)	1.01 (1.12)	0.187 (0.202)	0.0389 (0.0380)	0.123 (0.113)
$[\text{Am}(\mathbf{1})_2(\text{NO}_3)]^{2+}$	2.27 (2.15)	-1.06 (-0.91)	1.19 (1.34)	0.221 (0.241)	0.0418 (0.0417)	0.129 (0.120)
$\Delta_{\text{Am}/\text{Eu}}$	-	-	18% (19%)	19% (19%)	8% (10%)	-
$[\text{Eu}(\mathbf{2})_2(\text{NO}_3)]^{2+}$	2.31 (2.19)	-1.07 (-0.91)	1.00 (1.11)	0.186 (0.201)	0.0387 (0.0378)	0.122 (0.112)
$[\text{Am}(\mathbf{2})_2(\text{NO}_3)]^{2+}$	2.27 (2.15)	-1.06 (-0.91)	1.19 (1.34)	0.221 (0.241)	0.0417 (0.0415)	0.128 (0.119)
$\Delta_{\text{Am}/\text{Eu}}$	-	-	19% (20%)	19% (20%)	8% (10%)	-
$[\text{Eu}(\mathbf{3})_2(\text{NO}_3)]^{2+}$	2.31	1.07	1.00	0.186	0.0388	0.122
$[\text{Am}(\mathbf{3})_2(\text{NO}_3)]^{2+}$	2.27	1.06	1.19	0.221	0.0418	0.129
$\Delta_{\text{Am}/\text{Eu}}$	-	-	18%	19%	8%	-
$[\text{Eu}(\mathbf{4})_2(\text{NO}_3)]^{2+}$	2.31	1.07	1.01	0.187	0.0387	0.122
$[\text{Am}(\mathbf{4})_2(\text{NO}_3)]^{2+}$	2.27	1.06	1.18	0.222	0.0418	0.129
$\Delta_{\text{Am}/\text{Eu}}$	-	-	18%	18%	8%	-

^a $N(\Omega)$ = integrated electron density in atomic basin Ω , $q(\Omega)$ = total charge of basin Ω , $\lambda(\Omega)$ = localisation index of basin Ω , $\bar{\rho}_{\text{BCP}}$ = mean magnitude of the electron density at the BCPs, $\bar{\delta}(\Omega_1, \Omega_2)$ = mean delocalisation index between atomic basins Ω_1 and Ω_2 , $\overline{\nabla^2 \rho}_{\text{BCP}}$ = mean Laplacian of ρ at the BCPs and $\Delta_{\text{An}/\text{Ln}}$ = percentage by which a given metric is greater for An over Ln. B3LYP-derived values are given in parentheses. All values are in atomic units.

5.6.3 Energetics

SCF exchange reaction energies for the complexes of ligands **1-4** with the nona-aquo complexes were evaluated for comparison with the parent BTPhen ligand. The exchange reaction energies for reactions **5g-5n** are tabulated in **Table 5.10**, where reactions **5g-5j** are exchange reactions for the exchange for ligands **1-4** with the nona-aquo complexes and reactions **5k-5n** are for the exchange with the parent BTPhen ligand. Calculations were performed with the BHLYP *xc*-functional for all of the exchange reactions, and with the B3LYP *xc*-functional for ligands **1** and **2** only.

Table 5.10: SCF energies of reactions **5c** and **5g-5n**, calculated using the BHLYP/def(2)-TZVP//BHLYP/def(2)-SVP and B3LYP/def(2)-TZVP//BHLYP/def(2)-SVP model chemistries. B3LYP-derived values are given in parentheses.

	Reaction	E_r (eV)
5c	$[\text{Eu}(\text{BTPhen})_2(\text{NO}_3)]^{2+} + [\text{Am}(\text{H}_2\text{O})_9]^{3+} \rightarrow [\text{Eu}(\text{H}_2\text{O})_9]^{3+} + [\text{Am}(\text{BTPhen})_2(\text{NO}_3)]^{2+}$	-0.19 (-0.22)
5g	$[\text{Eu}(\mathbf{1})_2(\text{NO}_3)]^{2+} + [\text{Am}(\text{H}_2\text{O})_9]^{3+} \rightarrow [\text{Eu}(\text{H}_2\text{O})_9]^{3+} + [\text{Am}(\mathbf{1})_2(\text{NO}_3)]^{2+}$	-0.12 (-0.19)
5h	$[\text{Eu}(\mathbf{2})_2(\text{NO}_3)]^{2+} + [\text{Am}(\text{H}_2\text{O})_9]^{3+} \rightarrow [\text{Eu}(\text{H}_2\text{O})_9]^{3+} + [\text{Am}(\mathbf{2})_2(\text{NO}_3)]^{2+}$	-0.11 (-0.21)
5i	$[\text{Eu}(\mathbf{3})_2(\text{NO}_3)]^{2+} + [\text{Am}(\text{H}_2\text{O})_9]^{3+} \rightarrow [\text{Eu}(\text{H}_2\text{O})_9]^{3+} + [\text{Am}(\mathbf{3})_2(\text{NO}_3)]^{2+}$	-0.13
5j	$[\text{Eu}(\mathbf{4})_2(\text{NO}_3)]^{2+} + [\text{Am}(\text{H}_2\text{O})_9]^{3+} \rightarrow [\text{Eu}(\text{H}_2\text{O})_9]^{3+} + [\text{Am}(\mathbf{4})_2(\text{NO}_3)]^{2+}$	-0.18
5k	$[\text{Eu}(\mathbf{1})_2(\text{NO}_3)]^{2+} + [\text{Am}(\text{BTPhen})_2(\text{NO}_3)]^{2+} \rightarrow [\text{Eu}(\text{BTPhen})_2(\text{NO}_3)]^{2+} + [\text{Am}(\mathbf{1})_2(\text{NO}_3)]^{2+}$	0.07 (0.03)
5l	$[\text{Eu}(\mathbf{2})_2(\text{NO}_3)]^{2+} + [\text{Am}(\text{BTPhen})_2(\text{NO}_3)]^{2+} \rightarrow [\text{Eu}(\text{BTPhen})_2(\text{NO}_3)]^{2+} + [\text{Am}(\mathbf{2})_2(\text{NO}_3)]^{2+}$	0.08 (0.01)
5m	$[\text{Eu}(\mathbf{3})_2(\text{NO}_3)]^{2+} + [\text{Am}(\text{BTPhen})_2(\text{NO}_3)]^{2+} \rightarrow [\text{Eu}(\text{BTPhen})_2(\text{NO}_3)]^{2+} + [\text{Am}(\mathbf{3})_2(\text{NO}_3)]^{2+}$	0.06
5n	$[\text{Eu}(\mathbf{4})_2(\text{NO}_3)]^{2+} + [\text{Am}(\text{BTPhen})_2(\text{NO}_3)]^{2+} \rightarrow [\text{Eu}(\text{BTPhen})_2(\text{NO}_3)]^{2+} + [\text{Am}(\mathbf{4})_2(\text{NO}_3)]^{2+}$	0.01

The exchange reaction energies in **Table 5.10** show a reduction in the energetic favourability of ligands **1-4** for Am over Eu compared to the parent BTPhen ligand, suggesting that any increased selectivity seen for these functionalised BTPhen ligands is not electronic in origin. At the BHLYP level, ligand **4** is the most similar to the parent BTPhen ligand, with only a 0.01 eV difference between the two, while the reduction in favourability for ligands **3-4** is between

0.06 and 0.08 eV, with the largest difference representing an almost 60% reduction in selectivity. This reduction is less pronounced at the B3LYP level, where the exchange reactions for ligands **1** and **2** are only 0.03 and 0.01 eV less in favour of the actinide than the parent BTPhen ligand.

5.7 Part II: Conclusion

In **Part II** of this chapter, the effects of substitution of the phenanthroline moiety of the BTPhen ligand on the integrated properties of the electron density of the lone ligands and on the energetics and topological and integrated properties of their complexes with Am and Eu. For the lone ligands, small decreases in q , λ and N were seen for the binding nitrogens of the dibromo-substituted ligands compared to the parent ligand, while there was very little difference seen for the binding nitrogens of the (4-hydroxyphenyl)-substituted ligand. For the complexes of the substituted ligands, there was no appreciable difference between either the magnitudes or relative Am/Eu values of the topological and integrated properties of the electron density compared to the complexes of the parent BTPhen ligand. The exchange reaction energies for the substituted complexes were compared to the parent BTPhen ligand, and a decrease in the energetic favourability was observed for both the dibromo- and (4-hydroxyphenyl)-substituted ligands of between 0.01 and 0.08 eV, implying a different origin to any increased selectivity seen for these substituted ligands.

5.8 Part III: DTPA and Texaphyrin

In **Part III** of this chapter, the results of the DFT and QTAIM analysis of two non-SANEX ligands, DTPA and texaphyrin, are presented. DTPA is a ligand used in the TALSPEAK An^{III}/Ln^{III} separation process, while texaphyrins are not currently used for An^{III}/Ln^{III} separation, but are known to complex the trivalent lanthanides.

5.8.1 DTPA

Diethylenetriaminepentaacetic acid (DTPA, **Figure 5.11**) is an EDTA-like ligand used in the TALSPEAK (Trivalent Actinide-Lanthanide Separation by Phosphorous reagent Extraction from Aqueous Komplexes) Ln/An separation process.²

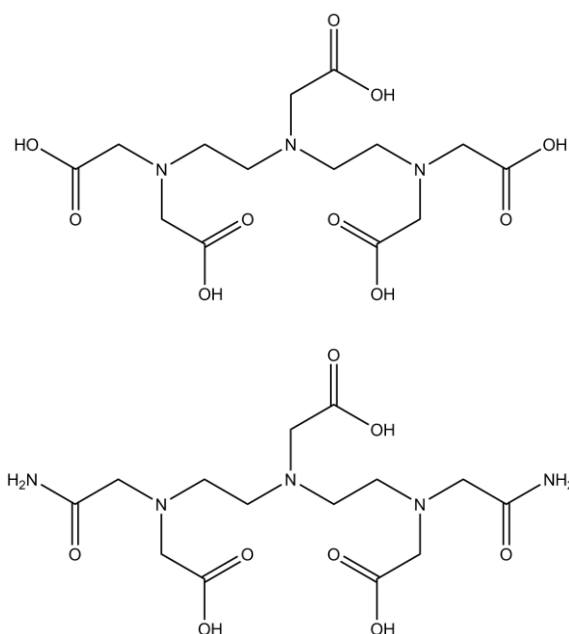


Figure 5.11: 2,2',2'',2'''-(((carboxymethyl)azanediyl)bis(ethane-2,1-diyl))bis(azanetriyl))tetraacetic acidDiethylenetriaminepentaacetic acid (DTPA, top) and 2,2'-(((carboxymethyl)azanediyl)bis(ethane-2,1-diyl))bis((2-amino-2-oxoethyl)azanediyl))diacetic acid (NH₂-DTPA, bottom)

TALSPEAK can be thought as a 'reverse' SANEX, where instead of the separation ligand extracting the actinides into the organic phase, they are instead held in the aqueous phase by a polyaminocarboxylic acid (such as DTPA) while the lanthanides are extracted into the organic phase.² Advantages of TALSPEAK are that it is resistant to irradiation, does not require high acid concentrations, has been performed in a pilot on the plant scale and DTPA and other reagents used in TALSPEAK are cheap and readily available.² Unlike BTP and BTPPhen, DTPA is

an octadentate mixed O/N-donor ligand, and binds to the metal centre through five oxygen atoms and three nitrogens.

In 2013, Roy *et al.* presented a computational investigation of the DTPA complexes of Nd and Am.¹⁶⁹ Calculated Gibbs free energies in aqueous solution were found to be in favour of Am complexation by ~ 1 kcal/mol, and QTAIM analysis of the bonding interaction was indicative of slightly more covalent character in the Am complexes than in the Nd complexes.¹⁶⁹ The larger values of ρ and H at the M—O BCPs than at the M—N BCPs, as well as results from NBO and Mulliken analysis, lead them to conclude that while the nitrogen atoms provide advantageous covalency interactions with the Am centre over the Nd centre, the oxygen atoms provide a more covalent interaction.¹⁶⁹ Based on this, they argued that the idea that nitrogen-only donor ligands were preferable over O-donor ligands should be reconsidered.¹⁶⁹

5.8.2 Texaphyrin

Texaphyrins (**Figure 5.12**) are tripyrrolic, penta-aza Schiff base macrocycles, so named due to their resemblance to the state flag of Texas, which have been demonstrated to form stable complexes with the trivalent lanthanides.^{112,170–173} Texaphyrins bear a strong resemblance to the more popular porphyrins, and are considered to be among the “expanded porphyrins”, which are larger porphyrin-like macrocycles with additional π -electrons and coordinating heteroatoms.

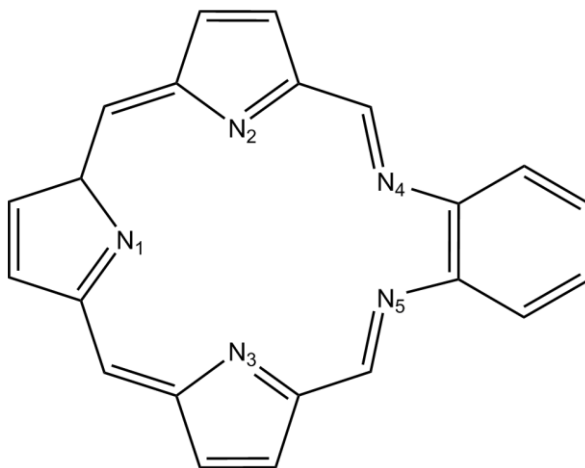


Figure 5.12: Texaphyrin ligand.

Unlike the porphyrins, the coordinated Ln^{III} ion in texaphyrin complexes does not sit in the plane of the molecule, but above it.^{112,171} Texaphyrins are not currently employed for An^{III}/Ln^{III} separation, however as nitrogen donor ligands which are known to coordinate the trivalent lanthanides, they present a novel opportunity for the application of the methodology

previously applied to known separation ligands. Ln^{III} texaphyrin complexes are stable and have applications in anticancer therapy.¹⁷⁰

5.9 Part II: Results

5.9.1 DTPA Results

To investigate the bonding nature and relative energetics of the DTPA ligand, Eu and Am complexes of DTPA and NH₂-DTPA were optimised. The latter ligand, NH₂-DTPA, was investigated in response to experimental work instigated by a collaborator of the group, and is a DTPA ligand in which two of the OH groups are replaced with NH₂ to approximate the effect of adding an amide group.¹⁷⁴

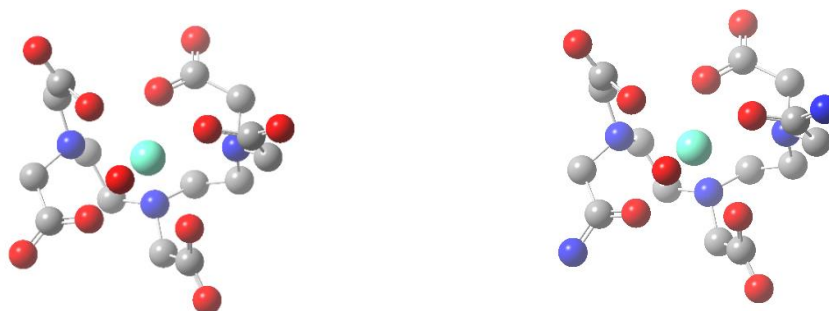


Figure 5.13: BHLYP/def(2)-SVP-optimised complexes of [Eu(DTPA)(H₂O)]²⁻, left, and [Eu(NH₂-DTPA)(H₂O)]²⁻, right. Structure shown is also representative of the Am complex. Hydrogen atoms are omitted for clarity.

In the DTPA complexes, all five of the OH groups were deprotonated, resulting in a complex with an overall charge of 2-, while the NH₂-DTPA complexes were neutral with all three OH groups deprotonated. The average metal-ligand bond lengths for these complexes are shown in **Table 5.11**.

Table 5.11: Average M—N, M—O_{DTPA} and M—O_H bond lengths of BHLYP/def(2)-SVP-calculated [Eu/Am(DTPA)(H₂O)]²⁻ and Eu/Am(NH₂-DTPA)(H₂O) geometries. All values are in angstroms (Å).

Complex	$\bar{R}(\text{M} - \text{N})$	$\bar{R}(\text{M} - \text{O}_{\text{DTPA}})$	$R(\text{M} - \text{O}_{\text{H}})$
[Eu(DTPA)(H ₂ O)] ²⁻	2.73	2.37	2.58
[Am(DTPA)(H ₂ O)] ²⁻	2.76	2.42	2.65
Eu(NH ₂ -DTPA)(H ₂ O)	2.74	2.38	2.53
Am(NH ₂ -DTPA)(H ₂ O)	2.77	2.42	2.57

The average metal-nitrogen bond lengths in both DTPA complexes were found to be considerably longer than those of the BTP and BTPhen complexes, while the average metal-oxygen bond lengths were shorter and comparable with those of the hydrated nitrate complexes. Due to the use of COSMO during optimisation, these bond lengths are not directly comparable with the gas-phase structures optimised by Roy *et al.*,¹⁶⁹ however the BHLYP-calculated metal-DTPA bond lengths of the Am complexes were longer than those of the Eu complexes, by 0.01 – 0.05 Å, a greater difference than that seen for their B3LYP-optimised structures. The average Am— and Eu—DTPA bond lengths were in reasonable agreement with available experimental data for the Nd complex of DTPA, for which the average M—N and M—O_{DTPA} bond lengths were 2.72 and 2.43 Å, respectively.¹⁷⁵ Additionally, the NH₂-DTPA bond lengths were very similar to those of the DTPA ligand, longer by only ~0.01 Å, suggesting that the replacement of the OH groups with an amide group would have little effect on the metal-ligand bond lengths.

BHLYP/def(2)-TZVP SPE calculations were performed on these optimised complexes and used for further QTAIM and energetic analysis, the results of which are displayed in **Table 5.12** and **Table 5.13**.

Table 5.12: Topological and integrated properties of B3LYP/def(2)-TZVP//B3LYP/def(2)-SVP-calculated electron densities of [Eu/Am(DTPA)(H₂O)]²⁻ and Eu/Am(NH₂-DTPA)(H₂O).^a

Complex	$q(\text{M})$	$\bar{q}(\text{N})$	$\bar{q}(\text{O}_{\text{DTPA}})$	$N(\text{M}) - \lambda(\text{M})$	$\bar{\delta}(\text{M}, \text{N})$	$\bar{\rho}_{\text{BCP}}(\text{M}-\text{N})$	$\bar{\delta}(\text{M}, \text{O}_{\text{DTPA}})$	$\bar{\rho}_{\text{BCP}}(\text{M}-\text{O}_{\text{DTPA}})$
[Eu(DTPA)(H ₂ O)] ²⁻	2.34	-1.13	-1.37	1.01	0.149	0.0309	0.256	0.0554
[Am(DTPA)(H ₂ O)] ²⁻	2.31	-1.12	-1.37	1.17	0.178	0.0338	0.292	0.0570
$\Delta_{\text{Am/Eu}}$	-	-	-	16%	20%	9%	14%	3%
Eu(NH ₂ -DTPA)(H ₂ O)	2.35	-1.13	-1.35	1.01	0.149	0.0307	0.250	0.0544
Am(NH ₂ -DTPA)(H ₂ O)	2.32	-1.12	-1.35	1.16	0.173	0.0327	0.285	0.0558
$\Delta_{\text{Am/Eu}}$	-	-	-	15%	16%	7%	14%	3%

^a $N(\Omega)$ = integrated electron density in atomic basin Ω , $q(\Omega)$ = total charge of basin Ω , $\lambda(\Omega)$ = localisation index of basin Ω , $\bar{\rho}_{\text{BCP}}$ = mean magnitude of the electron density at the BCPs, $\bar{\delta}(\Omega_1, \Omega_2)$ = mean delocalisation index between atomic basins Ω_1 and Ω_2 and $\Delta_{\text{An/Ln}}$ = percentage by which a given metric is greater for An over Ln. B3LYP-derived values are given in parentheses. All values are in atomic units.

Compared to the BTP and BTPhen complexes, the absolute values of $\bar{\rho}_{\text{BCP}}$ and $\bar{\delta}$ for the M—N bonds in the DTPA complexes were found to be lower in both of the DTPA complexes, while the comparatively larger absolute values for the M—O_{DTPA} bonds were found to be higher than in the hydrated nitrate complexes for both the nitrate and water oxygens. The lower absolute M—N values correlate with the longer bond lengths found for the DTPA complexes. As seen by Roy *et al.*,¹⁶⁹ the absolute values of ρ were greater in the M—O bonds than in the M—N bonds. However, in terms of relative measures the $\Delta\bar{\rho}_{\text{Am/Eu}}$ value is high for the M—N bonds, at 9% for the DTPA complex and 7% for the NH₂-DTPA complex, and the low values of 3% for the M—O bonds in both of the complexes brings the overall relative increase of ρ in the Am complexes down to 4% for both the DTPA and NH₂-DTPA complexes, below that for the BTP and BTPhen complexes. The same is true for the relative $\bar{\delta}$ values, which decrease to 16% and 15% for the DTPA and NH₂-DTPA complexes, respectively. This suggests that the use of the softer N-donor ligands for An^{III}/Ln^{III} separation is preferable over the hard O- or mixed O/N-donor ligands.

Table 5.13: SCF energies of reactions **5p-5t**, calculated using a B3LYP/def(2)-TZVP//B3LYP/def(2)-SVP model chemistry.

	Reaction	E_r (eV)
5p	[Eu(DTPA)(H ₂ O)] ²⁻ + [Am(H ₂ O) ₉] ³⁺ → [Eu(H ₂ O) ₉] ³⁺ + [Am(DTPA)(H ₂ O)] ²⁻	0.02
5q	[Eu(NH ₂ -DTPA)(H ₂ O)] ²⁻ + [Am(H ₂ O) ₉] ³⁺ → [Eu(H ₂ O) ₉] ³⁺ + [Am(NH ₂ -DTPA)(H ₂ O)] ²⁻	0.01
5r	[Eu(DTPA)(H ₂ O)] ²⁻ + Am(NO ₃) ₃ (H ₂ O) ₃ → Eu(NO ₃) ₃ (H ₂ O) ₃ + [Am(DTPA)(H ₂ O)] ²⁻	-0.05
5s	[Eu(NH ₂ -DTPA)(H ₂ O)] ²⁻ + Am(NO ₃) ₃ (H ₂ O) ₃ → Eu(NO ₃) ₃ (H ₂ O) ₃ + [Am(NH ₂ -DTPA)(H ₂ O)] ²⁻	-0.07
5t	[Eu(DTPA)(H ₂ O)] ²⁻ + [Am(NH ₂ -DTPA)(H ₂ O)] ²⁻ → [Eu(NH ₂ -DTPA)(H ₂ O)] ²⁻ + [Am(DTPA)(H ₂ O)] ²⁻	0.02

As well as exhibiting lower overall relative actinide covalency, the exchange reaction energies for reactions **5p-5s** show lower energetic favourability for the actinides than the BTP and BTPPhen ligands. The exchange reaction energies for the DTPA and NH₂-DTPA ligands with Eu/Am(NO₃)₃(H₂O)₃ were found to be -0.05 and -0.07 eV respectively, compared to -0.09 eV for BTP and -0.26 eV for BTPPhen.

5.9.2 Texaphyrin Results

Complexes of Am and Eu with a single texaphyrin ligand were optimised at the BHLYP/def(2)-SVP level, with two nitrate counterions and one water molecule also bound to the metal ion to maximise the coordination number, using the crystal structures of Ln^{III} texaphyrins reported by Sessler *et al.* as a guide.¹⁷¹ Average metal-ligand bond lengths for the optimised Eu/Am(Tex)(NO₃)₂(H₂O) complexes are shown in **Table 5.14**.

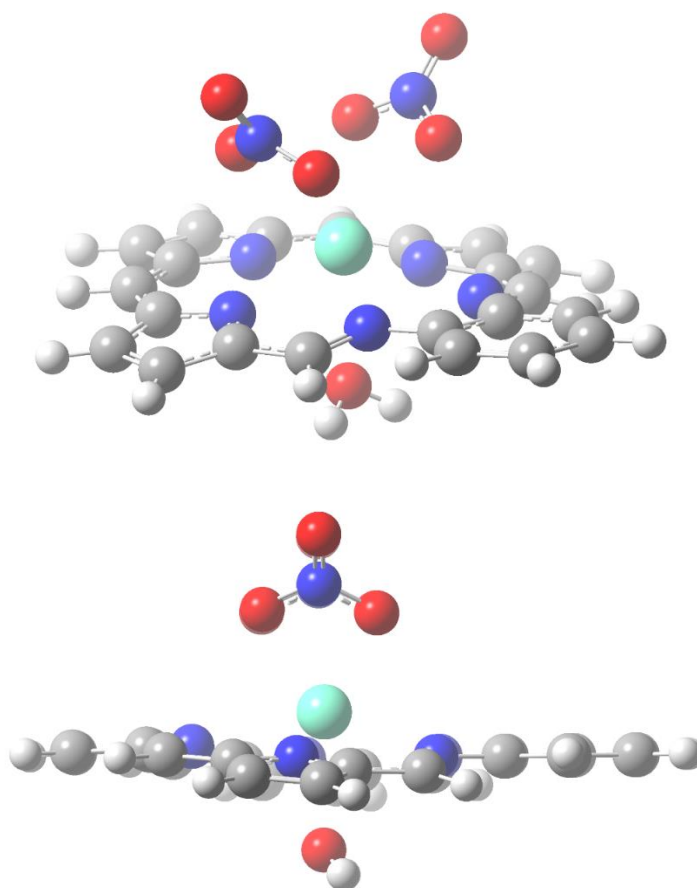


Figure 5.14: Optimised BHLYP/def(2)-SVP Eu(Tex)(NO₃)₂(H₂O) complex. Multiple viewing angles are shown, and the structure is also representative of the Am complex.

Table 5.14: Average M—N, M—O_N and M—O_H bond lengths of BHLYP/def(2)-SVP- and B3LYP/def(2)-SVP-calculated Eu/Am(Tex)(NO₃)₂(H₂O) geometries. All values are in angstroms (Å).

Complex	$\bar{R}(\text{M} - \text{N})$	$\bar{R}(\text{M} - \text{O}_\text{N})$	$R(\text{M} - \text{O}_\text{H})$
Eu(Tex)(NO ₃) ₂ (H ₂ O)	2.53	2.57	2.54
Am(Tex)(NO ₃) ₂ (H ₂ O)	2.55	2.61	2.61

While Sessler *et al.* reported a coordination number of 9 for the Eu^{III} complex with a single texaphyrin ligand,¹⁷¹ the two nitrate ligands remained bidentate in the optimised complex, retaining the initial coordination number of 10. The average metal-nitrogen bond length of 2.53 Å for the Eu complex was in reasonable agreement with the literature average of 2.47 Å reported by Sessler *et al.* for a similar Eu^{III} texaphyrin complex.¹⁷¹ The average bond lengths for the Am complexes were again found to be slightly longer than those of the Eu complexes, by 0.02 Å for the metal-nitrogen bond lengths, the same difference seen for the BTP and BTPPhen complexes. Average metal-nitrogen bond lengths were found to be shorter than in both the BTP and BTPPhen complexes by 0.08 Å and 0.04-0.05 Å respectively. However, due to the nature of the texaphyrin ligand, there was more variance in the metal-nitrogen bond lengths. In the Eu complex, the shortest two of these bond lengths were 2.45 Å (N₂, N₃, **Figure 5.12**), the longest two were 2.62 Å (N₄, N₅, **Figure 5.12**), and the last was inbetween at 2.52 Å (N₁, **Figure 5.12**). This pattern was also observed for the bond lengths of the Am complex. The average metal-oxygen bond lengths for the nitrate ligands was found to be within 0.01-0.02 Å of those of the hydrated nitrate complexes, while the metal-water bond length was much longer than in the aquo complexes, by 0.08-0.11 Å, likely due to the large steric bulk of the texaphyrin ligand.

To investigate whether enhanced actinide covalency is seen in the texaphyrin ligand, QTAIM and further DFT analysis was carried out using electron densities and energies from BHLYP/def(2)-TZVP SPE calculations performed on these optimised structures. The QTAIM metrics and exchange reaction energies for the Eu/Am(Tex)(NO₃)₃(H₂O) complexes are shown in **Table 5.15** and **Table 5.16**, respectively.

Table 5.15: Topological and integrated properties of B3LYP/def(2)-TZVP//B3LYP/def(2)-SVP-calculated electron densities of Eu/Am(Tex)(NO₃)₂(H₂O).^a

Complex	$q(\text{M})$	$\bar{q}(\text{N})$	$\bar{q}(\text{O}_\text{N})$	$N(\text{M}) - \lambda(\text{M})$	$\bar{\delta}(\text{M}, \text{N})$	$\bar{\rho}_{\text{BCP}}(\text{M}-\text{N})$
Eu(Tex)(NO ₃) ₂ (H ₂ O)	2.33	-1.34	-0.67	-1.01	0.220	0.0463
Am(Tex)(NO ₃) ₂ (H ₂ O)	2.29	-1.34	-0.66	-1.19	0.263	0.0502
$\Delta_{\text{Am}/\text{Eu}}$	-	-	-	19%	19%	9%

^a $N(\Omega)$ = integrated electron density in atomic basin Ω , $q(\Omega)$ = total charge of basin Ω , $\lambda(\Omega)$ = localisation index of basin Ω , $\bar{\rho}_{\text{BCP}}$ = mean magnitude of the electron density at the BCPs, $\bar{\delta}(\Omega_1, \Omega_2)$ = mean delocalisation index between atomic basins Ω_1 and Ω_2 and $\Delta_{\text{An}/\text{Ln}}$ = percentage by which a given metric is greater for An over Ln. B3LYP-derived values are given in parentheses. All values are in atomic units.

Table 5.16: SCF energies of reactions **5u** and **5v**, calculated using a B3LYP/def(2)-TZVP//B3LYP/def(2)-SVP model chemistry.

Reaction		E_r (eV)
5u	$\text{Eu(Tex)(NO}_3)_3(\text{H}_2\text{O}) + [\text{Am(H}_2\text{O)}_9]^{3+} \rightarrow [\text{Eu(H}_2\text{O)}_9]^{3+} + \text{Am(Tex)(NO}_3)_3(\text{H}_2\text{O})$	-0.06
5v	$\text{Eu(Tex)(NO}_3)_3(\text{H}_2\text{O}) + \text{Am(NO}_3)_3(\text{H}_2\text{O)}_3 \rightarrow \text{Eu(NO}_3)_3(\text{H}_2\text{O)}_3 + \text{Am(Tex)(NO}_3)_3(\text{H}_2\text{O})$	-0.13

The absolute values of $\bar{\rho}_{\text{BCP}}$ and $\bar{\delta}$ for the metal-nitrogen bonds were found to be larger for the texaphyrin complexes than in the BTP and BTPhen complexes by almost 50% for both the Eu and Am complexes; however, this correlates with the shorter bond lengths of the texaphyrin complexes. The relative values, $\Delta\bar{\rho}_{\text{Am}/\text{Eu}}$ and $\Delta\bar{\delta}_{\text{Am}/\text{Eu}}$, were found to be slightly higher than that of the BTPhen ligand, at 19% and 9% respectively. However, this enhanced covalency was not matched with enhanced stability, as the exchange reaction energies for the texaphyrin complexes were found to be less in favour of actinide complex formation than the BTPhen ligand, by 0.13 eV.

As mentioned earlier, and as discussed by Lan *et al.*, Am shows a reduced complexation ability with nitrates.^{52–54} This suggests that the nitrates in the texaphyrin complexes (and also the BTPhen complexes, as mentioned earlier) mask the selectivity of the ligand for the actinide. To investigate the selectivity of the texaphyrin ligand further without any competing nitrates, a dimer complex was considered, with no nitrate or water molecules bound to the metal ions. While no such complex has been reported in literature, there are many examples of lanthanide sandwich complexes with the porphyrins,^{176–181} and both the lanthanides and actinides have been shown to form sandwich molecules, such as the actinocenes.^{182–186} While this 10-coordinate nitrogen donor system was expected to display enhanced covalency, as in the

mono-texaphyrin complex, this system provided a further opportunity to investigate whether this leads to enhanced stability.

Optimisations of two orientations of the dimer complex were attempted at the BLYP/def(2)-SVP level, with the two texaphyrin ligands oriented with the six-membered rings either on the same 'end' of the complex or at opposite ends. The latter complex was lowest in energy, and was reoptimized with the B3LYP and BHLYP xc-functionals. The B3LYP-optimised complexes of Eu and Am and the BHLYP-optimised complex of Am converged successfully, however the BHLYP-optimised complex of Eu suffered from severe spin contamination and struggled to converge. To obtain BHLYP-derived QTAIM metrics and exchange reaction energies, BHLYP/def(2)-TZVP SPE calculations were performed on the B3LYP-optimised geometries. Bond lengths, QTAIM metrics and exchange reaction energies for the optimised $[\text{Eu}/\text{Am}(\text{Tex})_2]^+$ complexes are shown in **Tables 5.17** and **5.18**.

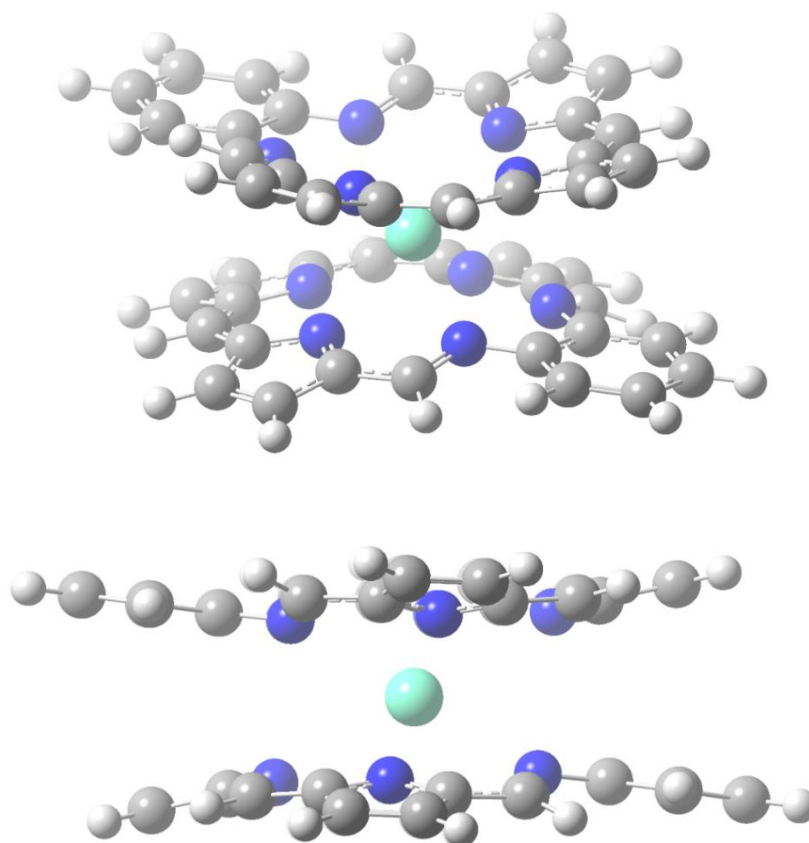


Figure 5.15: B3LYP/def(2)-SVP-optimised $[\text{Eu}(\text{Tex})_2]^+$ complex. General structure is also representative of the Am complex.

Table 5.17: Topological and integrated properties of BHLYP/def(2)-TZVP//B3LYP/def(2)-SVP-calculated electron densities of [Eu/Am(Tex)₂]⁺.^a

Complex	$q(M)$	$\bar{q}(N)$	$N(M) - \lambda(M)$	$\bar{\delta}(M, N)$	$\bar{\rho}_{BCP}(M-N)$
[Eu(Tex) ₂] ⁺	2.39	-1.28	0.831	0.148	0.0266
[Am(Tex) ₂] ⁺	2.33	-1.27	0.995	0.178	0.0304
$\Delta_{Am/Eu}$	-	-	20%	20%	14%

^a $N(\Omega)$ = integrated electron density in atomic basin Ω , $q(\Omega)$ = total charge of basin Ω , $\lambda(\Omega)$ = localisation index of basin Ω , $\bar{\rho}_{BCP}$ = mean magnitude of the electron density at the BCPs, $\bar{\delta}(\Omega_1, \Omega_2)$ = mean delocalisation index between atomic basins Ω_1 and Ω_2 and $\Delta_{An/Ln}$ = percentage by which a given metric is greater for An over Ln. B3LYP-derived values are given in parentheses. All values are in atomic units.

Table 5.18: SCF energies of reactions **5w-5z**, calculated using a BHLYP/def(2)-TZVP//B3LYP/def(2)-SVP model chemistry.

	Reaction	E_r (eV)
5w	[Eu(Tex) ₂] ⁺ + [Am(H ₂ O) ₉] ³⁺ → [Eu(H ₂ O) ₉] ³⁺ + [Am(Tex) ₂] ⁺	-0.29
5x	[Eu(Tex) ₂] ⁺ + Am(NO ₃) ₃ (H ₂ O) ₃ → Eu(NO ₃) ₃ (H ₂ O) ₃ + [Am(Tex) ₂] ⁺	-0.37
5z	[Eu(Tex) ₂] ⁺ + Am(Tex)(NO ₃) ₃ (H ₂ O) → Eu(Tex)(NO ₃) ₃ (H ₂ O) + [Am(Tex) ₂] ⁺	-0.24

The average metal-nitrogen bond lengths in the texaphyrin dimers were found to be far longer than in the mono-texaphyrin, BTP and BTPPhen complexes and also found to be the same for both Eu and Am, at 2.79 Å. However, individual bond lengths varied between ions due to the ligands moving in opposite directions in the same plane. While the average M—N bond lengths were the same for Eu and Am, individual bond lengths differed. In the Am complex the M—N₁ bond lengths were 0.05 Å longer, while the M—N₄ and M—N₅ bond lengths were 0.01 Å shorter.

In accordance with the longer bond lengths for the dimer complexes, the absolute values of $\bar{\rho}_{BCP}$ and $\bar{\delta}$ for the metal-nitrogen bonds were found to be smaller than in the mono-texaphyrin complexes. However, the relative values were not diminished by the decrease in bond length, and the values for $\Delta\bar{\rho}_{Am/Eu}$ and $\Delta\bar{\delta}_{Am/Eu}$ were found to be 14% and 20%. This value for the increase in $\bar{\rho}$ for the actinides over the lanthanides was far larger than for any other complex studied in this work. Furthermore, the exchange reaction energies for the dimer complexes were found to be very much in favour of actinide complex formation, at -0.37 for

reaction **5x**, which is 0.11 eV more in favour of the actinide than the analogous reaction for the BTPPhen ligand.[‡]

5.10 Part III: Conclusion

In **Part III** of this chapter, the stability and bonding nature of complexes of the TALSPEAK ligand DTPA and mono- and di-texaphyrin complexes has been investigated through QTAIM and energetic analysis, and compared to that of the BTPPhen and BTP complexes discussed earlier in this chapter and in **Chapter 4** respectively.

For the mixed oxygen and nitrogen donor DTPA complexes, there was found to be less overall enhanced covalency for the actinides over the lanthanides than in the BTP and BTPPhen complexes, evidenced by the low relative increase in $\bar{\rho}$ and $\bar{\delta}$ for the An—O_{DTPA} bonds over those for the Eu—O_{DTPA} bonds. As well as seeing less enhanced covalency for the actinide complexes of the DTPA ligands, SCF exchange reaction energies calculated for the DTPA and NH₂-DTPA complexes were found to be 0.04 and 0.05 eV less in favour of actinide complexation than the BTP ligand, which lends further evidence to the thought that enhanced covalency implies enhanced stability.

While the texaphyrin ligand is not currently employed as an An^{III}/Ln^{III} separation ligand, it is known to coordinate to the trivalent lanthanides. The QTAIM and energetic analysis of the mono-texaphyrin complexes presented here suggests that there is enhanced covalency in actinide complexes with texaphyrin compared to their lanthanide analogues, to an extent similar to that of the BTPPhen ligand. Furthermore, analysis of a novel di-texaphyrin complex exhibits a level of enhanced covalency with the actinides which surpasses that of BTPPhen, and indeed any other complex presented in this work, with a $\Delta\bar{\rho}_{Am/Eu}$ value of 14%, compared to 9% for BTPPhen, matched with exchange reaction energies which are 0.11 eV more in favour of actinide complexation than the BTPPhen ligand, again demonstrating an enhanced stability which correlates with enhanced covalency.

[‡] It should be noted that the [Eu/Am(Tex)₂]⁺ exchange reaction energies are calculated at the BHLYP/def(2)-TZVP//B3LYP/def(2)-SVP level, while the [Eu/Am(BTPPhen)₂(NO₃)₂]²⁺ reaction energies were calculated at the BHLYP/def(2)-TZVP//BHLYP/def(2)-SVP level. However, reaction energies were calculated at the BHLYP/def(2)-TZVP//B3LYP/def(2)-SVP level for the Eu/Am(Tex)(NO₃)₂(H₂O) complexes and were found to be only 0.01 eV less in favour of actinide complexation.

5.11 Electron Density vs. Bond Path Length Revisited

The results of the texaphyrin complexes prompted the earlier short study of the relationship between electron density and bond path length to be revisited, due to the much shorter and longer bond lengths of the mono- and di-texaphyrin complexes, respectively. A second plot of ρ_{BCP} against bond path length is shown in **Figure 5.16**.

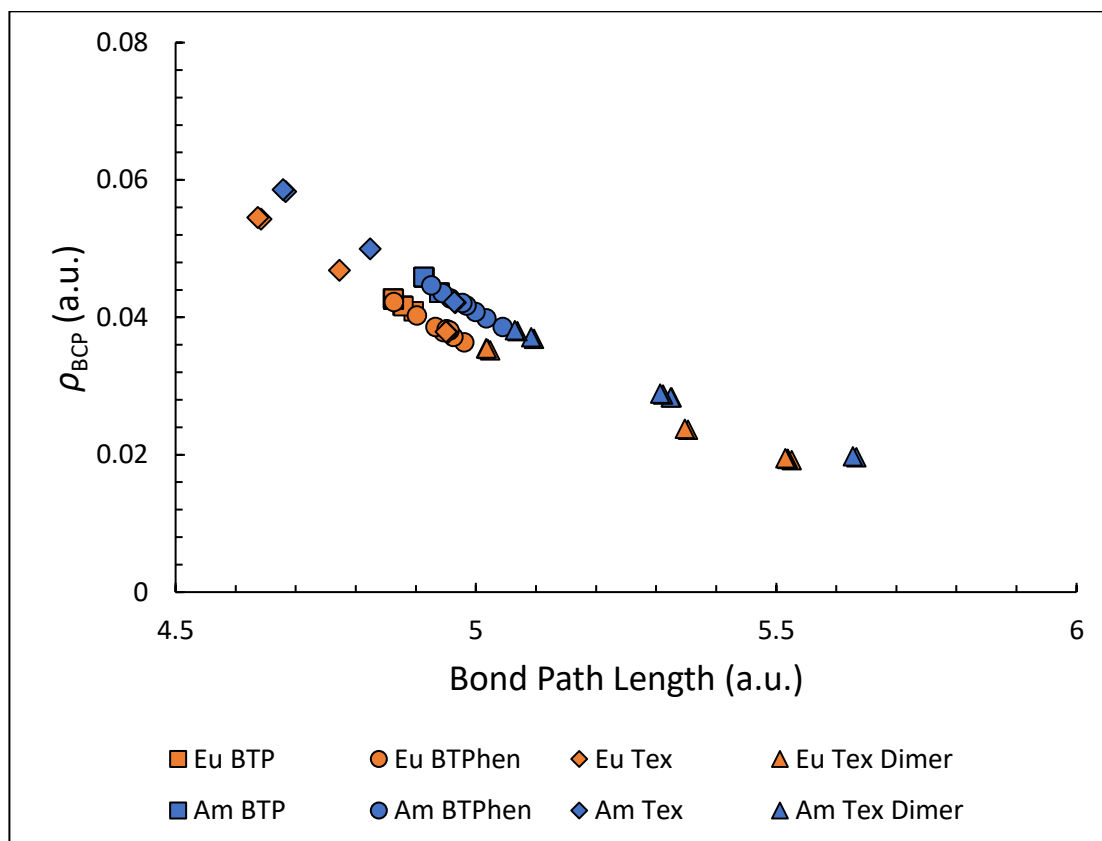


Figure 5.16: Plot of ρ_{BCP} against bond path length for $[\text{Eu}/\text{Am}(\text{BTP})_3]^{3+}$, $[\text{Eu}/\text{Am}(\text{BTPhen})_2(\text{NO}_3)_2]^{2+}$, $[\text{Eu}(\text{Tex})_2]^+$ and $\text{Am}(\text{Tex})(\text{NO}_3)_3(\text{H}_2\text{O})$.

As seen for the BTP and BTPhen ligands previously, the correlation between ρ_{BCP} and the bond path length is largely independent of the ligand for the texaphyrin complexes also.

5.12 General Conclusions

In this chapter, the relationship between enhanced covalency and stability has been explored further, by investigating the BTPPhen, DTPA and texaphyrin ligands. In **Part I** of this chapter, the BTPPhen ligand was compared to the BTP ligand and was found to display slightly higher values of $\Delta\bar{\rho}_{\text{Am/Eu}}$ and $\Delta\bar{\delta}_{\text{Am/Eu}}$ and SCF exchange reaction energies which were 0.17 eV more in favour of actinide complexation. Additionally, the hydrated nitrate complexes of Am and Eu were optimised and were found to favour lanthanide complexation, which results in exchange reaction energies for the separation ligands which are more in favour of actinide complexation when the aquo complexes of the previous chapter are replaced with hydrated nitrate complexes.

In **Part II**, several modifications of the BTPPhen ligand were investigated, specifically the addition of bromo and 4-hydroxyphenyl groups to the phenanthroline moiety. For the lone ligands, small changes in q , λ and N were seen for the binding nitrogens of substituted ligands compared to the parent ligand, however this did not result in any appreciable difference between either the magnitudes or relative Am/Eu values of the topological and integrated properties of the electron density in the complexes of these ligands with Am and Eu compared to the complexes of the parent BTPPhen ligand. A decrease in the energetic favourability was observed for both the dibromo- and (4-hydroxyphenyl)-substituted ligands, implying a different origin to any increased selectivity seen experimentally for these ligands.

In **Part III**, the DTPA and texaphyrin ligands were investigated, and found to both display enhanced covalency and stability for Am over Eu. For the mixed oxygen and nitrogen donor DTPA ligands, the overall increase in covalency for Am over Eu was found to be less than that of the BTP and BTPPhen ligands, with lower reaction energies to match, while a sandwich complex of two texaphyrin ligands was found to display both a larger increase in covalency and higher reaction energies than any of the other ligands studied in this thesis.

Chapter 6: Conclusions

The aim of this thesis was to investigate the bonding nature and selectivity of ligands employed for the separation of the trivalent lanthanides and actinides using computational methods (DFT, QTAIM). In **Chapter 3**, the trinitrate and hydrated nitrate complexes of the La, Gd, Lu and Cm were optimised with DFT and DFT-calculated binding energies were benchmarked against MP2 to test the methodology before applying it to the larger complexes of the separation ligands. Calculations using RECPs and the BHLYP functional were found to be in best agreement with MP2, and a functional dependency was observed: complexes optimised with the 'pure' GGA xc-functionals (PBE, BLYP, TPSS) exhibited high degrees of spin contamination, which was reduced with the hybrid-GGA xc-functionals as the degree of exact Hartree-Fock exchange in the functional increased. For the hydrated nitrate complexes, maximum coordination numbers of 11, 10, 10 and 10 were found for La, Gd, Lu and Cm respectively at the BHLYP/def(2)-SVP level in the presence of a continuum solvent. From these results, the B3LYP and BHLYP functionals were chosen to model the larger, and hence more expensive, complexes of the following chapters, and the hydrated nitrate complexes of Gd and Cm were later used to optimise the hydrated nitrate complexes of Eu and Am.

The nona-aquo and tris-BTP complexes of the trivalent lanthanides ($\text{Ln} = \text{Ce} - \text{Lu}$) and actinides ($\text{An} = \text{Cm}, \text{Am}$) were investigated in **Chapter 4**. The QTAIM was applied in a systematic study of Ln bond characterisation across the series for both the nona-aquo and tris-BTP complexes, confirming the general assumption that the bonding in these complexes is ionic in character and largely similar, observing a low value for $\bar{\rho}_{\text{BCP}}$ for all Ln and only a small variation across the series. For the An complexes of BTP, a small yet significant increase in $\bar{\rho}_{\text{BCP}}$ was observed compared to the Ln complexes, which was 3 standard deviations larger than the mean Ln value, and the integrated properties of the electron density also indicated enhanced covalency in the An complexes. This increase was also larger than that seen in the nona-aquo complexes, and implies a small electronic contribution to the selectivity found experimentally for the BTP ligand. SCF reaction energies for the exchange reaction between the nona-aquo and tris-BTP complexes were evaluated, revealing the Eu/Am and Gd/Cm exchange reactions to favour the An species, evidence of weak selectivity of the BTP ligand for An over Ln.

Chapter 5 is comprised of three parts. In **Part I**, the bonding nature in the Eu and Am complexes of BTP_{phen} was investigated and compared with those of BTP. QTAIM analysis revealed lower absolute values of $\bar{\rho}_{\text{BCP}}$ in the BTP_{phen} complexes than in the BTP complexes, but slightly larger relative measures of covalency, i.e. a larger percentage increase of $\bar{\rho}_{\text{BCP}}$ for

the Am complexes over the Eu complexes. Exchange reaction energies were evaluated for the BTP and BTPhen complexes, finding BTPhen to be more selective for Am over Eu than the BTP ligand by ~ 0.17 eV at the SCF level. The hydrated nitrate complexes of Am and Eu were also investigated, using the 9- and 10-coordinate hydrated nitrate complexes of Cm and Gd optimised in **Chapter 3** as a starting point. QTAIM analysis revealed the bonding in these complexes to be similar to the aquo complexes, and BHLYP-derived exchange reaction energies for the BTP and BTPhen ligands using the hydrated nitrates as a reference instead of the nona-aquo complexes shifted more in favour of the actinide for both separation ligands.

In **Chapter 5, Part II** several modifications of the BTPhen ligand were investigated, where the phenanthroline moiety of the ligand was functionalised with electron directing groups. A small effect on the charges, localisation indices and total number of electrons for the binding nitrogens was observed, however this did not translate to either greater absolute or relative measures of covalency in the QTAIM analysis of the complexes of these ligands. Exchange reaction energies for these complexes were found to be less than that of the parent BTPhen ligand, implying a different origin to any increase in selectivity seen for these substituted ligands.

The mixed O/N-donor ligand DTPA and the N-donor texaphyrin ligand were investigated in **Chapter 5, Part III**. Unlike the other ligands investigated in this work, these ligands are not used or proposed for use in the SANEX process. DTPA is a ligand used in the TALSPEAK separation process, and texaphyrins are not currently used for separation but are known to complex the trivalent lanthanides. QTAIM analysis of the DTPA complexes revealed that while the relative measures of covalency for the M—N bonds were similar to those of BTP and BTPhen, the low relative increases for the M—O bonds brought the overall relative increase in the Am complexes down. Exchange reaction energies for the DTPA complexes were also found to be less in favour of An complexation than the BTP and BTPhen complexes.

For texaphyrin, complexes with a single ligand were optimised with nitrate and water molecules filling the first coordination sphere, based on examples from literature. QTAIM analysis of these mono-texaphyrin complexes revealed large absolute values of $\bar{\rho}_{BCP}$ and relative measures of covalency which were slightly higher than that of the BTPhen ligand. However, this was not matched with enhanced stability, as measured by the exchange reaction energies. As it was believed that the nitrate ligands complexed to the metal centre were masking the selectivity for the actinide, as the trinitrate complexes favour complexation with the lanthanide ion, a novel di-texaphyrin sandwich complex was optimised and analysed,

finding levels of enhanced covalency which were greater than any other complex investigated in this work, and exchange reaction energies 0.11 eV more in favour of actinide complexation than BTPPhen.

A theme of this work has been whether enhanced covalency implies enhanced stability. This relationship has been demonstrated on several occasions: exchange reaction energies for BTP with water and nitrates favours BTP complexation of the actinides, and relative measures of covalency in the BTP complexes are greater than those in the nona-aquo and hydrated nitrate complexes. Reaction energies for BTPPhen are more in favour of actinide complexation than BTP, and relative measures of covalency in the BTPPhen complexes are slightly higher than in the BTP complexes. Reaction energies for DTPA are less in favour of actinide complexation than BTP, and relative measures of covalency are lower. Finally, the reaction energies for the di-texaphyrin complex were more in favour of actinide complexation than any other ligand studied, as were the relative measures of covalency in this complex. However, the relationship between enhanced covalency and stability was not universal: the mono-texaphyrin complex did not exhibit similar levels of stability to BTPPhen despite having similar measures of covalency; the relative measures of covalency in the BTPPhen complex were only slightly higher than those of BTP despite much larger reaction energies; and the modified BTPPhen ligands exhibited lower reaction energies than the parent BTPPhen ligand with no change in the relative measures of covalency. Additionally, another trend is apparent: the N-donor ligands (BTP, BTPPhen, texaphyrin) exhibit both greater relative measures of covalency and energetic favourability for An complexation than O- (water, nitrates) and mixed O/N-donor ligands (DTPA), in agreement with the general idea that 'softer' donor ligands are more selective for the actinides over the lanthanides.

It can be concluded that DFT calculations with hybrid-GGA *xc*-functionals and QTAIM analysis provide a useful and reliable method for assessing the covalent character and electronic stability of the Ln/An complexes. Further, the 'pure' GGA *xc*-functionals should be used with caution when applied to complexes of the f-elements, in particular those of Gd. The hybrid-GGA *xc*-functionals alleviate the spin contamination seen in the GGA-optimised complexes, though ideally multireference methods would be employed for study of these systems. While such simulations are not currently possible for systems of this size, recent advances make this ambition more realistic.

The DFT results presented in this work show evidence of the selectivity of several N- and mixed O/N-donor ligands for Am over Eu, and QTAIM analysis shows increased covalent bonding

character for the Am complexes over those of Eu. Further, it is argued that absolute measures of covalency are less important than relative measures of covalency, or the percentage by which the absolute measures of covalency are greater in the An complexes than in their Ln analogues. Overall, a tentative correlation between relative measures of enhanced covalency and stability has been demonstrated. Future theoretical work should aim to guide the synthesis of new ligands by investigating ways to enhance the covalent bonding character in the An complexes relative to that in the Ln complexes in order to maximise actinide selectivity. By doing so, the efficiency of solvent extraction technologies such as SANEX can be advanced, allowing for improved management of contaminated liquors.

In recent years, functionalised BTPPhen ligands have been designed with the aim of improving the actinide selectivity of the parent ligand through the addition of electron withdrawing/donating groups to the phenanthroline moiety. However, the QTAIM results presented in this thesis show that the addition of electron withdrawing/donating groups has a very small effect on the electron density at the binding nitrogens of the ligand which does not result in an increase in the amount of enhanced covalent character in the Am complexes over those of Eu, and DFT calculations show a decrease in the energetic preference for An complexation for the functionalised ligands. This highlights the importance of theoretical studies and how they can inform the synthesis of new and modified ligands for waste separation. In future, as only functionalisation of the phenanthroline moiety was investigated in this work, further experimental and theoretical studies could test the effects of substitution on the triazine moieties of the BTPPhen ligand with electron-directing groups. However, care must be taken to design such ligands without sacrificing the resistance to radiolysis and acid hydrolysis gained by the addition of groups such as CyMe₄.

Finally, it has been shown that while absolute measures of covalency in the M—O bonds of the complexes studied were greater than in the M—N bonds, relative measures of covalency were greatest in the M—N bonds. A novel texaphyrin sandwich complex was investigated, which had the most M—N bonds of those studied, 10, which is also the maximum coordination number found for Am and Eu. Of the complexes studied, this complex was found to have both the largest relative measures of covalency and to exhibit the greatest energetic preference for complexation with Am over Eu. This indicates that the field of An^{III}/Ln^{III} separation may be well served by attempted synthesis of the bis-texaphyrin sandwich complex. If synthesis of the sandwich complex is not possible, then other N-donor ligands which can achieve this level of coordination may be of interest.

Appendix A: Data used to Construct Graphs

Table A.1: Data used to construct **Figures 4.7i-4.7vi**; Mean values of ρ_{BCP} , $\nabla^2\rho_{\text{BCP}}$ and H_{BCP} at the Ln—O and Ln—N BCPs of $[\text{Ln}(\text{H}_2\text{O})_9]^{3+}$ and $[\text{Ln}(\text{BTP})_3]^{3+}$ (Ln = Ce – Lu), calculated with BHLYP. All values are given in a.u.

Ln	$[\text{Ln}(\text{H}_2\text{O})_9]^{3+}$, Ln—O			$[\text{Ln}(\text{BTP})_3]^{3+}$, Ln—N		
	$\bar{\rho}_{\text{BCP}}$	$\overline{\nabla^2\rho_{\text{BCP}}}$	\bar{H}_{BCP}	$\bar{\rho}_{\text{BCP}}$	$\overline{\nabla^2\rho_{\text{BCP}}}$	\bar{H}_{BCP}
Ce	0.0419	0.163	-8.34x10 ⁻⁴	0.0408	0.113	-3.36x10 ⁻³
Pr	0.0428	0.168	-9.97x10 ⁻⁴	0.0416	0.118	-3.45x10 ⁻³
Nd	0.0433	0.174	-1.03x10 ⁻³	0.0414	0.122	-3.28x10 ⁻³
Pm	0.0438	0.179	-1.03x10 ⁻³	0.0416	0.126	-3.19x10 ⁻³
Sm	0.0441	0.184	-1.02x10 ⁻³	0.0422	0.129	-3.32x10 ⁻³
Eu	0.0442	0.187	-9.91x10 ⁻⁴	0.0422	0.131	-3.29x10 ⁻³
Gd	0.0448	0.189	-7.98x10 ⁻⁴	0.0426	0.132	-3.42x10 ⁻³
Tb	0.0443	0.190	-1.00x10 ⁻³	0.0421	0.134	-3.25x10 ⁻³
Dy	0.0446	0.194	-1.13x10 ⁻³	0.0424	0.136	-3.45x10 ⁻³
Ho	0.0451	0.203	-8.74x10 ⁻⁴	0.0424	0.141	-3.11x10 ⁻³
Er	0.0455	0.209	-9.80x10 ⁻⁴	0.0424	0.143	-3.20x10 ⁻³
Tm	0.0453	0.209	-1.03x10 ⁻³	0.0424	0.143	-3.36x10 ⁻³
Yb	0.0453	0.212	-1.07x10 ⁻³	0.0422	0.147	-3.27x10 ⁻³
Lu	0.0456	0.214	-3.73x10 ⁻⁴	0.0427	0.148	-2.78x10 ⁻³
$\bar{\text{Ln}}$	0.0442	0.189	-9.83x10 ⁻⁴	0.0421	0.133	-3.27x10 ⁻³
MAD	8.1x10 ⁻⁴	0.013	6.9x10 ⁻⁵	4.1x10 ⁻⁴	8.7x10 ⁻³	1.1x10 ⁻⁴
MAD (%)	1.8	6.8	7.0	1.0	6.5	3.4

Table A.2: Data used to construct **Figures 4.8i-4.8vi**; Mean values of ρ_{BCP} , $\nabla^2\rho_{\text{BCP}}$ and H_{BCP} at the Ln—O and Ln—N BCPs of $[\text{Ln}(\text{H}_2\text{O})_9]^{3+}$ and $[\text{Ln}(\text{BTP})_3]^{3+}$ (Ln = Ce – Lu), calculated with B3LYP. All values are given in a.u.

Ln	$[\text{Ln}(\text{H}_2\text{O})_9]^{3+}$, Ln—O			$[\text{Ln}(\text{BTP})_3]^{3+}$, Ln—N		
	$\bar{\rho}_{\text{BCP}}$	$\overline{\nabla^2\rho}_{\text{BCP}}$	H_{BCP}	$\bar{\rho}_{\text{BCP}}$	$\overline{\nabla^2\rho}_{\text{BCP}}$	H_{BCP}
Ce	0.0405	0.1051	-0.0034	0.0418	0.1539	-0.0011
Pr	0.0411	0.1098	-0.0034	0.0427	0.1597	-0.0012
Nd	0.0412	0.1130	-0.0033	0.0432	0.1653	-0.0012
Pm	0.0407	0.1172	-0.0029	0.0437	0.1704	-0.0012
Sm	0.0416	0.1192	-0.0033	0.0439	0.1739	-0.0012
Eu	0.0416	0.1216	-0.0033	0.0440	0.1769	-0.0012
Gd	0.0415	0.1206	-0.0032	0.0428	0.1689	-0.0011
Tb	0.0415	0.1242	-0.0032	0.0440	0.1792	-0.0013
Dy	0.0415	0.1256	-0.0034	0.0442	0.1825	-0.0014
Ho	0.0419	0.1315	-0.0031	0.0447	0.1918	-0.0010
Er	0.0404	0.1277	-0.0029	0.0448	0.1955	-0.0011
Tm	0.0419	0.1350	-0.0033	0.0449	0.1972	-0.0012
Yb	0.0402	0.1307	-0.0030	0.0448	0.1998	-0.0013
Lu	0.0421	0.1373	-0.0028	0.0451	0.2014	-0.0006
$\bar{\text{Ln}}$	0.0413	0.1228	-0.0032	0.0439	0.1797	-0.0011
MAD	0.0005	0.0075	0.0002	0.0007	0.0128	0.0001
MAD (%)	1.2	6.1	6.3	1.6	7.1	9.1

Table A.3: Data used to construct **Figure 4.9**; Energies of **Reaction 4a** for Ln = Ce – Lu and An = Am, calculated using the B3LYP/def(2)-TZVP//B3LYP/def(2)-SVP and B3LYP/def(2)-TZVP//B3LYP/def(2)-SVP model chemistries. *[Ln(BTP)₃]³⁺ SPE obtained using the spin-constrained approach of Andrews *et al.*¹⁵⁸ †[Ln(BTP)₃]³⁺ and [Ln(H₂O)₉]³⁺ SPEs both obtained using the spin-constrained approach. Only reaction energies for An = Am are displayed; an identical trend is seen for An = Cm, shifted upward by 0.06 eV with B3LYP and down by 0.05 eV with B3LYP. An anomalous reaction energy for Ln = Pm is omitted for clarity.

Functional	Ce	Pr	Nd	Pm	Sm	Eu	Gd	Tb	Dy	Ho	Er	Tm	Yb	Lu
B3LYP	-0.16	-0.27	-0.04	-7.23	-0.06	-0.05	-0.07*	0.01 [†]	0.03 [†]	0.18	0.31	0.05	0.05	0.15
BHLYP	-0.33	-0.42	-0.10*	-9.57	-0.18	-0.01	-0.08	-0.14 [†]	-0.13 [†]	0.11	0.25	0.02	-0.01	0.04

Appendix B: Spin Contamination

Table B.1: Comparison between theoretical and calculated expectation values of \hat{S}^2 obtained for [Ln(H₂O)₉]³⁺ and [Ln(BTP)₃]³⁺ with the BLYP, B3LYP and BHLYP xc-functionals and the def(2)-SVP basis set.

Ln	S	$\langle \hat{S}^2 \rangle_{calc}$	$\langle \hat{S}^2 \rangle_{calc}$						
			[Ln(H ₂ O) ₉] ³⁺			[Ln(BTP) ₃] ³⁺			
			BLYP	B3LYP	BHLYP	BLYP	B3LYP	BHLYP	
Ce	1/2	0.75	0.75	0.75	0.75	0.75	0.75	0.75	0.75
Pr	1	2.00	2.00	2.00	2.00	2.00	2.00	2.00	2.00
Nd	3/2	3.75	3.75	3.75	3.75	3.76	3.75	3.75	3.75
Pm	2	6.00	6.01	6.00	6.00	6.03	6.01	6.00	6.00
Sm	5/2	8.75	8.78	8.76	8.75	8.87	8.76	8.75	8.75
Eu	3	12.00	12.05	12.01	12.01	12.21	12.01	12.01	12.01
Gd	7/2	15.75	16.08	15.96	15.76	16.12	15.87	15.76	15.76
Tb	3	12.00	-	12.60	12.60	13.03	12.56	12.56	12.56
Dy	5/2	8.75	-	9.27	9.25	9.48	9.23	9.20	9.20
Ho	2	6.00	6.00	6.00	6.00	6.00	6.00	6.00	6.00
Er	3/2	3.75	3.75	3.75	3.75	3.75	3.75	3.75	3.75
Tm	1	2.00	2.00	2.00	2.00	2.00	2.00	2.00	2.00
Yb	1/2	0.75	0.75	0.75	0.75	0.75	0.75	0.75	0.75
Lu	0	0	0	0	0	0	0	0	0

References

- (1) Baisden, P. A.; Choppin, G. R. In *Radiochemistry and Nuclear Chemistry in Encyclopedia of Life Support Systems (EOLSS)*; EOLSS: Oxford, UK, 2007; pp 228–289.
- (2) Natrajan, L.; Paden, M. H. L. In *Element Recovery and Sustainability*; 2013; pp 140–184.
- (3) Magill, J.; Berthou, V.; Haas, D.; Galy, J.; Schenkel, R.; Weise, H.; Heusener, G.; Tommasi, J.; Youinou, G. *Nucl. Energy J. Br. Nucl. Energy Soc.* **2003**, *42* (5), 263–277.
- (4) Choppin, G. R. *J. Less-Common Mater.* **1983**, *93*, 323–330.
- (5) Nash, K. *Solvent Extr. Ion Exch.* **1993**, *11* (4), 729–768.
- (6) Koch, L. *J. Less Common Met.* **1986**, *122*, 371–382.
- (7) Salvatores, M.; Palmiotti, G. *Prog. Part. Nucl. Phys.* **2011**, *66* (1), 144–166.
- (8) Actinide and fission product partitioning and transmutation, status and assessment report, OECD–Nuclear Energy Agency technical report, 1999.
- (9) Alstad, J.; Jahnsen, T.; Pappas, A. C. *J. Inorg. Nucl. Chem.* **1967**, *29* (9), 2155–2160.
- (10) Andreas Geist 2014, Actinide Separations Using N-Donor Compounds, PowerPoint presentation, Karlsruhe Institute of Technology, Karlsruhe.
- (11) McKibben, J. M. *Radiochim. Acta* **1984**, *36* (1–2), 3–15.
- (12) Kolarik, Z.; Müllich, U.; Gassner, F. *Solvent Extr. Ion Exch.* **1999**, *17* (1), 23–32.
- (13) Kolarik, Z.; Müllich, U.; Gassner, F. *Solvent Extr. Ion Exch.* **1999**, *17* (5), 1155–1170.
- (14) Hill, C.; Berthon, L.; Bros, P.; Dancausse, J.; Guillaneux, D. *Sanex-BTP process development studies*; 2003.
- (15) Kolarik, Z. *Chem. Rev.* **2008**, *108* (10), 4208–4252.
- (16) Lewis, F. W.; Hudson, M.; Harwood, L. *Synlett* **2011**, *2011* (18), 2609–2632.
- (17) Hudson, M. J.; Harwood, L. M.; Laventine, D. M.; Lewis, F. W. *Inorg. Chem.* **2013**, *52* (7), 3414–3428.
- (18) Weaver, B.; Kappelmann, F. A. *J. Inorg. Nucl. Chem.* **1968**, *30* (1), 263–272.
- (19) Cordier, P. Y.; Hill, C.; Baron, P.; Madic, C.; Hudson, M. J.; Liljenzin, J.-O. *J. Alloy. Compd.* **1998**, No. 271–273, 738.
- (20) Hagström, I.; Spjuth, L.; Enarsson, Å.; Liljenzin, J.-O.; Skålberg, M.; Hudson, M. J.; Iveson, P. B.; Madic, C.; Cordier, P. Y.; Hill, C.; Francois, N. *Solvent Extr. Ion Exch.* **1999**, *17*, 221.
- (21) Afsar, A.; Laventine, D. M.; Harwood, L. M.; Hudson, M. J.; Geist, A. *Chem. Commun. (Camb)*. **2013**, *49* (76), 8534–8536.
- (22) Drew, M. G. B.; Iveson, P. B.; Hudson, M. J.; Liljenzin, J.-O.; Spjuth, L.; Cordier, P. Y.; Enarsson, Å.; Hill, C.; Madic, C. *J. Chem. Soc., Dalt. Trans.* **2000**, 821.
- (23) Vitart, X.; Musikas, C.; Pasquiou, J. Y.; Hoel, P. **1986**, *122*, 275–286.
- (24) Mincher, B. J.; Modolo, G.; Mezyk, S. P. *Solvent Extr. Ion Exch.* **2009**, *27* (1), 1–25.

- (25) Mincher, B. J.; Modolo, G.; Mezyk, S. P. *Solvent Extr. Ion Exch.* **2009**, *27* (3), 331–353.
- (26) Mincher, B. J.; Modolo, G.; Mezyk, S. P. *Solvent Extr. Ion Exch.* **2009**, *27* (5–6), 579–606.
- (27) Mincher, B. J.; Modolo, G.; Mezyk, S. P. *Solvent Extr. Ion Exch.* **2010**, *28* (4), 415–436.
- (28) Trumm, S.; Geist, A.; Panak, P. J.; Fanghänel, T. *Solvent Extr. Ion Exch.* **2011**, *29* (2), 213–229.
- (29) Hudson, M. J.; Boucher, C. E.; Braekers, D.; Desreux, J. F.; Drew, M. G. B.; Foreman, M. R. S. J.; Harwood, L. M.; Hill, C.; Madic, C.; Marken, F.; Youngs, T. G. a. *New J. Chem.* **2006**, *30* (8), 1171.
- (30) Lewis, F. W.; Harwood, L. M.; Hudson, M. J.; Distler, P.; John, J.; Stamberg, K.; Núñez, A.; Galán, H.; Espartero, A. G. *European J. Org. Chem.* **2012**, *2012* (8), 1509–1519.
- (31) Foreman, M. R. S. J.; Hudson, M. J.; Geist, A.; Madic, C.; Weigl, M. *Solvent Extr. Ion Exch.* **2005**, *23* (5), 645–662.
- (32) Geist, A.; Hill, C.; Modolo, G.; Foreman, M. R. S. J.; Weigl, M.; Gompper, K.; Hudson, M. J. *Solvent Extr. Ion Exch.* **2006**, *24* (4), 463–483.
- (33) Lewis, F. W.; Harwood, L. M.; Hudson, M. J.; Drew, M. G. B.; Hubscher-Bruder, V.; Videva, V.; Arnaud-Neu, F.; Stamberg, K.; Vyas, S. *Inorg. Chem.* **2013**, *52* (9), 4993–5005.
- (34) Lewis, F. W.; Harwood, L.; Hudson, M. J.; Drew, M. G. B.; Desreux, J.; Vidick, G.; Bouslimani, N.; Modolo, G.; Wilden, A.; Sypula, M.; Vu, T.-H.; Simonin, J.-P. *J. Am. Chem. Soc.* **2011**, *133*, 13093–13102.
- (35) Magnusson, D.; Christiansen, B.; Foreman, M. R. S.; Geist, A.; Glatz, J.-P.; Malmbeck, R.; Modolo, G.; Serranol-Purroy, D.; Sorel, C. *Solvent Extr. Ion Exch.* **2009**, *27* (2), 97–106.
- (36) Bhattacharyya, A.; Gadly, T.; Mohapatra, P. K.; Ghosh, S. K.; Manna, D.; Ghanty, T. K.; Manchanda, V. K. *RSC Adv.* **2012**, *2* (18), 7066.
- (37) Denecke, M. a.; Panak, P. J.; Burdet, F.; Weigl, M.; Geist, A.; Klenze, R.; Mazzanti, M.; Gompper, K. *Comptes Rendus Chim.* **2007**, *10* (10–11), 872–882.
- (38) Banik, N. L.; Schimmelpfennig, B.; Marquardt, C. M.; Brendebach, B.; Geist, A.; Denecke, M. a. *Dalton Trans.* **2010**, *49* (0).
- (39) Banik, N. L.; Denecke, M. a.; Geist, A.; Modolo, G.; Panak, P. J.; Rothe, J. *Inorg. Chem. Commun.* **2013**, *29*, 172–174.
- (40) Steppert, M.; Walther, C.; Geist, A.; Fanghänel, T. *New J. Chem.* **2009**, *33* (12), 2437.
- (41) Trumm, S.; Panak, P. J.; Geist, A.; Fanghänel, T. *Eur. J. Inorg. Chem.* **2010**, *2010* (19), 3022–3028.
- (42) Trumm, S.; Lieser, G.; Foreman, M. R. S. J.; Panak, P. J.; Geist, A.; Fanghänel, T. *Dalton Trans.* **2010**, *39* (3), 923–929.
- (43) Adam, C.; Kaden, P.; Beele, B. B.; Müllich, U.; Trumm, S.; Geist, A.; Panak, P. J.; Denecke, M. a. *Dalton Trans.* **2013**, *42* (39), 14068–14074.
- (44) Apostolidis, C.; Schimmelpfennig, B.; Magnani, N.; Lindqvist-Reis, P.; Walter, O.; Sykora, R.; Morgenstern, A.; Colineau, E.; Caciuffo, R.; Klenze, R.; Haire, R. G.; Rebizant, J.; Bruchertseifer, F.; Fanghänel, T. *Angew. Chem. Int. Ed. Engl.* **2010**, *49* (36), 6343–6347.
- (45) Apostolidis, C.; Schimmelpfennig, B.; Magnani, N.; Lindqvist-Reis, P.; Walter, O.; Sykora,

- R.; Morgenstern, A.; Colineau, E.; Caciuffo, R.; Klenze, R.; Haire, R. G.; Rebizant, J.; Bruchertseifer, F.; Fanghänel, T. *Angew. Chemie* **2010**, *122* (36), 6487–6491.
- (46) Gaigalas, G.; Gaidamauskas, E.; Rudzikas, Z.; Magnani, N.; Caciuffo, R. *Phys. Rev. A* **2009**, *79* (2), 22511.
- (47) Guillaumont, D. *J. Phys. Chem. A* **2004**, *108*, 6893–6900.
- (48) Gutierrez, F.; Rabbe, C.; Poteau, R.; Daudey, J. P. *J. Phys. Chem. A* **2005**, *109* (19), 4325–4330.
- (49) Denecke, M. A.; Panak, P. J.; Weigl, M.; Schimmelpfennig, B.; Geist, A. *Inorg. Chem.* **2005**, *44* (23), 8418–8425.
- (50) Petit, L.; Adamo, C.; Maldivi, P. *Inorg. Chem.* **2006**, *45* (21), 8517–8522.
- (51) Banik, N. L.; Schimmelpfennig, B.; Marquardt, C. M.; Brendebach, B.; Geist, A.; Denecke, M. a. *Dalton Trans.* **2010**, *49* (0).
- (52) Lan, J.-H.; Shi, W.-Q.; Yuan, L.-Y.; Zhao, Y.-L.; Li, J.; Chai, Z.-F. *Inorg. Chem.* **2011**, *50* (19), 9230–9237.
- (53) Lan, J.-H.; Shi, W.-Q.; Yuan, L.-Y.; Feng, Y.-X.; Zhao, Y.-L.; Chai, Z.-F. *J. Phys. Chem. A* **2012**, *116* (1), 504–511.
- (54) Lan, J.-H.; Shi, W.-Q.; Yuan, L.-Y.; Li, J.; Zhao, Y.-L.; Chai, Z.-F. *Coord. Chem. Rev.* **2012**, *256* (13–14), 1406–1417.
- (55) Trumm, M.; Schimmelpfennig, B.; Geist, A. **2015**, *60* (August), 847–851.
- (56) Cramer, C. J. *Essentials of Computational Chemistry Theories and Models, Second Edition*; John Wiley & Sons, Ltd, 2004.
- (57) Jensen, F. *Introduction to Computational Chemistry, Second Edition*; John Wiley & Sons, Ltd, 2007.
- (58) Bader, R. F. W. *Atoms in Molecules: A Quantum Theory*; Oxford University Press: Oxford, 1990.
- (59) Matta, C. F.; Boyd, R. J. *An Introduction to the Quantum Theory of Atoms in Molecules*; 2007.
- (60) Fowles, G. R. *Am. J. Phys.* **1962**, *30* (308).
- (61) Born, M.; Oppenheimer, R. *Ann. Phys.* **1927**, *84*, 457.
- (62) Hartree, D. R. *Proc. Cambridge Phil. Soc.* **1928**, *24*, 426.
- (63) Slater, J. C. *Phys. Rev.* **1930**, *35*, 509.
- (64) Hückel, E. *Z. Phys.* **1931**, *70*, 204.
- (65) Møller, C.; Plesset, M. S. *Phys. Rev.* **1934**, *46*, 618.
- (66) Fermi, E. *Rend. Accad. Naz. Lincei* **1927**, *6*, 602–607.
- (67) Thomas, L. H. *Math. Proc. Cambridge Philos. Soc.* **1927**, *23*, 542–548.
- (68) Hohenberg, P.; Kohn, W. *Phys. Rev.* **1964**, *155*.
- (69) Kohn, W.; Sham, L. J. *Phys. Rev.* **1965**, *137*.

- (70) Sham, L. J.; Kohn, W. *Phys. Rev.* **1966**, *145*.
- (71) Sham, L. J.; Kohn, W. *Phys. Rev.* **1965**, *140*.
- (72) Perdew, J. P. *AIP Conf. Proc.* **2001**, *577* (May), 1–20.
- (73) Leeuwen, R. V. A. N.; Baerends, E. J. A. N. *Int. J. Quantum Chem.* **1994**, *52*, 711–730.
- (74) Gugelchuk, M. M.; Cui, Y. *J. Mol. Struct. THEOCHEM* **1996**, *365*, 111–117.
- (75) Perdew, J. P.; Wang, Y. *Phys. Rev. B* **1992**, *45* (23), 13244–13249.
- (76) Perdew, J. P.; Burke, K.; Ernzerhof, M. *Phys. Rev. Lett.* **1996**, *77* (18), 3865–3868.
- (77) Lee, C.; Yang, W.; Parr, R. G. *Phys. Rev. B* **1988**, *37* (2), 785–789.
- (78) Tao, J.; Perdew, J. P.; Staroverov, V.; Scuseria, G. *Phys. Rev. Lett.* **2003**, *91* (14), 146401.
- (79) Becke, A. D. *J. Chem. Phys.* **1993**, *98* (2), 1372–1377.
- (80) Becke, A. D. *Phys. Rev. A* **1988**, *38* (6), 3098–3100.
- (81) Vosko, S.; Wilk, L.; Nusair, M. *Can. J. Phys.* **1980**, *58* (8), 1200–1211.
- (82) Becke, A. D. *J. Chem. Phys.* **1993**, *98* (7), 5648–5652.
- (83) Perdew, J. P.; Ernzerhof, M.; Burke, K. *J. Chem. Phys.* **1996**, *105* (22), 9982.
- (84) Pyykkö, P. *Chem. Rev.* **1988**, *88*, 563–594.
- (85) Pyykkö, P. *Annu. Rev. Phys. Chem.* **2012**, *63* (1), 45–64.
- (86) Dirac, P. a. M. *Proc. R. Soc. A Math. Phys. Eng. Sci.* **1929**, *123* (792), 714–733.
- (87) Foldy, L. L.; Wouthuysen, S. A. *Phys. Rev.* **1950**, *78*, 29.
- (88) Reiher, M.; Wolf, A. *J. Chem. Phys.* **2004**, *121*, 2037–2047.
- (89) Reiher, M. *Wiley Interdiscip. Rev. Comput. Mol. Sci.* **2012**, *2* (1), 139–149.
- (90) Chang, C.; Pelessier, N.; Durand, M. *Phys. Scr.* **1986**, *34*, 294.
- (91) Faas, S.; Snijder, J. G.; van Lenthe, J. H.; van Lenthe, E.; Baerends, E. J. *Chem. Phys. Lett.* **1995**, *246*, 632.
- (92) Hülse, M.; Weigand, A.; Dolg, M. *Theor. Chem. Acc.* **2008**, *122* (1–2), 23–29.
- (93) Moritz, A.; Cao, X.; Dolg, M. *Theor. Chem. Acc.* **2006**, *117* (4), 473–481.
- (94) Stoll, H.; Metz, B.; Dolg, M. *J. Comput. Chem.* **2002**, *23* (8), 767–778.
- (95) Kerridge, A. *Chem. Commun.* **2017**, *53* (50), 6685–6695.
- (96) Lu, T.; Chen, F. *J. Comput. Chem.* **2012**, *33* (5), 580–592.
- (97) Bader, R. F. W. *J. Phys. Chem. a* **2009**, *113* (38), 10391–10396.
- (98) Ahlrichs, R.; Bär, M.; Häser, M.; Horn, H.; Kölmel, C. *Chem. Phys. Lett.* **1989**, *162* (3), 165–169.
- (99) Keith, T. A. TK Gristmill Software: Overland Park, KS, USA 2014.
- (100) Dennington, R.; Keith, T. A.; Millam, J. M. Semichem Inc.: Shawnee Mission, KS 2016.

- (101) Dobler, M.; Guilbaud, P.; Dedieu, A.; Wipff, G. *New. J. Chem.* **2001**, *25*, 1458–1465.
- (102) Dolg, M.; Stoll, H.; Preuss, H. *Theor. Chim. Acta* **1993**, *85*, 441–450.
- (103) Xi, J.; Lan, J.-H.; Lu, G.-W.; Zhao, Y.-L.; Chai, Z.-F.; Shi, W.-Q. *Mol. Simul.* **2014**, *40* (5), 379–386.
- (104) Dolg, M.; Stoll, H.; Savin, a.; Preuss, H. *Theor. Chim. Acta* **1989**, *75* (3), 173–194.
- (105) Cao, X.; Dolg, M. **2004**, *673*, 203–209.
- (106) Stuttgart-Dresden energy-consistent pseudopotentials, Stuttgart-Dresden energy-consistent pseudopotentials [Internet]. Available from: <http://www.tc.uni-koeln.de/PP/index.en.html>.
- (107) Eichkorn, K.; Weigend, F.; Treutler, O.; Ahlrichs, R. *Theor. Chem. Accounts Theory, Comput. Model. (Theoretica Chim. Acta)* **1997**, *97* (1–4), 119–124.
- (108) Weigend, F.; Ahlrichs, R. *Phys. Chem. Chem. Phys.* **2005**, *7* (18), 3297–3305.
- (109) Pantazis, D. a.; Neese, F. *J. Chem. Theory Comput.* **2011**, *7* (3), 677–684.
- (110) Pantazis, D. a.; Neese, F. *J. Chem. Theory Comput.* **2009**, *5* (9), 2229–2238.
- (111) Yang, J.; Dolg, M. *Theor. Chem. Acc.* **2005**, *113* (4), 212–224.
- (112) Cao, X.; Dolg, M. *Mol. Phys.* **2003**, *101* (15), 2427–2435.
- (113) Klamt, A.; Schüürmann, G. *Perkins Trans.* **1993**, *2*, 799–805.
- (114) Slater, J. C. *Phys. Rev.* **1935**, *81* (3), 385–390.
- (115) Staroverov, V. N.; Scuseria, G. E.; Tao, J.; Perdew, J. P. *J. Chem. Phys.* **2003**, *119* (23), 12129.
- (116) Panak, P. J.; Geist, A. *Chem. Rev.* **2013**, *113* (2), 1199–1236.
- (117) Colette, S.; Amekraz, B.; Madic, C.; Berthon, L.; Cote, G.; Moulin, C. *Inorg. Chem.* **2002**, *41* (26), 7031–7041.
- (118) Colette, S.; Amekraz, B.; Madic, C.; Berthon, L.; Cote, G.; Moulin, C. *Inorg. Chem.* **2004**, *43* (21), 6745–6751.
- (119) Ruff, C. M.; Müllich, U.; Geist, A.; Panak, P. J. *Dalton Trans.* **2012**, *41* (48), 14594–14602.
- (120) Beele, B. B.; Rüdiger, E.; Schwörer, F.; Müllich, U.; Geist, A.; Panak, P. J. *Dalton Trans.* **2013**, *42* (34), 12139–12147.
- (121) Berthet, J.-C.; Miquel, Y.; Iveson, P. B.; Nierlich, M.; Thuéry, P.; Madic, C.; Ephritikhine, M. *J. Chem. Soc. Dalt. Trans.* **2002**, *2* (16), 3265–3272.
- (122) Drew, M. G. B.; Guillaneux, D.; Hudson, M. J.; Iveson, P. B.; Russell, M. L.; Madic, C. *Inorg. Chem. Commun.* **2001**, *4* (1), 12–15.
- (123) Iveson, P. B.; Rivière, C.; Nierlich, M.; Thuéry, P.; Ephritikhine, M.; Guillaneux, D.; Madic, C. *Chem. Commun.* **2001**, 1512–1513.
- (124) de Sahb, C.; Watson, L. a; Nadas, J.; Hay, B. P. *Inorg. Chem.* **2013**, *52* (18), 10632–10642.
- (125) Yang, Y.; Hu, S.; Fang, Y.; Wei, H.; Hu, S.; Wang, D.; Yang, L.; Zhang, H.; Luo, S. *Polyhedron* **2015**, *95*, 86–90.

- (126) Zaiter, A.; Amine, B.; Bouzidi, Y.; Belkhiri, L.; Boucekkine, A.; Ephritikhine, M. *Inorg. Chem.* **2014**, *53* (9), 4687–4697.
- (127) Yang, Y.; Liu, J.; Yang, L.; Li, K.; Zhang, H.; Luo, S.; Rao, L. *Dalt. Trans.* **2015**, 8959–8970.
- (128) Bryantsev, V. S.; Hay, B. P. *Dalt. Trans.* **2015**, No. 44, 7935–7942.
- (129) Marie, C.; Miguiditchian, M.; Guillaumont, D.; Tosseng, A.; Berthon, C.; Guilbaud, P.; Duvail, M.; Bisson, J.; Guillaneux, D.; Pipelier, M.; Dubreuil, D. *Inorg. Chem.* **2011**, *50* (14), 6557–6566.
- (130) Trumm, M.; Schimmelpfennig, B. **2016**, *114* (6), 876–883.
- (131) Huang, Q.-R.; Kingham, J. R.; Kaltsoyannis, N. *Dalt. Trans.* **2015**, *44*, 2554–2566.
- (132) Woodall, S. D.; Swinburne, A. N.; Kerridge, A.; Pietro, P. Di; Adam, C.; Kaden, P.; Natrajan, L. S. *Chem. Commun.* **2015**, *51*, 5402–5405.
- (133) Di Pietro, P.; Kerridge, A. *Inorg. Chem.* **2016**, *55*, 573–583.
- (134) Di Pietro, P.; Kerridge, A. *Phys. Chem. Chem. Phys.* **2016**, *18*, 16830–16839.
- (135) Arnold, P. L.; Turner, Z. R.; Kaltsoyannis, N.; Pelekanaki, P.; Bellabarba, R. M.; Tooze, R. *P. Chem. - A Eur. J.* **2010**, *16* (31), 9623–9629.
- (136) Kerridge, A. *Dalton Trans.* **2013**, *42*, 16428–16436.
- (137) Beekmeyer, R.; Kerridge, A. *Inorganics* **2015**, *3*, 482–499.
- (138) Gregson, M.; Lu, E.; Tuna, F.; McInnes, E. J. L.; Hennig, C.; Scheinost, A. C.; McMaster, J.; Lewis, W.; Blake, A. J.; Kerridge, A.; Liddle, S. *Chem. Sci.* **2016**, *0*, 1–12.
- (139) Herve, A.; Bouzidi, Y.; Berthet, J.; Belkhiri, L.; Thuery, P.; Boucekkine, A.; Ephritikhine, M. *Inorg. Chem.* **2014**, *53*, 6995.
- (140) Wu, H.; Wu, Q.-Y.; Wang, C.-Z.; Lan, J.-H.; Liu, Z.-R.; Chai, Z.-F.; Shi, W.-Q. *Dalt. Trans.* **2015**, *44* (38), 16737–16745.
- (141) Löble, M. W.; Keith, J. M.; Altman, A. B.; Stieber, S. C. E.; Batista, E. R.; Boland, K. S.; Conradson, S. D.; Clark, D. L.; Lezama Pacheco, J.; Kozimor, S. a.; Martin, R. L.; Minasian, S. G.; Olson, A. C.; Scott, B. L.; Shuh, D. K.; Tyliczszak, T.; Wilkerson, M. P.; Zehnder, R. a. *J. Am. Chem. Soc.* **2015**, *137*, 2506–2523.
- (142) Krinsky, J. L.; Minasian, S. G.; Arnold, J. *Inorg. Chem.* **2011**, *50* (1), 345–357.
- (143) Altman, A. B.; Pacold, J. I.; Wang, J.; Lukens, W. W.; Minasian, S. G. *Dalt. Trans.* **2016**.
- (144) D'Angelo, P.; Spezia, R. *Chem. Eur. J.* **2012**, *18* (36), 11162–11178.
- (145) Becke, A. D. *Phys. Rev. A* **1988**, *38* (6), 3098–3100.
- (146) Lee, C.; Yang, W.; Parr, R. G. *Phys. Rev. B* **1988**, *37* (2), 785–789.
- (147) Becke, A. D. *J. Chem. Phys.* **1993**, *98* (7), 5648.
- (148) Stephens, P.; Devlin, F.; Chabalowski, C.; Frisch, M. J. *Phys. Chem.* **1994**, *98* (45), 11623–11627.
- (149) Dolg, M.; Stoll, H.; Preuss, H. *J. Chem. Phys.* **1989**, *90*, 1730–1734.
- (150) Cao, X.; Dolg, M. *J. Chem. Phys.* **2001**, *115* (16), 7348.

- (151) Küchle, W.; Dolg, M.; Stoll, H.; Preuss, H. *J. Chem. Phys.* **1994**, *100* (10), 7535.
- (152) Douglas, M.; Kroll, N. *Ann. Phys. (N. Y.)*. **1974**, *155*, 89–155.
- (153) Hess, B. *Phys. Rev. A* **1986**, *33* (6), 3742–3748.
- (154) Ciupka, J.; Cao-Dolg, X.; Wiebke, J.; Dolg, M. *Phys. Chem. Chem. Phys.* **2010**, *12* (40), 13215–13223.
- (155) D’Angelo, P.; Zitolo, A.; Migliorati, V.; Chillemi, G.; Duvail, M.; Vitorge, P.; Abadie, S.; Spezia, R. *Inorg. Chem.* **2011**, *50* (10), 4572–4579.
- (156) Allen, P. G.; Bucher, J. J.; Shuh, D. K.; Edelstein, N. M.; Craig, I. *Inorg. Chem.* **2000**, *39* (3), 595–601.
- (157) Kerridge, A. *RSC Adv.* **2014**, *4* (24), 12078–12086.
- (158) Andrews, J. S.; Jayatilaka, D.; Bone, R. G. A.; Handy, N. C.; Amos, R. D. *Chem. Phys. Lett.* **1991**, *183*, 423–431.
- (159) Nash, K. L. In *Metal-Ion Separation and Preconcentration*; Bond, A. H., Dietz, M. L., Rogers, R. D., Eds.; ACS Publications, 1999; pp 52–78.
- (160) Tirlir, A. O.; Passler, P. P.; Rode, B. M. *Chem. Phys. Lett.* **2015**, *625*, 120–126.
- (161) Pietro, P. Di; Kerridge, A. **2016**.
- (162) Fryer-Kanssen, I.; Austin, J.; Kerridge, A. *Inorg. Chem.* **2016**, *55* (20), acs.inorgchem.6b00968.
- (163) Whittaker, D. M.; Griffiths, T. L.; Helliwell, M.; Swinburne, A. N.; Natrajan, L. S.; Lewis, F. W.; Harwood, L. M.; Parry, S. a; Sharrad, C. a. *Inorg. Chem.* **2013**, *52* (7), 3429–3444.
- (164) Shannon, B. D.; H, M.; Baur, N. H.; Gibbs, O. H.; Eu, M.; Cu, V. **1976**.
- (165) Afsar, A.; Harwood, L. M.; Hudson, M. J.; Westwood, J.; Geist, A. *Chem. Commun.* **2015**, *51* (27), 5860–5863.
- (166) Edwards, A. C.; Wagner, C.; Geist, A.; Burton, N. A.; Sharrad, C. A.; Adams, R. W.; Pritchard, R. G.; Panak, P. J.; Whitehead, R. C.; Harwood, L. M. *Dalt. Trans.* **2016**, *45* (45), 18102–18112.
- (167) Afsar, A.; Laventine, D. M.; Harwood, L. M.; Hudson, M. J.; Geist, A. *Chem. Commun. (Camb)*. **2013**, *49* (76), 8534–8536.
- (168) Wu, H.; Wu, Q.; Wang, C.; Lan, J.; Liu, Z. **2016**, 8107–8117.
- (169) Roy, L. E.; Bridges, N. J.; Martin, L. R. *Dalton Trans.* **2013**, *42* (7), 2636–2642.
- (170) Preihs, C.; Arambula, J. F.; Magda, D.; Jeong, H.; Yoo, D.; Cheon, J.; Siddik, Z. H.; Sessler, J. L. *Inorg. Chem.* **2013**, *52* (21), 12184–12192.
- (171) Sessler, J. L.; Mody, T. D.; Hemmi, G. W.; Lynch, V. *Inorg. Chem.* **1993**, *32* (14), 3175–3187.
- (172) Sessler, J. L.; Tvermoes, N. a.; Guldi, D. M.; Mody, T. D.; Allen, W. E. *J. Phys. Chem. A* **1999**, *103* (7), 787–794.
- (173) Sessler, J. L.; Hemmi, G.; Mody, T. D.; Murai, T.; Burrell, A.; Young, S. W. **1994**, 43–50.
- (174) Langford, M. H. Development of a simplified soft-donor technique for trivalent

actinide-lanthanide separations, 2015.

- (175) Mondry, A.; Starynowicz, A. *Polyhedron* **2000**, *19* (7), 771–777.
- (176) Lodi Rizzini, A.; Krull, C.; Mugarza, A.; Balashov, T.; Nistor, C.; Piquerel, R.; Klyatskaya, S.; Ruben, M.; Sheverdyaeva, P. M.; Moras, P.; Carbone, C.; Stamm, C.; Miedema, P. S.; Thakur, P. K.; Sessi, V.; Soares, M.; Yakhou-Harris, F.; Cezar, J. C.; Stepanow, S.; Gambardella, P. *Surf. Sci.* **2014**, *630*, 361–374.
- (177) Cao, W.; Gao, C.; Zhang, Y.-Q.; Qi, D.; Liu, T.; Wang, K.; Duan, C.; Gao, S.; Jiang, J. *Chem. Sci.* **2015**, *6* (10), 5947–5954.
- (178) Kan, J.; Wang, H.; Sun, W.; Cao, W.; Tao, J.; Jiang, J. *Inorg. Chem.* **2013**, *52* (15), 8505–8510.
- (179) Sekhosana, K. E.; Manyeruke, M. H.; Nyokong, T. *J. Mol. Struct.* **2016**, *1121*, 111–118.
- (180) Sekhosana, K. E.; Nyokong, T. *Opt. Mater. (Amst)*. **2015**, *47*, 211–218.
- (181) Girolami, G. S.; Gorlin, P. A.; Milam, S. N.; Suslick, K. S.; Wilson, S. R. *J. Coordination Chem.* **1994**, *32* (1–3), 173–212.
- (182) Streitwieser, A.; Yoshida, N. *J. Am. Chem. Soc.* **1969**, *91* (26), 7528–7528.
- (183) Streitwieser, A.; Müller-Westerhoff, U. *J. Am. Chem. Soc.* **1968**, *90* (26), 7364.
- (184) Starks, D. F.; Parsons, T. C.; Streitwieser, A.; Edelstein, N. *Inorg. Chem.* **1974**, *13* (6), 1307–1308.
- (185) Karraker, D. G.; Stone, J. A.; Jones, E. R.; Edelstein, N. *J. Am. Chem. Soc.* **1970**, *92* (16), 4841–4845.
- (186) Ekuma, C. E.; Anisimov, V. I.; Moreno, J.; Jarrell, M. *Eur. Phys. J. B* **2014**, *87* (1), 23.